
Inferring the equation of state with multi-messenger signals from binary neutron star mergers

DISSERTATION

zur Erlangung des akademischen Grades
doctor rerum naturalium (Dr. rer. nat.)



vorgelegt dem Rat der
PHYSIKALISCH-ASTRONOMISCHEN FAKULTÄT
der
FRIEDRICH-SCHILLER-UNIVERSITÄT JENA
von
Matteo BRESCHI (M.Sc.)
geboren am 06.05.1992 in Pistoia (Italien)

REVIEWERS:

1. Prof. Dr. Sebastiano BERNUZZI (Friedrich-Schiller-Universität Jena)
2. Prof. Dr. Katerina CHATZIOANNOU (California Institute of Technology)
3. Prof. Dr. Nikolaos STERGIOULAS (Aristotle University of Thessaloniki)

DEFENSE DATE: 25.04.2023

Declaration of Authorship

I, Matteo BRESCHI, declare that this thesis titled, “Inferring the equation of state with multi-messenger signals from binary neutron star mergers” and the work presented in it are my own. I confirm that:

- This work was done wholly or mainly while in candidature for a research degree at this University.
- Where any part of this thesis has previously been submitted for a degree or any other qualification at this University or any other institution, this has been clearly stated.
- Where I have consulted the published work of others, this is always clearly attributed.
- Where I have quoted from the work of others, the source is always given. With the exception of such quotations, this thesis is entirely my own work.
- I have acknowledged all main sources of help.
- Where the thesis is based on work done by myself jointly with others, I have made clear exactly what was done by others and what I have contributed myself.

Signed:

Date:

Acknowledgements

I am grateful to the members of the CoRE Collaboration, the Prometeo-Virgo group, the *Extreme matter* and the *Tests of GR* subgroups of CBC group of LIGO-Virgo-KAGRA Collaboration (LVK) and the DFG-RTG *Physik Combo* group for discussions and contributions. In particular, I explicitly thank Sebastiano Bernuzzi, Walter Del Pozzo, Albino Perego and Michalis Agathos for important advises and for mentoring my academical studies. I extend warm greetings to my colleagues and friends who supported me during my graduate studies, Gregorio Carullo, Francesco Zappa, Francesco Maria Fabbri, Vsevolod Nedora, and Rossella Gamba.

The author acknowledges support by the EU H2020 under ERC Starting Grant, no. BinGraSp-714626 and from the Deutsche Forschungsgemeinschaft (DFG) under Grant No. 406116891 within the Research Training Group (RTG) 2522/1. The computational experiments were mainly performed on the ARA cluster at the Friedrich-Schiller-Universität Jena supported in part by DFG grants INST 275/334-1 FUGG and INST 275/363-1 FUGG and ERC Starting Grant, no. BinGraSp-714626. This research has made use of data obtained from the Gravitational Wave Open Science Center (GWOSC) [1], a service of LVK. LIGO is funded by the U.S. National Science Foundation. Virgo is funded by the French Centre National de Recherche Scientifique (CNRS), the Italian Istituto Nazionale della Fisica Nucleare (INFN) and the Dutch Nikhef, with contributions by Polish and Hungarian institutes. KAGRA is funded by Japanese National Research Foundation, with contributions by Korean and Taiwanese institutes.

Abstract

Matteo BRESCHI

*Inferring the equation of state with multi-messenger signals
from binary neutron star mergers*

The joint detection of the GW170817 and its electromagnetic counterparts was a milestone in multi-messenger astronomy. We investigate the observational constraints on the neutron star equation of state provided by multi-messenger data of binary neutron star mergers, analyzing the gravitational-wave transient GW170817 and its kilonova counterpart AT2017gfo and exploring new scenarios with next-generation gravitational-wave detectors. The LIGO-Virgo data of GW170817 are analyzed using different template models focusing on the implications for neutron star matter properties. We study the systematic tidal errors between current gravitational-wave models finding that waveform systematics dominate over statistical errors at signal-to-noise ratio $\gtrsim 100$. We study AT2017gfo using semi-analytical model showing that observational data favor multi-component anisotropic geometries to spherically symmetric profiles. By joining GW170817 and AT2017gfo information with the NICER measurements, we infer the neutron star equation of state constraining the radius $R_{1.4M_\odot}$ of a $1.4 M_\odot$ neutron star to $12.39_{-0.65}^{+0.70}$ km and the maximum mass M_{\max}^{TOV} to $2.08_{-0.09}^{+0.16} M_\odot$ (90% credible level). Finally, we explore future constraints on extreme-matter delivered by postmerger gravitational-waves from binary neutron star merger remnants. These transients can be detected with matched-filtering techniques and numerical-relativity-informed models for signal-to-noise ratios $\gtrsim 7$. Postmerger remnants can probe the high-density regimes of the nuclear equation of state, allowing the inference of the maximum neutron star mass M_{\max}^{TOV} with an accuracy of 12% (90% credible level). Moreover, postmerger transients can be used to infer the presence of non-nucleonic matter phases through the inference of softening of the equation of state. For particular binary configurations, softening effects of the equation of state can lead to breaking of quasiuniversal properties and earlier collapse into black hole. These deviations can be detected for postmerger signals with signal-to-noise ratio $\gtrsim 9$.

Published content and contributions

Publications as leading author

For each of the following manuscripts, I contributed to the drafting of the entire text, the production of all figures and tables, the production of all results, the implementation and the development of all computational methods.

1. **M. Breschi**, S. Bernuzzi, F. Zappa, M. Agathos, A. Perego, D. Radice, and A. Nagar, “Kilohertz gravitational waves from binary neutron star remnants: time-domain model and constraints on extreme matter,” *Phys. Rev.*, vol. D100, no. 10, p. 104029, 2019.
2. **M. Breschi**, R. O’Shaughnessy, J. Lange, and O. Birnholtz, “IMR consistency tests with higher modes on gravitational signals from the second observing run of LIGO and Virgo,” *Class. Quantum Grav.*, vol. 36, no. 24, 2019.
3. **M. Breschi**, A. Perego, S. Bernuzzi, W. Del Pozzo, V. Nedora, D. Radice, and D. Vescovi, “AT2017gfo: Bayesian inference and model selection of multicomponent kilonovae and constraints on the neutron star equation of state,” *Mon. Not. Roy. Astron. Soc.*, vol. 505, no. 2, pp. 1661–1677, 2021.
4. **M. Breschi**, R. Gamba, and S. Bernuzzi, “Bayesian inference of multimessenger astrophysical data: Methods and applications to gravitational waves,” *Phys. Rev. D*, vol. 104, no. 4, p. 042001, 2021.
5. **M. Breschi**, S. Bernuzzi, D. Godzieba, A. Perego, and D. Radice, “Constraints on the Maximum Densities of Neutron Stars from Postmerger Gravitational Waves with Third-Generation Observations,” *Phys. Rev. Lett.*, vol. 128, no. 16, p. 161102, 2022.
6. **M. Breschi**, S. Bernuzzi, K. Chakravarti, A. Camilletti, A. Prakash, and A. Perego, “Kilohertz gravitational waves from binary neutron star mergers: Numerical-relativity informed postmerger model,” (*Submitted to Phys. Rev. D*), 2022.

7. **M. Breschi**, R. Gamba, S. Borhanian, G. Carullo, and S. Bernuzzi, “Kilohertz gravitational waves from binary neutron star mergers: Inference of postmerger signals with the Einstein Telescope,” (*Submitted to Phys. Rev. D*), 2022.

Publications as coauthor

1. M. Agathos, F. Zappa, S. Bernuzzi, A. Perego, **M. Breschi**, and D. Radice, “Inferring Prompt Black-Hole Formation in Neutron Star Mergers from Gravitational-Wave Data,” *Phys. Rev. D*, vol. D101, no. 4, p. 044006, 2020.
Contributions: Results of Appendix A; Table 3.
2. S. Bernuzzi, **M. Breschi**, B. Daszuta, A. Endrizzi, D. Logoteta, V. Nedora, A. Perego, F. Schianchi, D. Radice, F. Zappa, I. Bombaci, and N. Ortiz, “Accretion-induced prompt black hole formation in asymmetric neutron star mergers, dynamical ejecta and kilonova signals,” *Mon. Not. Roy. Astron. Soc.*, Jun. 2020.
Contributions: Text of Section 5; Figures 8, 9, and 10; Table 3.
3. R. Gamba, **M. Breschi**, S. Bernuzzi, M. Agathos, and A. Nagar, “Waveform systematics in the gravitational-wave inference of tidal parameters and equation of state from binary neutron star signals,” *Phys. Rev. D*, vol. 103, no. 12, p. 124015, 2021.
Contributions: Text of Sections 2, and 4; Text of Appendix B; Method of Section 2; Figures 1, 4, 5, and 9; Table 4.
4. S. Schmidt, **M. Breschi**, R. Gamba, G. Pagano, P. Rettegno, G. Riemenschneider, S. Bernuzzi, A. Nagar, and W. Del Pozzo, “Machine learning gravitational waves from binary black hole mergers,” *Phys. Rev. D*, vol. 103, no. 4, p. 043020, 2021.
Contributions: Comments and discussions.
5. G. Riemenschneider, P. Rettegno, **M. Breschi**, A. Albertini, R. Gamba, S. Bernuzzi and A. Nagar, “Assessment of consistent next-to-quasicircular corrections and postadiabatic approximation in effective-one-body multipolar waveforms for binary black hole coalescences,” *Phys. Rev. D*, vol. 104, no. 10, p. 104045, 2021.
Contributions: Text of Section 5; Results of Section 5.
6. R. Gamba, **M. Breschi**, G. Carullo, P. Rettegno, S. Albanesi, S. Bernuzzi, and A. Nagar, “GW190521: A dynamical capture of two black holes,” (*Submitted to*

Nature), 2021.

Contributions: Results of GW190521 analysis.

7. A. Bonino, R. Gamba, P. Schmidt, A. Nagar, G. Pratten, **M. Breschi**, P. Rettengo, and S. Bernuzzi, “Inferring eccentricity evolution from observations of coalescing binary black holes,” (*Submitted to Phys. Rev. D*), 2022.

Contributions: Results of Sections 4 and 5.

Publications with LIGO-Virgo-KAGRA Collaboration

1. B. P. Abbott *et al.*, “Tests of general relativity with the binary black hole signals from the LIGO-Virgo catalog GWTC-1,” *Phys. Rev. D*, vol. 100, no. 10, p. 104036, 2019.

Contributions: Results of Section 5

2. B. P. Abbott *et al.*, “GW190412: Observation of a binary-black-hole coalescence with asymmetric masses,” *Phys. Rev. D*, vol. 102, no. 4, p. 043015, 2020.

Contributions: Reviewer for parameter estimation runs.

3. B. P. Abbott *et al.*, “GW190521: A Binary Black Hole Merger with a Total Mass of $150 M_{\odot}$,” *Phys. Rev. Lett.*, vol. 125, no. 101102, 2020.

Contributions: Reviewer for parameter estimation runs.

4. B. P. Abbott *et al.*, “Properties and Astrophysical Implications of the $150 M_{\odot}$ Binary Black Hole Merger GW190521,” *Astroph. J. Lett.*, vol. 900, no. 1, 2020.

Contributions: Reviewer for parameter estimation runs.

5. B. P. Abbott *et al.*, “GW190814: Gravitational Waves from the Coalescence of a 23 Solar Mass Black Hole with a 2.6 Solar Mass Compact Object,” *Astroph. J. Lett.*, vol. 896, no. 2, 2020.

Contributions: Reviewer for parameter estimation runs.

6. B. P. Abbott *et al.*, “GW190425: Observation of a Compact Binary Coalescence with Total Mass $\sim 3.4 M_{\odot}$,” *Astroph. J. Lett.*, vol. 892, no. 1, 2020.

Contributions: Reviewer for parameter estimation runs.

Talks and seminars

1. *Talk*: “Kilohertz gravitational-waveforms from neutron star merger remnants”, Workshop “*Astrophysics with GW detections*”, Sept. 2019, Nicolaus Copernicus Astronomical Center (CAMK) and University of Warsaw, Warsaw, Poland.
2. *Plenary talk*: “Inferring the nature of postmerger remnant in GW170817”, Workshop “*The first compact star merger event*”, Oct. 2019, European Centre for Theoretical Studies in Nuclear Physics and Related Areas (ECT*), Trento, Italy.
3. *Seminar*: “Bayesian analysis of multimessenger signals from neutron star collisions”, Invitation to Trento Institute for Fundamental Physics and Applications (TIFPA), Oct. 2019, Trento, Italy.
4. *Talk*: “GW170817 and AT2017gfo, a multimessenger Bayesian analysis”, 14th Edoardo Amaldi Conference on Gravitational Waves, Jul. 2021, Centre of Excellence for Gravitational Wave Discovery (OzGrav), Melbourne, Australia.
5. *Talk*: “Multimessenger constraints on the neutron star equation of state”, “*The gravitational wave physics and astronomy*” workshop (GWPAW), Dec. 2021, Albert Einstein Institute (AEI), Hannover, Germany.
6. *Seminar*: “Multimessenger Bayesian analysis of binary neutron star mergers”, Invitation to Gran Sasso Science Institute (GSSI), Jan. 2022, L’Aquila, Italy.
7. *Plenary talk*: “Multi-messenger studies of binary neutron stars mergers and perspectives with next-generation gravitational-wave detectors”, European Einstein Toolkit meeting, Sep. 2022, University College Dublin (UCD), Dublin, Ireland.

Contents

Declaration of Authorship	i
Acknowledgements	ii
Abstract	iii
Contents	viii
List of Figures	xi
List of Tables	xiii
List of Acronyms	xiv
List of Constants	xv
List of Symbols	xvi
Introduction	1
1 Bayesian inference	9
1.1 Definitions	10
1.2 Bayes' theorem	10
1.3 BAJES: the Bayesian Jeneer software	12
1.3.1 Pipeline	13
1.3.2 Parallelization	15
2 Inspiral gravitational-waves	17
2.1 Waveform models	17
2.1.1 Tidal interaction	22
2.2 Inference of GW170817	24
2.2.1 Source properties	27

2.2.2	Tidal inference	27
2.3	Parameter estimation errors	29
2.3.1	Statistical errors	30
2.3.2	Systematic errors	32
2.4	Black hole collapse	34
2.4.1	Threshold mass	35
2.4.2	Tidal threshold	37
3	Electromagnetic counterparts	38
3.1	Light-curve models	39
3.1.1	Single-component ejecta	39
3.1.2	Multi-component ejecta	41
3.2	Inference of AT2017gfo	44
3.2.1	Multi-component model selection	45
3.2.2	Ejecta properties	46
3.3	Multi-messenger parameter estimation	49
3.3.1	Mapping the dynamical ejecta properties	50
3.3.2	Incorporating electron fraction and disk mass	52
3.3.3	Inferring the neutron star radius	53
3.3.4	Including NICER information	54
4	Postmerger gravitational-wave models	59
4.1	Morphology	60
4.2	Quasiuniversal properties	62
4.2.1	Nodal points	63
4.2.2	Postmerger peak frequency	65
4.3	Numerical-relativity-informed models	66
4.3.1	NRPM	67
4.3.2	NRPM _w	67
4.3.3	Recalibration parameters	68
4.3.4	Unfaithfulness	69
4.4	Full-spectrum models	73
5	Next-generation gravitational-wave observations	75
5.1	Einstein Telescope	76
5.2	Postmerger inference	76

5.2.1	Injection settings	77
5.2.2	Detectability	78
5.2.3	Parameter estimation	80
5.3	Softening effects	83
5.3.1	Breaking of quasiuniversality	85
5.3.2	Consistency test	87
5.4	High-density constraints	89
5.4.1	Inferring the maximum density	91
5.4.2	Implications for the equation of state	93
Conclusions		95
A Sampling methods		101
A.1	Markov-chain Monte Carlo	101
A.2	Nested sampling	104
B Time-domain NRPM model		106
B.1	Modeling choices	106
B.1.1	Phase	106
B.1.2	Amplitude	108
B.1.3	Prompt collapse	108
B.2	Calibration	109
C Frequency-domain NRPM_w model		112
C.1	Wavelet components	112
C.1.1	Modulation modeling	113
C.1.2	Wavelet combination	115
C.2	Calibration	118
C.3	Computational costs	121
Bibliography		123

List of Figures

1	Mass-radius sequences	4
2	Binary neutron star merger	6
1.1	BAJES validation	14
1.2	BAJES parallelization	16
2.1	Gravitational waveform	19
2.2	GW170817: Masses and spins	26
2.3	GW170817: Tidal parameter	28
2.4	Signal power and tidal information	31
2.5	Tidal systematic errors	33
2.6	Threshold methods for prompt collapse	35
3.1	Multi-component kilonova	41
3.2	AT2017gfo: Light-curves	46
3.3	AT2017gfo: Dynamical and viscous ejecta	47
3.4	GW170817-AT2017gfo inference	50
3.5	Neutron star radius	54
3.6	GW170817-AT2017gfo-NICER constraints	58
4.1	Postmerger morphologies	60
4.2	Nodal points	64
4.3	Quasiuniversal relation of f_2	65
4.4	Unfaithfulness of postmerger models	70
4.5	Postmerger models and numerical relativity data	72
4.6	Unfaithfulness of full-spectrum model	74
5.1	Postmerger detectability	79
5.2	Recovered postmerger spectra	80
5.3	Recovered postmerger frequency	81
5.4	Recovered time of collapse	82

5.5	DD2 and BHBA ϕ	84
5.6	Softening effects	85
5.7	Consistency test for softening effects	87
5.8	High-density relations	90
5.9	Maximum density inference	92
5.10	Mass-radius constraints	93
3	Multi-messenger framework	100
B.1	NRPM template	107
B.2	NRPM frequencies	110
B.3	NRPM amplitudes and times	111
C.1	NRPM _w morphology	116
C.2	NRPM _w residuals	120
C.3	NRPM _w computational costs	121

List of Tables

3.1	Kilonova model selection	45
3.2	Multi-messenger parameter estimation	56

List of Acronyms

BBH	Binary black hole	BH	Black hole
BNS	Binary neutron star	BF	Bayes' factor
CBC	Compact binary coalescence	CDF	Cumulative distribution function
CPU	Central processing unit	DA	Data analysis
EM	Electromagnetic	EOB	Effective-one-body
EOS	Equation of state	ET	Einstein Telescope
FWHM	Full width at half maximum	GR	General relativity
GRHD	General-relativistic hydrodynamics	GRB	Gamma-ray burst
GW	Gravitational-wave	HOM	Higher-order mode
IFO	Interferometer	IR	Infrared
ISM	Interstellar medium	KN	Kilonova
LC	Light-curve	LVK	LIGO-Virgo-KAGRA
MCMC	Markov-chain Monte Carlo	MM	Multi-messenger
MPI	Message passing interface	MS	Model selection
NIR	Near infrared	XG	Next-generation
NR	Numerical relativity	NS	Neutron star
PC	Prompt collapse	PDF	Probability density function
PE	Parameter estimation	PM	Postmerger
PN	Post-Newtonian	PP	Point-particle
PSD	Power spectral density	PTMCMC	Parallel tempering MCMC
QNM	Quasi-normal mode	RMS	Root-mean-square
ROQ	Reduced-order-quadrature	SNR	Signal-to-noise ratio
TOV	Tolman-Oppenheimer-Volkoff	UV	Ultraviolet

List of Constants

Name	Symbol = Value
Pi	$\pi = 3.14159265358979\dots$
Euler's number	$e = 2.71828182845904\dots$
Speed of light	$c = 299792458 \text{ m s}^{-1}$
Universal gravitational constant	$G = 6.674 \times 10^{-11} \text{ m}^3 \text{ kg}^{-1} \text{ s}^{-2}$
Reduced Plank's constant	$\hbar = 1.054571817 \times 10^{-34} \text{ J s}$
Elementary charge	$e = 1.602176634 \times 10^{-19} \text{ C}$
Boltzmann's constant	$k_{\text{B}} = 1.380649 \times 10^{-23} \text{ J K}^{-1}$
Stephan-Boltzmann constant	$\sigma = 5.670374419 \times 10^{-8} \text{ W m}^{-2} \text{ K}^{-4}$
Electron mass	$m_e = 9.1093837015 \times 10^{-31} \text{ kg}$
Proton mass	$m_p = 1.67262192369 \times 10^{-27} \text{ kg}$
Neutron mass	$m_n = 1.67492749804 \times 10^{-27} \text{ kg}$
Solar mass	$M_{\odot} = 1.98847 \times 10^{30} \text{ kg}$
Nuclear saturation density	$\rho_{\text{sat}} = 2.7 \times 10^{17} \text{ kg m}^{-3}$

List of Symbols

Symbol	Name	Unit
\log	Natural logarithm	–
p	Probability density function	–
P	Cumulative distribution function	–
\mathcal{B}	Bayes' factor	–
\mathbf{d}	Array of measurements	–
$\boldsymbol{\theta}$	Parameters vector	–
t	Time	Second [s], millisecond [ms]
f	Frequency	Hertz [Hz], kilohertz [kHz]
m, M	Mass	Solar mass [M_{\odot}]
r, R	Separation, radius	Meter [m], kilometer [km]
v	Speed	Meter per second [m/s], speed of light [c]
P	Pressure	Dyne per squared centimeter [dyn cm^{-2}]
ρ	Density	Gram per cubed centimeter [g cm^{-3}]
q	Mass ratio	$[\geq 1]$
$\boldsymbol{\chi}$	Dimensionless spin vector	–
Λ	Dimensionless tidal parameter	–
D_L	Luminosity distance	Megaparsec [Mpc]
ι	Inclination angle	Radian

Introduction

Neutron stars (NSs) are compact stars with typical masses $M \simeq 1.4 M_{\odot}$ and equatorial radii $R \simeq O(10 \text{ km})$. These objects are created as a result of gravitational collapse of the central core of giant stars with mass $\sim 10 - 25 M_{\odot}$ [2, 3]. The gravitational collapse combined with the supernova (SN) compresses the star core to densities comparable to atomic nuclei, triggering electronic capture processes. Due to their significant compactness, i.e. $C = (GM)/(c^2 R) \simeq 0.1 - 0.3$, NSs are relativistic objects and their constituent matter reaches an extreme-density regime, i.e. $\rho \gtrsim \rho_{\text{sat}}$. In general relativity (GR), the hydrostatic equilibrium of spherically-symmetric self-gravitating objects, such as NSs, is governed by the Tolman-Oppenheimer-Volkoff (TOV) equation [4, 5] and by the equation of state (EOS), that defines the density-pressure relation $P(\rho)$ in the interior of the star [e.g. 6, 7, 8]. The determination of the NS EOS is an open theoretical problem since it requires the characterization of the nuclear many-body interaction in extreme conditions of density, neutron-proton asymmetry and temperature [9, 10, 11]. The central density of a NSs with mass of $1.4 M_{\odot}$ is expected to be $\sim 2\rho_{\text{sat}}$ [12]; while, for a $2 M_{\odot}$ NS, the central density may reach values $\gtrsim 4\rho_{\text{sat}}$. In these conditions, the actual nuclear constituents of NSs are largely uncertain [e.g. 12, 13] and astronomical data of NSs can provide important observational information [e.g. 14, 15, 16, 17]. In particular, binary neutron star (BNS) mergers can probe the properties of the nuclear matter thanks to the direct observation of dense matter in dynamical and strong-field conditions.

Astronomical observations of neutron stars. The existence of NSs has been proposed in 1933 by Baade and Zwicky [18] one year after the discovery of neutrons [19], in order to tentatively explain the massive SN remnants. Three decades later, the radio astronomers Hewish and Okoye [20] and Bell Burnell [21] detected radio pulses from stars that are now believed to be highly magnetized and rapidly spinning NSs, known as pulsars. A pulsar is a NS that emits beams of electromagnetic (EM) radiation out of their magnetic poles. The EM radiation originates pulses with a regular period that can be observed if a beam is pointing toward Earth. Of particular interest is

the discovery of Hulse and Taylor [22] in 1974 of the first pulsar in a binary system. Thanks to the measurement of the orbital period decay, this system provided the first indirect observational evidence for the existence of gravitational radiation [23]. Radio pulsars represented a milestone for the history of NS observations since they provided accurate estimates of the NS masses, proved the existence of NSs in binary systems, and allowed for the first tests of GR with compact binary coalescences (CBCs) [e.g. 23, 24, 25].

The promising observations of radio pulsars and the indirect proof of gravitational radiation increased the interest of scientific community for gravitational-wave (GW) observations. The development of the first GW detectors was mainly led by Weber [26, 27] in the late 1960s, with the employment of resonant bars coupled with piezoelectric transducers. However, these instruments did not permit a confident detection of GWs due to their narrow sensitivity band and the excess of thermal noise [28]. This pushed the community towards the development of improved instruments with wider sensitivity ranges, such as laser interferometers (IFOs), initiating the large-scale experiments of Laser Interferometer Gravitational-Wave Observatory (LIGO) [29, 30] and Virgo [31] at the European Gravitational Observatory (EGO). About a century after their theoretical prediction [32, 33], the first GW signal was been detected by the ground-based IFOs of LIGO on September 15, 2014 [34]. This unprecedented transient, known as GW150914, corresponded to the gravitational radiation emitted by a binary black hole (BBH) merger with binary mass $M = m_1 + m_2 \simeq 62 M_\odot$ located at a luminosity distance of ~ 400 Mpc. The detection of GW150914 opened a window on the GW universe, permitting new studies and investigations of several aspects of fundamental physics and observational astrophysics, such as strong-field gravity, astrophysical populations and cosmology [e.g. 35, 36, 37, 38].

The first direct observation of a BNS GW signal, namely GW170817 [39, 40], was recorded two years later, on August 17, 2017, by the ground-based IFOs LIGO and Virgo. GW170817 data are consistent with the gravitational radiation emitted by two inspiralling NSs. The transient lasted in the detectors for more than one minute, showing the characteristic chirping frequency pattern expected for these sources [41]. GW170817 was followed by a short gamma-ray burst (GRB), labeled GRB170817A [42], which reached the space observatories ~ 1.7 s after the binary coalescence time [43, 44]. Eleven hours later, several telescopes started to collect photometric and spectroscopical data from AT2017gfo, a kilonova (KN) transient coming from a coincident region of the sky [45, 46, 47, 48, 49, 50, 51, 52, 53]. The follow up of

the source lasted for more than a month and included also non-thermal emission from the GRB170817A afterglow [e.g., 54, 55].

More recently, LIGO-Virgo IFOs recorded a second BNS merger, i.e. GW190425 [56], with no identification of EM counterparts. This unfortunate result is primarily due to the fact that the source was located at a luminosity distance $\gtrsim 150$ Mpc and the signal was observed with high confidence only in a single IFO, leading to an inaccurate sky localization of the source, i.e. $\sim 10^4$ deg² at the 90% confidence level. Moreover, the GW190425 progenitors had a total mass $\gtrsim 3 M_{\odot}$, reinforcing the hypothesis of a faint KN transient [57, 58]. On the other hand, astronomical observatories identified a possible KN candidate associated to a long GRB [59]; however, the interpretation of this event is uncertain since no GW counterpart has been observed. In recent years, a facility providing new NS observations is the Neutron Star Interior Composition Explorer (NICER) [60, 61, 62, 63, 64, 65]. This telescope is located on the International Space Station and performs spectroscopic observations of the thermal and non-thermal emissions coming from known pulsars in the X-ray band. To date, NICER has provided estimates of the masses and the radii of PSR J0030+0451 and PSR J0740+6620.

The combined observation of GW170817, GRB170817A and AT2017gfo decreed the dawn of multi-messenger (MM) astronomy with CBCs [66]. MM inference of astrophysical events, such as BNS mergers, is a fundamental resource to shed light on the mechanism at the origin of the observed transients, obtain accurate measurements of the source properties and improve theoretical models, by gaining information from observational data. Among all the possible physical information that can be extracted from these events, in this *Thesis* we focus on constraints on the NS EOS [e.g. 67, 68, 69, 70, 71, 72]; however, we recall as relevant GW170817-AT2017gfo analyses the studies on cosmological expansion [73] and strong-field gravity [74]. Furthermore, in the coming years, current IFOs are expected to upgrade their sensitivities, increasing the signal-to-noise ratios (SNRs) of the observed sources and improving their progenitors properties identification [29, 30, 31, 75, 76, 77]. Moreover, the GW detector network is expected to extend by annexing the Kamioka Gravitational Wave Detector (KAGRA) [78] and implementing next-generation (XG) facilities [75, 77, 79]. These developments will provide a broader coverage of the sky and a wider range of sensitivity in the GW spectrum. In view of these new facilities, it is essential to develop a framework for MM data analysis (DA) of BNS mergers and EOS inference.

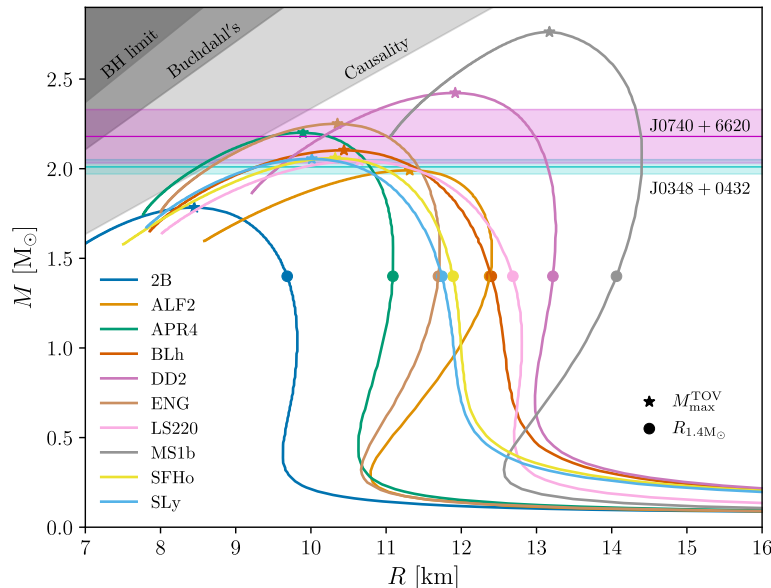


FIGURE 1: Exemplary set of mass-radius sequences for non-rotating zero-temperature NS extracted from polytropic and microphysical EOSs. For each EOS, we highlight the maximum mass configuration M_{\max}^{TOV} (stars) and the radius $R_{1.4M_{\odot}}$ for a $1.4 M_{\odot}$ NS (circles). The plot also shows the masses from two pulsar observations [87, 88] and the theoretical constraints.

The equation of state. The core of a non-rotating zero-temperature NS is typically modeled as a fluid of neutrons in β -equilibrium. The NS core is sustained by the neutron degeneracy pressure and repulsive nuclear forces that prevent it from collapsing into a black hole (BH). More accurate descriptions of NS cores include also protons, electrons and muons [e.g. 80]. Moving outward, the crust is expected to be composed of electrons and atomic nuclei, as well as of free neutrons [80]. Matching the predictions for the crust and the core, it is possible to estimate the pressure-density relation $P(\rho)$. The latter can be plugged in the TOV system in order to estimate the mass-radius sequence $M(R)$ for a non-rotating zero-temperature NS. The nuclear origin of the forces that sustain a NS permit the connection between the microscopical nuclear description of the interior and the macroscopical observable quantities, such as NS masses and radii. Furthermore, in a realistic scenario, the properties of NS matter are affected by several physical contributions that extend the previous description, such as finite temperatures [e.g. 81], rotational support [e.g. 82], neutrino trapping [e.g. 83] and non-nucleonic matter [e.g. 8, 84, 85, 86].

Figure 1 shows the mass-radius sequences extracted from an exemplary subset of

hadronic and polytropic EOSs together with a few notable theoretical and observational constraints. In this *Thesis*, we make use of nuclear EOSs computed in different works. The finite temperature, composition-dependent EOSs are: BHBA ϕ [85], BLh [8, 11], BLQ [8, 11, 86], DD2 [10, 89], LS220 [9], SFHo [90], SLy [80, 91]; the EOSs in piecewise polytropic forms are: ALF2 [92], ENG [93], MPA [94], MS1(b) [95], 2B, 2H, 15H, 125H, B, H, H4, HB from Ref. [6, 96] and the $\Gamma=2$ ideal gas EOS. In general, the low-density properties of EOS, i.e. $\rho \lesssim \rho_{\text{sat}}$, are extrapolated employing nuclear experimental results from hadron and heavy ions collisions [e.g. 97, 98, 99, 100, 101, 102, 103]. Moving toward higher densities, i.e. $\rho \gtrsim \rho_{\text{sat}}$, different approaches and modeling choices lead to different description of the NS matter. In particular, the radius $R_{1.4M_{\odot}}$ of a $1.4 M_{\odot}$ NS can span roughly the range 9–15 km, while the maximum mass $M_{\text{max}}^{\text{TOV}}$ for a non-rotating zero-temperature NS lies between $1.8 M_{\odot}$ and $2.7 M_{\odot}$. It is common practice to qualitatively label as *soft* EOSs the relations that sustain small radii and small $M_{\text{max}}^{\text{TOV}}$ (e.g. 2B and APR4), in order to distinguish them from the *stiff* EOSs that support larger values of $R_{1.4M_{\odot}}$ and $M_{\text{max}}^{\text{TOV}}$ (e.g. DD2 and MS1b). However, the presence of non-hadronic phases of matter may lead to a softening of the EOS, decreasing the maximum supported mass $M_{\text{max}}^{\text{TOV}}$ [67, 85, 86].

Fundamental theoretical results can only impose upper-bounds in the mass-radius diagram, denoting prohibited regions for the TOV solutions, that are localized in a very-high-density regime. The weaker constraint is given by pure GR arguments and it is labeled as the BH limit: this region yields to a compactness $C \geq 1/2$; then, this object is expected to collapse into a BH. The Buchdahl’s limit [104] comes as a consequence of the TOV equation imposing non-negative density and pressure and it requires the mass to be $M < 4Rc^2/9G$. Finally, the strongest theoretical constraint is given by the causality principle, for which the speed of sound in the NS matter is imposed to be smaller or equal than the speed of light c . We include in this context the estimates of NS masses from the massive radio pulsars PSR J0348+0432 [87] and PSR J0740+6620 [88], as shown in Figure 1. These values can be interpreted as lower bounds for the maximum mass $M_{\text{max}}^{\text{TOV}}$ of a non-rotating stable NS in equilibrium. In general, pulsar data show that the NS EOS sustains a maximum mass $M_{\text{max}}^{\text{TOV}} \gtrsim 2 M_{\odot}$.

The dynamics of binary neutron star mergers. The dynamics of BNS mergers is governed by multiple interactions that act on different timescales: gravitational fields determine the orbital dynamics; (strong) nuclear forces between the NS components determine the matter properties during the plunge; electroweak decays occur in the unbound matter after merger, brightening the EM counterparts. Furthermore, the

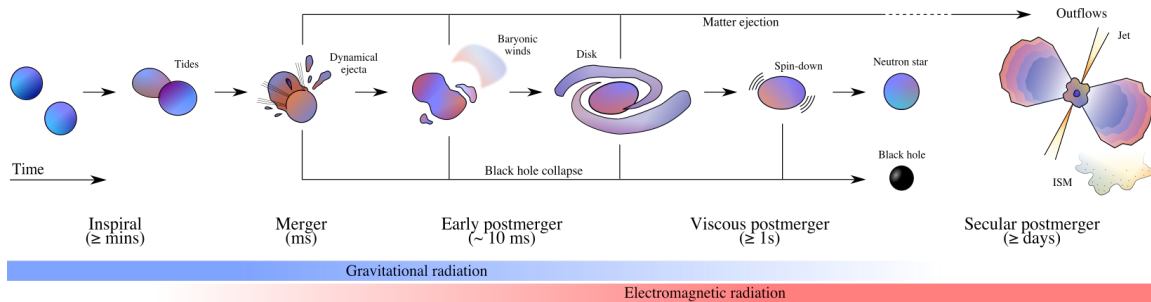


FIGURE 2: Schematic representation of a BNS merger. The cartoon highlights the consecutive stages of the system and the relevant phenomena that are expected to occur during the evolution. The typical timescale of the different stages are reported between brackets. The blue and red bands (at the bottom) show the nature of the transients emitted by the system during the consecutive stages, corresponding respectively to GW and EM radiations.

inclusion of finite-temperature effects and general-relativistic hydrodynamics (GRHD) is necessary in order to accurately model the evolution of a BNS system. The variety of interactions is reflected in several information carriers, that span from GWs to radio transients and make BNS mergers extraordinary system to test physical models against observational data. On the other hand, the complexity of these phenomena places challenging theoretical problems for the determination of a complete and unified model for BNS mergers. However, resorting to numerical relativity (NR) simulations [e.g. 105, 106, 107, 108, 109, 110, 111] we can access these extreme regimes, extracting information on the merger dynamics and characterizing the different stages of the system.

Figure 2 depicts the phenomenology of a BNS coalescence. If a binary forms through standard formation channels [29], eccentricity is efficiently radiated during the early evolution and the motion is circularized by the time the binary enters the frequency band of ground-based GW detectors. In these conditions, the NSs inspiral towards each with monotonically increasing orbital frequency, as described by post-Newtonian (PN) and effective-one-body (EOB) predictions [e.g. 112, 113, 114]. In general, binaries in quasi-circular orbits evolve from a low-velocity regime to a strong-field condition, dissipating energy through GWs. The radiated GWs carry the footprint of the BNS dynamics, characterized by a chirping frequency evolution and increasing amplitude. The maximum of the GW amplitude is conventionally denoted as the moment of merger. Approaching the merger, *tidal* effects become relevant and affect the outgoing gravitational radiation [e.g. 115, 116, 117]. For unequal mass binaries, tidal forces in proximity of the merger can cause partial or complete disruption of the low-mass NS [82, 118].

When the NSs collide, a considerable amount of neutron-rich hot material, known as *dynamical ejecta*, becomes unbounded at mildly relativistic velocities [119]. Subsequently, the NS cores merge together generating a dynamical remnant. Depending on the EOS and on the properties of the remnant, the final object can undergo a BH collapse at any time after the merger [e.g. 120, 121]. The case in which the BH forms promptly after the collision of the NS cores is known as prompt collapse (PC) [57, 122, 123, 124]. Crucially, the PC avoids bounces in the dynamics of the NS remnant, mitigating the ejection of shocked matter [125]. Moreover, if PC occurs, a large fraction of the tidally-disrupted ejected matter (if present) is expected to fall back into the BH remnant [82]. In general, when a BH forms, the central remnant stabilizes on timescales $\lesssim O(1 \text{ ms})$ and the GW signal dampens with characteristic frequencies and times defined by the quasi-normal modes (QNMs) of the BH [126].

If the remnant does not promptly collapse after the merger, the central object is dynamically unstable [82, 127] due to hydrodynamical and gravitational forces that cause the matter to stretch and wobble, favoring matter ejection and formation of *baryonic winds* [83, 128]. Rotation and thermal pressures are expected to provide additional support to sustain the remnant above the maximum rigidly-rotating mass limit during the early postmerger (PM) phase. On timescales $\lesssim 10 \text{ ms}$, the system loses a considerably part of its energy through GWs [129]. The PM GW signal is mainly characterized by a central frequency peak, known as f_2 and related with the rotational dynamics of the remnant [129, 130]. In this early stage, it is also expected a burst of neutrino radiation with luminosity peaks of $O(10^{53} \text{ erg s}^{-1})$ [131, 132].

For timescales of $O(10 \text{ ms})$ after merger, the majority of the disposable energy has been dissipated and the remnant undergoes a spin-down due to viscosity effects [125]. A stable NS remnant reaches an approximately axisymmetric configuration with a cold and slowly-rotating core, i.e. $T \sim O(10 \text{ MeV})$ and $\Omega \sim O(100 \text{ Hz})$ [83, 133, 134, 135, 136]. On these timescales, an *accretion disk* is expected to form in the surrounding the central object, triggering neutrino irradiation, nuclear recombination, magneto-hydrodynamic viscosity and driving mass outflows to the outer environment [137, 138, 139]. Moreover, the merger remnant is expected to launch a relativistic *jet* [140] that travels across the ejected matter leading to the formation of a GRB [141].

Whether the remnant collapses into BH or a massive NS originates, the BNS coalescence are expected to generate $O(10^{-2} M_{\odot})$ of unbounded matter in the surrounding environment. On timescales of a day after merger, the ejected material is expanding, thermalizing and undergoing several thermo-nuclear processes [142]. This matter

represents an ideal site for rapid-neutron-capture processes (r -processes). These interactions are responsible for the nucleosynthesis of elements heavier than iron, i.e. with mass number $A \gtrsim 58$ [143]. The production of heavy elements is associated to a characteristic EM transient called KN [50, 144, 145, 146, 147]. A KN transient is quasi-thermal EM emissions characterized by a luminosity peak located between the optical and near infrared (NIR) bands with typical magnitudes ~ 18 . The signals fades after timescales of 15 days after merger reaching magnitudes $\lesssim 20$. On much longer timescales, i.e. $O(10^3 \text{ days})$, the jet decelerates shocking the interstellar medium (ISM) and powering a non-thermal emission known as GRB afterglow [54, 55, 148]. A similar phenomenon is expected also from the high-velocity tails of the dynamical ejecta [149, 150].

The EOS properties have multiple implications on the BNS dynamics, such as the tidal effects during the late inspiral [117, 151], the PM dynamics of the remnant [e.g. 82, 122, 129, 152, 153, 154] and the properties of the unbound material [e.g. 125, 155, 156, 157]. Then, MM information is expected to impose significant constraints on the NS matter properties and consecutively on the behavior of nuclear interactions in extreme conditions.

Summary of contents. In this *Thesis*, we investigate the EOS constraints provided by observational data of BNS mergers, studying current MM observation of GW170817 and its KN counterpart, and exploring new perspectives with XG GW detectors. The analyses are performed within a Bayesian framework relying on the Bayesian Jenaer Software (BAJES) [158, 159]. The employed methods make use of NR data extracted from the database of the Computational Relativity (CoRE) Collaboration [57, 58, 82, 83, 86, 125, 160, 161]. This *Thesis* is structured as follows. Chapter 1, introduces the methods of Bayesian inference and we discuss the implementations of BAJES. Chapter 2 presents the studies on GW170817, discussing the implications for NS matter properties and studying statistical and systematic errors in tidal inference. In Chapter 3, we analyze the KN counterpart AT2017gfo and we perform MM EOS inference combining GW and KN information with NICER measurements. Chapter 4 discusses the PM GW signals from BNS remnants and the development of NR-informed PM models. In Chapter 5, we show GW DA applications of BNS transients with XG detectors, focusing on PM inference and high-density EOS constraints. Finally, in Conclusions, we present future plans and perspectives. We include a discussion on the sampling methods in Appendix A; while, Appendix B and Appendix C present in detail the development of the BNS PM models, respectively NRPM and NRPM w .

Chapter 1

Bayesian inference

The modern formulation of probability theory was developed by Bayes [162] in 1763 and successfully used by Laplace [163] in various scientific applications, from astronomy to medicine. These works are elegantly discussed in his book, in which he asserted: *la théorie des probabilités n'est que le bon sens réduit au calcul*¹. However, the Bayesian methods were largely forgotten until 1939, when Jeffreys [164] developed a comprehensive framework for Bayesian inference. In more recent times, these methods have been expounded and extended [e.g. 165, 166, 167, 168, 169, 170, 171]. Nowadays, Bayesian inference has become a standard DA method of astrophysical and cosmological events [e.g. 172, 173, 174, 175, 176], since it offers a generic statistical framework to rigorously test hypothesis against observational information. Given an observable event and a set of background hypotheses, Bayesian inference allows one to infer the properties of the observed data in terms of probability distributions, and also to select the best-fitting model among competing hypotheses. In particular, Bayesian methods are central tools used in GW astronomy to determine the source properties of an observed signal [177, 178, 179] and the related applications. Furthermore, Bayesian inference offers a suitable framework to combine different observational datasets from MM astronomical observations, such as GWs and EM counterparts emitted by BNS mergers [e.g. 16, 180].

This Chapter is structured as follows. We introduce the concept of probability in Section 1.1 and discuss the theoretical foundations of Bayesian inference in Section 1.2. Finally, Section 1.3 presents the implementation of the Bayesian framework used for this *Thesis*. The detailed discussion of the sampling methods implemented in the pipeline is deferred to Appendix A.

¹*The theory of probabilities is only common sense reduced to calculation.*

1.1 Definitions

Following the approach of Cox [181] and Jaynes [182], the probability of an event is interpreted as its degree of belief. For continuous stochastic variables, the probability of obtaining a specific realization is described by the cumulative distribution function (CDF) or analogously by the probability density function (PDF). Considering the random variable θ and its domain $\Theta \equiv [\theta_{\min}, \theta_{\max}]$ with generic boundaries (i.e. θ_{\min} and θ_{\max} can be independently finite or infinite), the CDF $P(\theta \leq \theta^*)$ evaluated at $\theta^* \in \Theta$ is the probability that θ will take a value lower than or equal to θ^* . This definition ensures that the CDF is a monotonic increasing function of every random variable θ . Note that $P(\theta > \theta^*) = 1 - P(\theta \leq \theta^*)$. The PDF $p(\theta)$ is defined as the density of the CDF with respect to the stochastic variable θ , i.e.

$$p(\theta) = \frac{d}{d\theta}P(\theta \leq \theta^*). \quad (1.1)$$

In other terms, the integral of the PDF $p(\theta)$ over a range $[\theta_1, \theta_2] \subseteq \Theta$ corresponds to the probability $P(\theta_1 \leq \theta \leq \theta_2)$. From Eq. (1.1), we have $p(\theta) \geq 0$ for all $\theta \in \Theta$ and $\int_{\Theta} p(\theta) d\theta = 1$. Given the probability of a stochastic variable of interest, it is possible to compute expectation values and credibility regions, that deliver the information on the inferred variable. Furthermore, in the context of DA, we are interested in the estimations of *conditional* PDFs $p(\theta|\lambda)$, i.e. the probability of θ given the condition λ , and *joint* PDFs $p(\theta, \lambda) = p(\theta|\lambda) p(\lambda)$, i.e. the probability that both θ and λ occur. Note that, if θ and λ are independent, then $p(\theta|\lambda) = p(\theta)$. These notions can be straightforwardly generalized to a multi-dimensional parameters' space.

The task of a Bayesian inference is the formulation and the computation of conditional probabilities for the quantities of interest. It is possible to classify this topic in two main problems: parameter estimation (PE) and model selection (MS). With PE we mean the evaluation of the characteristic conditional PDFs for the parameters that define the model. On the other hand, with MS we refer to the discrimination between competing models in light of the data, comparing the suitability of different assumptions directly on the observation.

1.2 Bayes' theorem

In real physical experiments, observational information is encoded in a set of data \mathbf{d} , the realization of which depends on the observable under consideration. Employing

a theoretical model based on some background hypotheses H and parameterized by a set of parameters $\boldsymbol{\theta}$, it is possible to extract this information in terms of posterior PDFs of the parameters $\boldsymbol{\theta}$, i.e. $p(\boldsymbol{\theta}|\mathbf{d}, H)$. This procedure takes advantage of the Bayes' theorem [183, 184, 185],

$$p(\boldsymbol{\theta}|\mathbf{d}, H) = \frac{p(\mathbf{d}|\boldsymbol{\theta}, H) p(\boldsymbol{\theta}|H)}{p(\mathbf{d}|H)}, \quad (1.2)$$

where $p(\mathbf{d}|\boldsymbol{\theta}, H)$ is the likelihood function, $p(\boldsymbol{\theta}|H)$ is the prior distribution and $p(\mathbf{d}|H)$ is the evidence. The likelihood function describes the probability of observing the data \mathbf{d} for a given combination of $\boldsymbol{\theta}$ under the assumption that the hypothesis H is true. Therefore, it encodes the observational information and it predicts the agreement between the observed data \mathbf{d} and the expected outcome for every given sample $\boldsymbol{\theta}$ of the parameter space. The prior PDF $p(\boldsymbol{\theta}|H)$ depicts the knowledge on the parameters before performing the estimation (or takes into account previous experimental results). Usually, the functional form of this term is chosen in accordance with geometrical or physically-motivated argumentation. The term $p(\mathbf{d}|H)$ is labeled as evidence and it represents the probability of observing the data \mathbf{d} given the hypothesis H . The evidence is also called marginalized likelihood since, according to the marginalization rule, it can be expressed as

$$p(\mathbf{d}|H) = \int_{\Theta} p(\mathbf{d}, \boldsymbol{\theta}|H) d\boldsymbol{\theta} = \int_{\Theta} p(\mathbf{d}|\boldsymbol{\theta}, H) p(\boldsymbol{\theta}|H) d\boldsymbol{\theta}, \quad (1.3)$$

where the integral is extended over the entire parameters space Θ . Subsequently, the PDF $p(\boldsymbol{\theta}|\mathbf{d}, H)$ represents the probability of the parameters $\boldsymbol{\theta}$ in light of the data overhauled by our *a priori* information. The knowledge of $p(\boldsymbol{\theta}|\mathbf{d}, H)$ allows us to compute the expectation of the statistical quantities of interest. From this argument it follows that, in order to perform PE, we have to introduce a prior distribution $p(\boldsymbol{\theta}|H)$ and a likelihood function $p(\mathbf{d}|\boldsymbol{\theta}, H)$; then, the properties of the model are encoded in the posterior distribution $p(\boldsymbol{\theta}|\mathbf{d}, H)$ that can be computed imposing Eq. (1.2).

In Eq. (1.2), for a fixed set of assumptions H , the evidence acts like a normalization constant; however, this quantity plays a crucial role in the context of MS. If we are interested in comparing two competing hypotheses, say H_A and H_B , in the Bayesian framework it is natural to introduce the odds ratio as, i.e.

$$\mathcal{O}_A^B = \frac{p(H_B|\mathbf{d})}{p(H_A|\mathbf{d})} = \frac{p(H_B)}{p(H_A)} \frac{p(\mathbf{d}|H_B)}{p(\mathbf{d}|H_A)}, \quad (1.4)$$

The ratio \mathcal{O}_A^B encodes the will of the data in favoring one model over another and it quantifies which one is better predicting the data. Assuming that the two hypotheses are equiprobable $p(H_B) = p(H_A)$, it is possible to reduce the computation to the ratio of the evidences, also known as Bayes' factor (BF),

$$\mathcal{B}_A^B = \frac{p(\mathbf{d}|H_B)}{p(\mathbf{d}|H_A)}. \quad (1.5)$$

If $\mathcal{B}_A^B < 1$ then the hypothesis H_A is preferred by the data, otherwise H_B is favored if $\mathcal{B}_A^B > 1$. However, this rule is not always straightforward since the estimation of the BF might suffer from uncertainties [186, 187]. Then, in order to achieve robust and conservative inferences, more stringent bounds are required in order to prefer a tested hypothesis [188].

1.3 BAJES: the Bayesian Jeneer software

In a realistic scenario, the form of the likelihood function is not always analytically determinable and the parameter space has usually a large number of dimensions. For these reasons, the evaluation of the posterior PDF and the estimation of its integral are performed with stochastic techniques. In particular, sampling methods have proven to be reliable and generic tools for the analysis of non-analytical forms and multi-dimensional parameter spaces [178, 189, 190, 191], capable to give robust and stable results. We defer to Appendix A for a detailed discussion of the sampling algorithms employed in this *Thesis*, i.e. Markov-chain Monte Carlo (MCMC) algorithms [e.g. 170, 192, 193, 194, 195] and nested sampling [185, 196, 197, 198, 199].

In order to tackle Bayesian DA problems, we developed BAJES [bajes] [158, 159], a PYTHON package for generic Bayesian inference with specific functionalities for GW and MM astrophysics. BAJES aims to provide a versatile and robust framework for generic Bayesian inference within a simple and clear approach. In order to achieve this task, the software relies on a modular and composed architecture and it implements logically specialized objects. Furthermore, we decided to keep a light-weight setup with minimal dependencies on external libraries. These properties make BAJES a simple and general tool with a wide range of applicability. The body of the BAJES software is constituted by two components: the `inf` module, that represents an implementation of the Bayesian logic, and the `obs` module, that contains the tools to manage and process physical data. Currently, `bajes.obs` includes two sub-modules: `gw` and `kn`.

The `gw` module provides the tools necessary to deal with GW analysis described in Chapter 2. The `kn` module supplies a framework for the analysis of KNe discussed in Chapter 3.

The Bayesian approach is constituted by three fundamental stages [169]: formulating a model, comparing the model with the data and inferring the properties of the model. The goal of the `inf` module is to provide a flexible and general interface capable to adapt itself to a broad variety of problems. The `bajes.inf` module supplies a `Prior` and a `Likelihood` objects, the combination of which defines the Bayesian model. Then, it is possible to fit the model to the data relying on a specific `Sampler` method. BAJES interfaces with the MCMC algorithm EMCEE [170] and the nested samplers CPNEST [197], DYNESTY [198] and ULTRANEST [199]. Moreover, BAJES includes a customized parallel tempering Markov-chain Monte Carlo (PTMCMC) sampler based on PTEMCEE [200]. The output of the sampling routines is the prediction of the conditioned probability of interest.

In the DA context, the statistical infrastructure has to be flanked by the physical characterization of the experimental data with the purpose of defining a full Bayesian model. Moreover, within a MM framework, it is essential to develop a flexible pipeline capable of combining different datasets and physical models. This issue can be tackled allowing the infrastructure to merge different Bayesian models, extending the considered parameter space and generalizing the definition of the likelihood function. This implies the use of large amounts of data and computationally expensive models. It follows that efficient parallelization techniques and well-calibrated proposal methods are necessary to optimize the performances of such a flexible pipeline. We discuss the pipeline provided with the BAJES package in Section 1.3.1 and we show parallelization performances of different sampling methods in Section 1.3.2.

1.3.1 Pipeline

BAJES provides an automatized pipeline for the inference of MM transients, with a particular focus on GW DA. By default, BAJES includes the likelihood definitions used for GW and KN studies, that can be combined in an unique MM framework. The package provides the data for the GW events released in the first gravitational-wave transients catalog (GWTC-1) [172] and the KN data of AT2017gfo corresponding to the bolometric magnitudes for different photometric bands [45, 46, 47, 48, 49, 50, 51, 52, 201]. Moreover, the GW sector of the pipeline includes additional functionalities, such as spectral calibration envelopes for recorded data [202], reparameterization of

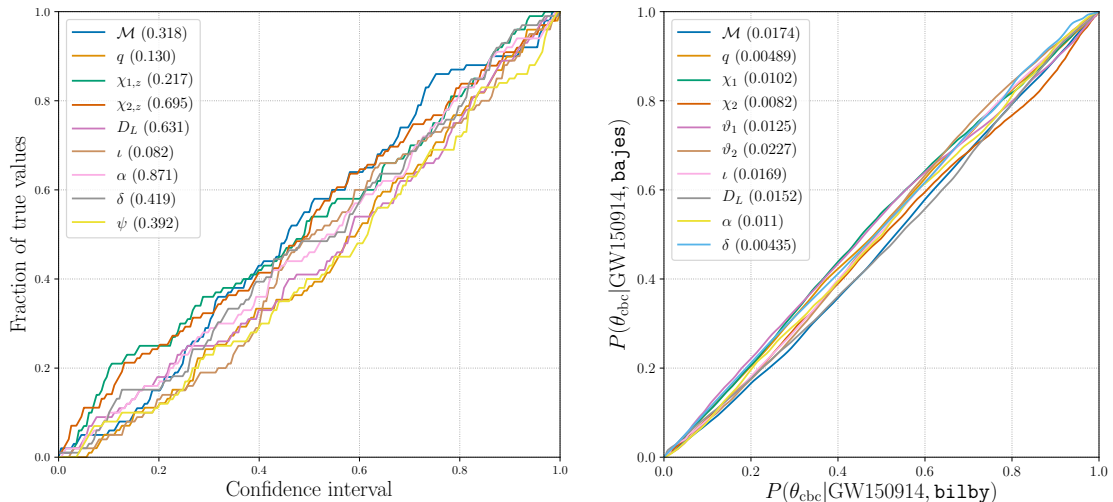


FIGURE 1.1: *Left panel:* Fraction of events found within a confidence interval of the estimated posterior PDFs. The data are estimated with a simulated set of 100 mock BBH signals. For every parameter, the label shows the p -value of the Kolmogorov-Smirnov test. *Right panel:* Probability-probability plot for the posteriors of GW150914 parameters. On the x -axis, the CDFs estimated with the BILBY pipeline and on the y -axis the same quantities computed with the BAJES pipeline. The legend shows the square root of the Jensen–Shannon divergence for each parameter.

noise curve uncertainties [177, 178], reduced-order-quadrature (ROQ) approximation for accelerating likelihood evaluations [203] and TOV solver [e.g. 6]. These tools are crucial in order to efficiently carry out robust and reliable inferences.

In order to validate the reliability of the GW pipeline, we perform a confidence interval test shown in Figure 1.1 (left). The confidence interval test has become a standard control check to verify the reliability of a pipeline [e.g. 173, 178, 204], since it ensures that the recovered probability PDFs are truly representative of the inferred confidence levels. For each parameter employed in the analyses, the test measures the fraction of true values that follow below a given credible level and, if the algorithm is well-calibrated, we expect this two quantities to be proportional. For our study, we generate 100 mock BBH GW signals of duration 8 s observed by the LIGO IFOs and we estimate the posterior PDFs using the DYNesty nested sampling with 1024 live points. For each parameter, we compute the p -value of Kolmogorov-Smirnov test, quantifying the consistency with uniformly distributed events. The results are shown between round brackets in Figure 1.1 (left). We estimate a combined p -value of 58%. This implies that the results are in agreement with analogous computations performed with a set of 9 random uniformly-distributed samples, confirming that the pipeline is well-calibrated.

The validation of the robustness of the implemented tools is verified by direct comparison with independent pipelines. In particular, we compare the posterior CDFs of GW150914 estimated with BAJES and with BILBY [204, 205, 206]. Figure 1.1 (right) shows the probability-probability plot of the marginalized posteriors recovered for every parameter. The probability-probability plot compares the CDFs estimated with two methods. Then, if two probability distributions are identical, the associated probability-probability plot is represented by a bisector line. In our case, the results coming from the two pipelines are largely consistent between each other, reporting deviations $< 15\%$ and Jensen-Shannon distances $\lesssim 2 \times 10^{-2}$ [207].

1.3.2 Parallelization

By default, BAJES analyses can be performed taking advantage of the parallel-threading PYTHON library. However, with this method the number of available processes is strictly limited by the size of the single machine and for non-trivial problems this could be a strong limitation. For this reason, BAJES implements a customized method for multi-nodes communication based on the message passing interface (MPI) protocol [208, 209, 210]. For ideal scaling, the execution-time of a machine computation is inversely proportional to the number of central processing units (CPUs), that leads to a linearly increase of the speedup. However, in a realistic scenario, the scaling performances of sampling techniques are affected by unavoidable computational steps serially performed and by the continuous exchange of information between different processes, required to adapt the evolution of the algorithm.

MCMC and nested sampling algorithms require separate treatments. The performances of MCMC sampling are typically quantified in terms of proposal acceptance and correlation length of the chains [170, 178, 200, 211, 212, 213], and generally the overall execution-time is determined by several contributions, such as the total number of chains, the complexity of the parameter space and the employed proposal techniques. Estimations of MCMC execution-times have shown that the efficiency drastically decreases for an increasing number of parallel chains [214, 215, 216]. Regarding nested sampling routines, their parallelization performances are well studied [see e.g. 191, 206, 217, 218, 219] and the theoretical speedup factor S_{NS} of this algorithm is expressed as a sub-linear scaling,

$$S_{\text{NS}}(n_{\text{live}}, n_{\text{cpu}}) = n_{\text{live}} \cdot \log \left(1 + \frac{n_{\text{cpu}}}{n_{\text{live}}} \right). \quad (1.6)$$

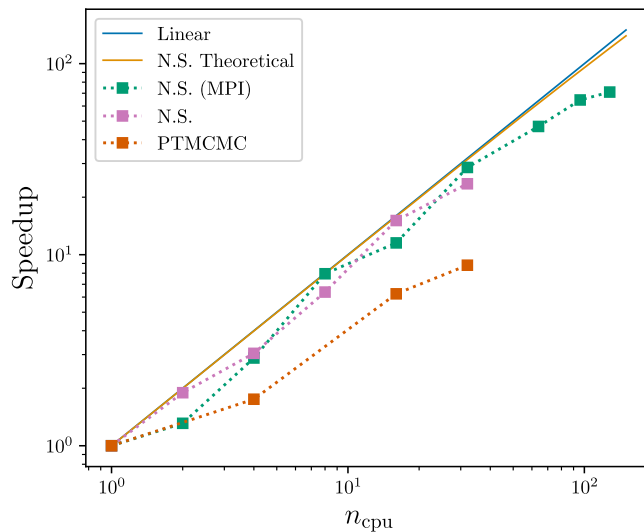


FIGURE 1.2: Scaling plot for the BAJES pipeline. The square markers are the measured speedup factors with respect to the serial execution-time. The settings for the PTMCMC (orange squares) and the nested sampling (pink squares for multi-threading and green squares for MPI) are discussed in Section 1.3.2. The blue solid line is the ideal linear scaling and the yellow solid line is the theoretical scaling of nested sampling in Eq. (1.6).

For $n_{\text{live}} \gg n_{\text{cpu}}$, the values predicted by Eq. (1.6) are comparable with a linear trend.

Figure 1.2 shows the measured speedup factors in the execution-time as a function of the number of CPUs for different samplers and different parallelization methods. The speedup factors are computed with respect to the execution-time measured from the serial job, i.e. $n_{\text{cpu}} = 1$. The execution-times are estimated from the BAJES GW pipeline using GW150914 [34] as target signal. For the PTMCMC, we estimate the speedup performing 10^3 iterations with 128×4 tempered chains, while, for nested sampling, we employ the DYNESTY software [198] with 1024 live points and tolerance equal to 0.1. The PTMCMC is not optimal in terms of execution-time scaling, mainly due to the serial swapping routine. However, it gives acceptable scaling performances with efficiency $\gtrsim 40\%$ up to $n_{\text{cpu}} \simeq 16$ using multi-threading methods. The results with MPI (not shown) are worst compared to multi-threading due to the data communication. Regarding the nested sampling, for a very small number of processes, roughly $n_{\text{cpu}} \lesssim 2$, the multi-threading method gives more efficient results, since the MPI protocol requires additional time for data communication. For an increasing number of CPUs, roughly $n_{\text{cpu}} \gtrsim 6$, the two parallelization methods give comparable results. However, the strength of MPI parallelization is the capability of accessing multiple CPUs located in different physical machines: the MPI interface implemented in BAJES gives an efficiency greater than 70% up to $n_{\text{cpu}} \simeq 100$.

Chapter 2

Inspiral gravitational-waves

On August 17, 2017 at 12:41:04 UTC the LIGO and Virgo GW detectors made their first observation of a low-mass CBC inspiral consistent with a BNS merger [39, 40, 172]. GW170817 lasted in the recorded data for more than 1 min, corresponding to the last $O(10^3)$ orbits before merger, and making this transient the loudest observed GW with a SNR of 32. This considerable GW power permitted a tight estimation of the binary mass and of the extrinsic properties of the source, such as distance and sky location. The signal vanishes before merger around ~ 600 Hz in the high-frequency detector noise, preventing the observation of a PM GW signal [220, 221] and avoiding a direct inference on the fate of the remnant.

In this Chapter, we analyze the LIGO-Virgo data corresponding to GW170817, focusing on the implication on the NS matter. In Section 2.1, we review the waveform models employed in the analysis. In Section 2.2, we introduce the GW PE framework and we present the recovered posterior distributions, discussing the properties of the source. Section 2.3 discusses systematic errors of current GW models, focusing on the impact on the inference of the tidal sector. Finally, in Section 2.4, we investigate possible PM scenarios quantifying the probability that the remnant underwent PC into BH.

2.1 Waveform models

The generation and the propagation of GWs can be predicted within GR at linearized level [222],

$$\square \left(h_{\mu\nu} - \frac{1}{2} \eta_{\mu\nu} h^\alpha{}_\alpha \right) = -\frac{16\pi G}{c^4} T_{\mu\nu}, \quad (2.1)$$

where $h_{\mu\nu}$ is the GW perturbation, $\eta_{\mu\nu}$ is the Minkowskian background metric, $\square = \partial_\alpha \partial^\alpha$ is the d'Alembertian operator and $T_{\mu\nu}$ is the stress-energy tensor of the source.

GR predicts two GW polarizations h_+ and h_\times , plus and cross respectively, that can be decomposed in (ℓ, m) multipoles as

$$h_+ - ih_\times = D_L^{-1} \sum_{\ell=2}^{\infty} \sum_{m=-\ell}^{\ell} h_{\ell m}(t) {}_{-2}Y_{\ell m}(\iota, \varphi), \quad (2.2)$$

where D_L is the luminosity distance, ${}_{-2}Y_{\ell m}$ are the $s = -2$ spin-weighted spherical harmonics and ι, φ are respectively the polar and azimuthal angles that define the orientation of the binary with respect to the observer. The leading-order term corresponds to the quadrupole component $(2, 2)$ of the source mass distribution [223]. Focusing on CBCs, as a first approximation the source term can be modeled as two inspiralling point-particles (PPs) with increasing frequency evolution defined by the GW energy. This computation leads to the Newtonian waveform [224, 225], that naturally introduces the concept of *chirp mass*,

$$\mathcal{M} = \frac{(m_1 m_2)^{3/5}}{M^{1/5}} = M \nu^{3/5}, \quad (2.3)$$

where $m_{1,2}$ are the component masses, $M = m_1 + m_2$ is the total mass and $\nu = m_1 m_2 / M^2$ is the symmetric mass ratio.

In order to take into account full-GR contributions and accurately estimate the radiated waveform for a fixed combination of parameters, high-precision methods are required to solve the two body problem in GR [e.g. 116, 226, 227, 228]. NR is an accurate and established approach that can provide GW templates for the whole binary evolution [e.g. 105, 106, 107, 108, 109, 110, 111]. Within this framework, the Einstein's equations [32] are numerically solved together with the dynamics of the source on a finite-size discrete grid. The numerical errors generally affects the results of the simulations [229, 230, 231] and they can be mitigated increasing the grid resolution, enforcing the robustness of the physical predictions. On the other hand, the computational cost drastically increases increasing grid resolution, incapacitating the practical use of NR templates for PE studies. For this reason, advanced analytical methods and accurate calibration techniques have been employed for the modeling of GW radiation [e.g. 232, 233, 234, 235]. Among the different methods, we focus on the following GW approximants, depicted in Figure 2.1 for an exemplary binary configuration. These families have shown to provide consistent results at the current SNRs [40].

- *Post-Newtonian approximation*: The PN framework [e.g. 236, 237, 238, 239,

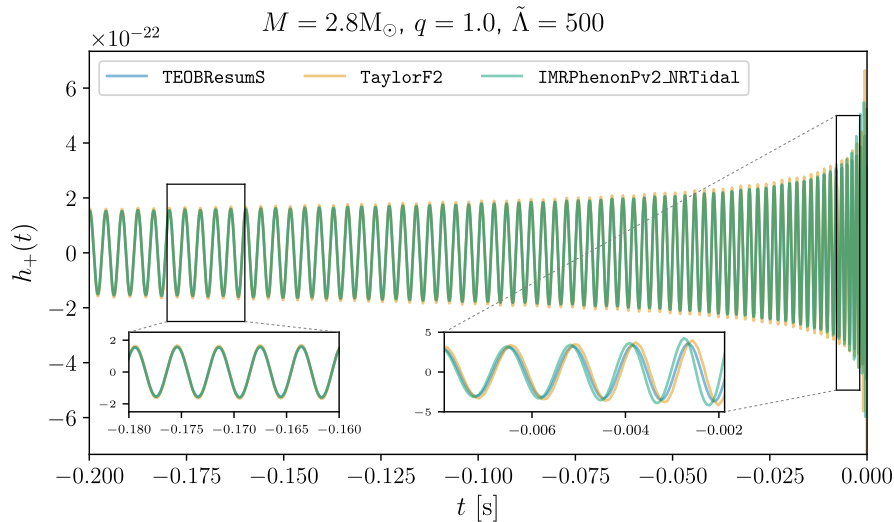


FIGURE 2.1: GW waveform templates for an exemplary combination of parameters of three different GW models. The templates are computed for a non-spinning equal-mass BNS with $M = 2.8 M_{\odot}$, $\tilde{\Lambda} = 500$ and $D_L = 40$ Mpc. The blue line shows `TEOBResumS`, the orange line shows `TaylorF2` and `PhenomPv2_NRTidal` is reported with green lines. The moment of merger corresponds to the origin of the time axis, i.e. $t_{\text{mrg}} = 0$. The subplots show two exemplary zooms, highlighting dephasing in proximity of the merger.

240, 241] is a theoretical milestone for the description of the two-body problem. This approach solves the dynamical evolution of an inspiralling compact binary with a perturbative method assuming low velocities and weak field approximations, which are reflected in the condition $v = (\pi GMf)^{1/3} \ll c$, where v is the characteristic velocity in the binary and f is the GW frequency. The metric $g_{\mu\nu}$ and the stress-energy tensor $T_{\mu\nu}$ are expanded in orders of $1/c$ in order to solve the Einstein's equations. The solution to this formalism gives us a time-domain template; however, a frequency-domain representation of the GW waveform can be obtained employing the stationary-phase approximation (SPA) [e.g. 242]. Finally, the frequency-domain GW template can be expressed as expansions in v/c , where the phase reads

$$\phi(v) = \phi_{\text{ref}} + 2\pi f t_{\text{ref}} + \frac{3c^5}{128\nu v^5} \sum_{i=0}^{\infty} \left(\alpha_i + \alpha'_i \log \frac{v}{c} + \alpha''_i \log^2 \frac{v}{c} + \dots \right) \left(\frac{v}{c} \right)^i \quad (2.4)$$

where ϕ_{ref} and t_{ref} are respectively reference phase and time and $\{\alpha_i, \alpha'_i, \alpha''_i, \dots\}$ are the PN coefficients that are functions of the intrinsic binary properties. The exact analytic solution of the gravitational radiation emitted by a PP binary is known up to the 3.5PN order [237] order and recent studies [243] introduced an

incomplete 5.5PN description of the GW phase. The PN results are expected to provide accurate descriptions of the motion and radiation of CBCs only during their early-inspiral stages, i.e. $GM/(c^2r) \ll 1$, where r is the separation between the binary components. In our studies, we consider the PN waveform labeled as `TaylorF2`, including 5.5PN PP description and 7.5PN tidal corrections [244].

- *Effective-one-body formalism:* The EOB formalism [112, 228, 245, 246, 247, 248, 249, 250] is an Hamiltonian approach that represents the general relativistic generalization of the reduced two-body problem, in which the system is described by a single orbiting object in an effective external potential. The key idea is to create a map between the real conservative dynamics and the effective motion of the reduced mass. This procedure is accomplished estimating an external metric such that the geodesic dynamics of a PP (with reduced mass $\mu = m_1 m_2 / M$) is equivalent to the original, relative PN-expanded dynamics. Finally, EOB framework is completed including radiation-reaction effects and defining a resummed expression for the Hamiltonian, that can be employed to solve the Hamilton-Jacobi equations for the reduced mass coordinates and their momenta. The EOB Hamiltonian \mathcal{H}_{EOB} can be written as

$$\mathcal{H}_{\text{EOB}} = Mc^2 \sqrt{1 + 2\nu(H_{\text{eff}} - 1)}, \quad (2.5)$$

where H_{eff} is the (μ -scaled) effective Hamiltonian. Using the mass-reduced phase-space variables $\{r, \varphi, p_r, p_\varphi\}$ for the effective mass and limiting to aligned-spin binaries [112, 114], the effective Hamiltonian can be expressed as $H_{\text{eff}} = H_{\text{orb}} + \tilde{G} p_\varphi$, where \tilde{G} is the gyro-gravitomagnetic contributions determining the spin-orbit couplings [251] and H_{orb} includes orbital contributions. The latter reads at 3PN as

$$H_{\text{orb}} = \sqrt{p_{r_*} + A(r, \nu) \left[1 + \frac{p_\varphi^2}{r_c^2} + 2\nu(4 - 3\nu) \frac{p_{r_*}^4}{r_c^2} \right]}, \quad (2.6)$$

where p_{r_*} is the momentum associated to the tortoise coordinate r_* , i.e. $p_{r_*} = \sqrt{A/B} p_r$, $\{A(r), B(r)\}$ are the EOB potentials defined in [114], and r_c is the centrifugal radius [114, 234, 252]. In particular, the radial potential $A(r)$ for a non-spinning PP binary can be written at 2PN order as $A(u) = 1 - 2u + 2\nu u^3$, where $u = GM/c^2 r$. Making use of NR data to calibrate high-order terms and non-quasi-circular corrections, the EOB prescription has shown to provide an

accurate representation of the CBC dynamics up to merger [e.g. 251, 253]. In our studies, we consider the frequency-domain EOB model `TEOBResumS` [254] computed from the corresponding time-domain counterpart employing SPA.

- *Phenomenological models:* Employing the results of NR simulations, it is possible to calibrate phenomenological GW models on targeted templates [255, 256, 257]. In particular, for quasi-circular CBCs, the analytical PN baseline is typically extended with additional degrees of freedom that are fit on NR data as functions of the binary properties. The modeling choices and the calibration set determine the accuracy of the model. Then, it is crucial to provide an optimal parameterization for the waveform properties and to accurately extract the information from NR data. Within the assumption of optimal modeling choices, the calibration of the additional degrees can be adjusted up to a requested design accuracy. The models are generally validated against an independent set of NR templates. This method leads to fully analytical waveform templates that can be directly used for PE studies. In our work, we focus on the phenomenological template `PhenomPv2_NRTidal` [258].

Given a model for the radiated GW polarization components $h_{+,\times}$ and the location of the source with respect to the observer, the signal can be projected on the requested IFO reducing the tensorial perturbation to a scalar time series,

$$h(t) = F_+ h_+(t) + F_\times h_\times(t), \quad (2.7)$$

where $F_{+,\times}$ are the antenna pattern functions of each polarization. that describe the sensitivity of the detector as functions of the polarization angle ψ and the sky location of the source, i.e. right ascension α and declination δ [259]. The resulting GW waveform $h(t)$ is a function of the binary parameters $\boldsymbol{\theta}_{\text{gw}}$,

$$\boldsymbol{\theta}_{\text{gw}} = \{m_1, m_2, \boldsymbol{\chi}_1, \boldsymbol{\chi}_2, \Lambda_1, \Lambda_2, D_L, \iota, \alpha, \delta, \psi, t_0, \phi_0\} \quad (2.8)$$

where $m_{1,2}$ are the mass components, $\boldsymbol{\chi}_{1,2}$ are the dimensionless spin parameters defined from the spin vectors of the binary components as $\boldsymbol{\chi}_i = c\mathbf{S}_i/(Gm_i^2)$ for $i = 1, 2$, D_L is the luminosity distance of the source, ι is the inclination angle between the total angular momentum and the line of sight, and $\{t_0, \phi_0\}$ are the reference quantities. We also introduce the mass ratio $q = m_1/m_2 \geq 1$, taken with the convention $m_1 \geq m_2$.

The tidal parameters $\Lambda_{1,2}$ are defined in the context of BNS mergers and introduced in the next section (Section 2.1.1).

2.1.1 Tidal interaction

Consider a static, spherically symmetric NS of mass m placed in a static external quadrupolar field \mathcal{E}_{ij} . In the local asymptotic rest frame of the NS for $r \rightarrow \infty$, the temporal metric coefficient is given by [260]

$$g_{00} = -1 + 2 \frac{Gm}{c^2 r} + 3 \frac{GQ_{ij}}{c^2 r^3} \left(n^i n^j - \frac{1}{3} \delta^{ij} \right) - \mathcal{E}_{ij} x^i x^j + \dots, \quad (2.9)$$

where $n_i = x_i/r$ and Q_{ij} is the NS quadrupole moment induced by the external field \mathcal{E}_{ij} . In Newtonian approximation, Q_{ij} is related with density perturbations of the NS [115]. Including GR contributions, these approximations are no longer valid, but the expansion of the metric Eq. (2.9) still holds in the asymptotically flat region.

In the adiabatic limit, the induced deformation Q_{ij} is expected to have a linear response to the external field \mathcal{E}_{ij} . Then, it is possible to introduce a (quadrupolar) tidal polarizability λ_2 [116, 226, 261, 262], i.e.

$$Q_{ij} = \lambda_2 \mathcal{E}_{ij}. \quad (2.10)$$

Note that in general the higher-order multipoles in Eq. (2.9) will have different couplings, i.e. λ_ℓ . We focus here on the dominant quadrupolar tidal effects; however, the tidal polarizabilities λ_ℓ for $\ell > 2$ can be related to the quadrupolar term λ_2 employing EOS-insensitive relations [263, 264, 265]. From linearized NS perturbation models [115, 266, 267], the tidal polarizability λ_2 can be expressed in terms of the NS radius, i.e.

$$\lambda_2 = \frac{2}{3} \frac{c^2}{G} k_2 R^5, \quad (2.11)$$

where k_2 is the quadrupolar gravito-electric Love number [see 115, 262, 268] and R is the NS radius. It is common practice to report λ_2 in its mass-scaled form; thus, we introduce the *dimensionless tidal polarizability* Λ as

$$\Lambda = \frac{2}{3} k_2 C^{-5}, \quad (2.12)$$

where C is the compactness of the NS. Eq. (2.12) explicitly shows the relation between the tidal parameter Λ and the EOS properties. The Love number k_2 has typical values

of $O(10^{-1})$ for NS masses of $1 - 2 M_\odot$ and it weakly depends on the NS radius. Thus, the value of the tidal parameter is dominated by the scaling $\Lambda \propto C^{-5}$, showing that soft EOSs predict smaller tidal parameters than stiff EOSs for a fixed NS mass.

Following PN arguments [269, 270, 271], the tidal effects in binary systems are computed fixing the external field \mathcal{E}_{ij} to the quadrupolar gravito-electric tidal moment of the companion, considering only monopole-quadrupole interactions. The energy of the system reads as

$$E = \frac{\mu v^2}{2} - \frac{\mu M}{r} \left(1 + \frac{\hat{\lambda}}{r^5} \right) + O(1/c^2), \quad (2.13)$$

where r is the relative separation, v is the relative velocity and $\hat{\lambda} = (3m_1/2m_2)\lambda_{2,1} + (3m_2/2m_1)\lambda_{2,2}$. The additional tidal term affects the GW signal, the phase of which can be written as $\phi(f) = \phi^{\text{PP}}(f) + \phi^{\text{T}}(f)$, where ϕ^{PP} is defined by the PP dynamics Eq. (2.4) and ϕ^{T} is the tidal contribution. The leading-order tidal term appears at 5PN order as $\phi^{\text{T}}(v) = -(117/256)(\tilde{\Lambda}/\nu)(v/c)^5$, where $\tilde{\Lambda}$ is the *reduced tidal parameter*,

$$\tilde{\Lambda} = \frac{16}{13} \left[\frac{(m_1 + 12m_2)m_1^4 \Lambda_1}{M^5} + (1 \leftrightarrow 2) \right]. \quad (2.14)$$

The next-to-leading tidal term enters at 6PN order and it is proportional to the asymmetric tidal parameter $\delta\tilde{\Lambda}$,

$$\delta\tilde{\Lambda} = \left[1 - \frac{7996}{1319} \frac{m_2}{m_1} - \frac{11005}{1319} \left(\frac{m_2}{m_1} \right)^2 \right] \frac{m_1^6 \Lambda_1}{M^6} - (1 \leftrightarrow 2). \quad (2.15)$$

Within the PN formalism, tidal corrections are computed up to 7.5PN [117, 244, 271], whereas spin-quadrupole terms are known up to 3.5PN [272].

The effects of tidal interaction are incorporated in the EOB formalism extending the definition of $A(r)$ potential and including the tidal contributions as $A(r) = A^{\text{PP}}(r) + A^{\text{T}}(r)$ [e.g. 116, 262, 273, 274, 275]. Following the description of the GR properties of NSs described above, the leading-order tidal term can be written as $A^{\text{T}}(u) = -\kappa_2^{\text{T}} u^6$, where κ_2^{T} is the (quadrupolar) tidal coupling defined as as

$$\kappa_2^{\text{T}} = 3\nu \left[\left(\frac{m_1}{M} \right)^3 \Lambda_1 + (1 \leftrightarrow 2) \right]. \quad (2.16)$$

The expression of $A^{\text{T}}(r)$ makes explicit the 5PN-order contribution of tidal effects,

analogously to the PN method. Moreover, $\kappa_2^T \propto C^{-5}$ similarly to $\tilde{\Lambda}$. The expression for the tidal potential $A^T(r)$ can be generalized including higher-order multipoles, i.e. $\ell > 2$ [116, 262].

Despite the relative high PN order, the tidal terms are expected to impact the GW waveform due to the large values predicted for the tidal polarizabilities, i.e. Λ is $O(100)$ for realistic EOSs. This argument makes it consistent to add the (high-order) tidal contributions to the (low-order) PP baseline description, since these terms formally correspond to comparable orders of magnitude in a numerical sense. Moreover, the relatively high order of tidal terms implies that these contributions become more significant as the separations between the binary components decreases.

2.2 Inference of GW170817

Ground-based GW detectors measure the local perturbations of the spacetime as time series, as shown in Eq. (2.7). Under the assumption that a physical GW transient $s(t)$ is recorded in the data, the detector output $d(t)$ is assumed to be the sum of the noise contribution $n(t)$ and the GW signal $s(t)$, i.e.

$$d(t) = n(t) + s(t). \quad (2.17)$$

In real observing conditions, the GW observations are performed simultaneously by a worldwide network of ground-based IFOs, permitting the correlation of multiple data segments so as to vet transient disturbances that can mimic GW signals [276, 277].

An accurate characterization of the noise is crucial in order to detect GWs and infer the properties of their sources. An improper noise modeling can lead to systematic PE biases. Typically, detector noise is assumed to satisfy the conditions of Gaussianity and stationarity. Then, a noise segment $n(t)$ of duration T can be fully characterized by the power spectral density (PSD) $S_n(f)$ [e.g. 278], defined as

$$\langle |n(f)|^2 \rangle = \frac{T}{2} S_n(f), \quad (2.18)$$

where the brackets $\langle \rangle$ denote the average over many noise realizations, each having duration T . Departures from stationarity result in correlations between samples in different frequency, while departures from Gaussianity can be identified by comparing the distribution of samples to a unit normal distribution. In the real scenario, the IFO noise is approximately Gaussian and locally stationary, i.e. the timescales associated

to non-stationary processes are larger than the GW characteristic times, with few exceptions such as glitches [179, 279].

If we dispose of a template $h(t)$ able to reproduce the *real signal* $s(t)$, it is possible to filter out the noise contribution revealing the presence of a signal in the observed data [158, 177, 178, 280]. In this context, we introduce the inner product between two time series, say $a(t)$ and $b(t)$, as

$$(a|b) = 4\Re \int_0^\infty \frac{a^*(f)b(f)}{S_n(f)} df, \quad (2.19)$$

where $a(f)$ is the Fourier transform of the time series $a(t)$,

$$a(f) = \int_{-\infty}^{+\infty} a(t) e^{-2\pi ift} dt, \quad (2.20)$$

and analogously for $b(f)$, while $S_n(f)$ is the noise PSD. Under the assumptions of Gaussian and stationary noise, we can define the GW likelihood function as

$$\log p(\mathbf{d}|\boldsymbol{\theta}_{\text{gw}}) \propto -\frac{1}{2}(h(\boldsymbol{\theta}_{\text{gw}}) - d|h(\boldsymbol{\theta}_{\text{gw}}) - d), \quad (2.21)$$

where every frequency-bin is assumed to be normally distributed with variance prescribed by the PSD. The likelihood Eq. (2.21) can be generalized for multiple detectors, assuming that the noise recorded by the different IFOs are independent of each other [177, 178].

Given a GW template model, it is possible to compute the evidence $p(\mathbf{d}|H_S)$ of the signal hypothesis marginalizing Eq. (2.21) over the prior domain. It is interesting to compare this value with the evidence of the noise hypothesis $p(\mathbf{d}|H_N)$, i.e. the assumption $h(t) = 0$, the evidence for which follows directly from Eq. (2.21). Then the ratio of these evidences corresponds to the BF of the signal vs. noise hypotheses, i.e. $\mathcal{B}_N^S = p(\mathbf{d}|H_S)/p(\mathbf{d}|H_N)$. In the context of GW inference, we often refer to this quantity just as \mathcal{B} . The BF encodes the will of the data in favoring the employed modeling over the no-signal assumption. Another characteristic quantity that is typically used to quantify the strength of a GW is the SNR. This quantity is introduced in the context of matched-filtering signal-processing and it is defined from Eq. (2.19) as

$$\text{SNR} = \frac{(d|h)}{\sqrt{(h|h)}}. \quad (2.22)$$

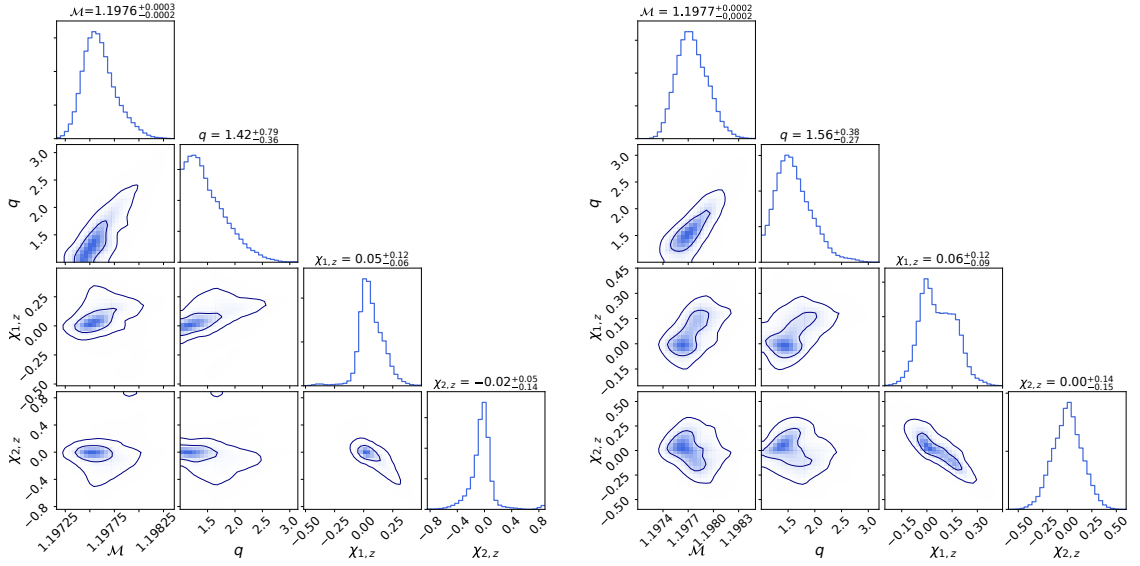


FIGURE 2.2: Posterior distributions for chirp mass \mathcal{M} (measured in M_{\odot}), mass ratio q and spin components $\chi_{i,z}$ for $i = 1, 2$ of GW170817 computed with PN (left) and EOB (right) waveform models. The contours show the 50% and 90% credibility regions. The quoted values are the medians and the 90% credibility levels.

The SNR estimates the power of the signal $h(t)$ enfolded in the data $d(t)$ weighted on the variance of the background noise. Note that, if $d(t) = h(t)$, then $\text{SNR} = \sqrt{\langle h|h \rangle}$. The latter is typically labeled as optimal SNR to distinguish it from the matched-filtered SNR, i.e. Eq. (2.22).

Within this framework, we analyze the GWOSC data of LIGO and Virgo centered around GPS time 1187008857 with a sampling rate of 4096 Hz and a duration of 128 s considering the frequency range from 20 Hz to 2 kHz [39]. The prior distribution is taken uniform in the mass and tidal components spanning the ranges $\mathcal{M} \in [1.18, 1.21] M_{\odot}$, $q \in [1, 8]$ and $\Lambda_{1,2} \in [0, 5000]$ and isotropic in spin components bounded to $|\chi_{1,2}| \leq 0.89$. We employ identical prior distribution for the extrinsic parameters as the one in [158], in particular the luminosity distance is taken volumetric in the range $D_L \in [5, 75]$ Mpc. The study is performed with the nested sampling algorithm [196] as implemented in the DYNESTY library [198], employing 2048 live points and including spectral calibration envelopes. We discuss the binary properties in Section 2.2.1, and the tidal parameters in Section 2.2.2.

2.2.1 Source properties

Figure 2.2 shows the posterior distributions for the parameters recovered employing the `TEOBResumS` model and the `TaylorF2` approximant assuming aligned spin components. The analysis is repeated with `PhenomPv2_NRTidal` template with precessing spin components. Interestingly, the recovered BFs and SNRs are consistent between different approximants, $\log \mathcal{B} \simeq 475$ and $\text{SNR} \simeq 32$, with negligible differences.

The recovered detector-frame chirp mass corresponds to $\mathcal{M} \simeq 1.1976 M_{\odot}$ with broad agreement between all the waveform models and errors of $O(10^{-4} M_{\odot})$ at the 90% credibility level. We remind that the chirp mass \mathcal{M} affects the phase evolution at the leading order and then it is the best constrained among the source parameters, as shown by the recovered posteriors. The mass ratio is constrained to be $q \lesssim 2.5$ at the 90% credibility level. Note that spin contributions correlate with the mass ratio, widening the recovered PDF. The spin components do not show departures from zero. Consistently with Ref. [40], we estimate an effective spin parameter $\chi_{\text{eff}} = 0.04_{-0.03}^{+0.06}$.

Regarding the luminosity distance, we estimate $D_L = 36.7_{-8.0}^{+6.2}$ Mpc for `TEOBResumS`, $D_L = 37.1_{-12.1}^{+10.3}$ Mpc for `TaylorF2` and $D_L = 38.5_{-11.4}^{+9.4}$ Mpc for `PhenomPv2_NRTidal`. Employing standard cosmological parameters [281], these values lead to a source-frame chirp mass of $\mathcal{M}_{\text{src}} \simeq 1.188 M_{\odot}$. The mass components fall in the NS range, i.e. $1\text{--}2 M_{\odot}$, validating the hypothesis of a BNS merger. Assuming equal-mass case ($q = 1$), the source-frame mass components can be roughly constrained around $\sim 1.36 M_{\odot}$, typical values expected for these compact objects. In all these analyses, the inclination angle is inferred to be $\iota \gtrsim \pi$ and the recovered sky location is $\{\alpha \simeq 3.42 \text{ rad}, \delta \simeq -0.35 \text{ rad}\}$ with errors of $O(10^{-2})$. The estimation of the extrinsic parameters is generally consistent with existing results [e.g. 40, 172, 254]. Moreover, the recovered sky position covers an area of $\sim 28 \text{ deg}^2$. Combined with the associated GRB information [66], the sky localization of the source facilitated and validated the identification of the KN counterpart (see Chapter 3).

2.2.2 Tidal inference

The main effect that allows us to confidently discriminate between merging NSs and BHs is the tidal interaction between the binary components. Figure 2.3 shows the recovered reduced tidal parameters $\tilde{\Lambda}$, where the posterior PDF have been re-weighted

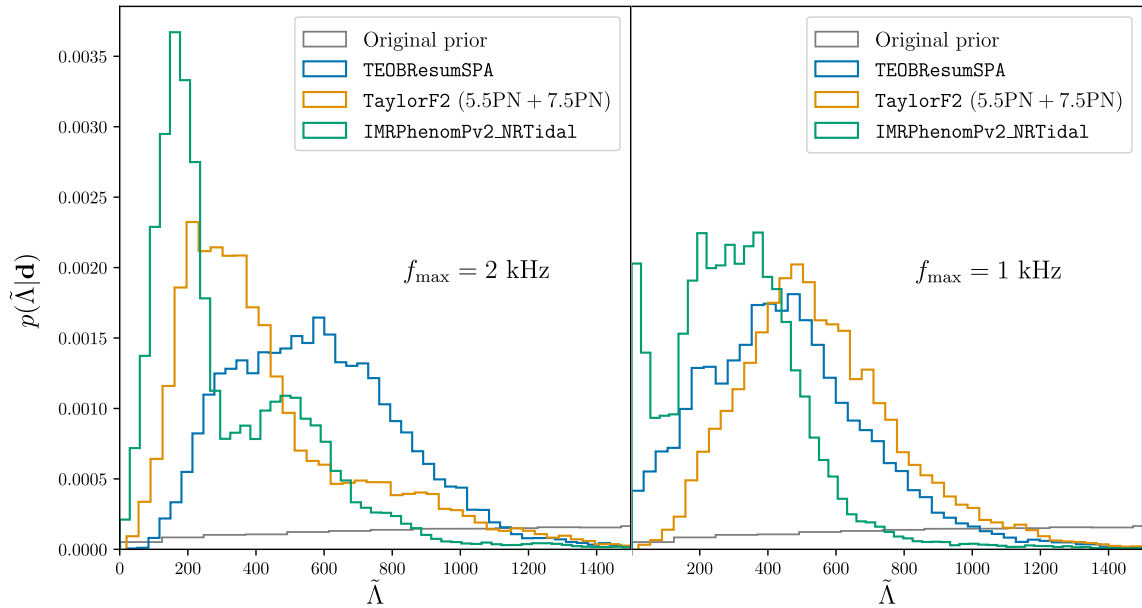


FIGURE 2.3: Posterior distributions for the reduced tidal parameter $\tilde{\Lambda}$ of GW170817 for different waveform models, i.e. EOB (blue), PN (orange) and phenomenological (green). The posteriors are re-weighted to a uniform prior, and the original prior is shown in gray. *Left panel:* Posterior PDFs computed with an upper-cutoff frequency $f_{\max} = 2$ kHz. *Right panel:* Posterior PDFs computed with an upper-cutoff frequency $f_{\max} = 1$ kHz.

to a uniform prior. The figure includes the results computed with different waveform models and upper cutoff-frequencies, i.e. $f_{\max} = 1$ kHz and 2 kHz, in order to investigate the effect of high-frequency contributions.

For the EOB model, the primary tidal parameter Λ_1 is constrained to be $\lesssim 950$ at the 90% credibility level, while the secondary component Λ_2 is more broadly distributed over the prior due to the correlations with the mass components. The recovered tidal parameter posterior estimates a value of $\tilde{\Lambda} = 607^{+477}_{-356}$ and its posterior distribution excludes the $\tilde{\Lambda} = 0$ hypothesis at the 90% credibility level. These results are in agreement with previous estimates obtained with EOB models [172, 254]. The asymmetric tidal parameter $\delta\tilde{\Lambda}$ shows a posterior distribution centered around non-zero values, i.e. $\delta\tilde{\Lambda} = 92^{+200}_{-258}$. However, the hypothesis $\delta\tilde{\Lambda} = 0$ is confidently included in the posterior support, corresponding to the 27th percentile. Employing PN and phenomenological templates, we obtain similar results. The primary tidal component is constrained below $\Lambda_1 < 700$ and the secondary is broadly distributed over the prior. The reduced tidal parameter is measured to be $\tilde{\Lambda} = 404^{+701}_{-246}$ for TaylorF2 and $\tilde{\Lambda} = 227^{+530}_{-148}$ for PhenomPv2_NRTidal. The asymmetric tidal term $\delta\tilde{\Lambda}$ is well constrained around zero

with an uncertainty of ~ 150 at the 90% credibility level for both models. The posteriors of the tidal parameter can be translated in EOS constraints using the solutions of the TOV equations, disfavoring very soft EOSs such as MS1b.

The main differences between the analyses with different f_{\max} lie in the results of the tidal sector. Overall, the recovered tidal parameters with $f_{\max} = 2$ kHz appear more constrained with respect to the cases with $f_{\max} = 1$ kHz. On the other hand, the choice of $f_{\max} = 2$ kHz enlarges multimodal and asymmetric behaviors in the posterior distribution of the reduced tidal parameter and systematic effects appear to be more relevant between different template families [282, 283, 284]. The posterior distributions for EOB and PN approximants show a good agreement with $f_{\max} = 1$ kHz. The differences in the $\tilde{\Lambda}$ parameters can be traced back to the modeling choices of the employed approximants [see 40, 172, 243]. Note also that `PhenomPv2_NRTidal` analysis includes the contribution of precessing spins, that introduce additional correlations with the BNS parameters. In general, the results estimated at 1 kHz show posteriors shifted toward lower values with respect to the analysis at 2 kHz, favoring the $\tilde{\Lambda} = 0$.

2.3 Parameter estimation errors

Following the work presented in Gamba et al. [284], we further investigate PE errors associated to the tidal parameter in GW BNS inferences, in order to understand and characterize the biases induced by the modeling choices. This study is also motivated by the results discussed in Section 2.1.1. Moreover, different studies [243, 284, 285, 286, 287, 288, 289, 290] have pointed out that the measured tidal parameters can be strongly biased depending on the employed description. The tidal parameters are of great relevance in our context since they permit the mapping between BNS GW observations and the EOS properties.

Statistical errors are the fluctuations related with the stochastic noise that affects the IFO and they are dominant for low SNR events. They affect the inference mainly widening the posterior distributions, leading to a decreasing accuracy of the measurement. In general, if the measurement is unbiased, we expect the true value to fall into the credibility interval of the posterior. On the other hand, the systematic errors refer to the incorrect interpretations of the observed data that generate biases in the posterior PDFs and might introduce multimodalities. The source of these errors is independent of the SNR, since they can be traced back to intrinsic differences in the

waveform models. Then, when the systematic errors overcome the statistical fluctuations, the inference of the BNS properties become dependent on the employed GW approximant.

We study the behavior of statistical errors in the Fisher approximation in Section 2.3.1 and the systematic waveform errors are discussed in Section 2.3.2.

2.3.1 Statistical errors

The Fisher approximation [226, 269, 291, 292] is an analytical framework that allows us to study the statistical quantities of interest in the Gaussian limit. Eq. (2.21) can be expanded around $\boldsymbol{\theta} \simeq \boldsymbol{\theta}_{\text{true}}$ obtaining a quadratic form at leading order, i.e.

$$\log p(\mathbf{d}|\boldsymbol{\theta}) \propto -\frac{1}{2}\Sigma_{ij}(\boldsymbol{\theta}_{\text{true}}) \Delta\theta^i \Delta\theta^j + O(\Delta\boldsymbol{\theta}^3), \quad (2.23)$$

where $\Delta\boldsymbol{\theta} = \boldsymbol{\theta} - \boldsymbol{\theta}_{\text{true}}$ and the covariance matrix Σ_{ij} corresponds to

$$\Sigma_{ij}(\boldsymbol{\theta}) = \left(\frac{\partial h}{\partial \theta^i} \middle| \frac{\partial h}{\partial \theta^j} \right). \quad (2.24)$$

The validity of this expansion holds in the limit of high SNRs, i.e. $d \rightarrow h$. We observe that the linear term in the expansion Eq. (2.23) has been neglected since we assume that $\boldsymbol{\theta}_{\text{true}}$ is a maximum for $\log p(\mathbf{d}|\boldsymbol{\theta})$. This condition is not valid when systematic errors are dominant.

Within the Fisher approach, the tidal information $I_{\tilde{\Lambda}\tilde{\Lambda}}(f)$ can be defined from the covariance Eq. (2.24) as

$$I_{\tilde{\Lambda}\tilde{\Lambda}}(f) = \frac{4}{S_n(f)} \left| \frac{\partial h(f)}{\partial \tilde{\Lambda}} \right|^2. \quad (2.25)$$

Figure 2.4 (left) compares the tidal information and the signal power gathered in each frequency bin, i.e. the integrand of the optimal SNR, for three exemplary equal-mass binary configurations with design sensitivities of current and XG detectors. We can evince that, while the signal power decreases for increasing frequency, the tidal information is primarily gathered at high frequencies, i.e. $f \gtrsim 500$ Hz. This behavior is expected considering that tidal interactions become more relevant to the BNS dynamics as the separation between the two companions decreases. This is reflected in the inference of the tidal sector justifying the widening of the posterior distributions for decreasing upper cutoff-frequency. In fact, the tidal information is related to the $\tilde{\Lambda}$

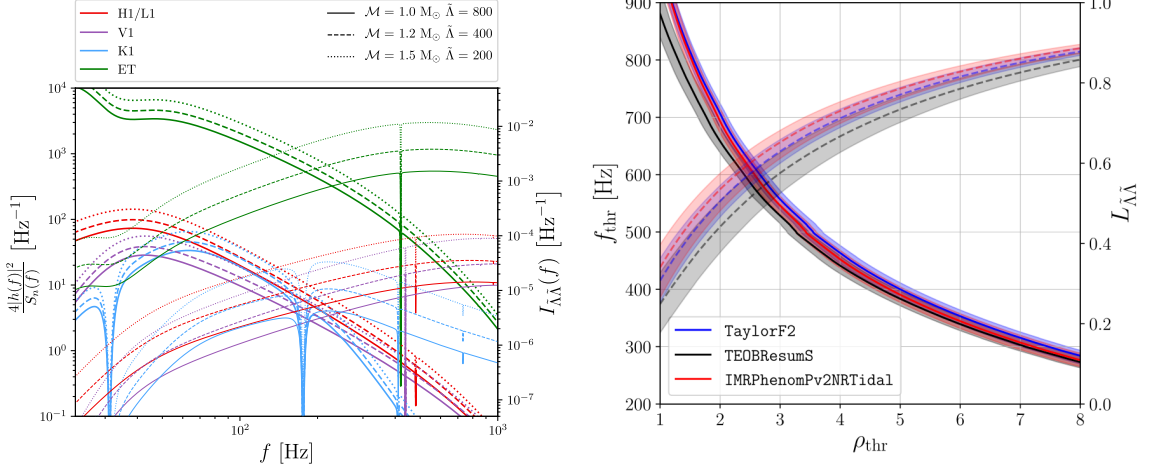


FIGURE 2.4: *Left panel:* Signal power (thick lines) and tidal information $I_{\bar{\Lambda}\bar{\Lambda}}$ (thin lines) as functions of the frequency for different binary configuration and detector sensitivities. Red lines refer to design LIGO sensitivity [29], purple lines refer to design Virgo sensitivity [293], blue lines refer to design KAGRA sensitivity [78] and green lines refer to fiducial ET-D sensitivity [75, 76]. Solid lines show low-mass binary $\mathcal{M} = 1 M_\odot$, dashed lines show intermediate-mass binary $\mathcal{M} = 1.2 M_\odot$ and dotted lines show high-mass binary $\mathcal{M} = 1.5 M_\odot$. *Right panel:* Threshold frequency f_{thr} (solid lines) and information loss $L_{\bar{\Lambda}\bar{\Lambda}}$ (dashed lines) as functions of the threshold SNR for GW170817 with different waveform templates. Blue lines refer to the PN model, black lines refer to the EOB model and red lines refer to the phenomenological model. The solid lines correspond to the median values and the bands are the 90% credible regions.

uncertainty through the Cramer-Rao bound, i.e.

$$\sigma_\Lambda^2 \geq \left(\frac{\partial h}{\partial \bar{\Lambda}} \middle| \frac{\partial h}{\partial \bar{\Lambda}} \right)^{-1}. \quad (2.26)$$

Aiming to the characterization of statistical fluctuations of the tidal parameter, it is interesting to investigate the amount of tidal information loss as function of the upper cutoff-frequency f_{thr} . Then, we introduce the (normalized) information loss as

$$L_{\bar{\Lambda}\bar{\Lambda}}(f_{\text{thr}}) = \frac{\int_{f_{\text{thr}}}^{\infty} I_{\bar{\Lambda}\bar{\Lambda}}(f) df}{\int_0^{\infty} I_{\bar{\Lambda}\bar{\Lambda}}(f) df}. \quad (2.27)$$

Eq. (2.27) quantifies the percentage of tidal information that is neglected reducing the upper cutoff-frequency to f_{thr} . On the other hand, the amount of signal loss can be

computed introducing a threshold SNR ρ_{thr} associated to the cutoff-frequency f_{thr} ,

$$\rho_{\text{thr}}^2 = 4 \int_{f_{\text{thr}}}^{\infty} \frac{|h(f)|^2}{S_n(f)} df. \quad (2.28)$$

Figure 2.4 (right) shows the evolution of $L_{\bar{\lambda}\bar{\lambda}}$ and f_{thr} as functions of ρ_{thr} , computed from the posterior PDFs of GW170817 for different waveform models. For $f_{\text{thr}} = 1$ kHz, we estimate $\rho_{\text{thr}} \lesssim 1$ denoting that a negligible amount of signal power is gained for $f > 1$ kHz. However, $L_{\bar{\lambda}\bar{\lambda}} \simeq 25\%$ for $f_{\text{thr}} = 1$ kHz showing that a considerable fraction of tidal information is not included in the inference. Moreover, the results of GW170817 show that $\sim 50\%$ of the tidal information is collected for $f > 650$ Hz, while, $\sim 5\%$ of the total SNR is collected above this threshold. Even if these results are computed within Fisher approach, hence neglecting the contribution of the stochastic detector noise, they allows us to better interpret the tidal inference at different cutoff frequencies. While a decreasing cutoff frequency will mildly affect the overall signal power, it will considerably affect the tidal inference.

2.3.2 Systematic errors

Systematic biases originate when a critical combination of parameters $\boldsymbol{\theta}_{\text{crit}} \neq \boldsymbol{\theta}_{\text{true}}$ minimizes the likelihood function Eq. (2.21), yielding to the condition $(\partial h / \partial \boldsymbol{\theta} | h - d) = 0$ in $\boldsymbol{\theta}_{\text{crit}}$. The existence of such critical value can be related to inaccurate modelings and representations of the GW templates. These inconsistencies can be investigated from the GW templates comparing the predictions of different prescriptions. Instead of examining the evolution of the waveform phases, we introduce the Q_ω as

$$Q_\omega = \frac{\omega^2}{\dot{\omega}}, \quad (2.29)$$

where $\omega = 2\pi f$ is the instantaneous GW frequency and $\dot{\omega}$ is its derivative with respect to the temporal variable. The Q_ω is related to the phase acceleration of the frequency-domain waveform and its integral over a fixed frequency range is proportional to the number of cycles performed within these frequencies. Thus, Q_ω can be employed for waveform comparison without ambiguities and information losses related to phase alignment. For each GW model, we estimate the Q_ω and we report in Figure 2.5 (right) the differences $\Delta Q_\omega = Q_\omega^{\text{TEOBResumS}} - Q_\omega^X$, with $X = \text{TaylorF2, PhenomPv2_NRTidal}$, estimated with respect to the EOB model for five exemplary combinations of intrinsic parameters. The differences ΔQ_ω show an increasing trend proportional to the

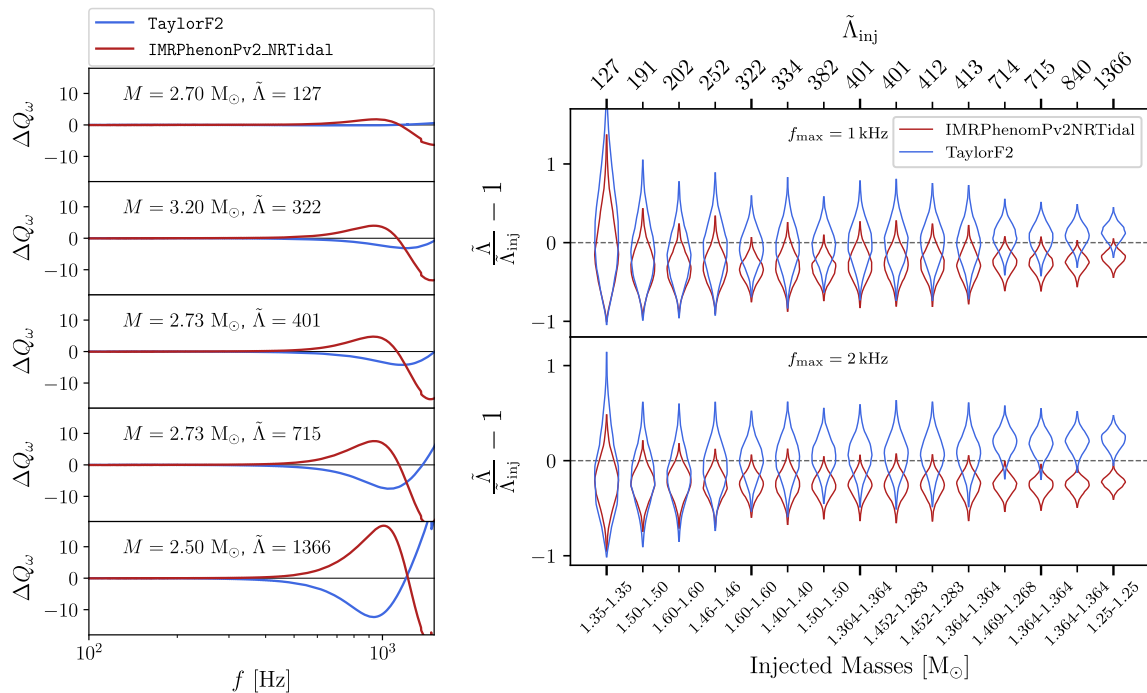


FIGURE 2.5: *Left panel:* Systematic differences ΔQ_ω of the Q_ω of TaylorF2 (blue) and PhenomPv2_NRTidal (red) with respect to TEOBResumS as function of the frequency for five exemplary combination of intrinsic parameters. *Right panel:* PDFs of the fractional deviation between the injected $\tilde{\Lambda}_{inj}$ and the inferred $\tilde{\Lambda}$. The color code show the approximant employed for the PE (red for PhenomPv2_NRTidal, blue for TaylorF2), and the results are displayed for two different frequency cutoffs $f_{max} = 1$ kHz (top) and 2 kHz (bottom). Thicker ticks identify the binary corresponding to the left panel.

frequency variable for $f < 1$ kHz. TaylorF2 and PhenomPv2_NRTidal behave in opposite direction showing respectively weaker and stronger matter effects compared to TEOBResumS. The differences are amplified for increasing $\tilde{\Lambda}$. We verified that the tidal sector is the largest contribution in the differences of the recovered ΔQ_ω [284]. These results qualitatively explain the tidal inference of GW170817. The impact of matter effects in PhenomPv2_NRTidal leads this approximant to recover a smaller $\tilde{\Lambda}$ compared to PN and EOB models. The broad consistency between TEOBResumS and TaylorF2 can be explained by a mixture of PP and tidal sectors.

In order to provide quantitative estimates of systematic errors, we perform a survey of mock PE studies. We generate 15 mock GW signals, label as *injections*, using the TEOBResumS waveform model for different combination of intrinsic parameters. The extrinsic parameters of the injected data are chosen to match the best-fitting parameters of GW170817. The SNRs of the injected signals lies in the range 82 – 94, depending on the specific combination of masses and tidal parameters. The mock data

are generated with LIGO-Virgo IFOs using the fiducial PSDs for design configurations. In order to avoid noise contributions and focus on waveform errors, we use zero-noise segments. The posterior PDFs are recovered with PE studies similarly to the ones discussed in Section 2.2 employing the `TaylorF2` and `PhenomPv2_NRTidal` template models. The data are analyzed employing low cutoff-frequency ($f_{\max} = 1$ kHz) and high cutoff-frequency ($f_{\max} = 2$ kHz), simulating the study of Section 2.2.

While the mass components are correctly estimated within the 90% credibility region, the inference of the tidal parameter shows biased results, similarly to the GW170817 case. Figure 2.5 (right) show the posterior PDFs of the relative deviation between the recovered $\tilde{\Lambda}$ and the injected value $\tilde{\Lambda}_{\text{inj}}$. We can see that the phenomenological model systematically underestimates the injected value, leading to biases larger than the 90% credible level for $\tilde{\Lambda} \gtrsim 350$. As matter effects grow, the deviation between the two approximants and the `TEOBResumS` baseline increases, reaching approximately $\pm 20\%$ when $\tilde{\Lambda}_{\text{inj}} = 1366$. Increasing f_{\max} , the differences in the recovery of $\tilde{\Lambda}$ between different models become larger, consistently with GW170817. Remarkably, the recovered tidal posterior for `PhenomPv2_NRTidal` do not show any multimodal behavior, in contrast to GW170817 analyses and consistently with analogous studies [39, 40]. `TaylorF2` do not show deviations above the 90% credibility intervals for the considered SNRs; while, `PhenomPv2_NRTidal` is systematically biased toward smaller values. Moreover, the recovered deviations are consistent with the results of the Q_ω study. Projecting our results on XG detectors [284], we estimate that systematic tidal errors will dominate over statistical fluctuations for $\text{SNR} \gtrsim 100$ with current waveform models, posing severe issues for GW DA and EOS inference with XG detectors.

2.4 Black hole collapse

The LIGO-Virgo detectors sensitivity at high frequencies was not sufficient to detect the signal corresponding to the merger and PM phases [40, 220, 221]. Hence, the question whether the merger outcome was a prompt BH formation or not must be answered using either the premerger GW signal or EM counterparts. A first answer was given by the interpretation of the EM counterparts observed with delays of seconds to days with respect to the GW and composed by a GRB and a KN [66, 70, 294]. Energetic and timing of the latter exclude both a prompt BH formation and a long-lived NS remnant. Most likely, the merger dynamics produced a massive NS that collapsed on timescales of ~ 0.01 to ~ 2 seconds. Such a conclusion is informed and

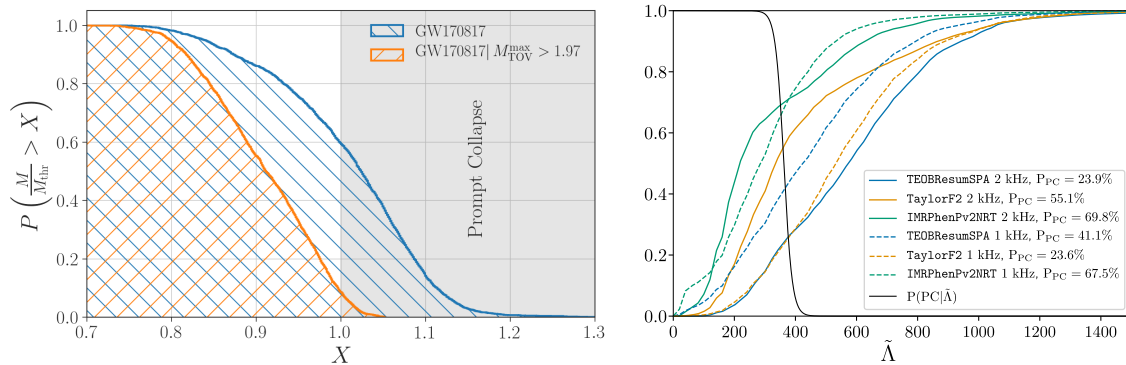


FIGURE 2.6: *Left panel:* PC analysis of GW170817 based on threshold mass method. The plot shows the CDFs on the ratio M/M_{thr} . The fraction of the posterior that lies above $X = 1$ gives the probability of PC with (blue) and without (orange) a constraint of $M_{\text{max}}^{\text{TOV}} \geq 1.97 M_{\odot}$. *Right panel:* PC probability for GW170817 based on the threshold- $\tilde{\Lambda}$ method. Solid (dashed) colored curves plot the posterior CDFs for $\tilde{\Lambda}$ for different approximants with $f_{\text{max}} = 2$ kHz ($f_{\text{max}} = 1$ kHz). The solid black sigmoid curve gives the prior PC probability at each value of $\tilde{\Lambda}$, based on NR simulations. The PC probabilities can be visually estimated by the value of each curve as it crosses the transition region.

supported by NR results that established the formation of massive NS remnants for canonical NS masses and EOSs supporting $M_{\text{max}}^{\text{TOV}} > 2 M_{\odot}$.

On the other hand, considering the premerger GW information, the posterior PDFs of the binary parameters can be combined with NR information in order to estimate the probability of PC P_{PC} , i.e. the probability that the remnant collapsed into BH immediately after merger. In the following sections, we employ the methods presented in Agathos et al. [122] in order to infer the prompt BH formation from the premerger GW data of GW170817. In particular, Section 2.4.1 discusses the method based on the threshold mass and Section 2.4.2 presents the method based on the tidal parameter.

2.4.1 Threshold mass

NR simulations indicate that a BNS merger will be followed by a PC into a BH, if the total gravitational mass M of the binary exceeds a threshold mass [295, 296],

$$M_{\text{thr}} = k_{\text{thr}} M_{\text{max}}^{\text{TOV}}, \quad (2.30)$$

where k_{thr} depends, in general, on the EOS, mass ratio, and spin. For typical hadronic equal-mass nonspinning binaries, the threshold coefficient in Eq. (2.30) is found in the range $1.3 \lesssim k_{\text{thr}} \lesssim 1.7$ [295, 296, 297]. This coefficient has shown an approximately

EOS-independent linear behavior in the maximum compactness C_{\max}^{TOV} of non-rotating equilibrium NS solution [122, 296]. Note that by inverting Eq. (2.30) and assuming that the merger did not promptly form a BH, one may obtain a bound on the maximum stable NS mass [69, 298, 299]. Using the results reported by [122, 160, 296, 297, 300], we find that k_{thr} can be estimated with the linear fit

$$k_{\text{thr}}(C_{\max}^{\text{TOV}}) = a_0 + a_1 C_{\max}^{\text{TOV}}, \quad (2.31)$$

where $\{a_0, a_1\} = \{2.392 \pm 0.064, -3.29 \pm 0.23\}$ are determined by a least-squared minimization method. Note that this relation has been recently recalibrated in Ref. [57] and extended in the large-mass-ratio regime in Ref. [124].

Within this framework, the threshold mass M_{thr} is a function of the progenitor masses and of the EOS properties. Then, disposing of a posterior representation of the EOS, the information can be translated in term of $\{M, M_{\text{thr}}\}$. This task can be achieved employing EOS-parameterized sampling [e.g. 301, 302]. These methods employ additional degrees of freedom in order to parameterize the EOS and they explore the parameters' space estimating the EOS posterior together with the BNS properties. The algorithm does not require the sampling of the tidal polarizabilities Λ_i since they can be estimated as functions of the NS masses for each EOS. These data naturally provide information on M_{\max}^{TOV} , C_{\max}^{TOV} and k_{thr} . Then, the fraction of the posterior distribution that lies above the diagonal is equal to the posterior PC probability, i.e.

$$P_{\text{PC}} = P(M > M_{\text{thr}}|d). \quad (2.32)$$

As an additional step, one may choose to impose further implicit constraints on the parameter space, such as requiring that the EOS support NS masses larger than a given value, e.g. the observation of the binary pulsar PSR J0348+0432 [87].

Figure 2.6 (left) shows the application of the threshold mass method to GW170817 data, reporting the posterior CDFs of M/M_{thr} . The results are computed by post-processing the publicly available LVK posterior samples [14] estimated with a phenomenological GW model and a spectral EOS parameterization based on the adiabatic index [301, 303]. We find a significant difference between the analyses with and without the M_{\max}^{TOV} constraint, that estimate the PC probability at 0.09 and 0.59 respectively. The reason is that the M_{\max}^{TOV} constraint removes part of the EOS parameter space that is too soft to support a NS mass of $1.97 M_{\odot}$. The effect on P_{PC} is significant, since the recovered binary parameters of GW170817 happen to lie close to the PC threshold.

2.4.2 Tidal threshold

By inspecting the NR database [300], we observe that all the reported PC mergers are captured by the condition $\tilde{\Lambda} < \tilde{\Lambda}_{\text{thr}}$ with $338 \lesssim \tilde{\Lambda}_{\text{thr}} \lesssim 386$. Then, instead of choosing a hard cutoff at a fixed value, we define an empirical PC probability as function of a given $\tilde{\Lambda}$ such that these bounds are included within the support of its distribution. We opt for a sigmoid-type conditional PC probability as

$$P(\text{PC}|\tilde{\Lambda}) = \left(1 + e^{\frac{\tilde{\Lambda}-\tilde{\Lambda}_0}{\beta}}\right)^{-1}, \quad (2.33)$$

which tends to 1 (0) for small (large) values of $\tilde{\Lambda}$. The values for the sigmoid parameters, i.e. the central value and the width, are chosen based on the available set of NR simulations in this region to be $\tilde{\Lambda}_0 \simeq 362$ and $\beta \simeq 13.7$ respectively. Then, once the posterior $p(\tilde{\Lambda}|d)$ is estimated via PE routines, the PC probability is simply computed by integrating the posteriors from the minimum value up to the threshold value using the sigmoid of Eq. (2.33) as a kernel

$$P_{\text{PC}} = \int P(\text{PC}|\tilde{\Lambda}) p(\tilde{\Lambda}|d) d\tilde{\Lambda}. \quad (2.34)$$

Figure 2.6 (right) shows the PC probability obtained with the threshold- $\tilde{\Lambda}$ method employing the posterior PDFs discussed in Section 2.2.2 (re-weighted to uniform prior). We find a PC probability between $P_{\text{PC}} \sim 24\%$ and $\sim 70\%$, depending on the waveform approximant and on the upper cutoff frequency used in the analysis. The waveform approximants estimating the largest $\tilde{\Lambda}$ give the smaller probabilities. The largest PC probability is obtained using the phenomenological model, which tends to introduce a systematic bias favoring PC (see Section 2.3). We observe that the parameters of GW170817 are measured around the threshold region both for the threshold-mass method and for the threshold- $\tilde{\Lambda}$ method. In general, these results seem to provide a non-definitive answer as to whether the BNS merger was followed by a PC to a BH. However, taking a more comprehensive point of view and including EM counterparts and heavy pulsar information, the PC hypothesis is strongly disfavored [e.g. 66, 146, 294].

Chapter 3

Electromagnetic counterparts

The spectrum of the KN transient AT2017gfo has been recorded from ultraviolet (UV) to NIR [49, 304] starting from ~ 11 hrs after the GW peak. This delay was due to the sky position of the source at the moment of the merger, which was located above the Southern Ocean making it inaccessible to the majority of the telescopes. At early times, the observed data showed a bright blue spectrum with a peak of magnitude ~ 17 in the g band 1 day after the merger (blue KN). Between five to seven days after merger, the peak moved towards NIR frequencies with fainter magnitudes around ~ 19 in the K_s band (red KN). In order to explain these features, the KN models require at least two ejecta components [e.g. 201, 305]. The presence of multiple shells of ejected matter evinces also from NR simulations, that indicate the existence of multiple engines that contribute to matter outflows, from the dynamical to the disk winds ejecta [137, 139, 306, 307, 308]. NR simulations also show that the geometry profiles of the ejecta are not spherically symmetric and their distributions are not homogeneous [83, 128, 139]. Given the challenges and uncertainties associated to the theoretical prediction of KN features, Bayesian inference and MS of the observational data can provide important insights on physical processes hidden in the KN signature.

In this Chapter, we perform Bayesian inference on the AT2017gfo data, investigating the geometry of the ejecta components and we constrain the EOS properties of NS matter combining the MM data. In Section 3.1, we review the light-curve (LC) model employed in this *Thesis*. We introduce the KN PE framework in Section 3.2 and we present the results of the MS, discussing the inferred ejecta properties. Finally, in Section 3.3, we perform MM EOS inference by combining KN and GW PEs through NR-calibrated relations and by considering the recent NICER observations [60, 61, 64, 65].

3.1 Light-curve models

After the BNS collision, an amount of $O(10^{-3} M_{\odot})$ is ejected on dynamical timescales and the accretion disk can reach $O(10^{-2} M_{\odot})$ on viscous timescales. The NS matter is neutron-rich and this environment represents an ideal site for r -process nucleosynthesis [e.g. 83, 146], which constitutes the primary engine that brightens the KN. The density conditions are such that that neutrons are captured much faster than the involved nuclei can decay and, once the neutron supply becomes insufficient, the temporarily formed nuclei decay toward the valley of β -stability. Thus, the energetic processes of the KN are governed by the nuclear forces that intervene in the environment surrounding the remnant. Moreover, the KN LCs depend on the intrinsic properties of the ejected matter, such as mass and velocity [125, 155, 156, 157], that can be related to the EOS [e.g. 309, 310].

The modeling of KNe is a challenging task due to the complexity of the underlying physics [146]. Current KN models suffer from theoretical uncertainties due to the incomplete knowledge of the thermalization processes [311, 312] and the energy-dependent photon opacities in r -process matter [309, 313]. Accurate descriptions of the radiation transport processes can help in this regard, offering a robust framework to model the energy transfer in the form of EM radiation [e.g. 312, 314, 315]. However, these implementations are generally based on numerical methods, significantly increasing the computational costs of the model and incapacitating the practical use for PE studies. Another source of error come from the choice of the ejecta profiles. Current KN models often use either simplistic ejecta profiles or simplistic radiation schemes [e.g., 128, 201, 316, 317]. Thus, due to the complicated (partially-modeled) underlying physics, the KN inference is subject to much larger systematic uncertainties compared to GW one.

In the following Sections, we first discuss the modeling of the KN LC from a single shell of ejected matter (Section 3.1.2), and we extend the discussion to the multi-component ejecta shells used in our analyses (Section 3.1.2).

3.1.1 Single-component ejecta

The KN model employed in our work is based on Ref. [128, 316, 318]. Let us consider a shell of ejected matter characterized by a mass density $\varrho(\mathbf{r})$, with total mass m_{ej} and gray opacity κ (mean cross section per unit mass). We assume that the shell is in homologous expansion symmetrically with respect to the equatorial plane with

root-mean-square (RMS) velocity v , such that its mean radius is $R \sim vt$ after a time t following the merger. Matter opacity to EM radiation can be expressed in terms of the optical depth τ , which is estimated as $\tau \simeq \rho\kappa R$. After the BNS collision, when matter becomes unbound and r -process nucleosynthesis occurs, the ejecta are extremely hot, $T \sim 10^9$ K [83, 319, 320]. However, at early times the thermal energy is not dissipated efficiently since the environment is optically thick ($\tau \gg 1$) and photons diffuse out only on the diffusion timescale until they reach the photosphere ($\tau = 2/3$). As the outflow expands, its density drops ($\rho \propto t^{-3}$) and the optical depth decreases, allowing photons to escape.

The key concept behind KNe is that photons can contribute to the EM emission at a given time t if they diffuse on a timescale comparable to the expansion timescales, i.e. if they escape from the shells outside R_{diff} , where R_{diff} is the radius at which the diffusion time $t_{\text{diff}} \simeq R\tau/c$ equals the dynamical time t [141, 146, 316]. Since $t_{\text{diff}} \propto t^{-1}$, a larger and larger portion of the ejecta becomes transparent with time. The luminosity peak of the KN occurs when the bulk of matter that composes the shell becomes transparent. As first approximation [321], the characteristic timescale at which the light curve peaks can be estimated as

$$t_{\text{peak}} = \sqrt{\frac{3m_{\text{ej}}\kappa}{4\pi\beta v c}}, \quad (3.1)$$

where the dimensionless factor β depends on the density profile of the ejecta. For a spherical symmetric, homologously expanding ejecta ($\beta \simeq 3$) with mass $m_{\text{ej}} = 10^{-2} M_{\odot}$, velocity $v = 0.1 c$ and opacity in the range $\kappa \simeq 1\text{--}50 \text{ cm}^2 \text{ g}^{-1}$, which are typical values respectively for lanthanide-free and for lanthanide-rich matter [322, 323], Eq. (3.1) predicts a characteristic t_{peak} in the range 1–10 days [294].

The radioactive r -process decays provide a time-dependent nuclear heating rate. An additional time dependence is introduced by the thermalization efficiency, i.e. the efficiency at which this nuclear energy thermalizes within the expanding ejecta [311, 312, 324, 325]. The time-dependent nuclear heating rate ϵ_{nuc} entering these calculations is approximated by an analytic fitting formula, derived from detailed nucleosynthesis calculations [311],

$$\epsilon_{\text{nuc}}(t) = 2 \epsilon_0 \epsilon_{\text{th}}(t) \epsilon_{\text{nr}}(t) \left[\frac{1}{2} - \frac{1}{\pi} \arctan \left(\frac{t - t_0}{\sigma} \right) \right]^{\alpha}, \quad (3.2)$$

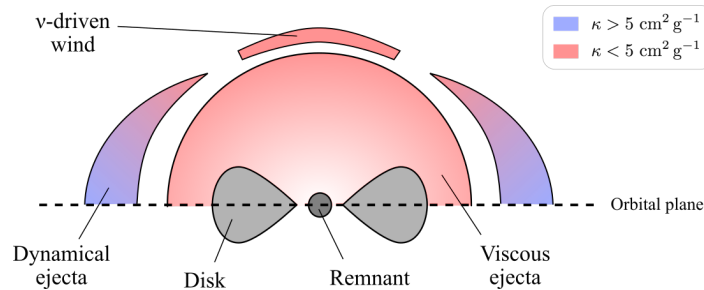


FIGURE 3.1: Graphic representation of a KN and BNS remnant. The figure highlights the ejecta components and the remnant with the accretion disk. The colors refer to the opacity of the environment, i.e. red for low opacities and blue for high opacities. The ejecta components are assumed to be symmetric with respect to the orbital plane (dashed line).

where $\sigma = 0.11$ s, $t_0 = 1.3$ s, $\alpha = 1.3$ and $\epsilon_{\text{th}}(t)$ is the thermalization efficiency tabulated according to Ref. [312]. The heating factor $\epsilon_{\text{nr}}(t)$ is introduced as in Ref. [16, 128] to improve the behavior of Eq. (3.2) in the regime of mildly neutron-rich matter [318]. Then, the total luminosity is calculated as

$$L = \int_{R_{\text{diff}}(\Omega)}^{R_{\text{ph}}(\Omega)} \dot{\epsilon}_{\text{nuc}} \varrho(\mathbf{r}) d^3r. \quad (3.3)$$

Note that the radii R_{diff} and R_{ph} are in principle functions of the solid angle Ω . The radiated power and the photospheric surface determine the effective emission temperature, T_{eff} through the Stefan-Boltzmann law, i.e. $T_{\text{eff}} = (L/\sigma S_{\text{ph}})^{1/4}$ where S_{ph} is the surface of the photosphere. In order to improve the description in the high-frequency bands (i.e. V, U, B and g) within the timescale of the KN emission [326], we introduce a floor temperature, i.e. a minimum value for T_{eff} . This is physically related to the drop in opacity due to the full recombination of the free electrons occurring when for the matter temperature drops below T_{floor} [144, 327].

3.1.2 Multi-component ejecta

A multi-component KN is described by multiple expanding ejecta shells that are in principle characterized by different profiles and properties, i.e. m_{ej} , v and κ . The total bolometric luminosity is given by the sum of the single contributions, i.e. $L(t) = \sum_k L^{(k)}(t)$ where k runs over the components. The outermost photosphere is the one that determines the thermal spectrum of the emission. Once R_{ph} and T_{eff} have been determined, the spectral flux at the observer location is computed as thermal radiation

from the photosphere, i.e.

$$F_\nu(\mathbf{n}, t) = \int_{\mathbf{n}_\Omega \cdot \mathbf{n} > 0} \left(\frac{R_{\text{ph}}(\Omega, t)}{D_L} \right)^2 B_\nu(T_{\text{eff}}(\Omega, t)) \mathbf{n} \cdot d\Omega \quad (3.4)$$

where \mathbf{n} is the unitary vector along the line of sight, \mathbf{n}_Ω is the unitary vector spanning the solid angle Ω , D_L is the luminosity distance, and $B_\nu(T_{\text{eff}})$ is the spectral radiance at frequency ν for a surface of temperature T_{eff} . Lastly, from Eq. (3.4), it is possible to compute the apparent bolometric magnitude mag_b in a given photometric band b as:

$$\text{mag}_b(\mathbf{n}, t) = -2.5 \log_{10} (F_{\nu_b}(\mathbf{n}, t)) - 48.6, \quad (3.5)$$

where ν_b is the effective central frequency of the photometric band b .

By inspecting NR and long-duration GRHD simulations [161, 314, 328], it is possible to understand the dynamics of the unbound matter identifying different ejecta component. An ejecta component is characterized by a physical engine that originates it, yielding to different geometries and compositions, e.g. dynamical ejecta and baryonic winds [128, 316, 318, 329]. Figure 3.1 shows a graphic representation of a three-component anisotropic KN. In our work, we assume the ejecta to be either spherical or axisymmetric with respect to the rotational axis of the remnant, and symmetric with respect to the equatorial plane. In general, the geometry of each ejecta component could be inferred through PE routines, using parameterized profiles. However, in order to limit the number of the total degrees of freedom and to avoid redundancies in the KN description, we consider fixed ejecta profiles and we perform MS in order to understand which configuration is preferred by the data. In our work, we include the following ejecta components.

- *Dynamical ejecta*: The BNS collision ejects unbound matter on the dynamical timescale, whose properties strongly depend on the total mass of the BNS, on the mass ratio and on the EOS [e.g. 119, 125, 138, 155, 156, 330, 331, 332]. This ejecta component is primarily generated by two engines. The first channel of dynamical ejection is related to tidal forces that occur in proximity of the merger and contribute in the formation of a equatorial outflow of matter. On the other hand, the BNS collision generates shocks at the contact interface between the merging stars unbinding a considerable amount of matter by hydrodynamical processes. In general, the expansion of this ejecta component has a velocity of roughly $v \sim 0.2c$. Moreover, the unbound matter is expected to have a composition similar to the one of the progenitors, i.e. low electron fraction

$Y_e < 0.25$ and large opacities. Nevertheless, neutrino irradiation (if significant), might increase the ejecta Y_e and prevents the formation of lanthanides. For the anisotropic analyses, the mass profile is taken to be $\varrho(\theta) \propto \sin \theta$, where θ is the polar angle, and the opacity profile is taken as a step function in θ characterized by the parameters $\{\kappa_{\text{low}}, \kappa_{\text{high}}\}$, respectively for low- and high-latitudes.

- *Disk's viscous ejecta:* Viscous torques of dynamical and magnetic origin can unbind matter from the disk around massive NSs or BHs [308, 333, 334]. This viscous component is expected to unbound a large fraction of the disk matter on longer timescale, reaching $m_{\text{ej}} \lesssim 10^{-1}M_{\odot}$, with a relatively low velocity, $v \lesssim 0.05c$. The corresponding ejecta are more uniformly distributed over the polar angle than the other components [320, 335]. Thus, $\varrho(\theta)$ is always assumed to be isotropic for this component. The presence or the lack of a massive NS in the center can influence the Y_e of these ejecta component.
- *Neutrino-driven wind:* Simulations of the remnant evolution in the aftermath of a BNS merger reveal the presence of other ejection mechanisms happening over the thermal and viscous evolution timescales [e.g. 137, 336, 337, 338, 339]. If the ejection happens while the remnant is still a relevant source of neutrinos, neutrino irradiation has enough time to increase Y_e above 0.25, preventing full r -process nucleosynthesis, especially close to the polar axis. Detailed simulations [137, 318, 340, 341] show that a relatively small fraction of the expelled disk localized around the polar axis contributes to this component and its velocity is expected to be $v \lesssim 0.1c$. For this component, we assume uniform mass distribution ϱ for $\theta \leq \pi/6$ and $\varrho = 0$ for $\theta > \pi/6$.

The intrinsic global parameters represent the properties of the source common to every component, such as the floor temperatures, $T_{\text{floor}}^{\text{Ni}}$ and $T_{\text{floor}}^{\text{LA}}$, and the heating rate constant ϵ_0 . In principle, the latter is a universal property which defines the nuclear heating rate as expressed in Eq. 3.2. The whole set of intrinsic parameters determines the physical dynamics of the system and, therefore, they determine the properties of the KN emission, irrespectively of the observer location. The extrinsic parameters are the luminosity distance of the source, D_L and the viewing angle ι . These parameters do not depend on the physical properties of the source and they are related with the observed signal through geometrical arguments. Finally, the set of KN parameters

employed in our model corresponds to

$$\boldsymbol{\theta}_{\text{kn}} = \left\{ \{m_{\text{ej}}, v, \kappa\}_i, T_{\text{floor}}^{\text{Ni}}, T_{\text{floor}}^{\text{LA}}, \epsilon_0, D_L, \iota \right\}, \quad (3.6)$$

where i runs over the number of employed components.

3.2 Inference of AT2017gfo

The properties of some ejecta components could be inferred extrapolating the tidal GW information [e.g. 294]. However, we take here the more comprehensive approach of analyzing the observed KN LCs with theoretical models within a Bayesian framework. The prior PDFs for all the parameters are taken uniform in their bounds, except for the followings. For the extrinsic parameters $\{D_L, \iota\}$, we set the priors equal to the marginalized posterior PDFs coming from the low-spin-prior measurement of GW170817 [172]; For the heating rate factor ϵ_0 , we use a uniform prior PDF in $\log \epsilon_0$, i.e. $p(\epsilon_0|H) \propto \epsilon_0^{-1}$, since this parameter strongly affects the LC and it is free to vary in a wide range. Moreover, we adopt a prior range according with the estimation given in Ref. [311]. We assume the sky position of the source to be known and the time of coalescence to be the same of the trigger time of GW170817 [39]. Furthermore, we do not take into account redshift contributions.

The data $\{d_{b,i}, \sigma_{b,i}\}$ are the apparent magnitudes observed from AT2017gfo, with their standard deviations, from [201]. The index b runs over all considered photometric bands, covering a wide photometric range from the UV to the NIR, while for each band b the index i runs over the corresponding sequence of N_b temporal observations. Additionally, the magnitudes have been corrected for Galactic extinction [342]. We introduce a Gaussian likelihood function in the apparent magnitudes with mean and variance, $d_{b,i}, \sigma_{b,i}^2$, from the observations of AT2017gfo,

$$\log p(\mathbf{d}|\boldsymbol{\theta}_{\text{kn}}) \propto -\frac{1}{2} \sum_b \sum_{i=1}^{N_b} \left[\frac{d_{b,i} - \text{mag}_{b,i}(\boldsymbol{\theta}_{\text{kn}})}{\sigma_{b,i}} \right]^2, \quad (3.7)$$

where $\text{mag}_{b,i}$ are the magnitudes predicted by the KN model. The likelihood definition Eq. (3.7) is in accordance with the residuals introduced in Ref. [128] and it takes into account the uncertainties due to possible technical issues of the instruments and generic non-stationary contributions, providing a good characterization of the noise.

TABLE 3.1: Logarithmic evidences for the analyzed KNe models. The geometries are either isotropic or anisotropic. The D label refers to the dynamical ejecta, the V label corresponds to the viscous ejecta, and the N label is the ν -driven wind. The evidences are normalized to the value of the isotropic one-component case, i.e. $\log p(\mathbf{d}|\text{Iso-D}) = -23510 \pm 1$

Geometry	Iso.	Iso.	Ani.	Ani.	Ani.	Ani.
Components	D	D+V	D	N+V	D+V	D+N+V
$\log \frac{p(\mathbf{d} \text{Model})}{p(\mathbf{d} \text{Iso-D})}$	0 ± 2	3791 ± 2	13590 ± 2	12407 ± 2	13954 ± 2	14071 ± 2

Given a Bayesian model for KN transients, it is possible to infer the ejecta composition and geometry directly from the observed data. Then, we perform Bayesian KN analyses on AT2017gfo employing the CPNEST [197] nested sampling algorithm with 1024 live points. We perform KN inference varying the number of ejecta components and considering two geometric configurations, i.e. isotropic and anisotropic. We present the MS results in Section 3.2.1 and we discuss the recovered ejecta properties in Section 3.2.2.

3.2.1 Multi-component model selection

Table 3.1 reports the evidences computed for the considered models. The results show an increasing trend with the number of models' components, in agreement with previous findings [e.g. 48, 128, 201]. Moreover, for a fixed number of components, the anisotropic description of the ejecta components is strongly preferred with respect to isotropic profiles, with a logarithmic BF of the order of $\sim 10^4$. According to the estimated evidences, the isotropic two-components model is already disfavored with respect to the anisotropic single-component. This is consistent with the hierarchy observed in the LC residuals, and the better match to the data for multi-component models. Moreover, the favored model is the three-component KN constituted by a fast dynamical ejecta (comprising both a red-equatorial and a blue-polar portion), a slow isotropic shell and a polar wind. These results confirm the non-trivial dependence of the LCs from the ejecta geometries and distributions. Note that the prior choices can affect the recovered BFs up to $O(10)$ [343, 344, 345]. Considering this additional uncertainty, the results on geometries remain robust.

The motivation for such results can be deduced comparing the observed data to the recovered LCs. Figure 3.2 shows the comparison between isotropic and anisotropic cases for the two-component case. This behavior is observed for all the considered cases. The isotropic models give a good fitting for early times and their LCs capture

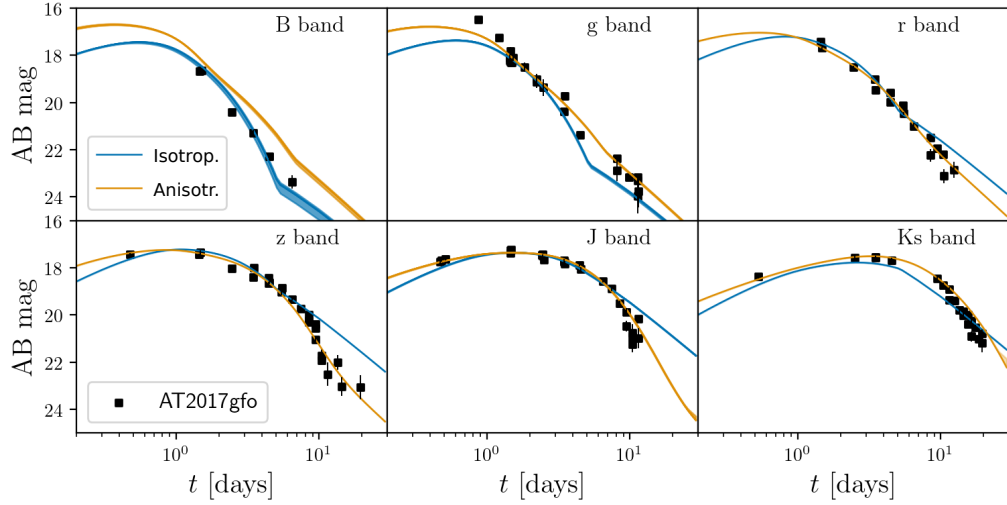


FIGURE 3.2: Recovered LCs for isotropic (blue) and anisotropic (orange) two-components models compared to the AT2017gfo data (black squares). The shadowed areas are the 90% of the LCs. Different panels show the absolute bolometric magnitudes for different photometric bands.

the general trends of the data. However, for times larger than ~ 8 days after merger, these models do not capture all the features of the data within the provided prior bounds. This inaccuracy is particularly evident in the NIR, where the LCs predicted by the isotropic models do not recover the correct slopes of the data. On the other hand, the anisotropic cases are more suitable at adapting the model to the different features present in the data, even for large time-scales. However, it overestimates the KN emission in the blue band.

Remarkably, none of the considered models is able to fully capture the trend described by the observed data in the Ks band for time larger than 10 days, within the provided prior bounds. This is expected from the simplified treatment of the radiation transport and the approximated heating rate in our models. This could indicate a significant deviation from the black-body emission adopted in our model at late times.

3.2.2 Ejecta properties

A general fact is that the marginalized posterior PDFs for the ejected mass of the viscous component is always constrained against the lower bound $10^{-2} M_{\odot}$, when this component is involved. Moreover, for the majority of the analyses, the distance parameter is biased towards larger values, inconsistently with the estimates from Ref. [39, 66], and the heating rate parameter ϵ_0 is generally overestimated comparing with

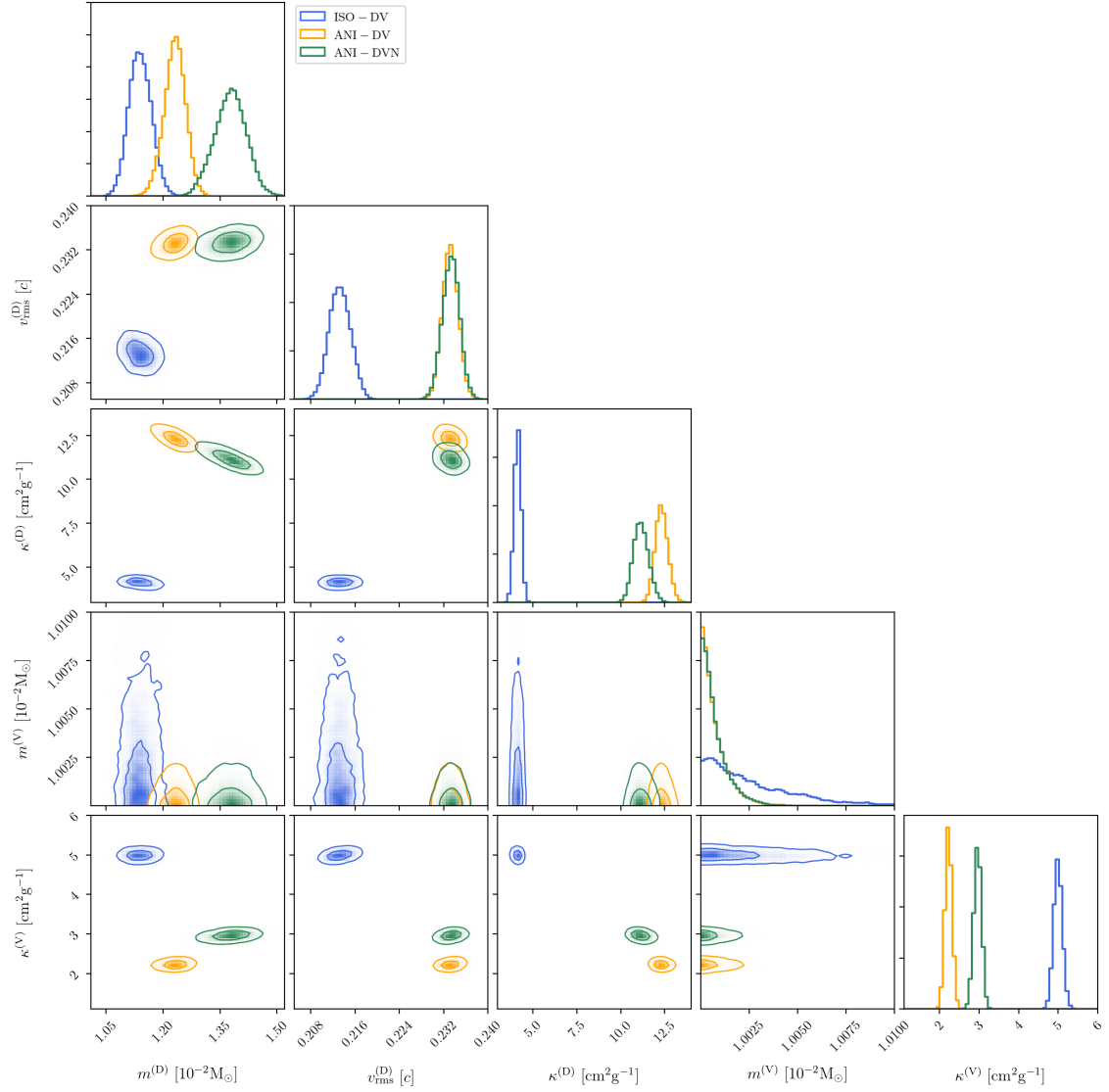


FIGURE 3.3: Marginalized posterior PDF for dynamical ejecta parameters for three selected cases: isotropic two-components (blue), anisotropic two-components (orange) and anisotropic three-components (green). For the dynamical component (D), we show the ejected mass m_{ej} , RMS velocity v and the opacity κ (low-latitude component for anisotropic cases). For the viscous component (V), we show the ejected mass m_{ej} and the opacity κ . The contours report the 50% and the 90% credible regions.

the estimates from nuclear calculations [311, 312, 327, 346, 347]. This behavior can be explained looking at Eq. (3.2) and (3.5): D_L and ϵ_0 are largely degenerate and both concur to determine the brightness of the observed LCs. Thus, the correlations between these parameters induce biases in the recovered values. The physical explanation of this effect can be motivated with the poor characterization of the model in the NIR bands. Note that this bias concurs in the overestimation of the LC in the high-frequency bands (i.e. U, B and V), where the number of measurements is lower with respect to the other employed bands. Furthermore, the viewing angle is biased toward larger values, roughly ~ 60 deg. The same trend is shown by the anisotropic three-component model employed in Ref. [201]. These results suggest that, under a modeling perspective, current KN description contains large theoretical uncertainties. Hence, the development and the improvements of KN templates is an urgent task in order to conduct reliable and robust analyses in the future.

Regarding the isotropic model, the individual most-likely value for dynamical ejected mass parameter lies around $\sim 10^{-2} M_\odot$, as shown in Figure 3.3 (blue), in agreement with the measurement presented in Ref. [294]. This range of values is slightly overestimating the expectations coming from NR simulations for the dynamical component [82, 83, 139, 161, 348]. This could be explained by considering the effect of the spiral-wave wind [139], that constitute a massive and fast ejecta on timescales of 10 – 100 ms. The spiral-wave wind is not considered as components in our models because it would be highly degenerate with the dynamical ejecta. The recovered opacity parameters are roughly $4\text{--}5 \text{ cm}^2 \text{ g}^{-1}$. The velocity of the dynamical component is greater than secular velocity, accordingly with the theoretical expectations. Comparing with other fitting models, the recovered ejected masses m_{ej} result smaller with respect to the analogous analysis of Ref. [201], while the results roughly agree with the estimations coming from Ref. [305]. However, it is not possible to perform an apples-to-apples comparison between these results, due to the systematic differences in modeling between the semi-analytical model and the radiative-transport methods employed in Ref. [201, 305].

Figure 3.3 shows also the posterior PDFs for the ejecta parameters for the anisotropic models for two (orange) and three (green) components. The latter gives the best-fitting results among the considered cases. Also for these cases, the dynamical ejected mass value lies around $\sim 10^{-2} M_\odot$, in agreement with previous estimates [294] and the recovered mass slightly overestimates the results coming from targeted NR simulations [82, 83, 139, 161, 348], similarly to isotropic case. The velocity is well constrained around

$\sim 0.23c$. The recovered low-latitude opacity corresponds roughly to $12 \text{ cm}^2 \text{ g}^{-1}$ and high-latitude opacity is constrained around the lower bound, $0.1 \text{ cm}^2 \text{ g}^{-1}$. This result can be explained by considering that the mass of the dynamical component slightly overshoots the NR expectations [82, 83, 139, 161, 348] (of a factor ~ 1.25), and by noticing that the ejected mass correlates with the luminosity distance and the heating factor (that are generally biased). This combination generates the overestimation of the data in the UV region. In order to improve the fitting to the observed data, the model tries to compensate this effect and the high-latitude opacity tends to move towards lower values. Furthermore, the dynamical component results into the faster ejected shell, validating the interpretation that this contribution is generated at dynamic time-scales. Concerning the viscous component, its velocity results an order of magnitude smaller than the one of the dynamical ejecta, in agreement with the expectations. This enforces the hypothesis for which the viscous ejecta contributes mostly to the red KN. The posterior PDF of opacity parameter peaks around $\sim 5 \text{ cm}^2 \text{ g}^{-1}$, denoting a medium opaque environment. These results agree with the studies presented in [138] and they contribute to the KN LC in the optical band.

The neutrino-driven wind component is employed only for the three-component anisotropic case. The posterior PDF for its ejected mass shows a bimodality and this degeneracy correlates with the heating rate parameter ϵ_0 . The marginalized posterior PDF for the ν -wind ejected mass has its dominant peak in proximity of $2.5 \times 10^{-3} M_\odot$, while the secondary mode is located slightly below $2 \times 10^{-3} M_\odot$. These results are largely consistent with aftermath computations [137] and with theoretical expectations [128], as it is for the recovered velocity and opacity parameters, corresponding to $v \simeq 0.05c$ and $\kappa \simeq 2.3 \text{ cm}^2 \text{ g}^{-1}$.

3.3 Multi-messenger parameter estimation

The combination of GW and EM signals coming from the same BNS merger allows to improve the constraints on the intrinsic properties of the system and the nuclear EOS. In this section, we employ NR information [161, 310] in order to map the KN posterior PDF of the preferred model (i.e. anisotropic three-component) into the BNS properties and we employ GW and EM information in the inference of the NS EOS. In Section 3.3.1, we discuss the mapping of the KN parameters and we show the joint GW-KN PE. Subsequently, in Section 3.3.2, we include the information of electron fraction and disk mass during the KN inference. In Section 3.3.3, we constrain the

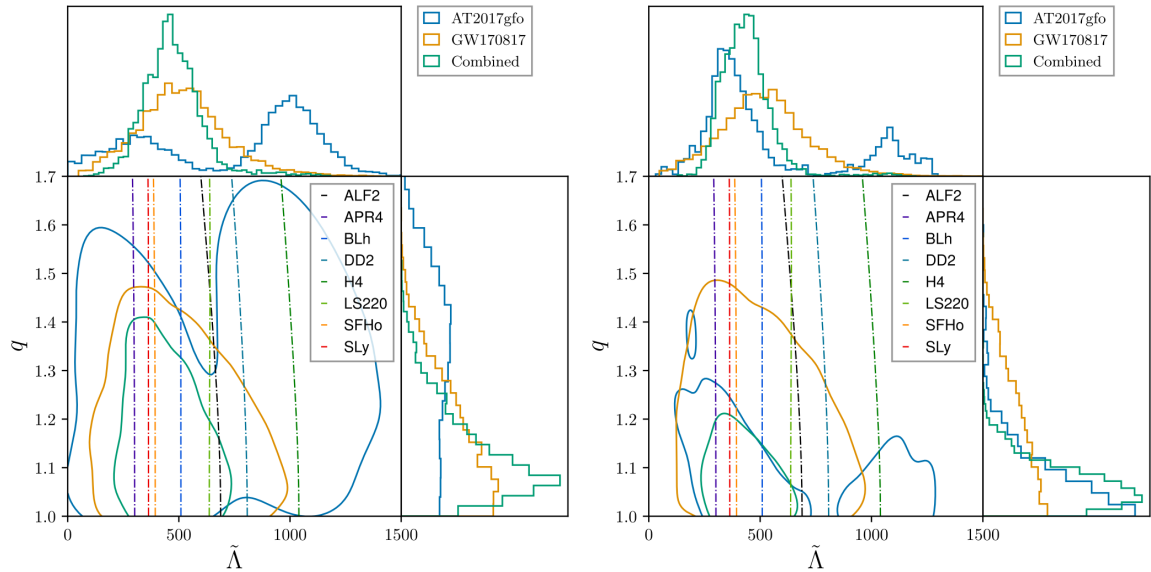


FIGURE 3.4: Posterior PDFs of tidal parameter $\tilde{\Lambda}$ and mass ratio q inferred from the joint GW170817-AT2017gfo PE study. *Left panel:* The blue solid lines refer to the resampled values extracted from the KN analysis. The orange solid lines refer to the GW results, where the samples have been weighted over a flat prior in $\tilde{\Lambda}$. The green solid lines are the combined inference. The contours represent the 90% credible regions. The plot shows the expectations of some representative EOS. *Right panel:* Posterior PDF in the $\{\tilde{\Lambda}, q\}$ plane analogously to the left panel but with the inclusion of Y_e and M_{disk} information.

NS radius through NR-calibrated relations. Finally, in Section 3.3.4, we perform MM EOS inference combining GW170817-AT2017gfo results with NICER observations.

3.3.1 Mapping the dynamical ejecta properties

The NR fits presented in [310] use simulations targeted to GW170817 [82, 83, 139, 161, 348] and give the mass m_{ej} and velocity v of the dynamical ejecta as functions of the BNS parameters $\{q, \tilde{\Lambda}\}$. In order to recover the posterior PDF of the latter, we adopt a resampling method, similar to the procedure presented in Ref. [305, 317]: a sample $\{q, \tilde{\Lambda}\}$ is extracted from the prior PDF exploiting the ranges $q \in [1, 2]$ and $\tilde{\Lambda} \in [0, 5000]$. In particular, the prior PDF is taken uniformly distributed in the tidal parameters $\tilde{\Lambda}$; while, regarding the mass ratio q , we employ a prior PDF uniform in the mass components, analogously to GW analyses [39, 158, 254]. Subsequently, the tuple $\{q, \tilde{\Lambda}\}$ is mapped into the dynamical ejecta parameters $\{m_{\text{ej}}, v\}$ using the NR formulae presented in Ref. [310]. Furthermore, since NR-calibrated relations carry non-negligible intrinsic uncertainties, we introduce calibration parameters $\{\alpha_m, \alpha_v\}$,

such that

$$\begin{aligned}\log_{10} m_{\text{ej}} &= (1 + \alpha_m) \cdot \log_{10} m_{\text{ej}}^{\text{fit}}(q, \tilde{\Lambda}), \\ v &= (1 + \alpha_v) \cdot v^{\text{fit}}(q, \tilde{\Lambda}).\end{aligned}\tag{3.8}$$

The calibration parameters $\alpha_{m,v}$ are sampled along the other parameters using a normally distributed prior with vanishing means and standard deviations prescribed by the relative uncertainties of NR fits equal to 0.2 for both. The likelihood is estimated in the dynamical ejecta parameter space $\{m_{\text{ej}}, v\}$ using a kernel density estimation of the marginalized posterior PDF recovered from the preferred KN model. The re-sampled posterior PDF is marginalized over the calibration parameters $\{\alpha_m, \alpha_v\}$. The BNS parameter space is explored using MCMC technique. Note that a correct characterization of the fit uncertainty is crucial, since this contribution is the largest source of error in the inference of $\{q, \tilde{\Lambda}\}$.

The posterior PDF in the $\{q, \tilde{\Lambda}\}$ plane as obtained from the dynamical ejecta properties fitted to AT2017gfo data is shown in Figure 3.4 (left). The measurement of the tidal parameter leads to $\tilde{\Lambda} = 900_{-780}^{+310}$, with a bimodality in the marginalized posterior PDF, due to the quadratic nature of the employed NR formulae, with modes $\tilde{\Lambda} \simeq 370$ and $\tilde{\Lambda} \simeq 1000$. The mass ratio is constrained to be lower than 1.54 at the 90% credibility level. The uncertainties of the KN measurement are larger than those of the GW analyses [39, 40, 254] due to the errors introduced by the NR fit formulae. Figure 3.4 (left) shows also the results coming from the GW170817 analysis with `TEOBResumS` [254], which employs a low-spin prior and a cutoff-frequency of 1 kHz. The GW posterior samples have been re-weighted with a rejection sampling to the prior PDFs employed in the KN study, in order to use the same prior information for both analyses. Under the assumption that GW170817 and AT2017gfo are generated by the same physical event, the $\{q, \tilde{\Lambda}\}$ posterior PDFs coming from the two independent analyses can be combined, in order to constrain the estimation of the inferred quantities. The joint probability PDF is computed as the product of the single terms,

$$p(q, \tilde{\Lambda} | \mathbf{d}_{\text{kn}}, \mathbf{d}_{\text{gw}}) \propto p(\mathbf{d}_{\text{gw}}, \mathbf{d}_{\text{kn}} | q, \tilde{\Lambda}) p(q, \tilde{\Lambda}) = p(\mathbf{d}_{\text{kn}} | q, \tilde{\Lambda}) p(\mathbf{d}_{\text{gw}} | q, \tilde{\Lambda}) p(q, \tilde{\Lambda}), \tag{3.9}$$

and the samples are extracted with a rejection sampling.

The combined inference, shown in Figure 3.4 (left), leads to a constraint on the mass ratio of $\lesssim 1.27$ and on the tidal parameter $\tilde{\Lambda} = 460_{-190}^{+210}$, at the 90% credibility level. The error on $\tilde{\Lambda}$ is $\sim 20\%$ at $1-\sigma$ level. Fixing the source-frame chirp mass

$\mathcal{M} = 1.188 M_{\odot}$, we can constrain the total binary mass $M \in [2.73, 2.75] M_{\odot}$ at the 90% credibility level. These estimates are in agreement with independent results from literature [e.g. 349, 350]. Our observational constraints disfavor stiff EOSs, such as DD2, and support mildly-soft EOSs, such as SFHo and BLh. Interestingly, GW170817-targeted NR simulations performed with these EOSs [161] show a delayed collapse on timescales of $O(10 \text{ ms})$, supporting the discussion of Section 2.4 and supporting studies of PM GW radiation (see Chapter 4).

3.3.2 Incorporating electron fraction and disk mass

From NR simulations, it is possible to estimate the average electron fraction, Y_e , of the dynamical ejecta [161, 310]. This quantity is the ratio of the net number of electrons to the number of baryons and it is tightly related with the opacity of the shell [83, 351, 352], since it mostly determines the nucleosynthesis rates in low-entropy neutron-rich matter. We compute the average opacity $\bar{\kappa}$ of a shell as the integral of the opacity over the polar angle weighted on the mass distribution,

$$\bar{\kappa} = \frac{1}{m_{\text{ej}}} \int_0^{\pi} \varrho(\theta) \kappa(\theta) \sin \theta \, d\theta. \quad (3.10)$$

Imposing the assumptions on the profiles of the dynamical ejecta, we get

$$\bar{\kappa} = \left(\frac{1}{2} + \frac{1}{\pi} \right) \kappa_{\text{low}} + \left(\frac{1}{2} - \frac{1}{\pi} \right) \kappa_{\text{high}}. \quad (3.11)$$

Thanks to this definition, it is possible to map the opacity $\bar{\kappa}$ into the electron fraction Y_e , using the relation presented in [309]. Subsequently, the Y_e can be related with the BNS parameters $\{q, \tilde{\Lambda}\}$, using NR fit formulae [310]. We introduce an additional calibration parameter α_Y , such that

$$Y_e = (1 + \alpha_Y) \cdot Y_e^{\text{fit}}(q, \tilde{\Lambda}), \quad (3.12)$$

with a Gaussian prior with mean zero and standard deviation of 0.2. This method allows us to take into account also the contribution of the opacity posterior PDF during the inference of the NS matter.

The employed KN model contains information also on the baryonic wind ejecta. These components are expected to be generated by the disk that surrounds the remnant [308, 334, 353], if present. The disk mass can be estimated from NR simulations

as function of the BNS parameters $\{q, \tilde{\Lambda}\}$, albeit with large uncertainties [70, 125, 310]. We map a fraction ξ of the disk mass M_{disk} into the mass of the baryonic wind components,

$$m_{\text{ej}}^{(\text{V})} + m_{\text{ej}}^{(\text{N})} = \xi \cdot M_{\text{disk}}, \quad (3.13)$$

where $m_{\text{ej}}^{(\text{V})}$ and $m_{\text{ej}}^{(\text{N})}$ are respectively the ejected masses of the viscous and the ν -wind components. The mass fraction ξ is sampled along the other parameters with a uniform prior in the range $[0.1, 0.5]$. We include the disk mass information together with the electron fraction contribution, previously discussed.

The posterior PDFs reinforced with the Y_e and the M_{disk} information are shown in Figure 3.4 (right). Focusing on the KN results, the Y_e contributions reinforce the constraint on the mass ratio posterior, giving $q \leq 1.18$ at 90% credibility level. This effect is motivated by the fact that high-mass-ratio BNS mergers are expected to have $Y_e \lesssim 0.1$ [82, 161]; while, the recovered electron fraction is $Y_e = 0.20_{-0.08}^{+0.04}$. On the other hand, the additional inclusion of M_{disk} information increases the agreement to the GW measurement and attenuates the bimodality of the $\tilde{\Lambda}$ KN posterior. The recovered mass fraction corresponds to $\xi = 0.14_{-0.04}^{+0.27}$. The joined inference with the GW posterior leads to a mass ratio $\lesssim 1.13$ and a tidal parameter of $\tilde{\Lambda} = 430_{-140}^{+180}$, at the 90% credibility. The inclusion of Y_e and M_{disk} information significantly narrowed the posterior PDF reducing the error on the $\tilde{\Lambda}$ measurement of 20% with respect to the study of Section 3.3.1.

3.3.3 Inferring the neutron star radius

Using the EOS-insensitive relation presented in Ref. [349, 354], it is possible to impose a constraint on the radius $R_{1.4M_\odot}$ of a NS of $1.4 M_\odot$. We employ the marginalized posterior PDF for the (source-frame) chirp mass \mathcal{M} coming from the GW170817 measurement [254] and the posterior on the tidal parameter $\tilde{\Lambda}$ obtained with the joint analyses AT2017gfo-GW170817. We adopt a resampling technique to account for the uncertainties in the NR-calibrated relations, introducing a Gaussian calibration coefficient with variance prescribed by Ref. [349, 354]. In Figure 3.5, the NS radius $R_{1.4M_\odot}$ estimation is compared with the mass-radius curves from a sample of nuclear EOS. We estimate $R_{1.4M_\odot} = 12.16_{-1.11}^{+0.89}$ km. The presented measurement agrees with the results coming from literature [14, 180, 349, 350, 354, 355, 356, 357, 358] and its overall error at $1-\sigma$ level corresponds roughly to 500 m. Our bounds impose observational constraints on the nuclear EOS, excluding both very stiff EOSs, such as DD2, BHB $\Lambda\phi$

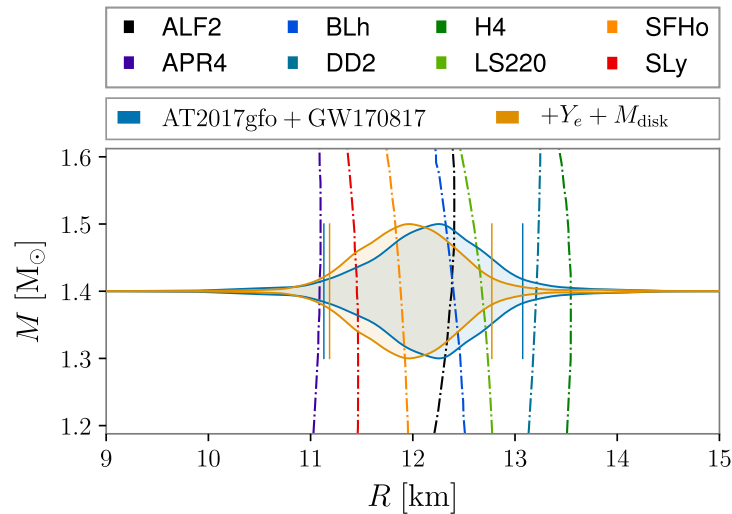


FIGURE 3.5: Posterior PDFs of the radius $R_{1.4M_{\odot}}$ estimated with the joined inference of AT2017gfo and GW170817 plotted on top of the mass-radius sequences extracted from a sample of nuclear EOSs (dashed lines). The blue solid line is computed using the mass and velocity information of the dynamical component and the orange solid curve takes into account also the contribution of electron fraction Y_e and disk mass M_{disk} .

and MS1b, and very soft equations, such as 2B. Moreover, the plot shows also the analogous results obtained including the additional information of electron fraction Y_e and disk mass M_{disk} . These analysis leads to the results of $R_{1.4M_{\odot}} = 11.99^{+0.82}_{-0.85}$ km at the 90% credibility level.

The relations employed here used exclusively targeted data and simulations with state-of-art treatment of microphysical EOSs and neutrino treatment [82, 83, 139, 161, 348]. However, the simulation sample is limited to about hundreds of simulations, with fitting errors that could be reduced by considering data at even higher grid resolutions [310]. For example, assuming all the fit formulae to be exact (i.e. removing all calibration terms), it will be possible to infer the $\tilde{\Lambda}$ parameter from AT2017gfo with an accuracy of $O(10)$, that corresponds to a constraint on the radius $R_{1.4M_{\odot}}$ of roughly 100 m.

3.3.4 Including NICER information

The constraints presented in Section 3.3.2 and 3.3.3 could be improved including the information of GRB170817A [44, 54, 150, 359, 360] and of more recent GW observations of BNS and BH-NS binaries [56, 361]. However, the relation between the GRB properties and the nuclear EOS are unknown and this messenger can only inform us

on the position and orientation of the source [66, 362]. On the other hand, the SNRs of the more recent GW observations is significantly smaller compared to GW170817 and these signals do not provide informative measurements of the tidal parameters. Thus, the inclusion of these events in the presented EOS inference is expected to mildly affect the overall results, as shown also in Ref. [363]. Going beyond BNS merger phenomena, the X-ray observatory NICER recently provided EOS constraints on the NS mass-radius by resolving the pulse profiles of known pulsars [60, 61, 62, 63, 64, 65]. The observation of PSR J0030+0451 and PSR J0740+6620 provided measurements of NS masses (respectively $1.34^{+0.15}_{-0.16} M_{\odot}$ and $2.07^{+0.07}_{-0.07} M_{\odot}$) and equatorial radii (respectively $12.7^{+1.1}_{-1.2}$ km and $12.4^{+1.3}_{-1.0}$ km). Interestingly, the mass of PSR J0030+0451 falls in the posterior support for the mass components of GW170817. Comparing the GW results with the NICER measurements, the EOB predictions show improved agreement compared to the other approximants, supporting the hypothesis of $\tilde{\Lambda} \gtrsim 200$ [284].

It is interesting to investigate the constraints on the NS EOS provided by the combination of GW-KN and the NICER data. We employ an EOS resampling in order to avoid usage of NR-calibrated relations. Employing the EOS set proposed in Ref. [364] as prior, the GW-KN and the NICER information can be (independently and jointly) imposed weighting the EOS samples by the corresponding posterior PDFs. The EOS prior [364] contains two-million EOS that support maximum NS mass above $M_{\text{max}}^{\text{TOV}} > 1.97 M_{\odot}$, consistently with pulsar observations of PSR J0348+0432 [87], and satisfy the condition $\Lambda < 800$ for a $1.4 M_{\odot}$ NS, in order to focus on the relevant posterior support of GW170817 [14, 39, 40]. The only additional assumptions used to construct the EOS set are the validity of GR and causality up to the central density of the maximum mass NS. For each EOS, the corresponding GW-KN probability is computed from the $\{\tilde{\Lambda}, q\}$ posterior PDF (including Y_e and M_{disk} information) as

$$\begin{aligned} p(\text{EOS}|\mathbf{d}_{\text{gw}}, \mathbf{d}_{\text{kn}}) &\propto p(\text{EOS}) \int p(\mathbf{d}_{\text{gw}}, \mathbf{d}_{\text{kn}}|\tilde{\Lambda}, q) p(\tilde{\Lambda}, q|\text{EOS}) d\tilde{\Lambda} dq \\ &\propto p(\text{EOS}) \int p(\tilde{\Lambda}, q|\mathbf{d}_{\text{gw}}, \mathbf{d}_{\text{kn}}) \delta(\tilde{\Lambda} - \tilde{\Lambda}_{\text{EOS}}(q)) d\tilde{\Lambda} dq, \end{aligned} \quad (3.14)$$

where the step makes use of the uniform prior on $\tilde{\Lambda}$. Moreover, δ is the Dirac function and $\tilde{\Lambda}_{\text{EOS}}(q)$ corresponds to the reduced tidal parameter predicted by the EOS as a function of the mass ratio q . This computation assumes a fixed chirp mass $\mathcal{M} = 1.188 M_{\odot}$. We opt to use the $\{\tilde{\Lambda}, q\}$ posterior instead of the $R_{1.4M_{\odot}}$ PDF in order to minimize errors and biases introduced by NR-calibrated relations. Similarly, for the NICER data, the EOS probability can be computed from the mass-radius posterior

TABLE 3.2: EOS constraints from MM PE. We remark that GW data corresponds to LIGO-Virgo (de-glitched) segments of GW170817 [172] and GW data are the photometric data of AT2017gfo [201]. NICER (Miller *et al.*) data correspond to mass-radius posterior PDFs of Ref. [60, 65]. NICER (Riley *et al.*) data correspond to mass-radius posterior PDFs of Ref. [61, 64]. The prior is the EOS set presented in Ref. [364]. The reported data are the medians and the 90% credible intervals of fiducial EOS properties.

MM data	$R_{1.4M_{\odot}}$ [km]	$\Lambda_{1.4M_{\odot}}$	M_{\max}^{TOV} [M_{\odot}]	R_{\max}^{TOV} [km]	$\log_{10} \left(\frac{P_{2\rho_{\text{sat}}}}{\text{dyn cm}^{-2}} \right)$	$\log_{10} \left(\frac{P_{4\rho_{\text{sat}}}}{\text{dyn cm}^{-2}} \right)$
Prior	$12.23^{+0.86}_{-0.80}$	371^{+135}_{-128}	$2.12^{+0.28}_{-0.13}$	$11.1^{+1.3}_{-1.0}$	$34.61^{+0.12}_{-0.15}$	$35.46^{+0.16}_{-0.10}$
GW-KN	$12.23^{+0.75}_{-0.80}$	372^{+135}_{-128}	$2.12^{+0.28}_{-0.14}$	$11.1^{+1.3}_{-1.0}$	$34.61^{+0.12}_{-0.15}$	$35.46^{+0.16}_{-0.10}$
NICER (Miller <i>et al.</i>)	$12.58^{+0.72}_{-0.82}$	461^{+127}_{-165}	$2.10^{+0.19}_{-0.11}$	$11.8^{+1.2}_{-1.2}$	$34.68^{+0.14}_{-0.15}$	$35.44^{+0.12}_{-0.13}$
NICER (Riley <i>et al.</i>)	$12.47^{+0.81}_{-0.94}$	429^{+152}_{-168}	$2.10^{+0.14}_{-0.09}$	$11.5^{+1.3}_{-1.3}$	$34.65^{+0.14}_{-0.18}$	$35.44^{+0.09}_{-0.10}$
GW-KN-NICER (Miller <i>et al.</i>)	$12.39^{+0.70}_{-0.65}$	407^{+119}_{-116}	$2.08^{+0.16}_{-0.09}$	$11.5^{+1.2}_{-1.1}$	$34.63^{+0.12}_{-0.11}$	$35.44^{+0.10}_{-0.10}$
GW-KN-NICER (Riley <i>et al.</i>)	$12.32^{+0.72}_{-0.72}$	389^{+125}_{-121}	$2.09^{+0.12}_{-0.09}$	$11.3^{+1.2}_{-0.9}$	$34.62^{+0.12}_{-0.13}$	$35.44^{+0.09}_{-0.08}$

PDFs of the pulsar observations [60, 61, 64, 65] as

$$p(\text{EOS}|\mathbf{d}_{\text{NICER}}) \propto p(\text{EOS}) \prod_k \int p(m, R|\mathbf{d}_k) \delta(m - m_{\text{EOS}}(R)) dm dR, \quad (3.15)$$

where $m_{\text{EOS}}(R)$ corresponds to the mass predicted by the EOS as a function of the NS radius R and k runs over all the observed NSs, i.e. PSR J0030+0451 (Miller [60] and Riley [61]) and PSR J0740+6620 (Miller [65] and Riley [64]). Eq. (3.15) is estimated separately for both available data sets, Miller [60, 65] and Riley [61, 64]. Finally, the joint GW170817-AT2017gfo-NICER EOS probability can be estimated as the product of Eq. (3.14) and Eq. (3.15) under the assumption that the measurements are independent. Notably, in addition to the study of Section 3.3.3, a EOS sampling method allows to infer the maximum-mass configuration supported by the NS EOS. However, note that the strongest constraints are expected to be provided around the densities (or the masses) of the progenitors.

Figure 3.6 shows the EOS posteriors in the mass-radius plane obtained imposing the GW-KN and the NICER posterior PDFs and Table 3.2 reports the posterior statistics some exemplary EOS properties. The GW-KN posterior Eq. (3.14) predicts a NS radius $R_{1.4M_{\odot}} = 12.23^{+0.75}_{-0.80}$ km and a maximum TOV mass $M_{\max}^{\text{TOV}} = 2.12^{+0.28}_{-0.14} M_{\odot}$. The inclusion of GW-KN improves the constraints on $R_{1.4M_{\odot}}$ and the pressures relation for densities $< 2\rho_{\text{sat}}$. The estimate on $R_{1.4M_{\odot}}$ is roughly consistent with the results of Section 3.3.3, recovered with NR-informed method, and it slightly overestimates similar results from literature [e.g. 14, 180], mainly due to the tidal systematic errors between GW models. The NICER posterior Eq. (3.14) of Miller [60, 65] favors stiffer EOSs and it predicts a NS radius $R_{1.4M_{\odot}} = 12.58^{+0.72}_{-0.82}$ km and a maximum NS mass

$M_{\text{max}}^{\text{TOV}} = 2.10_{-0.11}^{+0.19} M_{\odot}$. On the other hand, the NICER posterior of Riley [61, 64] shifts toward softer EOSs compared to Miller [60, 65], predicting a NS radius $R_{1.4M_{\odot}} = 12.47_{-0.94}^{+0.81}$ km and a maximum NS mass $M_{\text{max}}^{\text{TOV}} = 2.10_{-0.09}^{+0.14} M_{\odot}$. The two NICER inferences show broad agreement between each other. The results from Riley [61, 64] show improved constraints for $M_{\text{max}}^{\text{TOV}}$ and $P_{4\rho_{\text{sat}}}$ due to the narrow posterior PDF of the massive pulsar PSR J0740+6620. The joint MM GW170817-AT2017gfo-NICER inference significantly tightens the previous results. From the data of Miller [60, 65], we recover $R_{1.4M_{\odot}} = 12.39_{-0.65}^{+0.70}$ km and $M_{\text{max}}^{\text{TOV}} = 2.08_{-0.09}^{+0.16} M_{\odot}$; while, for Riley [61, 64], we recover $R_{1.4M_{\odot}} = 12.32_{-0.72}^{+0.72}$ km and $M_{\text{max}}^{\text{TOV}} = 2.09_{-0.09}^{+0.12} M_{\odot}$. The results computed with Miller [60, 65] data show narrower constraints of $R_{1.4M_{\odot}}$ due to the agreement with GW-KN analysis (employing EOB model [254, 284]). On the other hand, the Riley [61, 64] data confidently constrain the maximum TOV mass to $M_{\text{max}}^{\text{TOV}} \lesssim 2.2 M_{\odot}$ at the 90% credibility level. In general, the joint MM PEs show preference towards mildly stiff EOSs, such as BLh and LS220.

Similar MM inferences have been performed in Ref. [63, 180, 349, 350, 357, 358, 363, 365, 366, 367, 368, 369]. In order to connect the EOS properties to the BNS parameters, the majority of these methods rely on EOS-insensitive relations calibrated on NR data. Moreover, computational PE costs are generally improved employing finite-sized EOS priors or performing post-processing analysis of existing results. Notably, the EOS prior considered in our analyses is the largest set among those used in similar studies [180, 357, 363, 368]. Regarding the construction of the EOS prior, different studies typically employ different parameterizations and modelings, implying different prior assumptions between different analyses. However, the majority of the employed EOS sets include identical constraints from massive pulsars [87, 88] and from heavy-ion collisions [102, 103, 370, 371]. Thus, they share part of their prior information. As shown in Ref. [366], the EOS parameterization can have a non-negligible impact on the final results, suggesting that current inferences can be partially affected by prior information. However, all the approaches lead to a similar result of $R_{1.4M_{\odot}} \simeq 12$ km with errors of $\sim 0.5 - 1$ km. Comparing our results with Ref. [363], we observe a consistent estimates of $R_{1.4M_{\odot}}$, although our analysis recovers larger uncertainties of a factor ~ 1.5 . The main differences between our work and the results of Ref. [363] lie in the employed models, since we use EOB GW and anisotropic KN models, while Ref. [363] employs phenomenological GW and isotropic KN models. Moreover, Ref. [363] employs a coherent joint approach that takes into account full correlations of the parameters space and can lead to improved measurements.

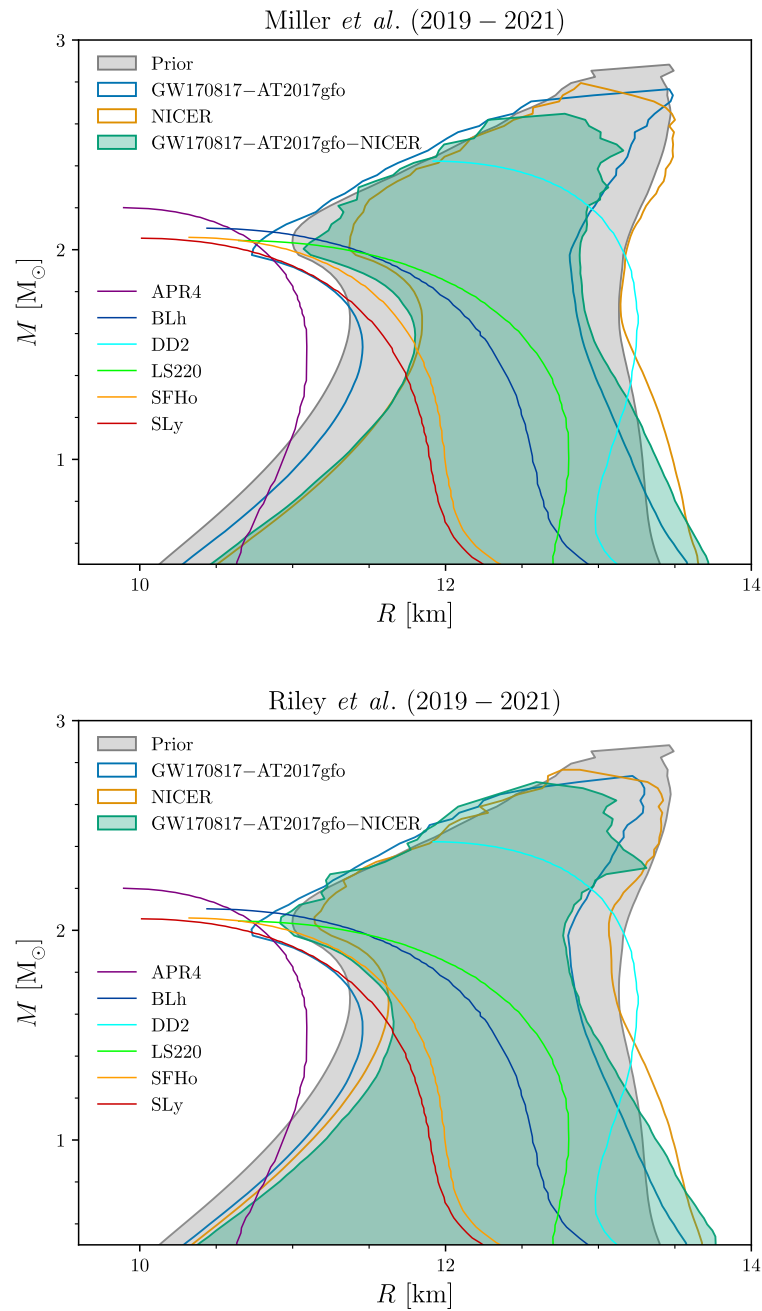


FIGURE 3.6: MM EOS constraints imposed by GW170817, AT2017gfo and NICER data. *Top panel:* The blue contour reports the GW170817-AT2017gfo constraint. The orange contour reports the NICER constraint of Miller [60, 65]. The joint GW170817-AT2017gfo-NICER is reported in green. The gray area (prior) corresponds to the prior, i.e. EOS set proposed in Ref. [364]. All contours report the 90% credibility regions. The plot shows also some exemplary EOSs. *Bottom panel:* EOS inference analogous to top panel but with the employment of NICER data from Riley [61, 64].

Chapter 4

Postmerger gravitational-wave models

Models of PM GWs were presented in Ref. [154, 372, 373, 374, 375, 376, 377, 378, 379, 380, 381, 382, 383]. These templates are phenomenological models that capture the main PM spectral features but do not attempt to model the underlining remnant's dynamics. The complex spectral frequencies are either inferred from the observations or (in part) fixed by EOS-insensitive relations that connect the main spectral features to the binary parameters. The relevance of these relations is twofold: on one hand they are used for waveform modeling, on the other hand they can be used to extract information from the analysis. Depending on whether the calibrated relations are employed or not during the GW inference, the templates might be used in fully-informed, partially informed or agnostic approach. Minimal-assumption models employs dimensionality reduction, learning algorithms or unmodeled approaches [374, 375, 376]. However, similar fitting factors can be achieved with significantly less modeling efforts in agnostic approaches based on wavelets or sinusoidal basis [379, 380, 383]. A main motivation for (partially) informed approaches is the possibility to design inspiral-merger-PM templates by consistently extending inspiral-merger templates [154, 381].

In this Chapter, we discuss the development and the validation of NR-informed model for GWs from BNS PM remnants. We review the main morphological properties of PM signals in Section 4.1. We present and discuss the main EOS-insensitive properties used for PM modeling in Section 4.2. We introduce the NR-informed PM models in Section 4.3, i.e. the time-domain approximant NRPM and its frequency-domain counterpart NRPM_w , discussing their faithfulness to NR data. Finally, Section 4.4 discusses the construction and the validation of full-spectrum GW model for BNS mergers. In this Chapter, we use geometrical units $G = c = 1$ in order to lighten the notation, except when differently stated.

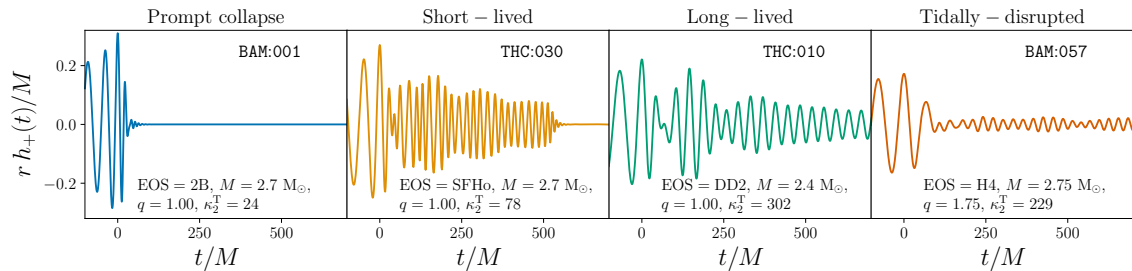


FIGURE 4.1: Representative examples of BNS PM morphologies. The reported NR simulations are extracted from the CoRE database [118, 160, 274]. The plot shows the time-domain waveforms together with simulation number, EOS, total mass M , mass ratio q and tidal polarizability κ_2^T . The waveforms are aligned such that $t_{\text{mrg}} = 0$.

4.1 Morphology

The PM waveform morphology and its connection to the remnant’s dynamics have been primarily studied employing NR simulations [e.g. 82, 118, 129, 130, 300, 372, 384, 385, 386, 387, 388, 389, 390, 391]. Figure 4.1 shows the PM signal in exemplary cases; the time axis is shifted to the moment of merger. A merger remnant is a massive, hot and rotating NS whose mass is usually larger than the maximum mass sustained by a cold, isolated TOV NS. It can either collapse to a BH or settle to a stable rotating NS on secular timescales.

Gravitational collapse to BH takes place as the remnant reaches densities comparable to the TOV’s maximum density [124]. The remnant of a very massive BNS can promptly collapse after the moment of merger and crucially before the first bounce of the two cores [120, 121]. A PC signal is shown in the first panel of Figure 4.1. In the case of an equal mass BNS, the PC is described by empirical relations relating the binary mass to the TOV maximum mass, discussed in Section 2.4.1. For very asymmetric BNS, the tidal disruption of the secondary drives the gravitational collapse [82] and is mainly controlled by the incompressibility parameter of nuclear matter around the TOV maximum density [124]. While a robust PC criterion is not known in these conditions [82, 123, 124], tidal disruption effects are of the order of current EOS effects in the equal-mass criterion, at least for mass-ratio $q \lesssim 1.4$ [57, 124]. PC mergers have the largest GW luminosities (at merger) [300] but the PM signal is the rapidly damped ringdown of the BH and it is practically negligible for the sensitivities of current and XG detectors.

If the remnant does not collapse into BH, the evolution of the NS is driven by

an intense emission of GWs lasting $\sim 10\text{--}20$ milliseconds (early PM) [133, 300]. During this phase, the remnant either collapses to BH (*short-lived* remnant) or settles to an approximately axisymmetric rotating NS (*long-lived* remnant). Examples of NR templates for short- and long-lived remnants are shown in the last three panels of Figure 4.1. The early PM phase is associated to a luminous GW transient at frequencies $2\text{--}4$ kHz [129, 372, 384, 385, 386, 388]. The spectrum of this transient is rather complex but has robust and well-studied features at a few characteristic frequencies. Most of the power is emitted in the $\ell = m = 2$ GW mode around the characteristic frequency f_2 . The f_2 frequency is extracted from simulation data and it was shown to correlate with various binary quantities in a EOS-insensitive way [e.g. 129, 130, 154, 388].

However, the PM spectrum is not composed of a discrete set of frequencies. The presence of broad peaks with typical full width at half maximum (FWHM) of $300\text{--}600$ Hz is a consequence of the efficiency of the emission process. Indeed, inspection of the time-domain waveform’s instantaneous frequency shows that $\omega_{22}(t)$ increases as the remnant becomes more compact and has a steep acceleration towards gravitational collapse [129]. Moreover, the instantaneous GW frequency has modulations with frequencies $f_0 \sim O(1\text{ kHz})$ that are stronger for remnants closer to collapse. These modulations are associated to the violent radial bounces of the remnant’s core prior to collapse. This effect introduces two secondary peaks in the PM spectrum at frequencies $f_{2\pm 0}$, respectively at larger and smaller frequencies than f_2 . These features are associated to hydrodynamical modes in the remnant [e.g. 385, 392, 393] and have been interpreted as nonlinear coupling between f_2 and f_0 [385], in analogy to perturbations of rotating NS [394, 395, 396].

When a NS remnant forms in an asymmetric binary, i.e. $q \gtrsim 1.5$, the signal can carry with it the footprint of tidal disruption. An example is shown in the fourth panel of Figure 4.1. The tidal disruption of the secondary object redistributes the matter over a larger volume surrounding the remnant. As a consequence, radial fluctuations are generally milder and the PM GW luminosity is smaller than the comparable-mass case. These dynamical features are reflected in the GW waveform, e.g. the PM amplitude can be significantly smaller than in the equal-mass cases and the f_0 frequency typically decreases to $O(100\text{ Hz})$ suppressing the subdominant peaks at frequencies $f_{2\pm 0}$.

The evolution of a NS remnant beyond the early PM phase is highly uncertain at present. It requires detailed simulations of viscous and nuclear processes on timescales beyond hundreds of milliseconds, for example to quantify precisely the mass accreting

or outflowing the central object. NS remnants after the early PM phase have an excess of both gravitational mass and angular momentum when compared to equilibrium configuration with the corresponding baryon mass [157, 161]. Possible mechanisms to shed (part of) this energy are long-term GW instabilities [397, 398] including one-arm instabilities [389, 399], that would lead to potentially detectable, long GW transients at $\lesssim 1$ kHz.

4.2 Quasiuniversal properties

From the study of the GW morphology of NR templates, it is possible to extract EOS-insensitive (*quasiuniversal*) properties for the PM waveform. This information is essential in order to map the morphological PM properties to the intrinsic binary parameters, i.e. masses, tides and spins, and construct NR-informed GW models for BNS PM remnants.

An heuristic justification in favor of the construction of quasiuniversal relations is given in Ref. [154, 274] and it can be summarized as follows using perturbative arguments. In the EOB description of the two-body dynamics, the interbinary potential $A(r)$ is the main quantity which describes the binary dynamics (see Section 2.1). The radial force governing the circular motion is given by

$$\frac{dA}{dr} = - (M/r)^2 \left[-2 + a_{\text{PP}}(\nu, r) + a_{\text{T}}(\kappa_2^{\text{T}}, \nu, r) \right] , \quad (4.1)$$

where a_{PP} and a_{T} are the PP and the tidal corrections to the Newtonian term respectively (we neglect here spin interactions) [114]. At leading order, the two terms above read

$$\hat{a}_{\text{PP}}(\nu, r) \propto \nu/r^2 \quad , \quad \hat{a}_{\text{T}}(\kappa_2^{\text{T}}, \nu, r) \propto -\kappa_2^{\text{T}}/r^3 \quad , \quad (4.2)$$

where the tidal contribution is parameterized by the tidal polarizability κ_2^{T} [116]. Hence, finite mass-ratio and tidal effects are parameterized at leading order by ν and κ_2^{T} . As noted in [274], in the strong field regime (where the expansion above is not accurate), the tidal term a_{T} can become numerically comparable to a_{PP} as $\kappa_2^{\text{T}} \sim O(100)$. This reflects the physical fact that the tidal term grows faster ($\sim 1/r^3$) at small separations than the non-tidal one ($\sim 1/r^2$). Based on this picture, it is thus natural to interpret the NR data in terms of κ_2^{T} because the latter is the theoretically justified parameter that encode the main effects of the EOS and masses on the dynamics.

The construction of quasiuniversal properties assumes that the formalism of Eq. (4.1) can be extended to early times after merger and that the inspiral-merger dynamics are the primary contributions to determine the PM outcome. However, this argument cannot be generalized for all the PM properties. For example, some PM quantity might correlate with physical properties that are not fully captured by the intrinsic binary parameters, e.g. viscous and turbulent phenomena, NS remnant collapse dynamics, and tidal disruption [153, 383, 400]. Moreover, other physical effects can lead to a *breaking* of quasiuniversality, i.e. a significant deviation from the prediction of the EOS-insensitive relation. This is expected as a result of the appearance of non-nucleonic degrees of freedom for some BNS configurations [86, 154, 401, 402]. In general, the lack of an analytical scheme for the analysis of NS merger remnants pose severe limits in the development of reliable and accurate GW models. Some studies naively tried to associate the BNS remnant dynamics to NS perturbation models [403, 404]. However, the NS remnant of a typical BNS (i.e. $M \simeq 2\text{--}3 M_{\odot}$) is far from the cold equilibrium assumed in the TOV equations [e.g. 67, 121, 127, 389]. For this reason, NR data are key to inform BNS PM models [154, 374, 376, 380, 383].

We rely on the NR data provided by the CORE database [57, 58, 82, 83, 86, 139, 160, 161, 348] and by the SACRA database [405, 406, 407]. We remark that these data include BNS simulations computed with ALF2 and BLQ EOSs, that include a phase transition to deconfined quark matter, and with BH $\Lambda\phi$ EOS, which takes into account the appearance of hyperons at high densities. The intrinsic parameters of the data cover the ranges $M \in [2.4, 3.4] M_{\odot}$, $q \in [1, 2]$, $\kappa_2^T \in [22, 458]$ and $\chi_{\text{eff}} \in [-0.14, +0.22]$. In the following subsections, we model the main morphological features extracted from NR data. In particular, we introduce the nodal points in Section 4.2.1 and we show the calibration of the characteristic PM frequency in Section 4.2.2.

4.2.1 Nodal points

Figure 4.2 illustrates some of the qualitative features extracted from the NR waveforms for short- and long-lived NS remnants. If the NS remnant does not collapse, the time-domain amplitude shows modulations related to the remnant bounces. In Figure 4.2, we identify as A_i the stationary points of the strain's occurring at times t_i with $i = 0, 1, 2, 3$. We label these times as *nodal points* and we assume this structure for the modeling of our PM GW templates. The amplitude maxima occur for odd indices; while, the minima have even indices. Amplitude maxima correspond to minima in the instantaneous GW frequency, and viceversa. This can be naively interpreted as a

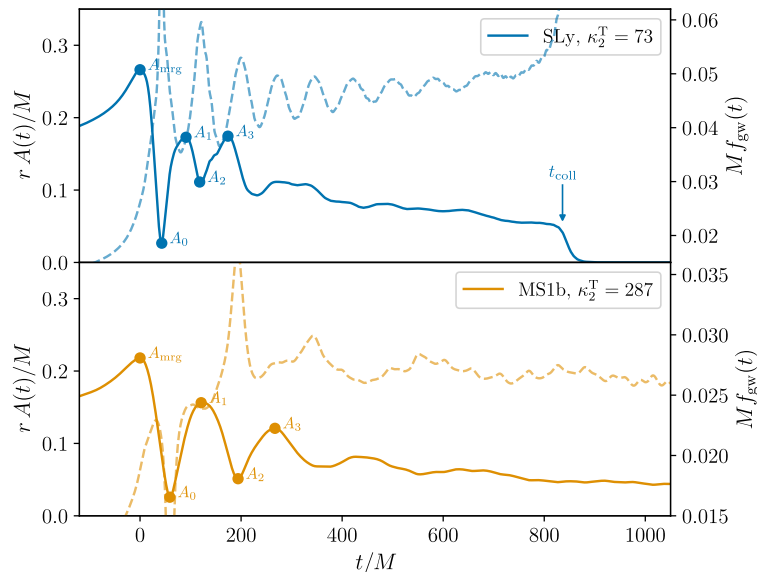


FIGURE 4.2: NR waveform from two exemplary BNSs with mass $M = 1.35 + 1.35 M_{\odot}$. The SLy BNS (top panel) is an example of short-lived remnant collapsing at $t/M \sim 850$ after merger time ($t_{\text{mrg}} = 0$). The MS1b BNS (bottom panel) is an example of long-lived remnant. The left axes and solid lines report the GW amplitude. The right axes and dashed lines report the instantaneous GW frequency. In both cases, the PM waveform amplitude has characteristics maxima and minima A_i at times t_i with $i = 0, \dots, 3$. Note the jump in the phase at t_0 , where the instantaneous frequency is not defined.

consequence of the conservation of the angular momentum of the remnant. Note that at t_0 the GW phase has a jump and the instantaneous frequency is discontinuous; this corresponds to a moment in which the remnant has a strongly suppressed quadrupolar deformation.

The PM properties at the nodal points $\{A_i, t_i\}$ are estimated from the time-domain NR data. The PM amplitudes A_i show a decreasing trend for increasing κ_2^{T} and for increasing mass ratio. This can be understood as the effects of stiffer EOSs and larger mass ratios that produce less violent dynamics in the remnant (for a fixed M). As a consequence of tidal disruption, the first amplitude A_0 increases with increasing mass ratio. In general, also the nodal times t_i show increasing trends for increasing mass ratios. However, this morphological choice is non-optimal for large mass ratio, i.e. $q > 1.5$, since these binaries show additional phase discontinuities and thus the determination of t_0 is non-trivial.

At timescales $\sim 10\text{--}20$ ms, the remnant has either collapsed or dissipated most of its energy via GWs. For long-lived remnants (MS1b in Figure 4.2), there is no significant GW emission at timescales $\gtrsim 50$ ms [389, 408]. For short-lived remnant (SLy in

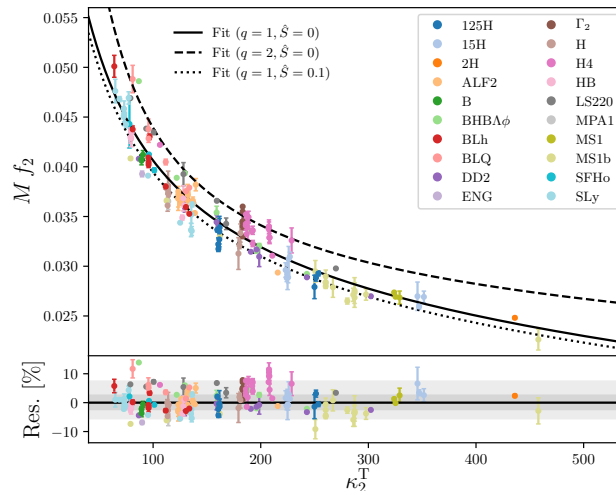


FIGURE 4.3: Quasi-universal relation for the PM peak frequency f_2 as function of the tidal polarizability κ_2^T . *Top panel:* Calibrated relations (black lines) compared to NR data (colored dots) extracted from the CORE and the SACRA databases. Each color corresponds to a different EOS. NR medians and error-bars are reported averaging over different numerical resolutions (when available) for the same binary configuration. *Bottom panel:* Relative residuals between the calibrated relation and the NR validation set. The gray areas show the 50% (dark) and 90% (light) credible regions of the residuals.

Figure 4.2), it is possible to introduce an additional nodal point in correspondence of the time of collapse into BH, reported as t_{coll} in Figure 4.2. After this time, the GW signal can be approximated using the QNMs complex frequencies estimated from BH perturbation theory given the properties of the final BH (i.e. mass and spin) [e.g. 126, 409, 410]. However, there are no available models capable to accurately predict the final mass and the spin of a remnant BH for a generic BNS coalescence. The final BH mass is expected to lie around the total binary mass M , since the total amount of radiated GW energy and of ejected matter correspond to few percents of it. On the other hand, the final BH spin can be only bounded to be smaller than the total angular momentum of the system at merger [82, 121].

4.2.2 Postmerger peak frequency

The main quantity for PM modeling is the dominant f_2 frequency peak. We extract the PM frequency f_2 from NR PM spectra of the (2, 2) mode. Generally, the f_2 frequency is estimated as the global maximum of the PM spectrum; however, when modulations are prominent and the PM segments are short (i.e. $\lesssim 8$ ms), the f_2 contribution is no longer the dominant peak and it needs to be identified in the local maxima.

The calibration is performed with a rational polynomial form in κ_2^T that is corrected with ν -dependent and spin-dependent terms (see Appendix C) [383]. Figure 4.3 show the f_2 quasiuniversal relation: the frequency Mf_2 primarily correlates with the tidal polarizability κ_2^T , while mass ratio and spin contributions mildly affect the overall value of this quantity. This relation is accurate to $\sim 4\%$ at $1-\sigma$ level ($6-7\%$ at 90% credibility level), that corresponds to an error of about 100 Hz (200 Hz). The latter is typically smaller than the FWHM of the spectrum peaks.

The bottom panel of Figure 4.3 shows data points with deviations larger than $2-\sigma$. Around $\kappa_2^T \simeq 207$, it is possible to identify a cluster of NR data corresponding to spinning unequal-mass H4 binaries $1.65+1.10 M_\odot$ with different combinations of spins [118, 391]. For these large mass-ratio cases, the spin corrections would require an improved treatment. The largest residual ($\sim 15\%$) is given by the non-spinning equal-mass binaries BHBA ϕ $1.50+1.50 M_\odot$ [67] and BLQ $1.40+1.40 M_\odot$ [86]. In both cases, the remnant collapses into BH shortly after merger, i.e. $t_{\text{coll}} \simeq 3$ ms, and the determination of the peak and secondary frequencies from this signal is rather delicate due to the short duration of the transient. From the Fourier spectra, it is possible to identify two dominant broad peaks at frequencies $Mf_{2-0} \simeq 0.036$ and $Mf_2 \simeq 0.048$ for the BHBA ϕ binary and $Mf_{2-0} \simeq 0.036$ and $Mf_2 \simeq 0.047$ for the BLQ binary. These values agree with the estimate of Mf_0 coming from the instantaneous GW frequency; however, the peak widths vary depending on the window used to smooth the NR data and it is not possible to clearly identify a carrier frequency and a modulation magnitude from the time-domain waveform. Consistently with Ref. [154] we chose to identify the second peak with f_2 and conservatively include it in the determination of the quasiuniversal relation. In contrast, the choice of the first peak as f_2 would be consistent with Ref. [67, 86], and the datapoints would not be outliers in the residual plot.

4.3 Numerical-relativity-informed models

For our models, we use the signal description modeled through the nodal points discussed in Section 4.2.1. The signal amplitude and phase are constructed in order to match the predictions of the nodal points assuming continuity except for the t_0 instant.

As shown in [154, 383], some PM properties cannot be accurately calibrated on NR data, while others show dependency on physical properties of the system that are not parameterized by the standard CBC parameters Eq. (3.6). For this reason, we

generally decide to leave some parameters free to vary, in order to be inferred during PE routines. These parameters are: the PM phase discontinuity in correspondence of t_0 which shows a strong dependence on the simulation's grid resolutions and on the physical models [e.g. 71, 229, 411]; the time of collapse is difficult to robustly determine from simulations due its dependence on grid resolution [154] and it strongly depends on the high-density properties of the EOS [67, 86, 412]; the frequency drift is also connected to the collapse dynamics and, as such, it can be affected by various processes, especially in long-lived remnants.

In the following sections, we discuss the developed models for PM BNS GW radiation, NRPM in Section 4.3.1 and NRPM_w in Section 4.3.2. For a more detailed discussion on the PM models, we remand to Appendix B and Appendix C. Subsequently, we discuss the method employed to include theoretical uncertainties in PE routines in Section 4.3.3 and we validate the PM models computing fitting-factors against an independent set of NR data in Section 4.3.4.

4.3.1 NRPM

In Ref. [154], we developed NRPM, a time-domain PM model calibrated on 148 NR data extracted from the CORE database [160] corresponding to non-spinning BNS mergers. The NR calibration set is bounded to $q = 1.5$ and includes 14 different EOSs. The merger segment uses the quasiuniversal predictions for the GW properties at merger and the corresponding GW frequency evolution is approximated with PN computations. Subsequently, the model is constructed connecting the quasiuniversal predictions for the nodal points using sinusoidal functions, including a phase discontinuity ϕ_{PM} in correspondence of t_0 . This model aims to capture the early-time amplitude and frequency modulations of the GW signals. For $t > t_3$, the signal is modeled as a damped sinusoidal with damping time β_{PM} and constant frequency f_2 . The damping time β_{PM} can be fixed via quasiuniversal relations or kept free to vary. Moreover, NRPM include an additional parameter α_{PM} that accounts for linear deviations from the frequency f_2 . Then, NRPM can be augmented including three additional parameters $\theta_{\text{free}}^{\text{NRPM}} = \{\phi_{\text{PM}}, \alpha_{\text{PM}}, \beta_{\text{PM}}\}$.

4.3.2 NRPM_w

In Ref. [383], we developed NRPM_w, a frequency-domain PM model calibrated on 618 NR data extracted from the CORE database [160] and the SACRA database [405, 406,

407] corresponding to aligned-spin BNS mergers. The calibration set includes NR data with $q \leq 2$ and $|\chi_i| \leq 0.2$ computed with 21 different EOSs. The model is constructed in the frequency-domain matching complex Gaussian wavelets with a morphology similar to Section 4.3.1. Differently from NRPM, the drift of the GW frequency at merger is calibrated on NR data, showing that tidal disruption can significantly affect this term. Moreover, the model includes complete description of damped frequency modulations based on analytic computations, that make explicit the effect of subdominant components. Similarly to NRPM, the updated model includes a phase discontinuity ϕ_{PM} in correspondence of t_0 and permit the parameterization of linear frequency evolution through α_{peak} . Moreover, NRPM \mathbf{w} includes a parameter t_{coll} in order to model the time of BH collapse, that defines the duration of the GW template. Then, the NRPM \mathbf{w} 's parameter space is extended with respect to the standard BNS space with three additional degrees of freedom, i.e. $\boldsymbol{\theta}_{\text{free}}^{\text{NRPM}\mathbf{w}} = \{\phi_{\text{PM}}, t_{\text{coll}}, \alpha_{\text{peak}}\}$.

4.3.3 Recalibration parameters

The EOS-insensitive relations developed in Section 4.2 carry intrinsic uncertainties due to small violations of universality (EOS dependence) and/or fitting inaccuracies. Calibration errors of the empirical relations should be taken into account every time such mappings are employed, in particular during the calculation of fitting factors and during PE, in order to perform robust predictions. This can be done by introducing appropriate parameters associated with the fluctuation of the residuals. A by-product of this process is that the additional flexibility is expected to significantly improve the data fitting by adjusting the PM morphology of the template to match the targeted signal, similarly to agnostic approaches [e.g. 375, 379].

Labeling Q a generic quantity estimated from a quasiuniversal relation calibrated on NR data, we introduce an associated *recalibration* δ_Q that affects the prediction Q^{fit} of the quasiuniversal relation as

$$Q = Q^{\text{fit}} (1 + \delta_Q). \quad (4.3)$$

The recalibration δ_Q corresponds to a fractional displacement from the prediction Q^{fit} of the quasiuniversal relation. The recalibration procedure employed here is similar to the spectral calibration envelopes used in GW analyses [202]. However, here we aim to integrate the model's uncertainties in the inference rather than the instrumental errors, similarly to the approach used in Eq. (3.8).

In GW inference applications, the recalibrations of each calibrated PM property are treated as standard parameters. In this context, it is key that the prior distribution used in the inference is a good representation of the residuals of the quasiuniversal relation. Following the methods of Ref. [16, 202], a simple approach is to consider a normally distributed prior with variance prescribed by the errors of the residuals. Interestingly, under the assumption that the NR error is subdominant compared to the physical breaking of quasiuniversality, the measurement of the recalibration parameters from the data could also be used to distinguish between different EOSs and observatively probe the breaking of quasiuniversality.

In the developed PM models, the recalibration parameters $\boldsymbol{\delta}_{\text{fit}} = \{\delta_i\}$ are considered for each calibrated quantity, see Eq. (B.6) for NRPM and Eq. (C.19) for NRPMw. These additional degrees of freedom mildly affect the merger portion, i.e. $t < t_0$ due to the accuracy of the empirical relations close to merger. However, the recalibrations have larger effects on the late-time PM features whose EOS-insensitive relations introduce larger uncertainties.

4.3.4 Unfaithfulness

We validate the PM models by computing their faithfulness \mathcal{F} against 102 NR waveforms of Refs. [58, 82, 125, 154, 161, 413] that were not used for the calibration. Among the considered simulations, 12 binaries show PC into BH. The validation set is composed by NR simulations of non-spinning BNS performed with THC [110] that include different neutrino treatments, turbulent viscosity schemes and five EOSs, i.e. BHBA ϕ [85], DD2 [10], LS220 [9], SFHo [90] and SLy [80]. The intrinsic binary properties cover the ranges $M \in [2.6, 3.4] M_\odot$, $q \in [1, 1.8]$ and $\kappa_2^T \in [47, 199]$. The unfaithfulness $\bar{\mathcal{F}} = 1 - \mathcal{F}$ between two waveform templates, say h_1 and h_2 , is defined as

$$\bar{\mathcal{F}}(h_1, h_2) = 1 - \max_{t_{\text{mrg}}, \phi_{\text{mrg}}} \frac{(h_1|h_2)}{\sqrt{(h_1|h_1)(h_2|h_2)}}, \quad (4.4)$$

where the maximization is performed over the coalescence time and phase, respectively t_{mrg} and ϕ_{mrg} . The inner product $(h_1|h_2)$ is defined in Eq. (2.19). For these computations, we employ the PSD curve of the XG detector ET [75, 76] (configuration D) and we integrate over the frequency range [1, 8] kHz. The unfaithfulness is computed employing the PM portions of the NR waveforms.

In Figure 4.4, we report histograms of the unfaithfulness computed for the following cases:

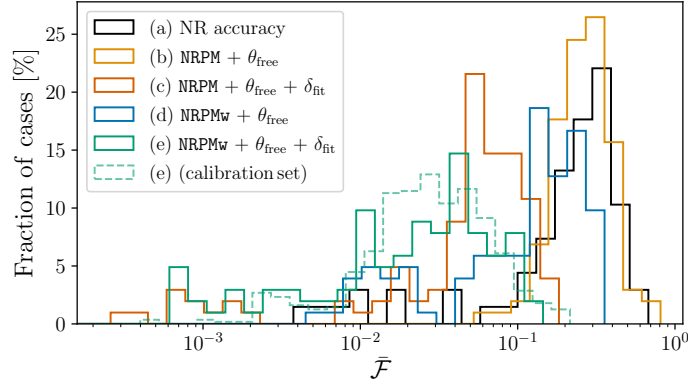


FIGURE 4.4: Unfaithfulness $\bar{\mathcal{F}}$ between PM models and NR data of the validation set [58, 82, 125, 154, 161, 413] employing ET-D sensitivity [75, 76]. Case (a) (black) shows the accuracy of the NR templates computed between different resolutions. For NRPM, case (b) (yellow) shows the results with $\theta_{\text{free}}^{\text{NRPM}}$ and case (c) (orange) includes the recalibration δ_{fit} . Analogously for NRPMw, case (d) (blue) shows the results with $\theta_{\text{free}}^{\text{NRPMw}}$ and case (e) (green) includes the recalibration δ_{fit} . The dashed histogram shows $\bar{\mathcal{F}}$ for case (e) computed over the calibration set of ~ 600 NR data.

- (a) Accuracy of the NR validation set;
- (b) NR validation set against NRPM, minimizing over $\theta_{\text{free}}^{\text{NRPM}}$ ($\delta_{\text{fit}} = 0$);
- (c) NR validation set against NRPM, minimizing over $\theta_{\text{free}}^{\text{NRPM}}$ and δ_{fit} ;
- (d) NR validation set against NRPMw, minimizing over $\theta_{\text{free}}^{\text{NRPMw}}$ ($\delta_{\text{fit}} = 0$);
- (e) NR validation set against NRPMw, minimizing over $\theta_{\text{free}}^{\text{NRPMw}}$ and δ_{fit} .

For a fixed BNS configuration, the accuracy of the NR validation set, shown in case (a), is computed as the unfaithfulness between the high-resolution NR waveform and the templates with lower resolutions. The values recovered from the considered set go from $\bar{\mathcal{F}} \simeq 0.7$ to $O(10^{-2})$, with a median value of $\bar{\mathcal{F}} \simeq 0.25$, similarly to Ref. [154]. These non-negligible errors originate from finite resolution of numerical data. For the remaining cases, i.e. (b) – (e), the minimization method is performed as follows. For each NR waveform, we compute the corresponding model template (NRPMw or NRPM) fixing the intrinsic parameters θ_{bin} to the values of the NR simulation and estimating the additional parameters (θ_{free} and δ_{fit}) minimizing the unfaithfulness $\bar{\mathcal{F}}$, i.e. Eq. (4.4), using a differential evolution method [414]. For each case and for each NR data, the additional degrees of freedom are independently varied over a physically-motivated range in order to estimate the $\bar{\mathcal{F}}$ minimum.

In case (b), NRPM with the inclusion of the $\theta_{\text{free}}^{\text{NRPM}}$ recovers a median value of $\bar{\mathcal{F}} \simeq 0.27$, roughly comparing NR accuracy. However, the majority of the recovered values lies above $\bar{\mathcal{F}} = 0.1$, i.e. 97%. The additional inclusion of the recalibration parameters, shown in (c), considerably enhances the quality of the recovered waveforms. The median $\bar{\mathcal{F}}$ decreases to 0.06. The $\bar{\mathcal{F}}$ distribution shows a tail with values $\bar{\mathcal{F}} \sim O(10^{-3})$, corresponding to short-lived remnants and PCs. The fraction of cases with $\bar{\mathcal{F}} < 0.1$ corresponds to 83% and we recovered $\bar{\mathcal{F}} < 0.2$ for all binaries in the validation set.

Moving to NRPMw, case (d) shows an overall improvement in the faithfulness compared to the equivalent case (b), with median $\bar{\mathcal{F}} \sim 0.13$ and a fraction of 38% with $\bar{\mathcal{F}} < 0.1$. We attributed this enhancement to the modeling choices employed in NRPMw, since the number of parameters minimized (θ_{free}) is the same as case (b). Moreover, case (d) shows a small cluster with $\bar{\mathcal{F}} \lesssim 3 \times 10^{-2}$ ($\sim 20\%$), mainly populated by short-lived remnant and prompt BH collapses. In case (e), the additional inclusion of recalibration terms considerably improves the agreement of NRPMw to the NR data. We obtain a median $\bar{\mathcal{F}}$ of 2.5×10^{-2} and report 94% of the validation set with $\bar{\mathcal{F}} < 0.1$. We recover similar statistics applying case (e) over the six-hundred NR simulations of the calibration set, shown with dashed line in Figure 4.4. Moreover, the histogram (e) shows that the cluster constituted by short-duration signals moves toward $\bar{\mathcal{F}} \simeq 10^{-2}$ and we recovered values comparable to or smaller than $\bar{\mathcal{F}} = 3 \times 10^{-2}$ for several long-duration transients, such as SLy 1.30+1.30 M_{\odot} , and unequal-mass binaries, such as DD2 1.50+1.25 M_{\odot} . The overall improvement with respect to the comparable case (c) is roughly half order of magnitude.

The significant improvement made by recalibration parameters suggests that inaccuracies in the EOS-insensitive relations are the largest source of error in the PM models. On the other hand, the $\bar{\mathcal{F}}$ values computed on simulations with different grid resolution or physical schemes suffer from considerable fluctuations for some binaries. Some examples are: LS220 1.47+1.27 M_{\odot} that gives $\bar{\mathcal{F}} = 1.5 \times 10^{-1}$ at standard resolution without turbulent viscosity and $\bar{\mathcal{F}} = 3.8 \times 10^{-2}$ at high resolution with turbulent viscosity; and LS220 1.35+1.35 M_{\odot} (with turbulent viscosity) that gives $\log_{10} \bar{\mathcal{F}} = 8.9 \times 10^{-2}$ at standard resolution and $\log_{10} \bar{\mathcal{F}} = 1.6 \times 10^{-2}$ at low resolution. These results suggest that the largest recovered $\bar{\mathcal{F}}$ might be related to inaccurate modeling choices for the late-time features or to excesses of numerical error in the data. Comparing with NRPMw's results (e), the majority of the recovered values lie below the NR accuracy threshold, representing an improvement with respect to the non-recalibrated scheme and validating the usage of NRPMw in practical data analysis.

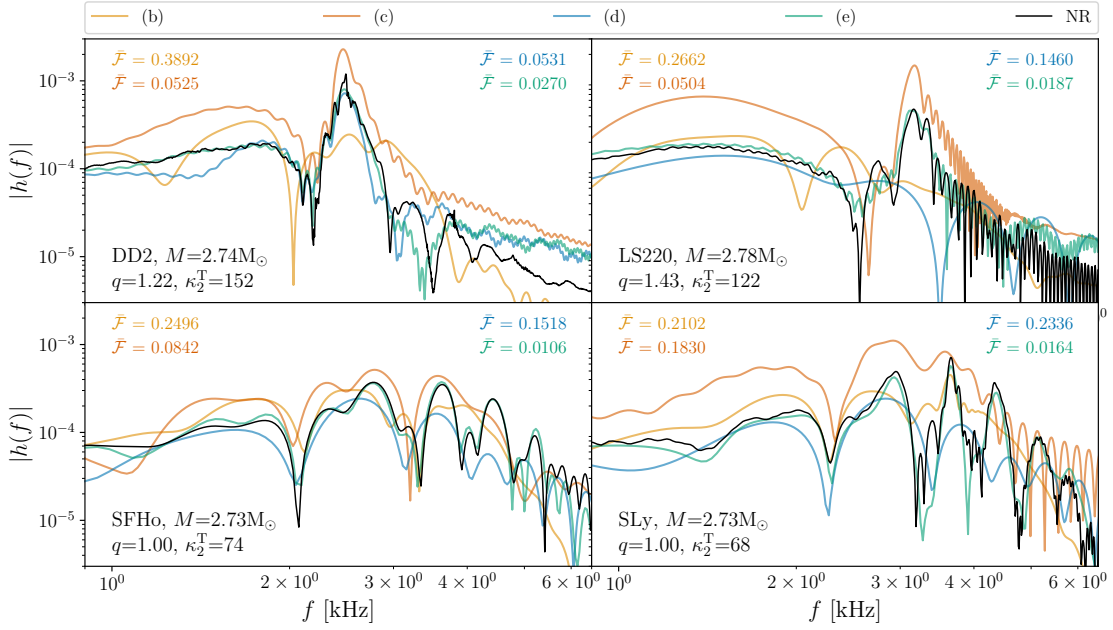


FIGURE 4.5: Comparison between PM models and exemplary NR data of the validation set. Colored lines show the spectra for the different models, analogously to Figure 4.4. Solid lines are used for NRPMw spectra and dashed lines are employed for NRPM. NR spectra are reported with black solid lines. The plot includes also the corresponding unfaithfulnesses estimated with NRPM and NRPMw, i.e. cases (b), (c), (d), and (e).

Considering the faithfulness condition proposed in Ref. [284, 415, 416] and fixing $N = 9$ as number of intrinsic parameters $\{\theta_{\text{bin}}, \theta_{\text{free}}\}$, the recovered upper-bound accuracy $\bar{\mathcal{F}} \simeq 10^{-1}$ of NRPMw in case (e) can be translated into a model robustness threshold of SNR ~ 7 . Above this threshold, systematic waveform errors can become relevant. The threshold moves to SNR ~ 11 if we include the recalibrations δ_{fit} as intrinsic parameters, i.e. $N = 22$. On the other hand, employing the recovered median value $\bar{\mathcal{F}} \simeq 2.5 \times 10^{-2}$, we estimate a faithfulness threshold SNR equal to 13 for $N = 9$ and 21 for $N = 22$. Considering an averaged threshold of SNR ~ 10 , this limit matches the requirements imposed by ET detector for (optimally-oriented) sources located at luminosity distances $\gtrsim 40$ Mpc [17, 154, 158, 378, 379]. These results implies that, for the current knowledge (limited by number and accuracy of NR templates), NRPMw includes the necessary degrees of freedom required to match PM GW signals for SNRs expected for XG detectors [17, 417].

Finally, Figure 4.5 shows the comparison between the PM model spectra and NR data for four exemplary cases extracted from the validation set. The first case is DD2 $1.509+1.235 M_{\odot}$ which generates a long-lived remnant, $t_{\text{coll}} \sim O(100 \text{ ms})$. NRPM recovers $\bar{\mathcal{F}} \simeq 0.4$ for the cases (b). The result improves to $\bar{\mathcal{F}} \simeq 5 \times 10^{-2}$ in case

(c); while, NRPMw gives $\bar{\mathcal{F}} \simeq 5 \times 10^{-2}$ in case (d) and $\bar{\mathcal{F}} \simeq 3 \times 10^{-2}$ in case (e). The second case is LS220 1.635+1.146 M_{\odot} with tidal-disruptive behavior. NRPMw (d) does not match the dominant PM peak returning $\bar{\mathcal{F}} \simeq 0.3$. Then, the recalibrations (e) strongly improve the agreement to NR data, leading to $\bar{\mathcal{F}} \simeq 2 \times 10^{-2}$. The remaining cases highlight the relevance of modulation effects in PM signals. The third case is SFHo 1.364+1.364 M_{\odot} and it generates a short-lived remnant with $t_{\text{coll}} \simeq 4$ ms. The comparison shows the flexibility of the recalibrated NRPMw (e) in capturing the several Fourier peaks, delivering $\bar{\mathcal{F}} \simeq 10^{-2}$. The last case is SLy 1.364+1.364 M_{\odot} , for which PM models does not match subdominant peaks, returning $\bar{\mathcal{F}} \simeq 0.2$ in case (c) and (d). However, the inclusion of recalibrations in (e) to leads to $\bar{\mathcal{F}} \simeq 2 \times 10^{-2}$.

4.4 Full-spectrum models

The NR-calibrated models NRPM and NRPMw can be used to extend existing inspiral-merger GW templates in the kilohertz regime, characterizing the full GW spectrum of BNS mergers. The employment of quasiuniversal relations facilitates the relation between the BNS parameters and the corresponding PM GW template.

Given an inspiral-merger model and a PM model, the attachment procedure employed to join these two regimes is the most relevant step for the construction of a full-spectrum template. For time-domain templates, the attachment can be directly performed joining the two waveforms at merger assuming continuity of GW phase and amplitude. An example is shown in Ref. [154], where we proposed the the first full-spectrum model for BNS mergers, combining `TEOBResumS` [234] and NRPM. Frequency-domain templates require a more accurate treatment. In order to avoid double-counting of the merger portion and ensure a smooth transition between the two regimes, we opt to remove the initial wavelet W_{fus} in NRPMw during attachment procedure. The GW signal description is determined by the inspiral-merger model for times earlier than the first nodal point, i.e. $t < t_0$ (see Section 4.2.1). In our studies, we extend the frequency-domain representation of `TEOBResumS` [254] with NRPMw.

We validate the full-spectrum model `TEOBResumS-NRPMw` computing fitting factors against a validation set of six non-spinning hybrid EOB-NR templates. The NR data of the validation set are computed with THC [110] which simulate microphysics, neutrino transport (with various schemes) and turbulent viscosity. The set includes two long-lived remnants (SLy with total mass 1.30+1.30 M_{\odot} [154] and LS220 1.40+1.20 M_{\odot} [83]), two short-lived remnants (SFHo 1.35+1.35 M_{\odot} [133] and BLQ

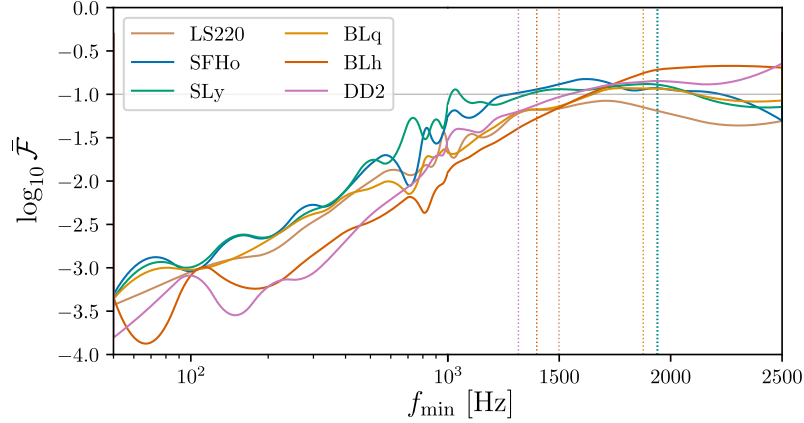


FIGURE 4.6: Recovered unfaithfulness $\bar{\mathcal{F}}$ between full-spectrum `TEOBResumS-NRPMw` model and hybrid EOB-NR data of a validation set [82, 83, 86, 133, 154, 402] employing ET-D sensitivity [75, 76]. For each binary, $\bar{\mathcal{F}}$ is computed as a function of the lower integration frequency, while the upper cutoff is fixed to 8 kHz. Vertical dashed lines report the merger frequency f_{mrg} estimated from NR data for each binary. A gray horizontal line indicates the value $\bar{\mathcal{F}} = 10^{-1}$.

1.40+1.40 M_{\odot} [86]), and two large-mass-ratio binaries with tidal disruptive morphology (DD2 1.80+1.08 M_{\odot} [402] and BLh 1.772+1.065 M_{\odot} [82]). The NR waveforms are extended in the early inspiral with the corresponding `TEOBResumS` template in order to cover the GW spectrum above 20 Hz. For the $\bar{\mathcal{F}}$ computation, we employ the fiducial ET-D sensitivity curve and we minimize over the additional PM parameters $\theta_{\text{free}}^{\text{NRPMw}}$ and the recalibrations δ_{fit} analogously to the study of Section 4.3.4.

Figure 4.6 shows the $\bar{\mathcal{F}}$ between `TEOBResumS-NRPMw` and the hybrid templates of the validation set as a function of the lower cutoff frequency f_{min} . `TEOBResumS-NRPMw` returns typical values between $10^{-3} - 10^{-4}$ over the full frequency range, consistently with SPA accuracy [254]. At $f_{\text{min}} \simeq 1$ kHz, the errors related to the PM portion affects the recovered $\bar{\mathcal{F}}$, showing values of $O(10^{-2})$. The $\bar{\mathcal{F}}$ increases up to $O(10^{-1})$ for $f_{\text{min}} \simeq f_{\text{mrg}}$ and, subsequently, it reaches a plateau consistent with the PM unfaithfulness of Section 4.3.4. We observe that typically the maximum $\bar{\mathcal{F}}$ occurs in proximity of f_{mrg} . This is related to an inaccurate modeling of the GW portion between $[t_{\text{mrg}}, t_0]$ due to matter effects that are not accounted in current inspiral-merger models. Thus, future inspiral-merger BNS templates need to correct these inaccuracies in order to provide a reliable representation around the merger.

Chapter 5

Next-generation gravitational-wave observations

From GW170817 posteriors of masses and tides, the merger frequency f_{mrg} is predicted to fall in the range 1.2 – 2 kHz [154]. The sensitivity of the detectors in August 2017 was insufficient to identify a signal at frequencies $f \gtrsim f_{\text{mrg}}$ and LVK searches for PM transients from a NS remnant in GW170817 data resulted in upper limits of $\sim 10^{-1} M_{\odot} c^2 \text{ Hz}^{-1}$ [40, 220, 221]. However, various works have suggested that for GW170817-like sources PM frequencies are accessible by improving the design sensitivity of current detectors by a factor two-to-three [220, 374, 418, 419]. In general, BNS PM remnants are one of the main targets of XG GW observatories [29, 76, 420, 421, 422, 423]. The significant complexity of the PM source emission implies that standard PE techniques, relying on extremely accurate models parameterized by the minimal set of the system’s degrees of freedom, can no longer be applied. For this reason, recent Bayesian studies of BNS PM transients employed largely different modeling choices, ranging from signal-agnostic reconstructions to semi-agnostic descriptions calibrated on NR simulations [e.g. 154, 374, 375, 376, 378, 379, 402, 418]. The advantage of agnostic techniques lies in an unbiased reconstruction of the signal, coming however at the price of losing information content buried in the noise. Semi-agnostic reconstructions, which can directly incorporate information from NR simulations, allow to dig deeper into the detector background and hence detect signals at lower SNR. However such measurements require extensive training datasets and the inclusion of all the relevant contributions in order to provide a faithful recovery of the signal’s properties.

In this Chapter, we employ the PM models NRPM and NRPMw in mock Bayesian inferences of GW signals from BNSs with the XG detector ET, investigating the PE performances and future EOS constraints. Section 5.1 presents the ET IFO. PM inference is performed in Section 5.2, focusing on detectability and constraints on the PM

properties. In Section 5.3, we discuss methods to infer EOS softening effects, introducing a consistency test based on full-spectrum inference. Finally, in Section 5.4, we investigate high-density EOS constraints provided by full-spectrum BNS GW signals.

5.1 Einstein Telescope

The ET detector is a XG facility for GW observations proposed by EGO and other European institutes [75, 76, 77, 417, 420, 424, 425, 426, 427]. ET design consists of a triad of underground laser IFOs arranged in an equilateral triangular shape. At each vertex, a photodetector measures the GW fluctuations employing laser beams running along the adjacent sides at a 60 degree angle. ET will improve the sensitivities of modern observatories by increasing the size of the IFO from the 3 km arm length of the Virgo detector to 10 km, and by implementing a series of new technologies. These include a cryogenic system, quantum technologies to reduce the laser fluctuations and noise-mitigation measures to reduce environmental perturbations. Moreover, the instrument will exploit a *xylophone-design* in which each GW detector is composed of two individual IFOs: a cryogenic low-power IFO with sensitivity plateau in the low-frequency band, roughly between 7 Hz and 20 Hz, and an high-power IFO that covers the higher portion of the spectrum, roughly above ~ 100 Hz. The combination of these two information channels yields an improved sensitivity over a larger frequency band compared to current infrastructures [e.g. 29, 30, 31, 179, 428, 429, 430]. The ET-D configuration discussed in Ref. [75] and employed in this Chapter has a sensitivity bucket covering the GW spectrum from ~ 5 Hz up to ~ 3 kHz. Such broad-band sensitivity is ideal for BNS observations. Low-frequency measurements follow the binary evolution for many cycles before merger extracting precise measurements of the progenitor's properties. In contrast, the high-frequency end, i.e. $\gtrsim 1$ kHz, enables the detection of PM signals at sensitivities that are unreachable by current infrastructures.

5.2 Postmerger inference

In this section, we perform full PE injection-recovery experiments using PM NR signals and NRPMw . The validation set is composed by the six non-spinning binaries discussed in Section 4.4. We present injection settings in Section 5.2.1. We discuss detectability performances in Section 5.2.2. We show PE results and posterior PDFs in Section 5.2.3.

5.2.1 Injection settings

We generate artificial GW data, i.e. the injections, for the triangular, triple-IFO ET detector [77, 417, 424], segmented into chunks of 1 s duration with a sampling rate of 16384 Hz. For each detector i , the artificial data series $d_i(t) = s_i(t) + n_i(t)$ is composed of the signal $s_i(t)$ projected onto the i -th detector and the respective noise contribution $n_i(t)$. We label with bold symbols the sets $\mathbf{s}(t) = \{s_i(t)\}$, $\mathbf{n}(t) = \{n_i(t)\}$, and $\mathbf{d}(t) = \{d_i(t)\}$ such that $\mathbf{d}(t) = \mathbf{s}(t) + \mathbf{n}(t)$. The injected signals correspond to the NR GW templates in order to study the performance of NRPMw in a more realistic scenario. The noise is assumed to be Gaussian, wide-sense stationary, and colored according to the fiducial PSD of ET-D [76]. The templates $s(t)$ are injected at seven different SNRs, i.e. 5, 6, 6.5, 7, 7.5, 8 and 10, which corresponds to locating the binaries at different luminosity distances. Moreover, the simulated binaries are oriented with $\iota = 0$, $\psi = 0$, and optimal sky position for the employed detector $\{\alpha = 2.621, \delta = 0.706\}$.

The PE studies on the artificial data are performed with the nested sampling algorithm ULTRANEST [199] with 3000 initial live points. The GW likelihood Eq. (2.21) is integrated over the frequency range [1, 8] kHz, in order to isolate the contribution from the PM signal. The sampling is performed in total mass $M \in [1, 6] M_\odot$ and mass ratio $q \in [1, 2]$, differently to what is presented in [154, 158], due to the analytical form of the empirical relations. In order to maintain a uniform prior in the mass components $m_{1,2}$, the prior $p(M, q|H_S)$ is modified according to [431]. We include aligned spin parameters and employ an isotropic prior with the constraint $|\chi_i| \leq 0.2$ for $i = 1, 2$. Tidal parameters Λ_1 and Λ_2 are sampled with a uniform prior in the range [0, 4000]. For the luminosity distance D_L , we use a volumetric prior in the range [20, 500] Mpc in order to confidently include the injected values. The remaining extrinsic parameters are treated according to [158]. Moreover, we include the PM parameters $\boldsymbol{\theta}_{\text{free}}^{\text{NRPMw}}$ in the PE routine and perform the sampling in the mass-scaled quantities using a uniform prior PDF for $t_{\text{coll}}/M \in [t_0/M, 3000]$, $M^2\alpha_{\text{peak}} \in [-10^{-5}, 10^{-5}]$ and $\phi_{\text{PM}} \in [0, 2\pi]$. Finally, we introduce in the sampling the recalibration parameters $\boldsymbol{\delta}_{\text{fit}}$ in order to account the intrinsic errors of the quasiuniversal relations. For these terms, we employ a normally distributed prior with zero mean and variance defined by the estimated relative errors [383].

The near-threshold SNR of the signals under consideration requires additional care when extracting information from a simulation study. As such, in order to investigate the impact of noise fluctuations, we generate artificial data $\mathbf{d}_k(t) = \mathbf{s}(t) + \mathbf{n}_k(t)$

by injecting the targeted template $\mathbf{s}(t)$ into different random noise realizations $\mathbf{n}_k = \{n_i(t)\}_k$, where i runs over the employed detectors and k runs over the noise realizations. We employ a total of five different noise realizations fixing the initialization seed of the pseudo-random number generator in the BAJES pipeline. The PE studies are performed on all the included realizations k for each signal $s(t)$ and every injected SNR. Once the posterior PDFs $p(\boldsymbol{\theta}|\mathbf{d}_k, H_S)$ are estimated for each k , we compute an overall posterior in order to average over the different noise realizations. The overall posterior PDF is computed equally weighting each noise realization and averaging the recovered posteriors, i.e.

$$p(\boldsymbol{\theta}|\mathbf{s}, H_S) \propto \sum_k p(\boldsymbol{\theta}|\mathbf{d}_k, H_S), \quad (5.1)$$

where k runs over the employed noise realizations. This approach aims to estimate an agnostic and comprehensive posterior distribution that correctly incorporates the full statistical uncertainties. As we will show below, such uncertainties are relevant when discussing some of the cases under consideration. This estimate will improve with a larger number of noise configurations, $k \gg 1$, and is limited only by the computational cost. In the limit of an infinite sum over all the possible noise realizations, Eq. (5.1) is equivalent to the posterior in zero-noise realization [432].

5.2.2 Detectability

Figure 5.1 shows the recovered mean, maximum and minimum BFs for the signal vs. noise hypothesis. In general, the BFs show the expected increasing trend deviating from $\log \mathcal{B} \simeq 0$ and recovering informative posterior distributions at PM SNR $\simeq 6$. Averaging over all the analyzed cases, the nominal detectability threshold is reached for PM SNR of $7.2_{-0.5}^{+0.8}$. These SNRs correspond to (optimally-oriented) binaries located at luminosity distances of ~ 100 Mpc, that are values consistent with recent observations of BNS mergers [56]. Employing estimates of BNS merger rates [433], the threshold distance of 100 Mpc can be translated in an upper limit of ~ 4 observable BNS mergers per year.

These results improve the results coming from damped-sinusoidal templates [378, 379] and are comparable with similar estimates performed with unmodeled studies [375]. On the other hand, when the employed template is a good representation of the signal, template-based analyses are expected to deliver better detectability threshold than model-independent estimates. Then, in this perspective, this claim might

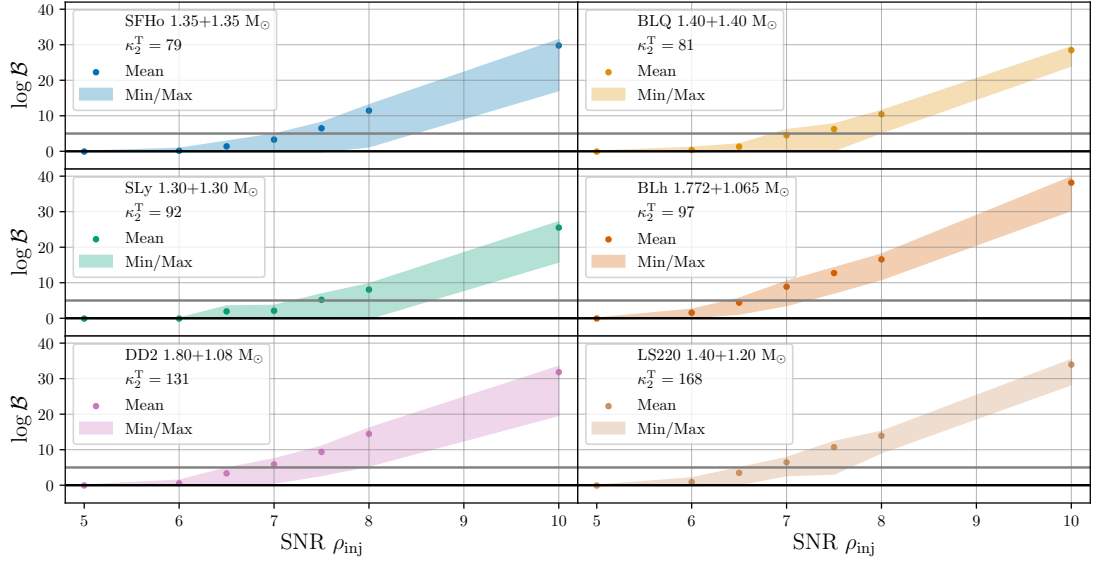


FIGURE 5.1: Logarithmic BFs $\log \mathcal{B}$ as functions of the PM SNR of the injected NR template. The dots refer to the mean values averaged over the different noise realizations and the shadowed areas correspond to the minimum and maximum values recovered in the survey.

Two horizontal lines identify $\log \mathcal{B} = 0$ (black) and $\log \mathcal{B} = 5$ (gray).

appear counterintuitive. However, the poorer (or comparable) results of template-based studies of PM transients with respect to more flexible models can be explained by the considerable mismatch between the employed template and the signal. In NRPMw, these biases are corrected with the recalibration δ_{fit} , accounting for deviations from the predictions of the calibrated relations.

Noise fluctuations affect the estimates, leading to larger threshold SNRs, with pronounced and non-homogeneous fluctuations. The recovered BFs for the binaries with $\kappa_2^T \lesssim 90$ have a slower trends compared with the other cases, showing $\log \mathcal{B} \lesssim 30$ for SNR 10. The corresponding PM transients show the most significant modulation effects among the considered cases and a short duration, except for SLy 1.30+1.30 M_\odot . Moreover, the characteristic PM peaks for these cases are located at higher frequency values compared to the other binaries, i.e. $f_2 \gtrsim 3$ kHz, where the noise contributions increase. The detectability threshold for these cases could be improved by a refined characterization of the frequency modulations (e.g. introducing a free modulation phase as a free parameter), or refining the late-time portion of the template (e.g. including the wavelet for the BH collapse).

Figure 5.2 shows the posterior PDFs of the recovered spectra for an illustrative noise realization at SNR 10. We opt to report this case because it corresponds to the loudest employed SNR and therefore the systematic errors between NRPMw model and

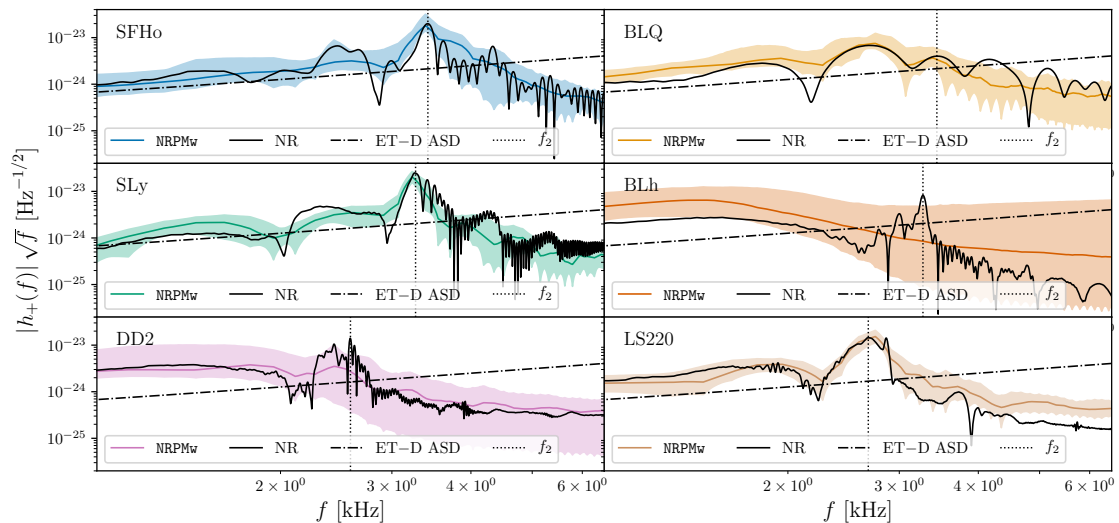


FIGURE 5.2: Posterior PDFs of the GW spectra for the PM plus polarization $h_+(f)$ recovered for PM SNR 10 for an illustrative noise realization. The colored lines report the medians and the shadowed regions correspond to the 90% credibility region. The injected spectra are reported with black solid lines and the corresponding f_2 peaks are denoted with vertical black dotted lines. Black dashed line show the noise amplitude spectral density (ASD) of ET-D, i.e. the square root of the PSD.

NR data are more evident. In general, the majority of the injected signals are included within the 90% credibility levels of the recovered spectra.

The large mass ratio binaries BLh and DD2 underestimate the characteristic PM peak. In particular, the predicted spectra for the BLh case is primarily informed by the merger portion of data and it strongly deviates from the injected value due to the faint PM burst that does not permit a clear identification of the dominant peak. The 90% credibility level of the recovered time-domain waveform shows a non-vanishing tail for late times; however, the median value is consistent with zero, showing that the signal is not resolved. These errors can be related with a non-optimal modeling for large mass ratios, i.e. $q > 1.5$. In particular, tidally-disruptive mergers show additional phase discontinuities and multiple bumps in the time-domain GW amplitude, related with the remnant dynamics.

5.2.3 Parameter estimation

In NRPM_w, the actual f_2 value is determined by several quantities. A first estimate relies on the binary parameters through the quasiuniversal relation. Then, the frequency drift parameter α_{peak} and the value of the respective recalibrations δ_{fit} can shift the

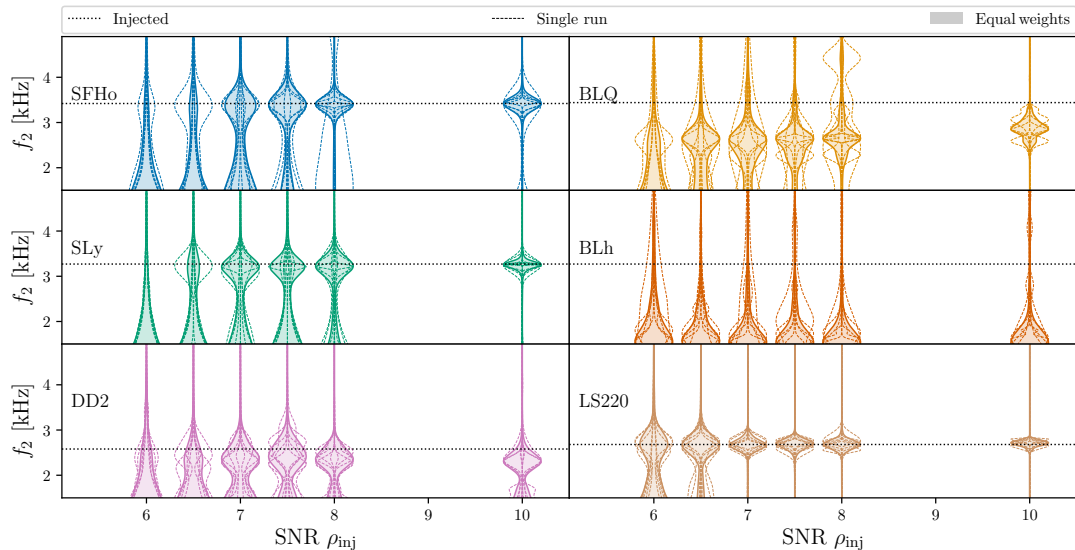


FIGURE 5.3: Posterior PDFs for the PM peak f_2 at the different PM SNRs recovered in the PE survey. For each case, thin dashed lines report the recovered posteriors for each run and the filled areas show the equally-weighted combined posterior PDFs. Black horizontal dotted lines indicate the values of the injected NR templates.

actual peak from the prediction of the quasiuniversal relation. Thus, a robust determination of the PM frequency can be estimated from the peak of the reconstructed spectra, consistently with the extraction method discussed in Section 4.2.2. For each sample, we generate the corresponding GW spectrum $h_{\text{NRPMw}}(f)$, considering only the time support $t > t_0$ in order to isolate the PM contribution of interest. Then, f_2 is identified as the (typically dominant) spectral peak of the carrier frequency component. When the template corresponds to prompt BH collapse, a prior sample is extracted.

Figure 5.3 shows the recovered posterior PDFs on f_2 as a function of the injected SNR. As mentioned in the previous section, for the majority of the cases the recovered posteriors report informative inferences for $\text{SNR} \gtrsim 6$ with errors of $O(1 \text{ kHz})$. The errors on the estimated f_2 decrease to $O(100 \text{ Hz})$ at PM SNR 10. At SNR 8, all posterior PDFs show informative measurements, with uncertainties ranging from 1 kHz to 500 Hz, and the injected NR values are included in the 90% credible regions. The uncertainties on the f_2 posteriors reach $O(100 \text{ Hz})$ at SNR 10 and systematic uncertainties start to play a more significant role. In particular, the analyses of the short-lived remnant BLQ show bimodalities in the f_2 posteriors for some noise realizations. These biases are attributable to subdominant couplings that have a larger contribution on the overall spectrum for short-lived remnants, whose power can exceed

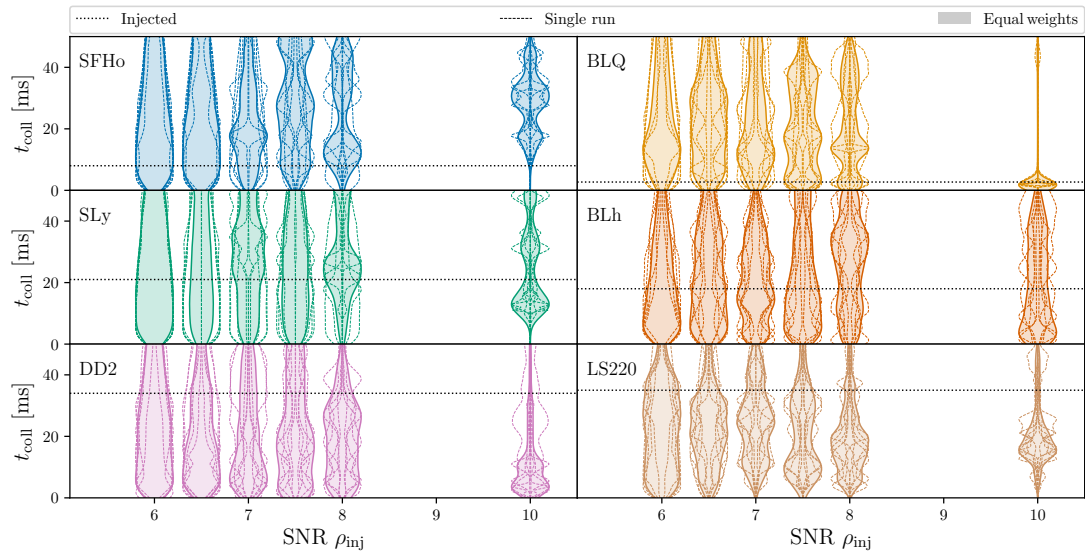


FIGURE 5.4: Posterior PDFs for the time of collapse t_{coll} at the different PM SNRs recovered in the PE survey. For each case, thin dashed lines report the recovered posteriors for each run and the filled areas show the equally-weighted combined posterior PDFs. Black horizontal dotted lines indicate the values of the injected NR templates.

that of the f_2 peak (see Figure 5.2). Similar biases are recovered also in the analysis of the DD2 binary. On the other hand, as discussed in Section 5.2.2, the inference of the BLh binary is not capable to resolve the f_2 peak.

Figure 5.4 shows the posterior PDFs for the time of BH collapse t_{coll} as functions of the injected SNR. This term is strongly affected by noise fluctuations, since the late-time signal tail is no more observable when its amplitude goes below the noise threshold. However, the injected values are generally included within the 90% credibility levels. The associated uncertainties go from $O(30 \text{ ms})$ at threshold SNR to $O(20 \text{ ms})$ at PM SNR 10. A particular case is the BLQ binary that corresponds to the most massive binary with the shortest PM transient among the considered cases. The corresponding posterior for SNR 10 is tightly constrained around the injected value, implying that t_{coll} can be better estimated for very-short-lived remnants. The inference of t_{coll} can be improved introducing the model for the remnant collapse in NRPMw [383]. However, the observation of the BH collapse is strongly limited by the sensitivity of the detectors at the corresponding BH frequencies, that occur at $f \gtrsim 6 \text{ kHz}$ for typical BNS systems.

The subdominant frequency f_0 is another relevant PM properties, since it can provide insights on the NS structure under the assumptions that it is related to the radial oscillations of the remnant [e.g. 109, 385, 434, 435, 436]. The recovered f_0

posteriors are generally broader than the f_2 ones, due to the weaker magnitude of these spectral peaks. The results show informative measurements for PM SNR $\gtrsim 7.5$ with errors of $O(1 \text{ kHz})$. The uncertainties decrease to $O(500 \text{ Hz})$ at PM SNR 10. Another interesting PM property is the frequency drift parameter α_{peak} . This term appears to be better constrained for long-lived equal-mass binaries, due to the nature of these PM GW transients, with errors of $O(0.1 \text{ kHz}^2)$ at PM SNRs of 8. However, for SNR $\gtrsim 10$, systematic errors become more relevant. A particular case is the LS220 binary, for which the recovered posterior overestimates the injected value due to the non-monotonic frequency evolution of the injected NR template. We verified that `NRPMw` recovers the initial slope of the LS220 transient, corresponding to the loudest contribution. For unequal-mass binary, α_{peak} is poorly constrained since the PM GW transient is fainter compared to equal-mass cases.

The intrinsic binary parameters are generally poorly constrained compared to the premerger analysis due to the considerably smaller SNR of the PM signal. The median binary masses M are typically shifted toward larger values, with errors of $O(1 M_\odot)$. Nevertheless, the injected values are always included in the 90% credible regions, indicating that our inference is unbiased at the SNRs under consideration. The mass ratio is typically well identified up to PM SNR ~ 8 with errors of ~ 0.6 at sensitivity threshold. For increasing SNRs, systematic errors become more dominant especially for equal-mass binaries, where the overall PM power is larger. The tidal polarizability κ_2^T shows systematic errors for PM SNR $\gtrsim 8$, underestimating the injected values. In a real scenario, these biases can be cured with the inclusion of premerger information.

5.3 Softening effects

Non-nucleonic matter phases at $\rho \gtrsim 3 \rho_{\text{sat}}$ can impact the remnant dynamics and leave detectable imprints on the GWs. Case studies considered matter models including hyperon production [e.g. 67, 401, 437] or zero-temperature models of phase transitions to quark-deconfined matter [e.g. 86, 401, 438]. These additional degrees of freedom lead to more compact NSs for masses $\gtrsim 1.5 M_\odot$ compared to nucleonic models, inducing a softening of the EOS. The detectability of these effects crucially depends on the densities at which the EOS softening takes place. We demonstrate the possibility of investigating the EOS softening at extreme densities using the PM GW observations. We discuss the specific case of BHBA ϕ and DD2 EOSs [67]. The BHBA ϕ EOS is identical to DD2 except that at densities $\rho \gtrsim 2.5 \rho_{\text{sat}}$ it softens due

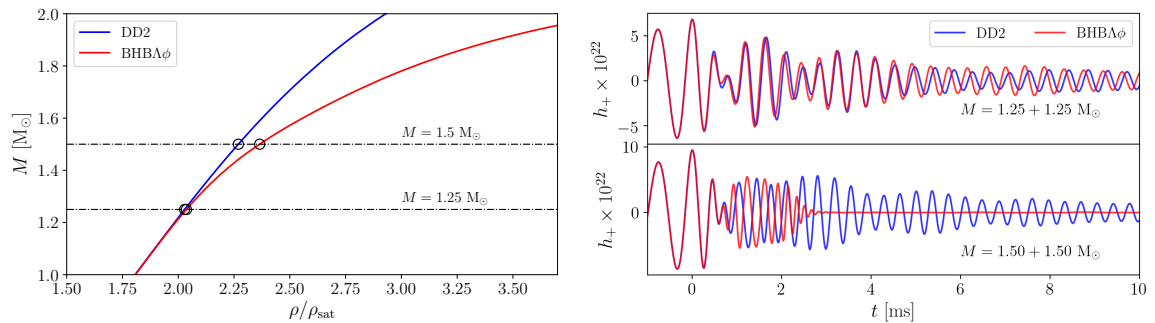


FIGURE 5.5: Comparison between the BHBA ϕ (red) and the DD2 (blue) EOSs and the corresponding BNS templates [67]. *Left panel:* Mass of individual TOV NSs as a function of the central density. The markers refer to simulated BNSs. *Right panel:* Plus polarization $h_+(t)$ of the NR waveforms for the simulated BNSs with mass $M = 3 M_\odot$ and $M = 2.5 M_\odot$. The binary are located at a fiducial distance of 40 Mpc. The origin of the time axis $t = 0$ corresponds to the moment of merger.

to the formation of Λ -hyperons. Inspiral-merger GW signals from binaries described by the two EOSs and $M \lesssim 3 M_\odot$ are indistinguishable since the individual progenitor NSs have maximal densities $\rho \lesssim 2.5\rho_{\text{sat}}$, similar compactnesses and tidal parameters, as shown in Figure 5.5 (left). On the other hand, for $M \gtrsim 3 M_\odot$ the PM remnants reach higher densities at which the two EOSs differ, leading to different PM GWs as shown in Figure 5.5 (right).

We consider a pair of high-mass binaries with $M = 3 M_\odot$. The DD2 $1.50+1.50 M_\odot$ binary has $f_2 \simeq 2.76$ kHz; while, the respective BHBA ϕ remnant has $f_2 \simeq 3.29$ kHz. As discussed in [383], the precise identification of f_2 is challenging for the BHBA ϕ binary due to the short duration of the PM signal. Here, we assume the second peak of the spectrum is f_2 . The difference between the two NR values is ~ 500 Hz, which corresponds to $\sim 18\%$. The BHBA ϕ data deviates of $\sim 3\text{--}\sigma$ from the prediction of the quasiuniversal relation presented in Section 4.2.2 ($f_2^{\text{fit}} = 2.88$ kHz), encoding a more compact remnant than the DD2 case. The two binaries have also different times of BH collapse: the DD2 case collapses at late times, i.e. $t_{\text{coll}} \simeq 21$ ms; while, the BHBA ϕ remnant collapses into BH shortly after merger with $t_{\text{coll}} \simeq 2.6$ ms. The BHBA ϕ $1.50+1.50 M_\odot$ binary shows the largest deviations from the quasiuniversal fits.

In the following sections, we discuss the detection of breaking of quasiuniversality via comparison of posteriors PDFs (Section 5.3.1) and we introduce a consistency test to identify EOS softening effects (Section 5.3.2).

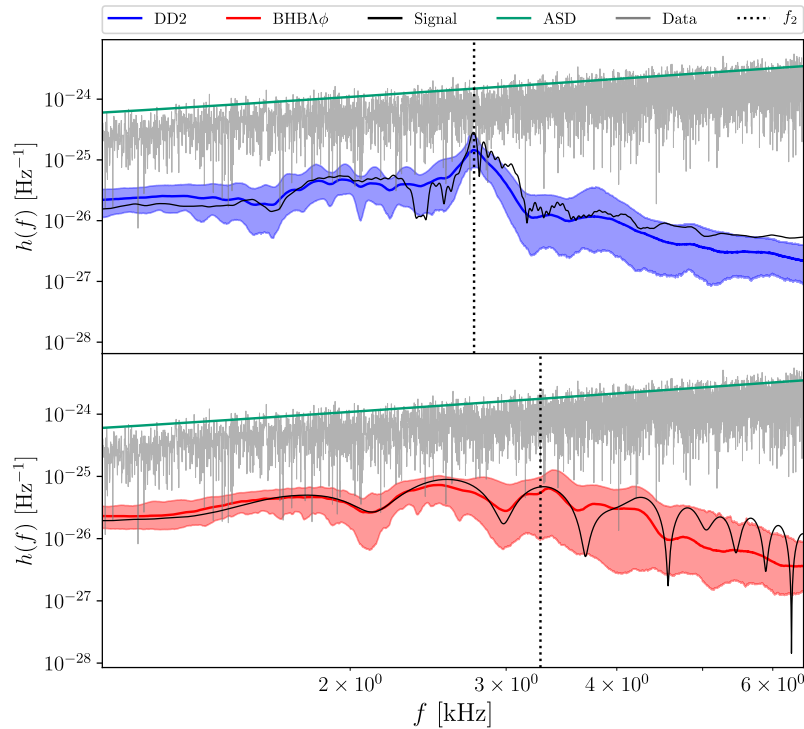


FIGURE 5.6: Posterior PDFs of the recovered spectra for the DD2 (top panel, blue) and the BHBA ϕ (bottom panel, red) binaries at PM SNR 8. The solid colored lines report the median spectrum and the contours show the 90% credible regions. The black solid lines correspond to the injected signals and black dotted lines correspond to the f_2 peak. The green lines show the PSD. The grey lines show the artificial data.

5.3.1 Breaking of quasiuniversality

The main question we address is whether an analysis of PM signal can inform us on the EOS softening effects at extreme densities, and what are the most relevant quantities that indicate the softening. Then, we perform Bayesian studies with NRPMw model and ET detector on the PM transients solely. The injected signals correspond to the DD2 and BHBA ϕ binaries with $M = 3 M_\odot$ and the PE analyses are performed within the same framework discussed in Section 5.2 with PM SNR 8 and 10 using a single noise realization.

The spectra recovered in the new analyses performed with NRPMw at PM SNR 8 are shown in Figure 5.6. The recovered SNRs are consistent with the injected values, recovering $7.5^{+1.0}_{-1.4}$ and a BF $\log \mathcal{B} = 6.3 \pm 0.2$ for the DD2 case; while, for the BHBA ϕ , we recover an SNR of $7.4^{+1.2}_{-1.2}$ and $\log \mathcal{B} = 6.5 \pm 0.2$. The posterior PDFs for the intrinsic

binary parameters do not show significant differences between the two cases. This is key in view of coherent and informative consistency tests [e.g. 154, 381]. We recover $M \simeq 4.3 M_{\odot}$ with an error of $\sim 1.5 M_{\odot}$. The mass ratios are constrained around the equal-mass case with errors of ~ 0.25 . The tidal polarizability κ_2^T underestimates the injected values with medians $\kappa_2^T \simeq 30$ and errors ~ 150 . The spins posteriors are dominated by the priors and not informative.

At SNR 8, the f_2 posteriors show different median values corresponding to $f_2 = 2.73_{-0.06}^{+0.05}$ kHz for DD2 and $f_2 = 3.2_{-1.0}^{+0.9}$ kHz for BHBA ϕ . The hypothesis $f_2^{\text{DD2}} = f_2^{\text{BHBA}\phi}$ lies on the 50% credibility level, indicating a mild breaking of quasiuniversality. This deviation is partially encoded in the related recalibration parameters that recovered opposite values, i.e. $\delta_{f_2} = -1_{-4}^{+7}$ % for DD2 and $\delta_{f_2} = 2_{-9}^{+6}$ % for BHBA ϕ . In this context, the inclusion of the recalibration coefficients is crucial since they allow the observed PM peak to deviate from the prediction of the quasiuniversal relation for a common combination of intrinsic binary parameters. However, the short duration of the BHBA ϕ transient and the strong modulations can introduce biases and multimodalities in the estimates of the associated peak frequency, as also shown in the analysis of the BLQ binary in Section 5.2. Another quantity that encodes the softening of the EOS at high densities is the time of BH collapse t_{coll} . A softer EOS allows the NS remnant to reach higher densities, yielding to an earlier BH collapse for comparable masses [67, 86, 412]. The recovered posteriors at SNR 8 for t_{coll} give $t_{\text{coll}} = 28_{-24}^{+36}$ ms for DD2 and $t_{\text{coll}} = 6_{-4}^{+41}$ ms for BHBA ϕ , consistently with the injected values. Even if this term can be strongly affected by noise fluctuations at low SNRs, as discussed in Section 5.2.3, the estimate of t_{coll} appears to be less biased and more conservative compared to the f_2 one.

In order to validate the robustness of the inference, we repeat the analysis injecting the signals at PM SNR 10. The recovered SNRs are $7.8_{-1.2}^{+1.2}$ for the DD2 case and $7.6_{-1.9}^{+1.8}$ for the BHBA ϕ case, consistently with the corresponding mismatches of $\sim 10^{-1}$ for both NR templates. The dominant systematic appears in the f_2 posterior PDF for BHBA ϕ . This posteriors shows pronounced multimodalities due to the contribution of the subdominant coupled frequencies $f_{2\pm 0}$, as discussed previously. The median values and the 90% credibility intervals correspond to $f_2 = 2.75_{-0.03}^{+0.03}$ kHz for the DD2 binary and $f_2 = 3.7_{-2.7}^{+0.3}$ kHz for the BHBA ϕ binary, excluding the $f_2^{\text{DD2}} = f_2^{\text{BHBA}\phi}$ hypothesis within $\sim 65\%$ credibility level. The t_{coll} posterior PDFs predict $t_{\text{coll}} = 54_{-41}^{+5}$ ms for the DD2 binary and $t_{\text{coll}} = 16_{-13}^{+11}$ ms for the BHBA ϕ binary. The t_{coll} medians show significant fluctuations due to noise contributions especially for the long-lived DD2

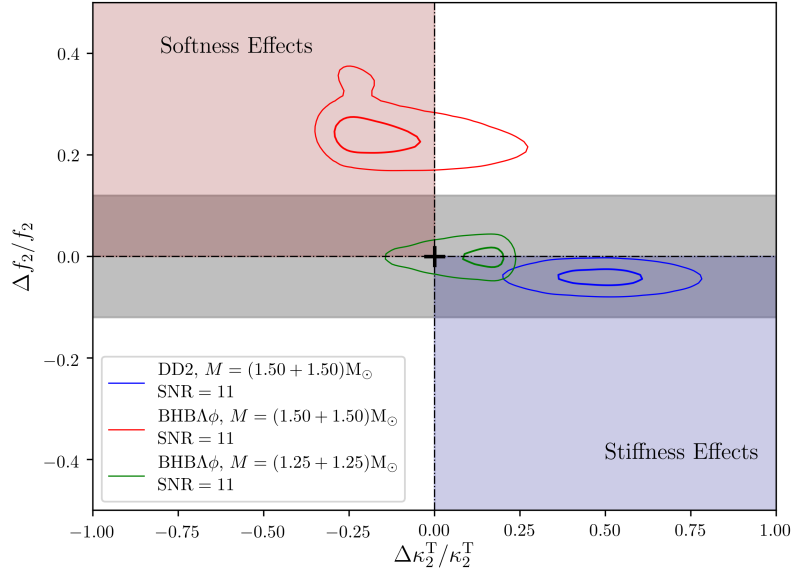


FIGURE 5.7: Posterior PDFs for the deviation from the quasiuniversality defined in Eq. 5.2 for characteristic PM frequency f_2 and tidal coupling κ_2^T . The contours report the 50% and the 90% credibility regions. Red lines refer to low-mass BHBA ϕ binary, blue lines refer to high-mass DD2 binary and red lines refer to high-mass BHBA ϕ binary. The red area denotes deviations due to softening effects, while blue area identify the stiffening effects. The grey band report the 90% credibility region of the f_2 EOS-insensitive relation.

case; however, the uncertainties tighten with respect to SNR 8, denoting convergence toward the injected value.

These results show that the short-lived binaries (such as the BHBA ϕ case) show more ambiguous f_2 posteriors for increasing SNRs; while, the t_{coll} posterior unambiguously converged to the true value for increasing SNR, as shown also by the BLQ binary in Section 5.2.3. On the other hand, for the long-lived binaries (such as the DD2 case), the f_2 posterior is typically unbiased and the t_{coll} posterior is more affected by noise fluctuations, but including the injected value within the 90% credibility intervals. Thus, the measurement of t_{coll} is expected to be a robust probe of softening effects in the NS EOS for PM SNR $\gtrsim 9$.

5.3.2 Consistency test

In order to better characterize the deviations from quasiuniversality in a realistic scenario of BNS GW detection, we employ `TEOBResumS` and `NRPM` in the analysis of the inspiral-merger-PM data of the high-mass DD2 and BHBA ϕ BNSs [154]. Moreover, we

include in the analysis the low-mass BHBA ϕ binary with $M = 2.5 M_{\odot}$, whose morphology is identical to the corresponding DD2 case. The corresponding NR templates are shown in Figure 5.5 (right). The data are generated as EOB-NR hybrid waveforms. We analyze 128 s of data with sampling rate of 16 kHz injecting the signal with PM SNR 11 using the three-detector LIGO-Virgo network at design sensitivity [29, 31].

Following the approach of Ref. [38, 439], we introduce a consistency test that aims to reveal breaking of quasiuniversality in the PM frequency f_2 . For each injected signal, we perform PE analysis on the PM data only (labeled as ‘PM’), on the inspiral-merger data only (labeled as ‘IM’) and on the full-spectrum data (labeled as ‘IMPM’). As discussed in Ref. [439], inspiral-merger-PM consistency tests rely on the cutoff frequency f_{cut} used to split the low-frequency and high-frequency regimes. In our case study, the cutoff frequency is defined by the merger frequency of the known injected (2, 2) waveform, i.e. $f_{\text{cut}} \simeq f_{\text{mrg}}$. In a realistic scenario, the cutoff frequency can be estimated from the full-spectrum posterior using EOS-insensitive relations for the merger frequency for the dominant (2, 2) mode [121, 154, 383]. Then, we can introduce the (fractional) deviation from the quasiuniversal prediction as

$$\frac{\Delta f_2}{f_2} = \frac{f_2^{\text{PM}} - f_2^{\text{IM}}}{f_2^{\text{IMPM}}}, \quad \frac{\Delta \kappa_2^{\text{T}}}{\kappa_2^{\text{T}}} = \frac{\kappa_2^{\text{TPM}} - \kappa_2^{\text{TIM}}}{\kappa_2^{\text{TIMPM}}}. \quad (5.2)$$

Note that f_2^{IM} is computed using EOS-insensitive relations, while f_2^{PM} and f_2^{IMPM} are estimated from the waveform spectra as discussed in Section 5.2.3. Formally, the computation of $p(\Delta f_2/f_2, \Delta \kappa_2^{\text{T}}/\kappa_2^{\text{T}})$ is performed with a probabilistic approach. Given the posteriors $\{f_2, \kappa_2^{\text{T}}\}_i$ for $i = \text{IM}, \text{PM}, \text{IMPM}$, the posterior PDF of $\Delta f_2 = f_2^{\text{PM}} - f_2^{\text{IM}}$ and $\Delta \kappa_2^{\text{T}}$ are estimated

$$p_{\Delta}(\Delta f_2, \Delta \kappa_2^{\text{T}} | \mathbf{d}_{\text{IM}}, \mathbf{d}_{\text{PM}}) = \int p(f_2, \kappa_2^{\text{T}} | \mathbf{d}_{\text{PM}}) p(\kappa_2^{\text{T}} - \Delta \kappa_2^{\text{T}}, f_2 - \Delta f_2 | \mathbf{d}_{\text{IM}}) df_2 d\kappa_2^{\text{T}}. \quad (5.3)$$

Eq. (5.3) is the convolution product between the inspiral-merger PDF and the PM PDF. Then, defining $\varepsilon_{f_2} = \Delta f_2/f_2$ and $\varepsilon_{\kappa_2^{\text{T}}} = \Delta \kappa_2^{\text{T}}/\kappa_2^{\text{T}}$, the posterior PDF for the quantities in Eq. (5.2) can be computed from the recovered posterior PDFs as

$$p(\varepsilon_{f_2}, \varepsilon_{\kappa_2^{\text{T}}}) = \int (\kappa_2^{\text{T}} f_2) p_{\Delta}(\varepsilon_{f_2} \cdot f_2, \varepsilon_{\kappa_2^{\text{T}}} \cdot \kappa_2^{\text{T}} | \mathbf{d}_{\text{IM}}, \mathbf{d}_{\text{PM}}) p(f_2, \kappa_2^{\text{T}} | \mathbf{d}_{\text{IMPM}}) df_2 d\kappa_2^{\text{T}}. \quad (5.4)$$

As discussed in Ref. [439], $p(f_2, \kappa_2^{\text{T}} | \mathbf{d}_{\text{IMPM}})$ represents our best guess for the $\{f_2, \kappa_2^{\text{T}}\}$ posterior and it is used in Eq. (5.4) to weight the contributions of the inspiral and PM

inferences. Within this approach the origin of the axes, i.e. $\Delta f_2 = 0$ and $\Delta \kappa_2^T = 0$, represents the null-hypothesis for which no deviation from quasiuniversality is observed. On the other hand, a deviation of the posterior PDF towards the region with $\Delta f_2/f_2 > 0$ (< 0) and $\Delta \kappa_2^T/\kappa_2^T < 0$ (> 0) can be interpreted with EOS softening (stiffening) effects.

Figure 5.7 shows the posterior PDFs estimated for the three considered binaries. The low-mass BHBA ϕ case confidently include the null hypothesis within the 90% credibility level of the posterior. The high-mass DD2 case show mild deviations toward the stiffness portion of the plane, with $\Delta \kappa_2^T/\kappa_2^T = 0.5_{-0.3}^{+0.3}$ at the 90% credibility level. However, $\Delta f_2/f_2$ is consistent with zero within the fit uncertainty. On the other hand, the high-mass BHBA ϕ case show deviations toward the softness portion of the plane, with $\Delta \kappa_2^T/\kappa_2^T = -0.2_{-0.2}^{+0.5}$ and $\Delta f_2/f_2 = 0.2_{-0.1}^{+0.2}$, significantly above the fit uncertainty and including the injected difference within the 90% credibility interval.

These results show that it is possible to observe departures from the quasiuniversal predictions employing PM transients. Remarkably, we stress that the breaking of a quasiuniversal relation within a given credibility level does not necessarily imply the presence of an EOS softening. Instead, more generally, such a breakdown has to be interpreted as the invalidation of a particular empirical relation due to physical effects that not captured by the constructed fit. Similarly, a EOS softening might break a quasiuniversal relation only in a marginally significant way, as in our case study, or the remnant's densities might be such that these effects are not evident, e.g. small mass binaries $M \ll 3 M_\odot$ [67, 86].

5.4 High-density constraints

As discussed in Section 5.2.3, at the threshold SNR of 7 the inference on f_2 delivers a result accurate at ~ 20 %. As shown by previous works [440, 441], the f_2 peaks correlates with the NS radii $R_{1.6M_\odot}$ and $R_{1.8M_\odot}$ of a $1.6 M_\odot$ and $1.8 M_\odot$ NS respectively. Thus, the PM frequency could be translated into an estimate of the radius of a non-rotating equilibrium star of fixed mass with an uncertainty of ~ 2 km. In a real scenario this is not particularly interesting since the radius (or equivalently the tidal parameters, $R \sim \tilde{\Lambda}^{1/5}$ [442, 443]) will be known with a better accuracy from the inspiral-merger analysis. We find from our analyses that inspiral-merger inference at the minimal PM SNR delivers $\delta \tilde{\Lambda}/\tilde{\Lambda} \sim 4$ % and $\delta R/R \sim 2$ % [17, 154]. More interesting is to explore constraints on the radius of the maximum mass (most compact) non-rotating

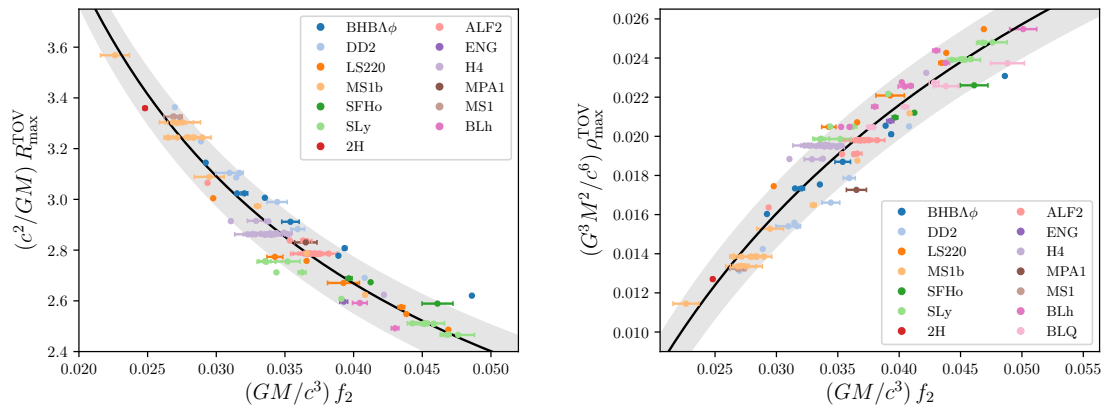


FIGURE 5.8: Empirical relations for the minimum radius $R_{\text{max}}^{\text{TOV}}$ (left panel) and the maximum central density $\rho_{\text{max}}^{\text{TOV}}$ (right panel) of a non-rotating NS as function of the PM peak frequency f_2 . The colored markers show the data extracted from NR simulations of CORE database for different EOSs. Each marker corresponds to a different binary configuration and the error bars are computed using different numerical resolutions (when available). The shadowed areas report the 90% credibility region of the quasiuniversal relations.

equilibrium NS $R_{\text{max}}^{\text{TOV}}$ [152, 154], since the latter corresponds to the largest matter densities that can be reached for a given EOS. Using the 263 NR data extracted from the CORE database [82, 86, 125, 160, 161], we find an approximate relation in the form

$$\frac{c^2}{GM} R_{\text{max}}^{\text{TOV}} = a_0 \left[1 + a_1 \left(\frac{\pi GM}{c^3} f_2 \right)^{-4/5} \right], \quad (5.5)$$

where $a_0 = 1.03 \pm 0.02$, $a_1 = 0.30 \pm 0.01$, are determined by a standard least-squared minimization method with $\chi^2 = 0.4$. The NR data includes binaries with NS masses in the range $1-2 M_{\odot}$ and dimensionless spin magnitudes ≤ 0.2 . The predicted $R_{\text{max}}^{\text{TOV}}$ has an error of $\sim 2\%$ at $1-\sigma$ level. Figure 5.8 (left) shows the calibrated relation together with the NR data used for calibration. Measurements of PM signals at the minimum SNR deliver an estimation of $R_{\text{max}}^{\text{TOV}}$ accurate at $O(10\%)$.

A PM detection can also provide lower bounds on the maximum TOV mass $M_{\text{max}}^{\text{TOV}}$ [122, 296]; although, multiple PM observations could provide a few percent measurement [152] complementary to that from an inspiral EOS inference [14, 444, 445]. On the other hand, we observed that the PM peak correlates to the maximum central density $\rho_{\text{max}}^{\text{TOV}}$ of a non-rotating equilibrium NS with a weak dependence on the EOS [17]. The existence of this relation was suggested by previous works [152, 296, 446], but the relation obtained there involves the binary configurations with the largest possible mass that does not promptly collapse to BH. We propose a more general approach

that improves the previous NR-calibrated relations providing direct link between a PM observable property and a high-density EOS feature. Figure 5.8 (right) shows the approximate quasiuniversal relation $\rho_{\max}^{\text{TOV}}(f_2)$ compared to the calibration NR sample of 289 simulations of the CORE database [82, 86, 125, 160, 161]. The sample includes binaries with NS masses in the range $1-2 M_{\odot}$ and dimensionless spin magnitudes ≤ 0.2 . The relation $\rho_{\max}^{\text{TOV}}(f_2)$ fits to the expression:

$$\frac{G^3 M^2}{c^6} \rho_{\max}^{\text{TOV}} = a_0 \left[1 + a_1 \left(\frac{\pi G M}{c^3} f_2 \right)^{-1/6} \right]. \quad (5.6)$$

where $a_0 = 0.136 \pm 0.002$, $a_1 = -0.595 \pm 0.001$ are determined by a standard least-squared minimization method at $\chi^2 = 0.016$ corresponding to a relative error of $\sim 6\%$ at $1-\sigma$ level.

The right-hand sides of Eq. (5.5) and Eq. (5.6) can be entirely determined from the measurement of the binary mass M and the PM peak frequency f_2 . Hence, the maximum-mass properties $\{R_{\max}^{\text{TOV}}, \rho_{\max}^{\text{TOV}}\}$ can be best inferred from a full-spectrum BNS GW observation. Figure 5.8 includes BHBA ϕ and BLQ BNS data that show deviations comparable or larger than the 90% credibility level of the EOS-insensitive relations. Thus, Eq. (5.5) and (5.6) (and consequently the Bayesian methods that rely on them) are expected to break for particular binary and EOS configurations. Interestingly, the employed NR sample show milder deviations from quasiuniversality for the ρ_{\max}^{TOV} relation.

We next discuss the potential accuracy of such measurement using a mock Bayesian inference study with ET detector and NRPM model. In the next Sections, we show how to constrain the high-density EOS properties, i.e. ρ_{\max}^{TOV} and R_{\max}^{TOV} , from a full-spectrum BNS GW data (Section 5.4.1) and we investigate the implications of such a measurement for the EOS (Section 5.4.2).

5.4.1 Inferring the maximum density

We inject into an artificial noise strain generated with ET-D PSD two simulated signals extracted from fiducial equal-mass non-spinning BNSs. The first case is a binary with mass $M = 2.73 M_{\odot}$ and a stiff EOS DD2 [10] and the second corresponds to a binary of $M = 2.6 M_{\odot}$ and a soft EOS SLy [80]. For our case study, we perform full Bayesian analyses of the PM signals at different SNR and employ the Fisher matrix approach to estimate the uncertainties of the parameters measured from the inspiral signals. Fisher matrix analyses of the inspiral-merger signals are performed

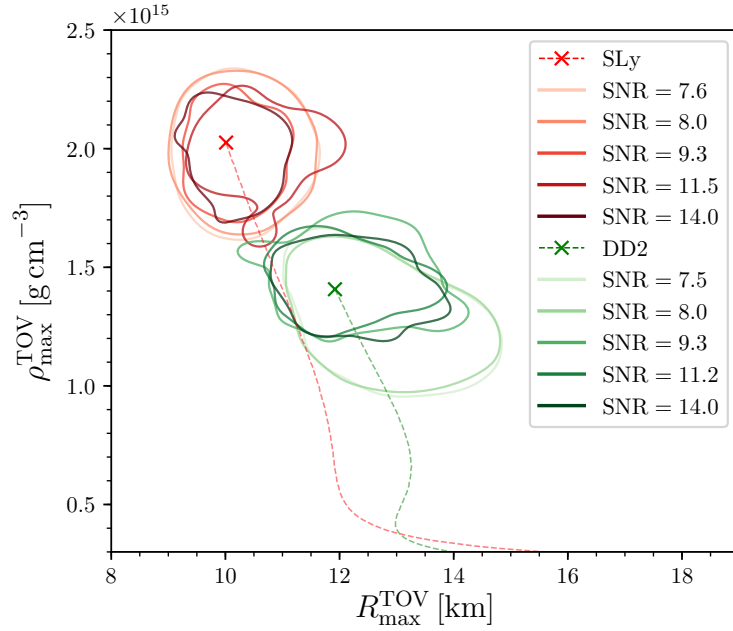


FIGURE 5.9: Posterior PDF for $\{\rho_{\max}^{\text{TOV}}, R_{\max}^{\text{TOV}}\}$ compared to the EOS of the injected signals. The contours show the 90% credibility regions. Green and red lines correspond respectively to the results obtained with DD2 and SLy EOSs and color intensities refer to the injected SNR of the PM data. The dashed lines show the central density as function of the NS radius and the crosses denote the maximum-density values.

with GWBENCH [447]. NR data are injected in a segment of 1 s with a sampling rate of 16 kHz. The sampling is performed with DYNesty [198] with 3200 live points analyzing the frequency region from 1 kHz to 8 kHz. The prior PDF is assumed to be uniform in the mass components, spanning the ranges $M \in [1.5, 6] M_{\odot}$ and $q \in [1, 2]$, and in the individual NS quadrupolar tidal parameters $\Lambda_i \in [0, 5000]$ for $i = 1, 2$. Spin magnitudes are kept fixed to zero. The extrinsic parameters are treated as discussed in [158], with volumetric prior for the luminosity distance in the range $[5, 500]$ Mpc. Moreover, we include the additional parameters, i.e. $\theta_{\text{free}}^{\text{NRPM}}$ and δ_{fit} , in the PE routines.

Once the NRPM analyses are completed, the posterior PDF for $\{\rho_{\max}^{\text{TOV}}, R_{\max}^{\text{TOV}}\}$ is obtained by combining the posteriors of M from the inspiral analysis and the posteriors of f_2 from the PM analysis using a resampling strategy. In particular, the samples $\{M, f_2\}$ are mapped into $\{\rho_{\max}^{\text{TOV}}, R_{\max}^{\text{TOV}}\}$ using Eq. (5.5) and Eq. (5.6). The uncertainties of the fits are taken into account introducing appropriate recalibration parameters, similarly to Section 3.3. The result is shown in Figure 5.9. The injected values, denoted with crosses, confidently lay within the 90% credibility regions of the recovered posterior PDFs. The true ρ_{\max}^{TOV} value is recovered at the detectability threshold with

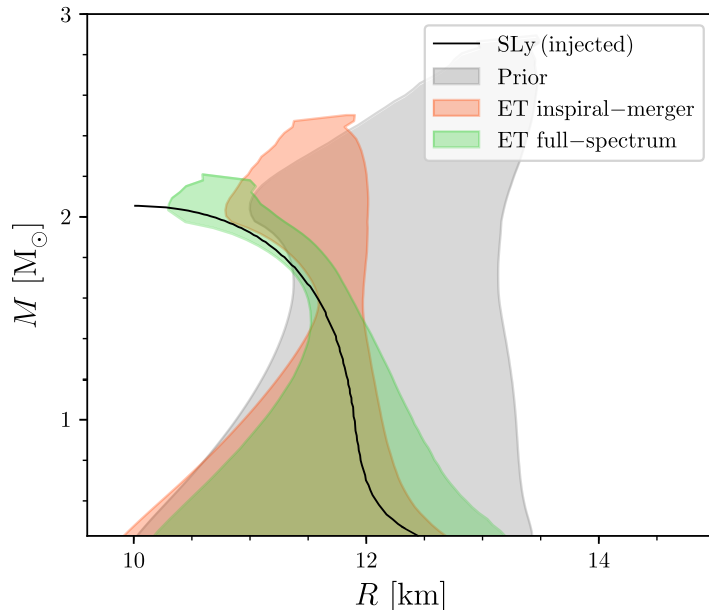


FIGURE 5.10: Mass-radius diagram constraints from a single full-spectrum ET BNS observation with PM SNR 10 (total SNR 180). The gray area (prior) corresponds to the two-million EOS sample of Ref. [364]. The orange and green areas are the 90% credibility regions given by inspiral-merger and inspiral-merger-PM inferences respectively. The full-spectrum (green) posterior confidently agrees with the injected EOS (black) within the 90% credibility region.

an error of $\sim 15\%$ at the 90% credibility level. At the same SNR, the uncertainty on the radius $R_{\text{max}}^{\text{TOV}}$ are of the order of 30% (90% credibility level). Such precision is sufficient to distinguish soft and stiff EOSs within the 90% credibility regions, as illustrated using the SLy and DD2 cases. Notably, the inference on $\rho_{\text{max}}^{\text{TOV}}$ hits the theoretical uncertainties on the quasiuniversal relation in Eq. (5.6) at SNR ~ 10 . A more precise measure is either not possible, because at that level the relation $\rho_{\text{max}}^{\text{TOV}}(f_2)$ becomes EOS-dependent, or it requires a more precise quasiuniversal relation from improved simulations.

5.4.2 Implications for the equation of state

To illustrate the potential impact of this approach, we show how a single detection of PM signal at SNR 10 (total SNR 180 and luminosity distance of 120 Mpc) can constrain the mass-radius relation for NSs. We take the SLy binary as fiducial binary. The analysis makes use of the two-million EOS sample of Ref. [364], similarly to study in Section 3.3.4. We assign a weight to each EOS sample corresponding to the posteriors of the masses and the tidal parameters from the inspiral-merger (labeled as

‘IM’) and with the maximum density and minimum radius posteriors from the PM measurement, i.e.

$$p(\text{EOS}|\mathbf{d}_{\text{IM}}) \propto p(\text{EOS}) \prod_{i=1,2} \int p(m_i, \Lambda_i|\mathbf{d}_{\text{IM}}) \delta(\Lambda_i - \Lambda_{\text{EOS}}(m_i)) dm_i d\Lambda_i, \quad (5.7)$$

$$p(\text{EOS}|\mathbf{d}_{\text{IM}}, \mathbf{d}_{\text{PM}}) \propto p(\text{EOS}) p(\mathbf{d}_{\text{IM}}|\text{EOS}) p\left(\mathbf{d}_{\text{PM}} \middle| R_{\text{max}, \text{EOS}}^{\text{TOV}}, \rho_{\text{max}, \text{EOS}}^{\text{TOV}}\right), \quad (5.8)$$

where Λ_{EOS} , $R_{\text{max}, \text{EOS}}^{\text{TOV}}$ and $\rho_{\text{max}, \text{EOS}}^{\text{TOV}}$ are respectively the tidal parameter, the minimum radius and the maximum central density predicted by the EOS.

Figure 5.10 shows the 90% credibility regions of the posterior PDFs in the mass-radius diagram. The inspiral-merger posteriors Eq. (5.7) give the strongest constraint. They are mostly informative at the EOS at densities $\rho \simeq 2\rho_{\text{sat}}$ corresponding to the individual NS components of the binary [448]. This inference leads to a measurement of the maximum NS mass of $M_{\text{max}}^{\text{TOV}} = 2.13_{-0.14}^{+0.20} M_{\odot}$ (90% credibility level), consistent with the injected value ($2.05 M_{\odot}$). However, the EOS posterior shows a biased behavior for high mass values, i.e. $M \gtrsim 1.5 M_{\odot}$, excluding the SLy sequence from the 90% credibility region. This shows that the inspiral-merger signal does not directly constrain the high-density EOS and the inferred $M_{\text{max}}^{\text{TOV}}$ represents an extrapolation based on the EOS representation and, therefore, more subjected to the prior choices. Notably, the considered ET BNS signal provides a constraint on $R_{1.4M_{\odot}}$ that is tighter than current GW170817 estimate of a factor $\gtrsim 4$.

The inclusion of PM information in Eq. (5.8) strengthens the agreement with the injected EOS at higher densities allowing a measurements of $M_{\text{max}}^{\text{TOV}} = 2.04_{-0.06}^{+0.08} M_{\odot}$, which agrees with the injected value and carries an error lower than 7% and it improves over current MM estimates of a factor ~ 1.5 . The joint constraint reduces of $\sim 60\%$ the $P(\rho)$ posterior area of the initial EOS sample leading to tight pressure constraints at fiducial densities, i.e. $\log_{10}(P_{2\rho_{\text{sat}}}/\text{dyn cm}^{-2}) = 34.52_{-0.04}^{+0.04}$ and $\log_{10}(P_{4\rho_{\text{sat}}}/\text{dyn cm}^{-2}) = 35.39_{-0.03}^{+0.04}$ at the 90% credibility level. For a detection at the sensitivity threshold (PM SNR ~ 7), we find that the measured maximum NS mass is $M_{\text{max}}^{\text{TOV}} = 2.07_{-0.09}^{+0.15} M_{\odot}$ with a relative error of roughly $\sim 12\%$. The multiple observation of about five PM BNS transients at sensitivity threshold can lead to a measurement of the maximum NS mass with an error of $\sim 5\%$ [379, 418]. This information provides narrow observational constraints that would significantly inform nuclear models in the very-high-density regimes, i.e. $\rho > 3\rho_{\text{sat}}$, which are unreachable conditions for modern nuclear experiments.

Conclusions

In this *Thesis*, we inferred the nuclear EOS from current MM observations of BNS mergers and presented perspectives of full-spectrum GW observations with XG detectors. The joint analysis of multiple messengers is key in order to achieve improved constraints on the source properties. NR data are fundamental resources for BNS modeling, driving the construction of empirical templates and calibration of EOS-insensitive relations. Moreover, the analyses of GWs from BNS PM remnants with XG detectors have proven the capabilities of these signals in constraining the high-density EOS properties. Exploratory studies with XG detectors are crucial to understand the capabilities of these instruments and investigate limitations of current methods.

Gravitational-wave analysis. The GW DA of GW170817 predicts a source-frame chirp mass $\mathcal{M} \simeq 1.188$ and a reduced tidal parameter $200 \lesssim \tilde{\Lambda} \lesssim 800$. The $\tilde{\Lambda}$ PDFs recovered with larger cutoff frequency $f_{\max} = 2$ kHz show larger systematic biases between different waveform templates compared to the $f_{\max} = 1$ kHz analyses. This can be understood by studying the tidal information. The latter is primarily gathered in the high-frequency portion of the spectrum, i.e. $f \gtrsim 500$ Hz; thus, a larger f_{\max} takes into account a larger amount of tidal information, highlighting systematic biases. Significant waveform systematics are to be expected for GW170817-like signals observed by advanced and XG IFOs. At design sensitivity, the expected bias in the reduced tidal parameter between `TEOBResumS`, `TaylorF2` and `PhenomPv2_NRTidal` is about $2\text{-}\sigma$, for typical BNS parameters as shown in Section 2.3.2. This would reflect in systematics on the NS radius of about 1 km (10%), that are comparable or well above of the current best estimates of the NS radius [14, 349, 354, 355, 357]. Moving to higher sensitivities and XG detectors, we estimate that the systematics between the approximants become dominant over statistical errors at SNRs of $O(100)$. This implies that EOS constraints from the potentially most informative events will be harmed by tidal waveform systematics. A possible solution to overcome current systematic errors in GW templates is the full calibration of waveform approximants on high-precision NR data with the employment of learning algorithms [e.g. 235, 449].

Kilonova analysis. The KN DA of AT2017gfo shows that the anisotropic description of the ejecta components is strongly preferred with respect to isotropic profiles, with a logarithmic BF of the order of $\sim 10^4$. Moreover, the favored model is the three-component KN constituted by a fast dynamical ejecta (comprising both a red-equatorial and a blue-polar portion), a slow isotropic shell and a polar wind. The dynamical ejecta mass lies around $\sim 10^{-2} M_{\odot}$ with typical velocities of $\sim 0.2 c$ and gray opacities of $\sim 10 \text{ cm}^2 \text{ g}^{-1}$, consistently with Ref. [294]. Resorting to NR-calibrated relations, the information on the dynamical ejecta and the disk mass can be employed to constrain the BNS intrinsic parameters. Using the KN data solely, we constrain the mass ratio to be ≤ 1.18 at the 90% credibility level. Under a modeling perspective, current KN description contains large theoretical uncertainties, such as thermalization effects, heating rates and energy-dependent photon opacities [e.g. 347]. These effects propagate into systematic biases in the global parameters of the model. Hence, the development and the improvements of KN templates is an urgent task in order to conduct reliable and robust analyses in the future [450]. In particular, an improved modeling for the thermo-nuclear heating rates and for the dynamics of the disk's winds are relevant short-term tasks [16, 120, 128]. In addition to the KN modeling uncertainties discussed above, another source of error of our estimates is the accuracy of the NR-calibrated formulae used to map the ejecta properties in terms of the BNS parameters. The current simulation set is limited to $O(100)$ of simulations, with fitting errors that could be reduced by considering data at even higher grid resolutions [310].

Multi-messenger analysis. Combining the GW-KN inference we constrain the radius of a $1.4 M_{\odot}$ non-rotating NS to $R_{1.4M_{\odot}} = 12.23_{-0.80}^{+0.75}$ km at the 90% credibility level. Including X-ray pulsar data of NICER observatory [60, 65], this measurement can be improved to $R_{1.4M_{\odot}} = 12.39_{-0.65}^{+0.70}$ km, corresponding to a maximum TOV mass of $M_{\text{max}}^{\text{TOV}} = 2.08_{-0.09}^{+0.16} M_{\odot}$. These results favor mildly soft EOSs, such as BLh [8] and LS220 [9]. Comparing our results with the literature, we note that all studies show broad agreement with each other, constraining $R_{1.4M_{\odot}}$ between 11 – 13 km [e.g. 16, 63, 357, 358, 363, 367, 368, 369]. This broad agreement might be related to the limited EOS information that does not allow to reveal systematic errors between different methods; or it can indicate that current MM inferences are affected by the prior information used to parameterize the EOS [366].

The inclusion of low-SNR GW events of NSs mergers [56, 361] is not expected to significantly enhance the presented estimates, since the tidal sector of these mergers is poorly constrained. Also the GRB information [44, 54, 150, 359, 360] is not expected

to improve the current EOS constraints, since the physics behind GRB emission in the context of BNS mergers and its connection to the EOS are uncertain [e.g. 451, 452, 453]. Current studies of GRB emission in BNS mergers are primarily driven by GRHD simulations [e.g. 454, 455, 456, 457, 458, 459, 460, 461, 462] and the mainstream interpretation relates the prompt GRB launch to the BH formation [44]. Within the *fireball* model [463, 464], the observable non-thermal GRB radiation is formed in an optically thick and highly relativistic outflow characterized by a Lorentz factor Γ , when kinetic energy is conveyed to particles through internal shocks. On longer timescales, i.e. $O(10^3 \text{ days})$, the interaction of the structured jet with the surrounding medium yields to a non-thermal emission powered by synchrotron radiation, as shown by the re-brightening of GRB170817A in the X-ray band [149, 150]. In general, a robust mapping between the source parameters and the GRB properties, e.g. initial energy E_0 and the Lorentz factor Γ , is currently unknown. Thus, the availability of robust models for the generation and emission of GRBs, with a clear map to the source and EOS properties, is key in order to tighten the current EOS constraints and to construct an optimal MM framework for BNS DA. Nonetheless, the usage of a joint MM likelihood, with a coherent joint PE for different messengers, can improve the estimations of the correlations between the parameters, tightening additionally the constraints [363]. The majority of MM PE methods rely on EOS-insensitive relations typically calibrated on NR data; thus, the development of high-precision NR infrastructures can yield to improved observational constraints.

Postmerger remnants. GW signals from BNS PM remnants are predicted to lie in the kilohertz regime and they are one of the main targets of XG IFOs [75, 76]. NS remnants are primarily studied and modeled employing NR simulations [e.g. 154, 374, 376, 380, 383]. Nonetheless, the employment of NR-calibrated relations facilitate the construction of full-spectrum GW models, permitting the attachment to inspiral-merger templates [154]. On the other hand, the EOS-insensitive relations introduce theoretical errors that can be taken into account during the PE routines including appropriate recalibration parameters. DA applications show that NR-informed PM models can provide informative measurements for PM SNRs $\gtrsim 7$, comparing the performances of minimal-assumption models [e.g. 375, 379]. The uncertainties on f_2 are $O(1 \text{ kHz})$ at PM SNR 7 and $O(100 \text{ Hz})$ at PM SNR 10. However, systematic errors arise for short-lived and large-mass-ratio remnants for SNR $\gtrsim 8$ primarily related to an inaccurate identification of the characteristic PM peak. In a real scenario of full-spectrum BNS observation, the f_2 measurement can be translated in constraints on the maximum

NS mass $M_{\text{max}}^{\text{TOV}}$ with errors of $\sim 12\%$ at sensitivity threshold, providing information at matter densities unreachable with modern nuclear experiments on Earth. Moreover, PM signals can inform us on the appearance of non-nucleonic degrees of freedom. The considered BNSs simulated with non-nucleonic EOSs (ALF2 [92], BHBA $\Lambda\phi$ [85], and BLQ [8, 86]) consistently show earlier BH formation compared to the hadronic counterparts [e.g. 67, 86, 401]. These deviations can be revealed for PM SNR $\gtrsim 9$ comparing the inferred time of collapse t_{coll} with theoretical predictions of targeted NR simulations. Another possible imprint of an EOS softening in the signal is the breaking of the quasiuniversal relations that characterizes the spectral features. We consider a short-lived remnant as a case study and demonstrate that $\sim 3\text{--}\sigma$ violations of EOS-insensitive relations are potentially observable at PM SNR 8. In the future, it would be interesting to verify the performances of NR-informed PM models against NR templates computed with more extreme EOSs that show neater deviations from the quasiuniversal trends [e.g. 381, 401]. In general, more accurate studies of BNS merger with non-nucleonic EOSs, driven by high-precision NR simulations [e.g. 67, 86, 412], are essential in order to comprehensively characterize to what extent the breaking of EOS-insensitive relations can probe EOS softening.

Simulated data of BNS remnants show that the full EOS information might be relevant for an accurate modeling of BNS remnants. This conclusion is suggested by studies of merger outcomes and PM dynamics, that show correlation with generic EOS properties [17, 124]. Nonetheless, turbulent viscosity and different neutrino treatments affect the characteristic time-scales of subdominant effects [e.g. 383, 465, 466]. Then, an improved NR-calibrated PM models could be achieved relying on regression methods and learning algorithms trained on high-precision NR data with the combined information of the full EOS. On the other hand, a clear relation between the dynamics of BH collapse and the source properties is crucial for PM modeling and for interpretation of EM counterparts [e.g. 57, 122, 124]. In this context, the observational GW data of BNS remnants can unambiguously provide evidence in favor of prompt or delayed BH collapse, guiding the mapping between the source properties and the PM dynamics.

Perspectives with next-generation detectors. Considering XG sensitivities, the sky localizations provided by GW detectors will significantly improve, facilitating the identification of EM counterparts [29, 426]. The combination of multiple MM data can maximize the gained observational information, improving the constraints on the NS EOS and clarifying the behavior of nuclear matter in extreme conditions of density.

However, the PE analysis of BNS signals with XG detectors might become an Herculean problem within the current framework due to the theoretical and practical challenges placed by the expected signals. In addition to tidal and PM modeling issues, XG IFOs are expected to detect eccentric contributions in BNS mergers enhancing systematic differences between different modeling schemes [e.g. 251, 467, 468]. These events are expected from computations of period decay from binary radio pulsar observations [22, 23]. GW data from highly-eccentric BNS mergers can also reveal the signatures of f -mode oscillations of the NS components [469, 470]. Other examples of physical effects that will require an accurate modeling are GW higher-order modes (HOMs) [253, 471] and magnetic fields [457, 472]. Moreover, PE studies with XG detectors will compute the matched-filtered analyses of broad frequency ranges, i.e. from $O(1 \text{ Hz})$ to $\gtrsim 4 \text{ kHz}$, and long segments, i.e. $\gtrsim O(1 \text{ hr})$, demanding the inclusion of frequency-dependent (or time-dependent) antenna pattern functions [e.g. 473, 474, 475]. Another urgent issue posed by high-SNR and long-duration GWs is related to the computational costs of these PE analyses. Parallelization methods are key for PE of BNS signals associated to long data segments $\gtrsim 100 \text{ s}$. The BAJES runs discussed in Chapter 2 were efficiently performed on 128 CPUs with total execution-time of $\sim 1 \text{ day}$. However, the current implementation will not be sufficient to perform XG PE studies within comparable timescales due to the larger number of computations. Nevertheless, for increasing SNRs, the gained information grows proportionally narrowing the posterior PDF. Then, the sampler must minutely explore the parameter space, requiring longer convergence times and demanding the employment of efficient proposal methods [e.g. 476]. Moreover, in a full MM approach, the analysis includes also EM counterparts and EOS parameterization, which can considerably increase the computational costs. In order to overcome these limitations, XG EOS inferences might be confronted with improved parallel methods for sampling algorithms [e.g. 158, 206, 476] and acceleration techniques for the likelihood evaluations [e.g. 203, 235, 477, 478].

Outlook. In summary, Figure 3 shows the current astrophysical MM framework for EOS inference. The low-density region, i.e. $\rho \lesssim \rho_{\text{sat}}$, can be constrained by hadrons and heavy ions collisions [e.g. 102, 103, 370, 371]. The observations of pulsars with radio and X-rays impose bounds on the mass-radius sequence through the measurement of NS masses and radii. Inspiralling BNSs, such as GW170817, can provide constraints at the densities of the progenitors, labeled as intermediate densities, i.e. $\rho_{\text{sat}} \lesssim \rho \lesssim 3\rho_{\text{sat}}$. Generic binary systems with at least a NS component can also deliver similar information [e.g. 153, 479, 480]. On the other hand, BNS PM GWs carry information

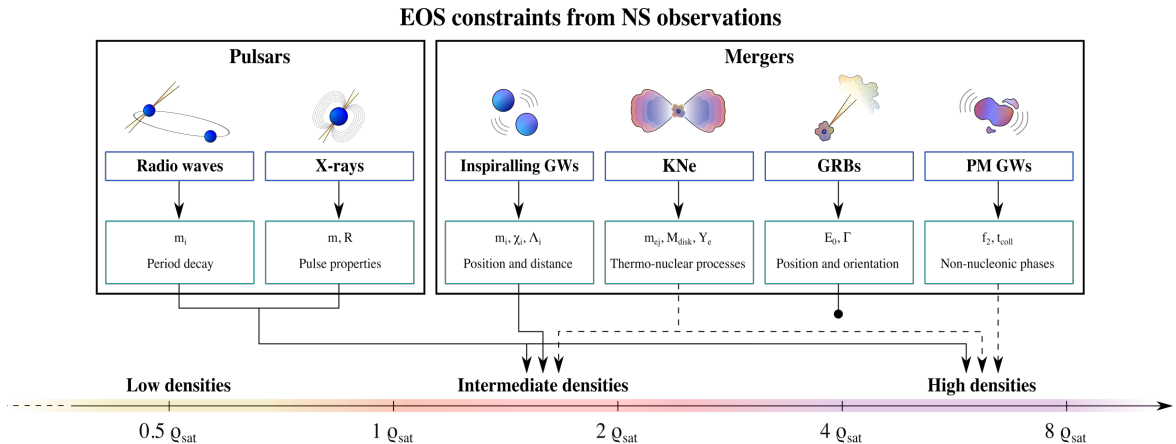


FIGURE 3: Design and information channels of the current MM framework for EOS inference with astronomical NS observations. Each black box encloses a different source. Dark blue boxes report the observable signals and light blue boxes show the information that can be extracted from each source. The horizontal axis reports the densities of the associated EOS constraints. Dashed lines indicates that the connection between the measured parameters and the EOS properties relies on NR-inform methods.

on the NS remnant’s densities, reported as high densities, i.e. $\rho \gtrsim 3\rho_{\text{sat}}$. The KN observations provide information over a broad range: dynamical ejecta can constrain the intermediate densities and disk’s properties inform the estimate of maximum NS mass [481]. GRB parameters are not currently connected to EOS properties. In this context, we can also include possible sources that might be observed in the future, such as core-collapsing SNe that inform us on the NS formation [e.g. 482, 483, 484], and continuous GWs from isolated NSs that provide information on the inertia tensor of the source NSs [e.g. 485, 486, 487]. The inclusion of all available information is key in order to cover a broad range of densities.

We are currently planning the development of a full MM infrastructure in BAJES, in order to perform coherent joint analysis of MM data taking into account full correlations of parameters space. Moreover, we plan to include a TOV solver for EOS-parameterized inference, permitting more accurate explorations of the parameters space compared to finite-sized EOS priors. Other ongoing developments are the ROQ approximation for full-spectrum BNS GWs, a combined multi-threading–MPI parallelization scheme, and methods for XG detectors, such as time-dependent antenna patterns [488]. The availability of a comprehensive Bayesian MM pipeline will also permit validation studies of current methods and models with consistent injection-recovery PEs, that are currently absent in literature.

Appendix A

Sampling methods

A motivation for the employment of sampling methods in the estimation of targeted PDFs can be extracted from Ref. [183, 489] using simple scaling arguments. For an arbitrary function f defined on a N -dimensional support, its integral can be computed resorting to a numerical grid approximation. However, for large N , the computational cost grows as L^N , where L is the characteristic size of the parameter space, e.g. the number of grid points. Nonetheless, the accuracy of the estimation depends on the chosen grid-step. On the other hand, the standard random-walk strategies implemented in sampling algorithms behave similarly to thermalization processes, with typical costs proportional to N^2 . Moreover, in the context of statistical DA, the errors associated to sampling estimates depend only on the variance of the targeted PDF and are independent from N . These properties make sampling methods optimal tools to explore multi-dimensional parameters spaces.

In this Appendix, we discuss the main sampling methods employed in this work. We introduce the MCMC methods in Section A.1 and the nested sampling algorithm [185, 196, 197, 198, 199] in Section A.2.

A.1 Markov-chain Monte Carlo

A generic MCMC algorithm is a random iterative process that explores the parameter space by extracting samples according to a given probability (or potential). The output of this procedure is a set of independent samples representative of the target probability density.

The MCMC routine can be summarized as follows. A chain is initialized with a random prior sample, sat θ_0 . This position is evolved and a new sample θ^* is proposed according to predefined proposal methods [e.g. 177, 178, 490, 491, 492, 493, 494, 495,

496]. The new sample $\boldsymbol{\theta}^*$ is accepted with probability

$$\min \left[1, \frac{p(\boldsymbol{\theta}^*|\mathbf{d}, H)}{p(\boldsymbol{\theta}_0|\mathbf{d}, H)} \frac{q(\boldsymbol{\theta}_0|\boldsymbol{\theta}^*)}{q(\boldsymbol{\theta}^*|\boldsymbol{\theta}_0)} \right], \quad (\text{A.1})$$

where $q(\boldsymbol{\theta}_i|\boldsymbol{\theta}_j)$ is the proposal density function computed between $\boldsymbol{\theta}_i$ and $\boldsymbol{\theta}_j$. Note that, according with prescription Eq. (A.1), the probability of the proposed sample is not required to be strictly greater than that of the current sample. If $\boldsymbol{\theta}^*$ is accepted $\boldsymbol{\theta}_1 = \boldsymbol{\theta}^*$; otherwise, $\boldsymbol{\theta}_1 = \boldsymbol{\theta}_0$. This procedure is iterated for $\boldsymbol{\theta}_1$ and generally for $\boldsymbol{\theta}_i$, collecting a chain of samples. In modern MCMC implementations [e.g. 170, 200], the algorithms typically employ multiple simultaneous chains, in order to improve the exploration of the parameters space and the correlations between the samples. The algorithm eventually converges to the target PDF after a certain amount of iterations, labeled as *burn-in*, that depends on the complexity of the parameters space and on the sampling settings. After this time, the routine starts the collection of independent posterior samples. Given a set of posterior samples, it is possible to estimate the evidence using the approximation

$$p(\mathbf{d}|H) \approx \frac{1}{n_{\text{samples}}} \sum_{i=1}^{n_{\text{samples}}} p(\boldsymbol{\theta}_i|\mathbf{d}, H), \quad (\text{A.2})$$

where the index $i = 1, \dots, n_{\text{samples}}$ runs over the posterior samples.

The MCMC algorithm disposes of a light-weighted and versatile settings. However, for non-trivial PDFs, (e.g. large number of degrees of freedom and prominent multimodalities), these methods could present issues, such as inaccurate exploration of the parameter space. These issues can be mitigated resorting to a large number of parallel chains or to problem-specific proposal methods. Another issue of MCMC techniques is related to Eq. (A.2). This approximation carries non-negligible uncertainties that prevent an accurate estimation of the evidence.

On the other hand, PTMCMC methods [e.g. 193, 194, 195, 200] perform improved exploration of the parameter space and it provides a more accurate estimations of the evidence integral compared to standard MCMC strategies. The main difference with standard MCMC is the introduction of an inverse temperature coefficient $\beta = 1/T \in [0, 1]$ in the computation of posterior PDF, i.e.

$$p_\beta(\boldsymbol{\theta}|\mathbf{d}, H) \propto [p(\mathbf{d}|\boldsymbol{\theta}, H)]^\beta p(\boldsymbol{\theta}|H). \quad (\text{A.3})$$

Each chain is associated with a value of β and the algorithm proceeds as a standard MCMC for every chain using the corresponding tempered posterior Eq. (A.3). For $T = 1$, the tempered posterior is identical to the original one, focusing on the estimation of the likelihood bulge. The contribution of the likelihood function is mitigated by increasing values of T , up to the limit $T \rightarrow \infty$ where the posterior is identical to the prior. The high-temperature chains will be able to freely explore the majority the prior support, inspecting the tails of the targeted posterior distribution and providing a good coverage of the entire prior volume. Moreover, the algorithm proposes swaps between pairs of chains, received with acceptance

$$\min \left[1, \left(\frac{p(\mathbf{d}|\boldsymbol{\theta}_i, H)}{p(\mathbf{d}|\boldsymbol{\theta}_j, H)} \right)^{\beta_j - \beta_i} \right], \quad (\text{A.4})$$

where $\boldsymbol{\theta}_i$ and β_i are respectively the last sample and the inverse temperature of the i -th chain, and analogously for j . The swapping procedure permits to propagate the information of the high-temperature chains to the low-temperature ones and viceversa, improving the correlation between the samples.

Using the auxiliary coefficient β and thermodynamic integration [497], it is possible to write the evidence as

$$\log p(\mathbf{d}|H) = \int_0^1 \log p_\beta(\mathbf{d}|H) d\beta. \quad (\text{A.5})$$

Eq. (A.5) can be estimated through numerical integration. The terms $\log p_\beta(\mathbf{d}|H)$ correspond to the expectation values of $\log p(\mathbf{d}|\boldsymbol{\theta}, H)$ for the different tempered posterior, i.e.

$$\log p_\beta(\mathbf{d}|H) = \int p_\beta(\boldsymbol{\theta}|\mathbf{d}, H) \log p(\mathbf{d}|\boldsymbol{\theta}, H) d\boldsymbol{\theta}. \quad (\text{A.6})$$

For a fixed β , Eq. (A.6) can be estimated applying Eq. (A.2) to the tempered posterior samples. Then, the integral Eq. (A.5) is approximated using the trapezoidal rule integrating over the initial β ladder. The PTMCMC represents an improved version of a standard MCMC technique, that aims to provide much accurate estimations of the evidence. However, the accuracy of the estimation Eq. (A.5) strongly depends on the number of employed temperatures. In complex situations, the total number of chains needed to accurately estimate the evidence could overcome the number of available processes, affecting the efficiency of the sampler [498].

A.2 Nested sampling

The nested sampling [185, 196] is a computational Bayesian method designed to accurately estimate the evidence integral and provide a set of posterior samples. The main advantage of this technique is the reduction of the multidimensional integral Eq. (1.3) to a one-dimensional problem [499, 500], introducing the variable

$$X(\lambda) = \int_{p(\mathbf{d}|\boldsymbol{\theta}, H) > \lambda} p(\boldsymbol{\theta}|H) d\boldsymbol{\theta}. \quad (\text{A.7})$$

The quantity $X(\lambda)$ is usually labeled as *prior mass* and it corresponds to the cumulative prior volume covering all likelihood values greater than λ . The prior mass takes values in the range $[0, 1]$, where $X = 1$ corresponds to the entire prior volume and $X = 0$ corresponds to the maximum likelihood value. Thanks to Eq. (A.7), the likelihood can be written as function of the prior mass, i.e. $p(\mathbf{d}|X(\lambda), H) = \lambda$, from which follows the evidence,

$$p(\mathbf{d}|H) = \int_0^1 p(\mathbf{d}|X, H) dX. \quad (\text{A.8})$$

Eq. (A.8) has a further advantage: by definition, the likelihood $p(\mathbf{d}|X, H)$ is a monotonic decreasing function of X . Accomplishing the transformation $\boldsymbol{\theta} \rightarrow X$ involves dividing the unit prior mass range into small bins and sorting them by likelihood.

In order to accomplish this task, standard nested sampling routines require an input number of live points n_{live} and a real positive number ζ representing the final tolerance of the computation. The live points are samples of the parameter space that are evolved during the routine. Starting from a set of n_{live} initial samples (usually extracted from the prior distribution), the live point with lowest likelihood value, say $\boldsymbol{\theta}_i$, is discarded and replaced with a new point $\boldsymbol{\theta}_i^*$ extracted from the prior distribution that satisfies the relation $p(\mathbf{d}|\boldsymbol{\theta}_i^*, H) > p(\mathbf{d}|\boldsymbol{\theta}_i, H)$. The new point $\boldsymbol{\theta}_i^*$ is usually proposed using internal MCMC routines. The procedure is repeated taking the lowest-likelihood live point at every iteration, such that the algorithm starts inspecting the entire prior volume ($X_0 = 1$), and it moves toward lower values of the prior mass, i.e. $X_0 > \dots > X_i > 0$, up to the the most likely sample(s). The n -th extracted sample can be taken as representative element of the respective isoprobability level of likelihood and, since the algorithm accepts strictly increasing likelihood values, it ensures that each level is nested in the previous one. At the n -th iteration, the evidence is approximated from

Eq. (A.8) using trapezoidal rule,

$$p_n(\mathbf{d}|H) \approx \frac{1}{2} \sum_{k=1}^n (X_{k-1} - X_{k+1}) p(\mathbf{d}|\boldsymbol{\theta}_k, H), \quad (\text{A.9})$$

where k runs over all collected nested samples and X_k is estimated with the expectation value [500], i.e. $X_k \approx e^{-k/n_{\text{live}}}$. Then, we can deduce that the average volume occupied by a live point corresponds to the n_{live} -th part of the current prior mass.

The specific stopping condition depends on the requested sampler. In general, if the algorithm converged to the global maximum-likelihood value $\max[p(\mathbf{d}|\boldsymbol{\theta}, H)]$, at the n -th iteration the evidence is expected to vary at most of

$$\Delta_n \simeq \max [p(\mathbf{d}|\boldsymbol{\theta}, H)] \cdot X_n. \quad (\text{A.10})$$

The general stopping criterion requires that the estimated evidence is not expected to change more than a factor e^ζ , i.e.

$$\zeta \geq \log \left(1 + \frac{\Delta_n}{p_n(\mathbf{d}|H)} \right). \quad (\text{A.11})$$

When the stopping condition is satisfied, the sampler includes the contributions of the remaining live points to the overall evidence. The evidence is computed summing all the likelihood contributions from each nested level weighted on the expected difference in prior mass, according to Eq. (A.9). The posterior PDF can be reconstructed by the chain of nested samples weighting them by their posterior weights [501].

The nested sampling routine offers a much better architecture for evidence estimation than MCMC techniques. In general, the estimated log-evidence carries a statistical uncertainty inversely proportional to n_{live} due to the marginalization over the prior mass. On the other hand, numerical errors are dominated by the use of point estimates and by the length of the MCMC sub-chains n_{MCMC} used to propose new samples, as shown in Ref. [177]. These errors can be mitigated improving the exploration of the parameters space during the MCMC proposal steps. Note that also the estimation of the posterior samples is affected by statistical and numerical uncertainty [219].

Appendix B

Time-domain NRPM model

In this Appendix, we discuss the modeling of the time-domain GW approximant for BNS PM remnants, labeled as NRPM [154]. We employ geometrical units $G = c = 1$ as convention throughout the whole Chapter in order to simplify the notation. We discuss the NRPM modeling in Section B.1 and the NR calibration in Section B.2

B.1 Modeling choices

Our PM model builds on the results of [129, 300, 502] that showed the PM frequency peak correlates with the tidal parameter and generalizing the approach to similar relations for other characteristic frequencies of the spectrum and for the waveform's amplitudes and characteristic times. As mentioned in Chapter 4, nonlinear couplings between proper modes result in new frequencies given by $f_{2\pm 0} = f_2 \pm f_0$. In the case of BNS mergers, the two secondary peaks in the GW spectra can be interpreted as the nonlinear pulsations of the remnant $f_{2\pm 0}$ [385]. In the following sections, we discuss the NRPM modeling of phase (Section B.1.1) and amplitude (Section B.1.2). Finally, in Section B.1.3, we discuss the approximations employed to model PC. Figure B.1 shows an exemplary NRPM template compared to the corresponding NR data.

B.1.1 Phase

We assume the PM GW frequency is composed of the three main characteristic frequencies f_{2-0} , f_2 , f_{2+0} and construct a model for $f(t)$ as follows. The frequency model starts at $t = t_{\text{mrg}} = 0$ with the value of the merger frequency f_{mrg} calibrated on NR data; while, its derivative \dot{f}_{mrg} is estimated from a PN approximation, i.e.

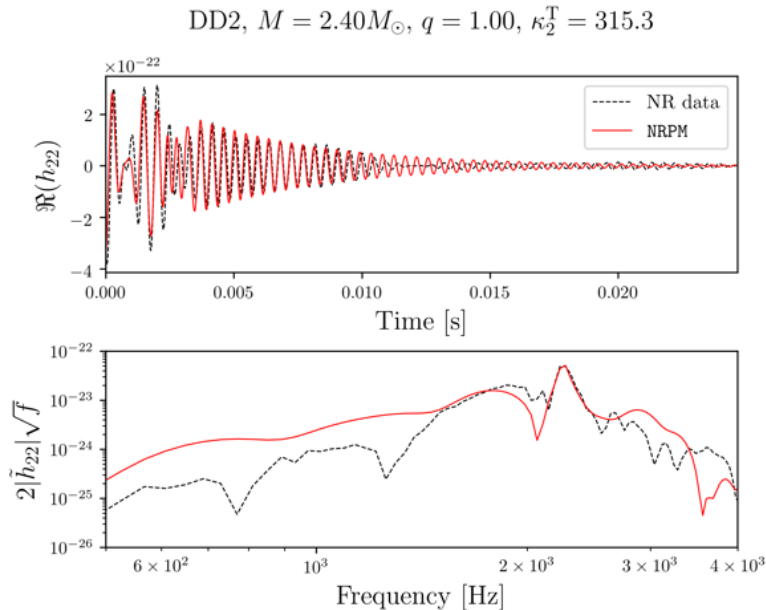


FIGURE B.1: Comparison between an exemplary NRPM template (solid red lines) and the corresponding NR data (dashed black lines). The binary corresponds to an equal-mass non-spinning BNS with $M = 2.4 M_{\odot}$ and DD2 EOS located at 40 Mpc. The unfaithfulness of NRPM model and the NR data corresponds to $\bar{F} \simeq 0.13$ with LIGO design PSD [29]. *Top panel:* Time-domain waveforms. *Bottom panel:* Frequency-domain spectra.

$\dot{f}_{\text{mrg}} = \dot{f}_{\text{PN}}(f = f_{\text{mrg}})$. Subsequently, we construct a piece-wise function for the time-domain frequency imposing

$$f(t_{\text{mrg}}) = f_{\text{mrg}}, \quad (\text{B.1a})$$

$$f(t_0 \leq t \leq t_1) = f_{2-0}, \quad (\text{B.1b})$$

$$f(t_2) = f_{2+0}, \quad (\text{B.1c})$$

$$f(t \geq t_3) = f_2. \quad (\text{B.1d})$$

A cubic interpolant is used to join f_{mrg} to f_{2-0} in the interval $[t_{\text{mrg}}, t_0]$ fixing the values of the function and of the first derivatives at the interval's extrema. The frequency oscillation in the intervals $[t_1, t_2]$ and $[t_2, t_3]$ is modeled with a sine function in such a way that f_{2+0} is a maximum and preserving the continuity and the differentiability of $f(t)$. Note the model can be reduced to a single-frequency one by simply joining f_{mrg} to f_2 at t_0 and omitting $f_{2\pm 0}$.

In order to model linear frequency evolution [379], it is possible to augment the frequency model for $t > t_3$ as $f(t \geq t_3) = f_2 \cdot [1 + \alpha_{\text{PM}}(t - t_3)]$. Moreover, in correspondence of t_0 , it is possible to include an additional phase ϕ_{PM} affects the

phase evolution of NRPM introducing a phase discontinuity. As previously discussed in Chapter 4, these effects are motivated by studies of NR data. Finally, the phase of the waveform is given by integrating the frequency model,

$$\phi(t) = 2\pi \int_0^t f(t') dt' + \phi_0 , \quad (\text{B.2})$$

where ϕ_0 is either arbitrary chosen or fixed by requiring continuity with an inspiral-merger phase.

B.1.2 Amplitude

We assume the PM amplitude has stationary points according to the nodal points (Section 4.2.1) and that it decays exponentially after the third node. A continuous model for $A(t)$ is constructed assuming

$$A(t_{\text{mrg}}) = A_{\text{mrg}} , \quad (\text{B.3a})$$

$$A(t_i) = A_i , \quad (\text{B.3b})$$

$$A(t \geq t_3 + 5) = A_3 \exp[-\beta_{\text{PM}}(t - t_3)] \quad (\text{B.3c})$$

and using sinusoidal functions to connect maxima and minima. The damping term β_{PM} is set as the time scale at which the waveform amplitude is 1/100 of the merger value, i.e. when A falls below the threshold $A(t)/A_{\text{mrg}} = 10^{-2}$. Indicating t_4 such time, one obtains

$$\beta_{\text{PM}} = \frac{\log(100 A_3/A_{\text{mrg}})}{t_4 - t_3} . \quad (\text{B.4})$$

The timescale $1/\beta_{\text{PM}}$ is identified from simulations and has range $\sim[3, 70]$ ms for BNS masses distributed $M \sim [2.5, 3] M_{\odot}$, if no collapse to a BH happens before [133]. However, β_{PM} can be promoted to additional degree of freedom, improving the fitting of the characteristic PM peak. This is also motivated by the relation between the time of collapse and the high-density EOS properties [67, 86, 412] (see Chapter 4).

B.1.3 Prompt collapse

PC could be modeled employing Eq. (2.30) if we dispose of full EOS information. For NRPM, we follow an alternative route, similar to Section 2.4.2. By analyzing the NR data of the CoRe collaboration, we have found that the condition $\kappa_2^{\text{T}} < 80$ can broadly capture PCs [300]. By further combining the estimate with Eq. (2.30) for a sample of

non-rotating NS models, leads to the following criterion for PC [300]

$$\kappa_2^{\text{T}} < \kappa_{\text{thr}}^{\text{T}} = 80 \pm 40 . \quad (\text{B.5})$$

We adopt the above criterion in NRPM, setting $A(t > t_0) = 0$ if this condition is satisfied. In the context of a Bayesian PE, the threshold value can be either prescribed or included in the set of intrinsic parameters.

This assumption is a simplification as the PC threshold is primarily determined by the EOS pressure support at large densities (or the maximum mass). For example, for a EOS sufficiently soft at the PM densities $\rho \gtrsim 3\rho_{\text{sat}}$ and admitting small compactness at inspiral densities ($\rho \sim 2\rho_{\text{sat}}$), Eq. (2.30) might incorrectly predict a NS remnant signal instead of a BH PC [57, 124]. Improvements in the modeling of the PC threshold and the waveform amplitudes for the short-lived cases are crucial to inform PM GW modeling. Currently, the PC models are strongly bounded to the available sample of high-precision NR simulations [57, 123, 124] and the models will improve as more accurate data become available.

B.2 Calibration

NRPM model is characterized by 14 parameters, i.e.

$$\boldsymbol{\theta}_{\text{PM}} = \{t_0, t_1, t_2, t_3, t_4, A_{\text{mrg}}, A_0, A_1, A_2, A_3, f_{\text{mrg}}, f_2, f_{2-0}, f_{2+0}\} . \quad (\text{B.6})$$

These quantities are related to the binary properties using NR information. Moreover, as discussed in Section B.1, NRPM can be augmented with additional parameters, i.e.

$$\boldsymbol{\theta}_{\text{free}} = \{\phi_{\text{PM}}, \beta_{\text{PM}}, \alpha_{\text{PM}}\} . \quad (\text{B.7})$$

This extension of the parameters space is motivated by investigations of NR simulations. Note that the promotion of β_{PM} to free parameter remove the dependency on the EOS-insensitive relation for t_4 .

We use 172 simulations of the CORE collaboration [125, 160]. The CORE database includes data computed with two different NR codes, BAM [503, 504] and THC [110], that simulate microphysics, neutrino transport (with various schemes) and turbulent viscosity. The set of simulations covers the range $q \in [1, 1.5]$ and $\kappa_2^{\text{T}} \in [73, 458]$. The frequency information is extracted from the spectra by identifying the three dominant

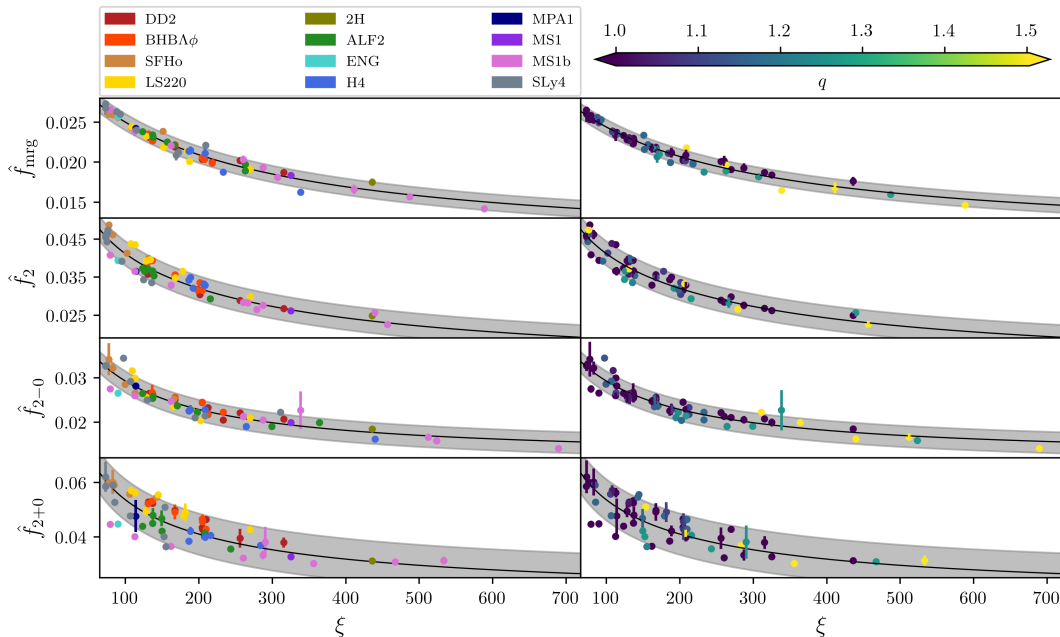


FIGURE B.2: EOS-insensitive relations developed for the characteristic PM frequencies of NRPM, i.e. the merger frequency f_{mrg} , the dominant PM peak f_2 and the subdominant components $f_{2\pm 0}$. The markers show the values extracted from the NR set used for calibration and the associated error-bars are estimated using different grid resolutions (when available). The colors report the different EOSs (left) and mass ratios (right). The predictions of the EOS-insensitive relations is reported with solid black lines and the gray contours correspond to the 90% confidence intervals.

peak frequencies. Amplitudes A_i and the related times t_i are extracted from the time-domain nodal points. Specifically, we construct fit models using the variable

$$\xi = \kappa_2^{\text{T}} + c(1 - 4\nu) , \quad (\text{B.8})$$

where the constant c is also a fitting parameter. The frequency and amplitude at merger A_{mrg} , and the peak frequencies are well described by rational functions in the form

$$Q_{\text{Rational}}(\kappa_2^{\text{T}}, \nu) = F_0 \frac{1 + n_1\xi + n_2\xi^2}{1 + d_1\xi + d_2\xi^2} , \quad (\text{B.9})$$

where $\{F_0, n_1, n_2, d_1, d_2\}$ are the fitting parameters. The amplitudes A_i for $i = 0, 1, 2, 3$ and the times t_i are instead fit by linear polynomials in ξ

$$Q_{\text{Linear}}(\kappa_2^{\text{T}}, \nu) = p_0 + p_1\xi , \quad (\text{B.10})$$

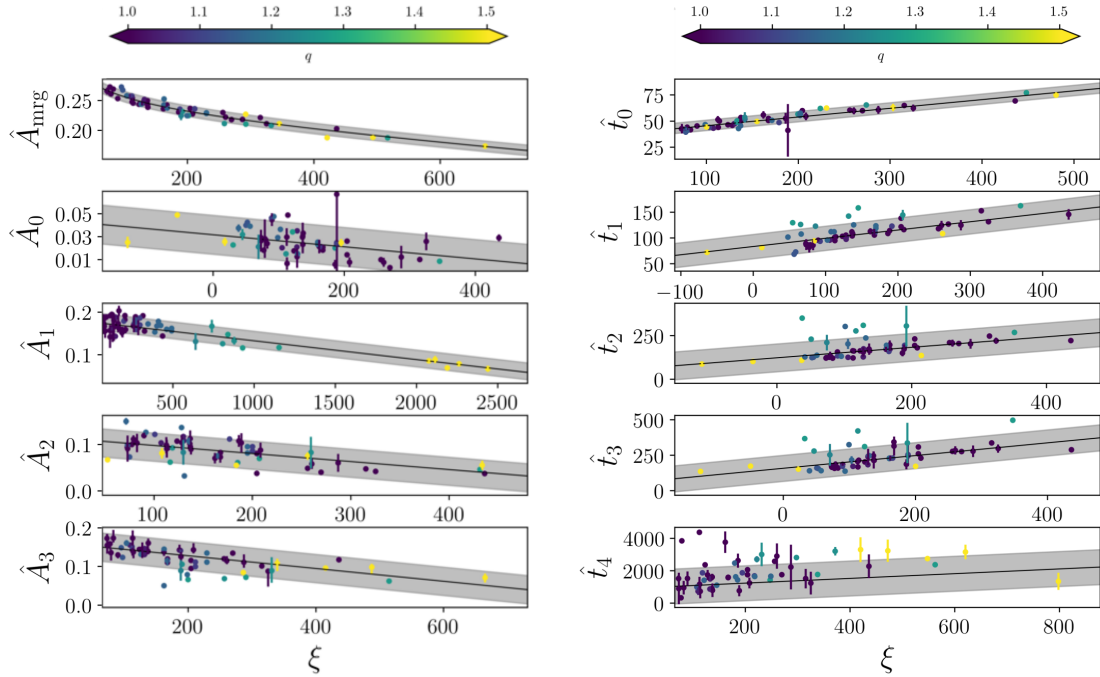


FIGURE B.3: EOS-insensitive relations developed for the characteristic PM amplitudes (left) and times (right) of NRPM. The markers show the values extracted from the NR set used for calibration and the associated error-bars are estimated using different grid resolutions (when available). The colors report the different mass ratios. The predictions of the EOS-insensitive relations is reported with solid black lines and the gray contours correspond to the 90% confidence intervals.

where $\{p_0, p_1\}$ are fitting parameters. The fitting is performed using a least squared method.

Figure B.2 and Figure B.3 show the calibrated relations employed in NRPM. The characteristic frequencies are generally well estimated, with errors from 2% for f_{mrg} to $\sim 10\%$ for $f_{2\pm 0}$ at $1-\sigma$ level. The EOS-insensitive relation for f_2 has an intrinsic error of $\sim 5\%$. The frequency f_{2+0} model is the most uncertain for the available data due to faint contribution in the spectrum. Figure B.3 shows that, while PM amplitude fits are well captured by the model ($\chi^2 \sim 10^{-1}$), the PM times are more uncertain ($\chi^2 > 1$) with the uncertainty growing for larger times. This is expected since the quantities at later times are less correlated with pre-merger parameters and NR data are themselves more uncertain the longer the simulation is.

Appendix C

Frequency-domain NRPM_w model

In this Appendix, we discuss the modeling of the frequency-domain GW approximant for BNS PM remnants, labeled as NRPM_w [383]. We discuss the wavelet components and their combination modeling in Section C.1. We present the NR calibration of the PM properties in Section C.2. Finally, Section C.3 discuss computational costs related to PM approximants. We employ geometrical units $G = c = 1$ as convention throughout the whole Chapter in order to simplify the notation.

C.1 Wavelet components

In order to develop an analytical NR-informed PM model for BNS mergers in the frequency-domain, we first introduce a truncated complex Gaussian wavelet $W(t)$,

$$W(t; \alpha, \beta, \gamma, \tau) = \begin{cases} e^{\alpha t^2 + \beta t + \gamma} & \text{if } t \in [0, \tau] \\ 0 & \text{otherwise} \end{cases} \quad (\text{C.1})$$

where $\alpha, \beta, \gamma \in \mathbb{C}$ are time-independent parameters and the real interval $[0, \tau]$ defines the non-vanishing support of W . The coefficients $\{\alpha, \beta, \gamma\}$ can be interpreted as follows: $\Re(\alpha)$ and $\Re(\beta)$ determine respectively the concavity and the initial slope of the time-domain wavelet amplitude; $\Im(\alpha)$ and $\Im(\beta)$ define respectively the slope and the initial value of the time-domain frequency evolution; γ is an overall factor determining initial amplitude and phase. The wavelet W is the basic component of NRPM_w.

The frequency-domain wavelet $W(f)$ can be analytically computed from Eq. (C.1) using Gaussian integrals,

$$W(f) = \frac{e^\gamma}{2} \sqrt{\frac{\pi}{\alpha}} e^{-z^2} [\operatorname{erfi}(z + \sqrt{\alpha}\tau) - \operatorname{erfi}(z)] , \quad (\text{C.2})$$

where $z(f)$ encodes the frequency dependency,

$$z(f) = \frac{\beta - 2\pi i f}{2\sqrt{\alpha}}, \quad (\text{C.3})$$

and $\text{erfi}(z)$ is the imaginary error function. For $\alpha = 0$, Eq. (C.2) is not defined and it is replaced by a Lorentzian function. Moreover, a direct implementation of Eq. (C.2) can lead to floating point overflow in certain portions of the parameter space. In these cases, we employ the analytical approximations [383]. Furthermore, we introduce a global time-shift τ_0 in order to allow the wavelet to move on the time axis. The time-shift τ_0 changes the wavelet support to $[\tau_0, \tau + \tau_0]$ and it is easily implemented by a unitary factor, i.e. $W(f; \tau_0) = W(f) e^{-2\pi i f \tau_0}$.

In the following paragraphs we describe how different wavelets are combined based on the universal features of the PM signal that are identified by characteristic nodal points. We present the modeling of amplitude and frequency modulations in Section C.1.1. We show the construction of the dominant $\ell = m = 2$ mode in Section C.1.2.

C.1.1 Modulation modeling

Amplitude and frequency modulations are prominent features of the PM spectrum, as discussed in Section 4.1. NR simulations show that the main GW modulations are given in the $m = 0$ channel, and are associated to the quasi-radial density oscillations of the remnant [505]. We associate this mode to the fundamental frequency f_0 and, for the modeling of the (2, 2) mode, we consider only the modulation couplings between f_2 and f_0 . Moreover, we neglect possible frequency evolution of the subdominant mode f_0 , i.e. this frequency component is assumed to be constant in time. Modulation effects appear after the collision of the NR cores, for $t > t_0$, when the remnant is strongly deformed and dynamically unstable.

Amplitude modulations can be easily taken into account by employing a combination of wavelets. Labeling the amplitude-modulated wavelet as \check{W} , we can write

$$\check{W}(t) = W(t) [1 + \Delta_{\text{am}} \sin(\Omega_{\text{am}} t + \phi_{\text{am}})] = W(t) - \frac{i\Delta_{\text{am}}}{2} \sum_{k=\pm 1} k W(t) e^{ik(\Omega_{\text{am}} t + \phi_{\text{am}})}, \quad (\text{C.4})$$

where Δ_{am} defines the magnitude, Ω_{am} the modulation frequency and ϕ_{am} the initial phase of the modulation. Eq. (C.4) can be transformed in the Fourier space obtaining

$$\check{W}(f) = W(f) - \frac{i\Delta_{\text{am}}}{2} \sum_{k=\pm 1} k W^{(k)}(f), \quad (\text{C.5})$$

where

$$W^{(k)}(f) = W(f; \alpha, \beta + ik\Omega_{\text{am}}, \gamma + ik\phi_{\text{am}}, \tau). \quad (\text{C.6})$$

Eq. (C.5) shows explicitly that an amplitude-modulated wavelet \check{W} can be easily written in terms of the Gaussian wavelets W and it introduces two subdominant contributions in the Fourier domain that are displaced with respect to the primary peak of $\pm\Omega_{\text{am}}$.

Frequency modulations affect the phase evolution of the time-domain wavelet. We implement a frequency-modulated wavelet \tilde{W} defining the frequency evolution as

$$\omega_{\tilde{W}}(t) = \omega_W(t) - \Delta_{\text{fm}} e^{-\Gamma_{\text{fm}} t} \sin(\Omega_{\text{fm}} t + \phi_{\text{fm}}), \quad (\text{C.7})$$

where $\omega_{\tilde{W}}$ is the instantaneous frequency of the frequency-modulated wavelet \tilde{W} , ω_W is the instantaneous frequency of the Gaussian wavelet W , and Δ_{fm} , Γ_{fm} , Ω_{fm} , $\phi_{\text{fm}} \in \mathbb{R}$ are the parameters that define the frequency modulations, i.e. Δ_{fm} is the initial frequency displacement, Γ_{fm} the inverse damping time, Ω_{fm} the modulation frequency and ϕ_{fm} the initial phase. As shown in Ref. [383], the frequency-modulated wavelet \tilde{W} can be rewritten in terms of the frequency-domain Gaussian wavelet W using Taylor expansion, i.e.

$$\tilde{W}(f) = e^{iF_0} \sum_{n=0}^{\infty} \left(\frac{\Delta_{\text{fm}}}{2|\beta_{\text{fm}}|^2} \right)^n \frac{w_n(f)}{n!}, \quad (\text{C.8})$$

where

$$w_n(f) = \sum_{k=0}^n \binom{n}{k} (\beta_{\text{fm}}^*)^k (-\beta_{\text{fm}})^{n-k} W(f; \alpha, \beta_{n,k}, \gamma_{n,k}, \tau), \quad (\text{C.9a})$$

$$F_0 = \frac{\Delta_{\text{fm}}}{|\beta_{\text{fm}}|^2} (\Gamma_{\text{fm}} \sin \phi_{\text{fm}} + \Omega_{\text{fm}} \cos \phi_{\text{fm}}), \quad (\text{C.9b})$$

$$\beta_{\text{fm}} = \Gamma_{\text{fm}} + i\Omega_{\text{fm}} \quad (\text{C.9c})$$

$$\beta_{n,k} = \beta - n\Gamma_{\text{fm}} + i(n - 2k)\Omega_{\text{fm}}, \quad (\text{C.9d})$$

$$\gamma_{n,k} = \gamma_{\text{fm}} + i(n - 2k)\phi_{\text{fm}}, \quad (\text{C.9e})$$

and $\{\alpha, \beta, \gamma, \tau\}$ are the parameters of the corresponding non-modulated wavelet. Eq. (C.8) generates several Fourier contributions centered around the frequencies $\mathfrak{S}(\beta) \pm n\Omega$, as expected from these modulations. Note that, differently from the amplitude modulations shown in Eq. (C.4), the frequency modulation contributions presented in Eq. (C.7) includes damped behavior, i.e. $\Gamma_{\text{fm}} \neq 0$ a priori. This term is needed to properly characterize the different time-scales of the PM frequency components f_2 and f_0 .

Combining the definitions of \check{W} in Eq. (C.5), and \tilde{W} in Eq. (C.8), it is possible to write a general modulated Gaussian wavelet, labeled as \widetilde{W} . We consider amplitude modulations over the interval $[t_0, t_3]$ and frequency modulations for $t > t_0$. We fix the modulation frequencies to $\Omega_{\text{am}} = \Omega_{\text{fm}} = 2\pi f_0$. The amplitude modulation magnitude Δ_{am} and phase ϕ_{am} are fixed by the values of the GW amplitudes at the nodal points, i.e. $\{t_i, A_i\}$ for $i = 1, 2, 3$. The frequency-modulation inverse damping time Γ_{fm} is assumed to be identically zero for $t < t_1$; then, it is fixed to a constant positive value calibrated on NR data. Furthermore, NR simulations show that amplitude and frequency modulations approximately fluctuate in opposite directions (see Section 4.2.1); i.e. amplitude maxima occur at frequency minima and viceversa. Then, the frequency modulation phase ϕ_{fm} is fixed in order to satisfy this requirement.

C.1.2 Wavelet combination

The NRPMw model is constructed by describing each part of the PM signal between different nodal points with a modulated wavelet component. The overall strain h_{22} is computed summing all the contributions. Differently from Appendix B, here we do not introduce t_4 and we assume $t_{i+1} - t_i$ to be constant, for $i = 0, 1, 2$. Hence, the nodal points can be reduced to two independent parameters: the moment t_0 of the first amplitude's minimum after merger, and a characteristic time-scale T_0 that is computed as the difference $t_3 - t_1$. The time-scale T_0 defines the subdominant frequency $f_0 \simeq T_0^{-1}$ that characterizes the modulations of the PM signal.

The use of wavelets allow us to assign a clear interpretation of each parameter employed in the model. The combination of different wavelets can capture rather complex signal morphologies. The majority of the physical quantities (times, amplitudes and frequencies) is estimated using quasiuniversal relations calibrated on NR simulations (see Section C.2).

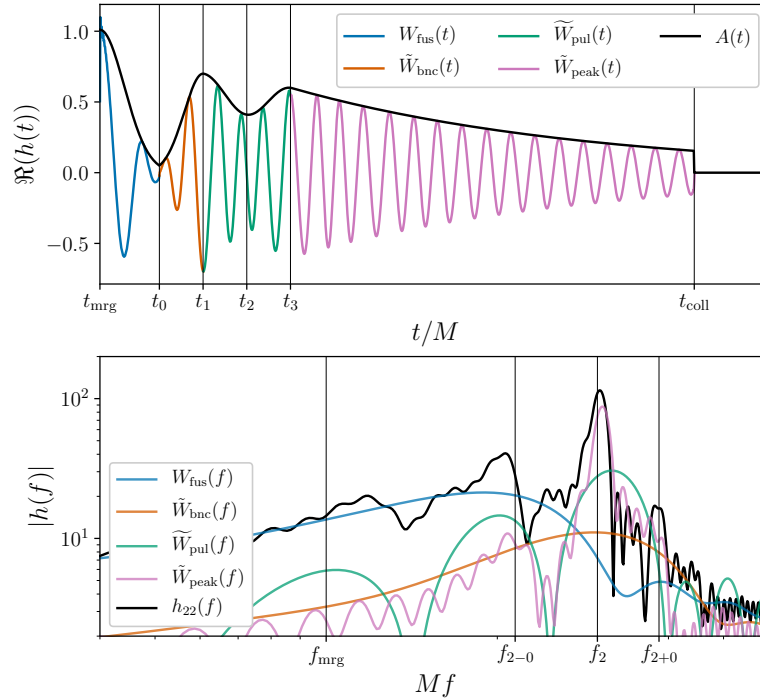


FIGURE C.1: Exemplary case showing the morphology of NRPMw model. Different wavelet components are reported with different colors: W_{fus} in blue, \tilde{W}_{bnc} in orange, \tilde{W}_{pul} in green, and \tilde{W}_{peak} in purple. *Top panel:* The time-domain components and the overall GW amplitude $A(t)$ (black line) and the characteristic times with vertical lines, i.e. the time of the merger t_{mrg} , the nodal points t_i for $i = 0, 1, 2, 3$ and the time of collapse t_{coll} . *Bottom panel:* The Fourier spectra of each component, the overall h_{22} spectrum (black line) and the characteristic PM frequencies (vertical lines), i.e. the merger frequency f_{mrg} , the PM peak f_2 and the subdominant couplings $f_{2\pm 0} = f_2 \pm f_0$.

The time-domain $\ell = m = 2$ mode is modeled employing a combination of four different wavelet components,

$$h(f) \approx W_{\text{fus}}(f) + \tilde{W}_{\text{bnc}}(f) + \tilde{W}_{\text{pul}}(f) + \tilde{W}_{\text{peak}}(f), \quad (\text{C.10})$$

assuming continuity in amplitude and phase (except for a phase-shift ϕ_{PM} , see later) for the time-domain counterpart. The combination of wavelets includes the following terms that are shown in color in Figure C.1:

1. W_{fus} (*fusion*) describes the signal after merger and up to t_0 , corresponding to the fusion of the NS cores. The wavelet has an initial frequency f_{mrg} and non-vanishing frequency drift α_{mrg} calibrated on NR data. The wavelet W_{fus} is written

as

$$W_{\text{fus}}(f) = W(f; \alpha = \frac{\log(A_0/A_{\text{mrg}})}{t_0^2} - i\alpha_{\text{mrg}}, \beta = -2\pi i f_{\text{mrg}}, \gamma = \log A_{\text{mrg}} - i\phi_{\text{mrg}}, \tau = t_0, \tau_0 = 0). \quad (\text{C.11})$$

2. \tilde{W}_{bnc} (*bounce*) describes the signal corresponding to the bounce after the collision of the cores. The phase has a discontinuity ϕ_{PM} at t_0 . Moreover, for $t > t_0$, all wavelets include frequency modulations with the subdominant frequency f_0 . The wavelet \tilde{W}_{bnc} is written as

$$\begin{aligned} \tilde{W}_{\text{bnc}}(f) &= \tilde{W}(f; \alpha = \frac{\log(A_0/A_1)}{(t_1 - t_0)^2}, \beta = \frac{2 \log(A_1/A_0)}{t_1 - t_0} - 2\pi i f_2, \\ &\gamma = \log A_0 - i\phi_{\text{bnc}}, \tau = t_1 - t_0, \tau_0 = t_0 \\ &\Delta_{\text{fm}} = \Delta_{\text{fm}}, \Gamma_{\text{fm}} = 0, \Omega_{\text{fm}} = 2\pi f_0, \phi_{\text{fm}} = \phi_{\text{fm}}), \end{aligned} \quad (\text{C.12})$$

where

$$\phi_{\text{bnc}} = \phi_{\text{mrg}} + \phi_{\text{PM}} + 2\pi f_{\text{mrg}} t_0 + \alpha_{\text{mrg}} t_0^2. \quad (\text{C.13})$$

3. \tilde{W}_{pul} (*pulsating*) describes the emission up to t_3 during which the remnant is typically highly dynamical. This component includes amplitude modulations with the subdominant frequency f_0 that are designed to match the nodal points, i.e. $A(t_i) = A_i$ for $i = 1, 2, 3$. Since the largest amount of the GW luminosity is emitted at times $\lesssim 5$ ms [300], an accurate modeling of the early-PM dynamics is key in order to maximize the faithfulness. The wavelet \tilde{W}_{pul} is written as

$$\begin{aligned} \tilde{W}_{\text{pul}}(f) &= \tilde{W}(f; \alpha = 0, \beta = \frac{\log(A_3/A_1)}{t_3 - t_1} - 2\pi i f_2, \\ &\gamma = \log A_1 - i\phi_{\text{pul}}, \tau = t_3 - t_1, \tau_0 = t_1, \\ &\Delta_{\text{am}} = 1 - \frac{A_2}{\sqrt{A_1 A_3}}, \Omega_{\text{am}} = 2\pi f_0, \phi_{\text{am}} = 0, \\ &\Delta_{\text{fm}} = \Delta_{\text{fm}}, \Gamma_{\text{fm}} = \Gamma_{\text{fm}}, \Omega_{\text{fm}} = 2\pi f_0, \phi_{\text{fm}} = \phi_{\text{fm}}), \end{aligned} \quad (\text{C.14})$$

where

$$\phi_{\text{pul}} = \phi_{\text{bnc}} + 2\pi f_2 (t_1 - t_0). \quad (\text{C.15})$$

4. \tilde{W}_{peak} (*peak*) describes the signal after the luminosity peak. The associated wavelet is modeled as a damped sinusoidal with initial frequency f_2 , damping

time β_{peak} and linear frequency evolution parameterized by the drift α_{peak} . This component characterizes the dominant Fourier peak and it lasts until the time of collapse parameterized by t_{coll} . The wavelet \tilde{W}_{peak} is written as

$$\begin{aligned}\tilde{W}_{\text{peak}}(f) &= \tilde{W}(f; \alpha = -i\alpha_{\text{peak}}, \beta = \beta_{\text{peak}} - 2\pi i f_2, \\ \gamma &= \log A_3 - i\phi_{\text{peak}}, \tau = t_{\text{coll}} - t_3, \tau_0 = t_3 \\ \Delta_{\text{fm}} &= \Delta_{\text{fm}} e^{-\Gamma_{\text{fm}}(t_3 - t_1)}, \Gamma_{\text{fm}} = \Gamma_{\text{fm}}, \\ \Omega_{\text{fm}} &= 2\pi f_0, \phi_{\text{fm}} = \phi_{\text{fm}}),\end{aligned}\tag{C.16}$$

where

$$\phi_{\text{peak}} = \phi_{\text{pul}} + 2\pi f_2(t_3 - t_1).\tag{C.17}$$

Additionally, the GWs emitted after the BH collapse can be modeled as a fifth term in Eq. (C.10), i.e. W_{coll} . Knowing the properties of the final BH, this component could be modeled with the QNMs of the remnant [126, 506]. However, we set here $W_{\text{coll}} = 0$ since this component is expected to have a mild impact on the NRPMw accuracy for XG sensitivities.

Figure C.1 shows an example of the discussed contributions in time- and frequency-domain, with the different terms appearing in Eq. C.10 shown in different colors. The overall spectrum shows the typical PM patterns: a dominant peak centered around f_2 , a weaker peak at lower frequencies corresponding to the merger dynamics and subdominant peaks due to modulations. The superposition of the wavelet components generates several local minima and maxima in the overall h_{22} spectrum. Moreover, the destructive interference of the wavelets originates a local minimum typically located between f_{mrg} and f_2 . This feature is also generally observed in BNS PM spectra extracted from NR simulations. Moreover, the sharp cut at t_{coll} in time-domain waveform originates the ringing effects observed in the h_{22} spectrum. The further inclusion of W_{coll} will mitigate this effect, yielding to a smoother waveform representation.

C.2 Calibration

The NRPMw model is characterized by 17 parameters, i.e.

$$\begin{aligned}\boldsymbol{\theta}_{\text{PM}} &= \{\phi_{\text{PM}}, \phi_{\text{fm}}, t_0, t_{\text{coll}}, A_{\text{mrg}}, A_0, A_1, A_2, A_3, \\ &f_{\text{mrg}}, f_2, f_0, \Delta_{\text{fm}}, \Gamma_{\text{fm}}, \beta_{\text{peak}}, \alpha_{\text{mrg}}, \alpha_{\text{peak}}\}.\end{aligned}\tag{C.18}$$

Most of these quantities can be related to the binary properties using NR information. We chose to map only a subset of θ_{PM} and let some other parameters to be determined by the inference or any other minimization procedure with given data. In particular, we map 13 parameters, i.e.

$$\theta_{\text{fit}} = \{A_{\text{mrg}}, A_0, A_1, A_2, A_3, f_{\text{mrg}}, f_2, f_0, t_0, \beta_{\text{peak}}, \alpha_{\text{mrg}}, \Delta_{\text{fm}}, \Gamma_{\text{fm}}\}, \quad (\text{C.19})$$

as functions of the intrinsic BNS parameters, i.e. $\{m_i, \chi_i, \Lambda_i\}$ for $i = 1, 2$. We fix ϕ_{fm} by the modulations as discussed in Section C.1.1, and we leave three additional degrees of freedom, i.e.

$$\theta_{\text{free}} = \{\phi_{\text{PM}}, t_{\text{coll}}, \alpha_{\text{peak}}\}. \quad (\text{C.20})$$

This choice is motivated by the fact that these three parameters cannot be robustly mapped using NR data.

The calibration set of binaries includes the public available non-precessing NR simulations of the CORE [58, 82, 86, 160] and the SACRA [405, 406, 407] databases. The final dataset is composed by 618 simulations and it includes 190 different binary configurations computed with three independent NR codes and 21 different EOSs, including a hyperons and phase transition to deconfined quark matter at high densities. The intrinsic parameters of the data cover the ranges $M \in [2.4, 3.4] M_{\odot}$, $q \in [1, 2]$, $\kappa_2^{\text{T}} \in [22, 458]$ and $\chi_{\text{eff}} \in [-0.14, +0.22]$. Among the considered dataset, 80 simulations ($\sim 13\%$ of the sample) resulted in PCs and $\sim 40\%$ of the total data is composed by equal-mass non-spinning binaries. The presented quasiuniversal relations extend those in Section C including effects of large mass ratios, i.e. $q > 1.5$, and aligned spins with $|\chi_{\text{eff}}| \lesssim 0.2$.

The mapping between binary and NRPMw parameters is performed on the *mass-rescaled* PM parameters using a factorized fitting function (for any quantity Q),

$$Q^{\text{fit}} = a_0 Q^{\text{M}}(X) Q^{\text{S}}(\hat{S}, X) Q^{\text{T}}(\kappa_2^{\text{T}}, X), \quad (\text{C.21})$$

where $Q^{\text{M}} = 1 + a_1^{\text{M}} X$ includes the mass ratio contributions in terms of the $X = 1 - 4\nu$ parameter; $Q^{\text{S}} = 1 + p_1^{\text{S}} \hat{S}$ takes into account spin corrections in terms of the spin parameter [507]

$$\hat{S} = \left(\frac{m_1}{M}\right)^2 \chi_1 + \left(\frac{m_2}{M}\right)^2 \chi_2, \quad (\text{C.22})$$

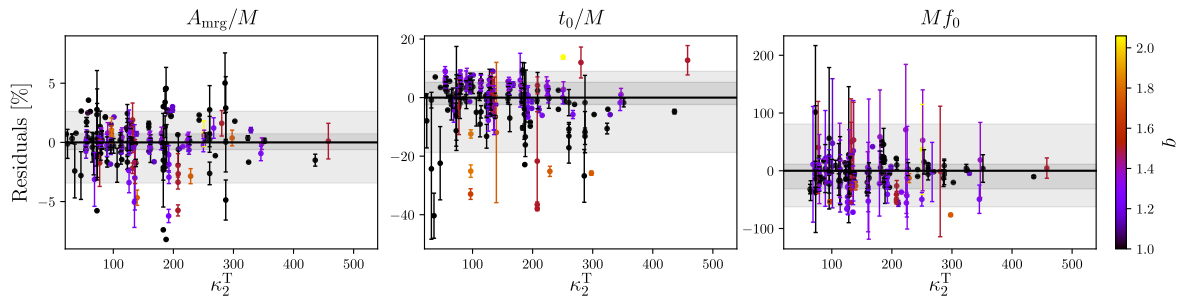


FIGURE C.2: Residuals between NR data and the predictions of the quasiuniversal relations for three exemplary PM parameters, i.e. A_{mrg} (right panel), t_0 (central panel) and f_0 (left) panel. The residuals are reported as functions of the tidal coupling κ_2^{T} and colored according to the mass ratio q . Each marker shows the residual computed with a different BNS configuration, where the circle is the mean value and the error bar reports the maximum and minimum recovered values. The gray band correspond to the 90% (light) and 50% (dark) credibility regions. The plots highlight that the accuracy of the calibrated relations decreases for late-time features.

and $p_1^{\text{S}} = a_1^{\text{S}}(1 + b_1^{\text{S}}X)$. The term

$$Q^{\text{T}} = \frac{1 + p_1^{\text{T}} \kappa_2^{\text{T}} + p_2^{\text{T}} \kappa_2^{\text{T}2}}{1 + p_3^{\text{T}} \kappa_2^{\text{T}} + p_4^{\text{T}} \kappa_2^{\text{T}2}}, \quad (\text{C.23})$$

takes into account tidal effects in terms of κ_2^{T} and with $p_i^{\text{T}} = a_i^{\text{T}}(1 + b_i^{\text{T}}X)$. The coefficients $\{a_i, b_i\}$ are determined fitting the NR data. We note that the choice of the fitting function in Eq. (C.21) might be not unique nor optimal; we have experimented with few functions and found Eq. (C.21) sufficiently simple, general and accurate for our purposes. The choice of a rational function for $Q^{\text{T}}(\kappa_2^{\text{T}})$ is instead motivated by the argumentation of Section 4.2 [129, 151, 153, 154]. We stress the importance of using mass-rescaled quantities in quasiuniversal relations [129, 154]. The fitting is performed using a least squared method.

Figure C.2 shows the residuals for three exemplary PM quantities, i.e. A_{mrg} , t_0 and f_0 . The calibration of the PM peak frequency f_2 has been discussed in Section 4.2.2. Regarding the amplitude A_{mrg} and the frequency at merger f_{mrg} , these properties show similar trends to the ones of Appendix B with errors smaller than 3%. The time t_0 of the first nodal point can be also well captured by the EOS-insensitive relations with errors of $\sim 10\%$. The NR-calibrated relations for the quantities $\{A_{\text{mrg}}, f_{\text{mrg}}, t_0\}$ are constructed to match the BBH values within the nominal error bars for $\kappa_2^{\text{T}} \rightarrow 0$ [507]. The frequency slope α_{mrg} at merger shows uncertainties of $\sim 75\%$ with clear trends in the tidal parameter and in the mass ratio. In particular, large-mass-ratio binaries

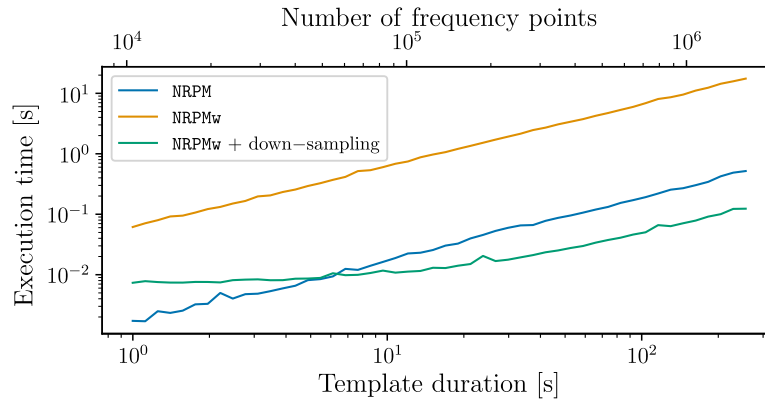


FIGURE C.3: Computational costs for NRPM (blue line) and NRPMw as function of the template duration. For NRPMw, we show the performances without down-sampling (orange line) and with down-sampling (green line). The top axis shows the corresponding number of points in the frequency axis. The templates are computed for an equal-mass BNS remnant with $M = 2.6 M_{\odot}$ and $\tilde{\Lambda} = 492$. The segment is generated with sampling frequency of 16 kHz. We impose an additional lower cutoff at frequency $f_{\min} = 20$ Hz.

(i.e. $q \gtrsim 1.5$) show $\alpha_{\text{mrg}} \lesssim 0$ due to tidal disruption. The subdominant frequency f_0 is computed from the nodal points as T_0^{-1} and it shows errors of $\sim 60\%$. This quantity shows a non-monotonic dependency on the tidal coupling κ_2^{T} for $q \simeq 1$ and it decreases for increasing mass ratio to values an order of magnitude smaller than in the equal-mass case. The PM amplitudes A_i of $i = 1, 2, 3$ have been discussed in Section 4.2.1 and they show errors between 15% and 40%, except for A_0 , which has uncertainties of $\gtrsim 60\%$ since this quantity is comparable in magnitude to NR errors. The damping time β_{peak} of the decaying tail is estimated using the approximation for exponential sinusoidal functions, i.e. $\beta_{\text{peak}} \simeq \max(A(t))/[2 \max(A(f))]$. Despite errors of $\sim 30\%$, the β_{peak} relation predicts a decreasing value for increasing mass ratios, in agreement with the tidally disruptive dynamics of high-mass ratio mergers. The frequency-modulation parameters Δ_{fm} and Γ_{fm} are estimated from the instantaneous NR frequencies and they show errors $> 70\%$.

C.3 Computational costs

Figure C.3 shows the execution times for the computations of NRPM and NRPMw. The costs associated to these models can be easily studied due to their fully analytical forms. As the number of evaluation points grows, the computational times increase

proportionally. However, NRPMw is more expensive than NRPM of ~ 1.5 orders of magnitude due to multiple wavelet evaluations. In practical implementations, we limit the expansion in Eq. (C.8) to $n = 4$ since it provides an accurate representation of the main spectral peaks.

In order to further reduce computational costs of NRPMw, the frequency axis is down-sampled to a constant binning of 10 Hz before the wavelet computations. Once NRPMw is computed over the down-sampled axis, its amplitude and phase are linearly interpolated in order to estimate the model over the initial frequency axis. This reduced frequency binning can be explained by the fact that PM signals are confidently shorter than 100 ms, implying spectral features are broader than the chosen binning. The accuracy of the down-sampling strategy is validated by computing the unfaithfulness between the standard NRPMw and the down-sampled version, recovering $\bar{\mathcal{F}} \lesssim O(10^{-6})$. This implementation significantly improves NRPMw performances. For short-duration templates, i.e. < 10 s, the execution times of the down-sampled NRPMw model show a constant execution time of ~ 10 ms. In this regime, the most expensive contributions are the multiple computations of the wavelets with a weight $\gtrsim 90\%$. Note that this strategy is expected to become inefficient for segments shorter than 62.5 ms. Then, we avoid down-sampling procedures when the template duration is shorter than this threshold. For long-duration templates, i.e. $\gtrsim 10$ s, the computational times are dominated by the costs associated to the linear interpolation with a contribution of $\sim 85\%$ at duration 256 s, i.e. $\sim 2 \times 10^6$ points in the frequency axis. However, the recovered times improve by ~ 2 orders of magnitude over standard NRPMw results and by a factor ~ 6 over NRPM performances.

Bibliography

- [1] LIGO Scientific and Virgo Collaboration. <https://www.gw-openscience.org>. Gravitational-Wave Open Science Center.
- [2] S. L. Shapiro and S. A. Teukolsky. *Black holes, white dwarfs, and neutron stars : the physics of compact objects*. 1983.
- [3] J. M. Lattimer and M. Prakash. “Neutron Star Observations: Prognosis for Equation of State Constraints”. In: *Phys. Rept.* 442 (2007), pp. 109–165. DOI: 10.1016/j.physrep.2007.02.003. arXiv: astro-ph/0612440.
- [4] J. R. Oppenheimer and G. M. Volkoff. “On Massive neutron cores”. In: *Phys. Rev.* 55 (1939), pp. 374–381. DOI: 10.1103/PhysRev.55.374.
- [5] R. C. Tolman. “Static solutions of Einstein’s field equations for spheres of fluid”. In: *Phys. Rev.* 55 (1939), pp. 364–373.
- [6] J. S. Read et al. “Constraints on a phenomenologically parameterized neutron-star equation of state”. In: *Phys. Rev.* D79 (2009), p. 124032. DOI: 10.1103/PhysRevD.79.124032. arXiv: 0812.2163 [astro-ph].
- [7] J. M. Lattimer and M. Prakash. “The Equation of State of Hot, Dense Matter and Neutron Stars”. In: *Phys. Rept.* 621 (2016), pp. 127–164. DOI: 10.1016/j.physrep.2015.12.005. arXiv: 1512.07820 [astro-ph.SR].
- [8] D. Logoteta, A. Perego, and I. Bombaci. “Microscopic equation of state of hot nuclear matter for numerical relativity simulations”. In: (Dec. 2020). DOI: 10.1051/0004-6361/202039457. arXiv: 2012.03599 [nucl-th].
- [9] J. M. Lattimer and F. D. Swesty. “A Generalized equation of state for hot, dense matter”. In: *Nucl. Phys.* A535 (1991), pp. 331–376. DOI: 10.1016/0375-9474(91)90452-C.
- [10] S. Typel et al. “Composition and thermodynamics of nuclear matter with light clusters”. In: *Phys. Rev.* C81 (2010), p. 015803. DOI: 10.1103/PhysRevC.81.015803. arXiv: 0908.2344 [nucl-th].

-
- [11] I. Bombaci and D. Logoteta. “Equation of state of dense nuclear matter and neutron star structure from nuclear chiral interactions”. In: *Astron. Astrophys.* 609 (2018), A128. DOI: 10.1051/0004-6361/201731604. arXiv: 1805.11846 [astro-ph.HE].
- [12] P. Haensel, A. Y. Potekhin, and D. G. Yakovlev. *Neutron stars 1: Equation of state and structure*. New York, USA: Springer, 2007.
- [13] W. D. Arnett and R. L. Bowers. “A Microscopic Interpretation of Neutron Star Structure”. In: *Astrophys. J. Suppl. Series* 33 (1977), pp. 415–436.
- [14] B. P. Abbott et al. “GW170817: Measurements of neutron star radii and equation of state”. In: *Phys. Rev. Lett.* 121.16 (2018), p. 161101. DOI: 10.1103/PhysRevLett.121.161101. arXiv: 1805.11581 [gr-qc].
- [15] T. Dietrich et al. “New Constraints on the Supranuclear Equation of State and the Hubble Constant from Nuclear Physics – Multi-Messenger Astronomy”. In: (Feb. 2020). arXiv: 2002.11355 [astro-ph.HE].
- [16] M. Breschi et al. “AT2017gfo: Bayesian inference and model selection of multi-component kilonovae and constraints on the neutron star equation of state”. In: (Jan. 2021). arXiv: 2101.01201 [astro-ph.HE].
- [17] M. Breschi et al. “Constraints on the Maximum Densities of Neutron Stars from Postmerger Gravitational Waves with Third-Generation Observations”. In: *Phys. Rev. Lett.* 128.16 (2022), p. 161102. DOI: 10.1103/PhysRevLett.128.161102. arXiv: 2110.06957 [gr-qc].
- [18] W. Baade and F. Zwicky. “Remarks on Super-Novae and Cosmic Rays”. In: *Phys. Rev.* 46 (1 1934), pp. 76–77. DOI: 10.1103/PhysRev.46.76.2. URL: <https://link.aps.org/doi/10.1103/PhysRev.46.76.2>.
- [19] J. Chadwick. “The Existence of a Neutron”. In: *Proc. Roy. Soc. Lond. A* 136.830 (1932), pp. 692–708. DOI: 10.1098/rspa.1932.0112.
- [20] A. Hewish and S. E. Okoye. “Evidence for an Unusual Source of High Radio Brightness Temperature in the Crab Nebula”. In: *Nature* 207.4992 (July 1965), pp. 59–60. DOI: 10.1038/207059a0.
- [21] S. J. Bell Burnell. “Little Green Men, White Dwarfs or Pulsars?” In: *Cosmic Search* 1.1 (Jan. 1979), p. 16.
- [22] R. Hulse and J. Taylor. “Discovery of a pulsar in a binary system”. In: *Astrophys. J.* 195 (1975), pp. L51–L53. DOI: 10.1086/181708.

- [23] J. Weisberg, D. Nice, and J. Taylor. “Timing Measurements of the Relativistic Binary Pulsar PSR B1913+16”. In: *Astrophys.J.* 722 (2010), pp. 1030–1034. DOI: 10.1088/0004-637X/722/2/1030. arXiv: 1011.0718 [astro-ph.GA].
- [24] M. Kramer et al. “Tests of general relativity from timing the double pulsar”. In: *Science* 314 (2006), pp. 97–102. DOI: 10.1126/science.1132305. arXiv: astro-ph/0609417 [astro-ph].
- [25] A. Noutsos et al. “Understanding and improving the timing of PSR J0737–3039B”. In: *Astron. Astrophys.* 643 (2020), A143. DOI: 10.1051/0004-6361/202038566. arXiv: 2011.02357 [astro-ph.HE].
- [26] J. Weber. “Detection and Generation of Gravitational Waves”. In: *Phys. Rev.* 117 (1 1960), pp. 306–313. DOI: 10.1103/PhysRev.117.306. URL: <https://link.aps.org/doi/10.1103/PhysRev.117.306>.
- [27] J. Weber. “Gravitational-Wave-Detector Events”. In: *Phys. Rev. Lett.* 20 (23 1968), pp. 1307–1308. DOI: 10.1103/PhysRevLett.20.1307. URL: <https://link.aps.org/doi/10.1103/PhysRevLett.20.1307>.
- [28] J. Weber. “Observation of the Thermal Fluctuations of a Gravitational-Wave Detector”. In: *Phys. Rev. Lett.* 17 (24 1966), pp. 1228–1230. DOI: 10.1103/PhysRevLett.17.1228. URL: <https://link.aps.org/doi/10.1103/PhysRevLett.17.1228>.
- [29] B. Abbott et al. “Prospects for Observing and Localizing Gravitational-Wave Transients with Advanced LIGO, Advanced Virgo and KAGRA”. In: *Living Rev. Rel.* 21.1 (2018), p. 3. DOI: 10.1007/s41114-018-0012-9. arXiv: 1304.0670 [gr-qc].
- [30] J. Aasi et al. “Advanced LIGO”. In: *Class. Quant. Grav.* 32 (2015), p. 074001. DOI: 10.1088/0264-9381/32/7/074001. arXiv: 1411.4547 [gr-qc].
- [31] F. Acernese et al. “Advanced Virgo: a second-generation interferometric gravitational wave detector”. In: *Class. Quant. Grav.* 32.2 (2015), p. 024001. DOI: 10.1088/0264-9381/32/2/024001. arXiv: 1408.3978 [gr-qc].
- [32] A. Einstein. “Zur Allgemeinen Relativitätstheorie”. In: *Sitzungsber. Preuss. Akad. Wiss. Berlin (Math. Phys.)* 1915 (1915). [Addendum: *Sitzungsber. Preuss. Akad. Wiss. Berlin (Math. Phys.)* 1915, 799–801 (1915)], pp. 778–786.
- [33] A. Einstein. “Über Gravitationswellen”. In: *Sitzungsber. Preuss. Akad. Wiss. Berlin (Math. Phys.)* 1918 (1918), pp. 154–167.

- [34] B. P. Abbott et al. “Observation of Gravitational Waves from a Binary Black Hole Merger”. In: *Phys. Rev. Lett.* 116.6 (2016), p. 061102. DOI: 10.1103/PhysRevLett.116.061102. arXiv: 1602.03837 [gr-qc].
- [35] B. P. Abbott et al. “The Rate of Binary Black Hole Mergers Inferred from Advanced LIGO Observations Surrounding GW150914”. In: *Astrophys. J.* 833.1 (2016), p. L1. DOI: 10.3847/2041-8205/833/1/L1. arXiv: 1602.03842 [astro-ph.HE].
- [36] B. P. Abbott et al. “Astrophysical Implications of the Binary Black-Hole Merger GW150914”. In: *Astrophys. J.* 818.2 (2016), p. L22. DOI: 10.3847/2041-8205/818/2/L22. arXiv: 1602.03846 [astro-ph.HE].
- [37] B. P. Abbott et al. “Tests of general relativity with GW150914”. In: *Phys. Rev. Lett.* 116.22 (2016). [Erratum: *Phys. Rev. Lett.* 121,no.12,129902(2018)], p. 221101. DOI: 10.1103/PhysRevLett.116.221101, 10.1103/PhysRevLett.121.129902. arXiv: 1602.03841 [gr-qc].
- [38] M. Breschi et al. “Inspirational-Merger-Ringdown Consistency Tests with Higher Modes on Gravitational Signals from the Second Observing Run of LIGO and Virgo”. In: (2019). arXiv: 1903.05982 [gr-qc].
- [39] B. P. Abbott et al. “GW170817: Observation of Gravitational Waves from a Binary Neutron Star Inspiral”. In: *Phys. Rev. Lett.* 119.16 (2017), p. 161101. DOI: 10.1103/PhysRevLett.119.161101. arXiv: 1710.05832 [gr-qc].
- [40] B. P. Abbott et al. “Properties of the binary neutron star merger GW170817”. In: *Phys. Rev.* X9.1 (2019), p. 011001. DOI: 10.1103/PhysRevX.9.011001. arXiv: 1805.11579 [gr-qc].
- [41] T. Damour, B. R. Iyer, and B. Sathyaprakash. “Frequency domain P approximant filters for time truncated inspiral gravitational wave signals from compact binaries”. In: *Phys.Rev.* D62 (2000), p. 084036. DOI: 10.1103/PhysRevD.62.084036. arXiv: gr-qc/0001023 [gr-qc].
- [42] V. Savchenko et al. “INTEGRAL Detection of the First Prompt Gamma-Ray Signal Coincident with the Gravitational-wave Event GW170817”. In: *Astrophys. J.* 848.2 (2017), p. L15. DOI: 10.3847/2041-8213/aa8f94. arXiv: 1710.05449 [astro-ph.HE].

- [43] M. Ajello et al. “Fermi-LAT Observations of High-Energy γ -Ray Emission Toward the Galactic Center”. In: *Astrophys. J.* 819.1 (2016), p. 44. DOI: 10.3847/0004-637X/819/1/44. arXiv: 1511.02938 [astro-ph.HE].
- [44] B. P. Abbott et al. “Gravitational Waves and Gamma-Rays from a Binary Neutron Star Merger: GW170817 and GRB 170817A”. In: *Astrophys. J.* 848.2 (2017), p. L13. DOI: 10.3847/2041-8213/aa920c. arXiv: 1710.05834 [astro-ph.HE].
- [45] D. A. Coulter et al. “Swope Supernova Survey 2017a (SSS17a), the Optical Counterpart to a Gravitational Wave Source”. In: *Science* (2017). [Science358,1556(2017)]. DOI: 10.1126/science.aap9811. arXiv: 1710.05452 [astro-ph.HE].
- [46] R. Chornock et al. “The Electromagnetic Counterpart of the Binary Neutron Star Merger LIGO/VIRGO GW170817. IV. Detection of Near-infrared Signatures of r-process Nucleosynthesis with Gemini-South”. In: *Astrophys. J.* 848.2 (2017), p. L19. DOI: 10.3847/2041-8213/aa905c. arXiv: 1710.05454 [astro-ph.HE].
- [47] M. Nicholl et al. “The Electromagnetic Counterpart of the Binary Neutron Star Merger LIGO/VIRGO GW170817. III. Optical and UV Spectra of a Blue Kilonova From Fast Polar Ejecta”. In: *Astrophys. J.* 848 (2017), p. L18. DOI: 10.3847/2041-8213/aa9029. arXiv: 1710.05456 [astro-ph.HE].
- [48] P. S. Cowperthwaite et al. “The Electromagnetic Counterpart of the Binary Neutron Star Merger LIGO/Virgo GW170817. II. UV, Optical, and Near-infrared Light Curves and Comparison to Kilonova Models”. In: *Astrophys. J.* 848.2 (2017), p. L17. DOI: 10.3847/2041-8213/aa8fc7. arXiv: 1710.05840 [astro-ph.HE].
- [49] E. Pian et al. “Spectroscopic identification of r-process nucleosynthesis in a double neutron star merger”. In: *Nature* (2017). DOI: 10.1038/nature24298. arXiv: 1710.05858 [astro-ph.HE].
- [50] S. J. Smartt et al. “A kilonova as the electromagnetic counterpart to a gravitational-wave source”. In: *Nature* (2017). DOI: 10.1038/nature24303. arXiv: 1710.05841 [astro-ph.HE].
- [51] N. R. Tanvir et al. “The Emergence of a Lanthanide-Rich Kilonova Following the Merger of Two Neutron Stars”. In: *Astrophys. J.* 848 (2017), p. L27. DOI: 10.3847/2041-8213/aa90b6. arXiv: 1710.05455 [astro-ph.HE].

- [52] M. Tanaka et al. “Kilonova from post-merger ejecta as an optical and near-infrared counterpart of GW170817”. In: *Publ. Astron. Soc. Jap.* (2017). DOI: 10.1093/pasj/psx121. arXiv: 1710.05850 [astro-ph.HE].
- [53] S. Valenti et al. “The discovery of the electromagnetic counterpart of GW170817: kilonova AT 2017gfo/DLT17ck”. In: *Astrophys. J.* 848.2 (2017), p. L24. DOI: 10.3847/2041-8213/aa8edf. arXiv: 1710.05854 [astro-ph.HE].
- [54] M. Nynka et al. “Fading of the X-Ray Afterglow of Neutron Star Merger GW170817/GRB 170817A at 260 Days”. In: *Astrophys. J. Lett.* 862.2 (2018), p. L19. DOI: 10.3847/2041-8213/aad32d. arXiv: 1805.04093 [astro-ph.HE].
- [55] A. Hajela et al. “Two Years of Nonthermal Emission from the Binary Neutron Star Merger GW170817: Rapid Fading of the Jet Afterglow and First Constraints on the Kilonova Fastest Ejecta”. In: *Astrophys. J. Lett.* 886.1 (2019), p. L17. DOI: 10.3847/2041-8213/ab5226. arXiv: 1909.06393 [astro-ph.HE].
- [56] B. Abbott et al. “GW190425: Observation of a Compact Binary Coalescence with Total Mass $\sim 3.4M_{\odot}$ ”. In: *Astrophys. J. Lett.* 892 (2020), p. L3. DOI: 10.3847/2041-8213/ab75f5. arXiv: 2001.01761 [astro-ph.HE].
- [57] R. Kashyap et al. “Numerical relativity simulations of prompt collapse mergers: threshold mass and phenomenological constraints on neutron star properties after GW170817”. In: (Nov. 2021). arXiv: 2111.05183 [astro-ph.HE].
- [58] A. Camilletti et al. “Numerical relativity simulations of the neutron star merger GW190425: microphysics and mass ratio effects”. In: (Apr. 2022). arXiv: 2204.05336 [astro-ph.HE].
- [59] J. C. Rastinejad et al. “A Kilonova Following a Long-Duration Gamma-Ray Burst at 350 Mpc”. In: (Apr. 2022). arXiv: 2204.10864 [astro-ph.HE].
- [60] M. C. Miller et al. “PSR J0030+0451 Mass and Radius from *NICER* Data and Implications for the Properties of Neutron Star Matter”. In: *Astrophys. J.* 887.1 (2019), p. L24. DOI: 10.3847/2041-8213/ab50c5. arXiv: 1912.05705 [astro-ph.HE].
- [61] T. E. Riley et al. “A *NICER* View of PSR J0030+0451: Millisecond Pulsar Parameter Estimation”. In: *Astrophys. J.* 887.1 (2019), p. L21. DOI: 10.3847/2041-8213/ab481c. arXiv: 1912.05702 [astro-ph.HE].

- [62] G. Raaijmakers et al. “A *NICER* view of PSR J0030+0451: Implications for the dense matter equation of state”. In: *Astrophys. J. Lett.* 887.1 (2019), p. L22. DOI: 10.3847/2041-8213/ab451a. arXiv: 1912.05703 [astro-ph.HE].
- [63] G. Raaijmakers et al. “Constraints on the Dense Matter Equation of State and Neutron Star Properties from *NICER*’s Mass–Radius Estimate of PSR J0740+6620 and Multimessenger Observations”. In: *Astrophys. J. Lett.* 918.2 (2021), p. L29. DOI: 10.3847/2041-8213/ac089a. arXiv: 2105.06981 [astro-ph.HE].
- [64] T. E. Riley et al. “A *NICER* View of the Massive Pulsar PSR J0740+6620 Informed by Radio Timing and XMM-Newton Spectroscopy”. In: *Astrophys. J. Lett.* 918.2 (2021), p. L27. DOI: 10.3847/2041-8213/ac0a81. arXiv: 2105.06980 [astro-ph.HE].
- [65] M. C. Miller et al. “The Radius of PSR J0740+6620 from *NICER* and XMM-Newton Data”. In: *Astrophys. J. Lett.* 918.2 (2021), p. L28. DOI: 10.3847/2041-8213/ac089b. arXiv: 2105.06979 [astro-ph.HE].
- [66] B. P. Abbott et al. “Multi-messenger Observations of a Binary Neutron Star Merger”. In: *Astrophys. J.* 848.2 (2017), p. L12. DOI: 10.3847/2041-8213/aa91c9. arXiv: 1710.05833 [astro-ph.HE].
- [67] D. Radice et al. “Probing Extreme-Density Matter with Gravitational Wave Observations of Binary Neutron Star Merger Remnants”. In: *Astrophys. J.* 842.2 (2017), p. L10. DOI: 10.3847/2041-8213/aa775f. arXiv: 1612.06429 [astro-ph.HE].
- [68] B. Margalit and B. D. Metzger. “Constraining the Maximum Mass of Neutron Stars From Multi-Messenger Observations of GW170817”. In: *Astrophys. J.* 850.2 (2017), p. L19. DOI: 10.3847/2041-8213/aa991c. arXiv: 1710.05938 [astro-ph.HE].
- [69] A. Bauswein et al. “Neutron-star radius constraints from GW170817 and future detections”. In: *Astrophys. J.* 850.2 (2017), p. L34. DOI: 10.3847/2041-8213/aa9994. arXiv: 1710.06843 [astro-ph.HE].
- [70] D. Radice et al. “GW170817: Joint Constraint on the Neutron Star Equation of State from Multimessenger Observations”. In: *Astrophys. J.* 852.2 (2018), p. L29. DOI: 10.3847/2041-8213/aaa402. arXiv: 1711.03647 [astro-ph.HE].

- [71] T. Dietrich et al. “High-resolution numerical relativity simulations of spinning binary neutron star mergers”. In: *2018 26th Euromicro International Conference on Parallel, Distributed and Network-based Processing (PDP)*. 2018, pp. 682–689. DOI: 10.1109/PDP2018.2018.00113. arXiv: 1803.07965 [gr-qc]. URL: <https://inspirehep.net/record/1663472/files/1803.07965.pdf>.
- [72] B. P. Abbott et al. “Model comparison from LIGO–Virgo data on GW170817’s binary components and consequences for the merger remnant”. In: *Class. Quant. Grav.* 37.4 (2020), p. 045006. DOI: 10.1088/1361-6382/ab5f7c. arXiv: 1908.01012 [gr-qc].
- [73] B. P. Abbott et al. “A gravitational-wave standard siren measurement of the Hubble constant”. In: *Nature* (2017). DOI: 10.1038/nature24471. arXiv: 1710.05835 [astro-ph.CO].
- [74] B. P. Abbott et al. “Tests of General Relativity with GW170817”. In: *Phys. Rev. Lett.* 123.1 (2019), p. 011102. DOI: 10.1103/PhysRevLett.123.011102. arXiv: 1811.00364 [gr-qc].
- [75] S. Hild et al. “Sensitivity Studies for Third-Generation Gravitational Wave Observatories”. In: *Class. Quant. Grav.* 28 (2011), p. 094013. DOI: 10.1088/0264-9381/28/9/094013. arXiv: 1012.0908 [gr-qc].
- [76] S. Hild. “Beyond the Second Generation of Laser-Interferometric Gravitational Wave Observatories”. In: *Class. Quant. Grav.* 29 (2012), p. 124006. DOI: 10.1088/0264-9381/29/12/124006. arXiv: 1111.6277 [gr-qc].
- [77] M. Punturo et al. “The Einstein Telescope: A third-generation gravitational wave observatory”. In: *Class. Quant. Grav.* 27 (2010), p. 194002. DOI: 10.1088/0264-9381/27/19/194002.
- [78] Y. Aso et al. “Interferometer design of the KAGRA gravitational wave detector”. In: *Phys. Rev. D* 88.4 (2013), p. 043007. DOI: 10.1103/PhysRevD.88.043007. arXiv: 1306.6747 [gr-qc].
- [79] N. Singh et al. “Exploring compact binary populations with the Einstein Telescope”. In: (Dec. 2021). arXiv: 2112.04058 [astro-ph.HE].
- [80] F. Douchin and P. Haensel. “A unified equation of state of dense matter and neutron star structure”. In: *Astron. Astrophys.* 380 (2001), pp. 151–167. eprint: astro-ph/0111092.

- [81] J. Kaplan et al. “The Influence of Thermal Pressure on Equilibrium Models of Hypermassive Neutron Star Merger Remnants”. In: *Astrophys. J.* 790 (2014), p. 19. DOI: 10.1088/0004-637X/790/1/19. arXiv: 1306.4034 [astro-ph.HE].
- [82] S. Bernuzzi et al. “Accretion-induced prompt black hole formation in asymmetric neutron star mergers, dynamical ejecta and kilonova signals”. In: *Mon. Not. Roy. Astron. Soc.* (June 2020). DOI: 10.1093/mnras/staa1860. arXiv: 2003.06015 [astro-ph.HE].
- [83] A. Perego, S. Bernuzzi, and D. Radice. “Thermodynamics conditions of matter in neutron star mergers”. In: *Eur. Phys. J. A* 55.8 (2019), p. 124. DOI: 10.1140/epja/i2019-12810-7. arXiv: 1903.07898 [gr-qc].
- [84] I. Bombaci. “Quark matter in compact stars: Astrophysical implications and possible signatures”. In: *Recent developments in theoretical and experimental general relativity, gravitation and relativistic field theories. Proceedings, 11th Marcel Grossmann Meeting, MG11, Berlin, Germany, July 23-29, 2006. Pt. A-C.* 2008, pp. 605–628. DOI: 10.1142/9789812834300_0025. arXiv: 0809.4228 [gr-qc].
- [85] S. Banik, M. Hempel, and D. Bandyopadhyay. “New Hyperon Equations of State for Supernovae and Neutron Stars in Density-dependent Hadron Field Theory”. In: *Astrophys. J. Suppl.* 214.2 (2014), p. 22. DOI: 10.1088/0067-0049/214/2/22. arXiv: 1404.6173 [astro-ph.HE].
- [86] A. Prakash et al. “Signatures of deconfined quark phases in binary neutron star mergers”. In: (June 2021). arXiv: 2106.07885 [astro-ph.HE].
- [87] J. Antoniadis et al. “A Massive Pulsar in a Compact Relativistic Binary”. In: *Science* 340 (2013), p. 6131. DOI: 10.1126/science.1233232. arXiv: 1304.6875 [astro-ph.HE].
- [88] H. T. Cromartie et al. “Relativistic Shapiro delay measurements of an extremely massive millisecond pulsar”. In: *Nat. Astron.* 4.1 (2019), pp. 72–76. DOI: 10.1038/s41550-019-0880-2. arXiv: 1904.06759 [astro-ph.HE].
- [89] M. Hempel et al. “New Equations of State in Simulations of Core-Collapse Supernovae”. In: *Astrophys. J.* 748 (2012), p. 70. DOI: 10.1088/0004-637X/748/1/70. arXiv: 1108.0848 [astro-ph.HE].

- [90] A. W. Steiner, J. M. Lattimer, and E. F. Brown. “The Neutron Star Mass-Radius Relation and the Equation of State of Dense Matter”. In: *Astrophys. J.* 765 (2013), p. L5. DOI: 10.1088/2041-8205/765/1/L5. arXiv: 1205.6871 [nucl-th].
- [91] A. S. Schneider, L. F. Roberts, and C. D. Ott. “Open-source nuclear equation of state framework based on the liquid-drop model with Skyrme interaction”. In: *Phys. Rev. C* 96.6 (2017), p. 065802. DOI: 10.1103/PhysRevC.96.065802. arXiv: 1707.01527 [astro-ph.HE].
- [92] M. Alford et al. “Hybrid stars that masquerade as neutron stars”. In: *Astrophys. J.* 629 (2005), pp. 969–978. DOI: 10.1086/430902. arXiv: nucl-th/0411016.
- [93] L. Engvik et al. “Asymmetric nuclear matter and neutron star properties”. In: *Astrophys. J.* 469 (1996), p. 794. DOI: 10.1086/177827. arXiv: nucl-th/9509016.
- [94] H. Mütter, M. Prakash, and T. L. Ainsworth. “The nuclear symmetry energy in relativistic Brueckner-Hartree-Fock calculations”. In: *Phys. Lett. B* 199 (1987), pp. 469–474. DOI: 10.1016/0370-2693(87)91611-X.
- [95] H. Müller and B. D. Serot. “Relativistic mean field theory and the high density nuclear equation of state”. In: *Nucl. Phys. A* 606 (1996), pp. 508–537. DOI: 10.1016/0375-9474(96)00187-X. arXiv: nucl-th/9603037 [nucl-th].
- [96] B. D. Lackey, M. Nayyar, and B. J. Owen. “Observational constraints on hyperons in neutron stars”. In: *Phys. Rev. D* 73 (2006), p. 024021. DOI: 10.1103/PhysRevD.73.024021. arXiv: astro-ph/0507312.
- [97] J. W. Negele and D. Vautherin. “Neutron star matter at sub-nuclear densities”. In: *Nucl. Phys., A, v. A207, no. 2, pp. 298-320* (Jan. 1973). DOI: 10.1016/0375-9474(73)90349-7. URL: <https://www.osti.gov/biblio/4480535>.
- [98] K. Oyamatsu. “Nuclear shapes in the inner crust of a neutron star”. In: *Nuclear Physics* 561 (1993), pp. 431–452.
- [99] C. P. Lorenz, D. G. Ravenhall, and C. J. Pethick. “Neutron star crusts”. In: *Phys. Rev. Lett.* 70 (4 1993), pp. 379–382. DOI: 10.1103/PhysRevLett.70.379. URL: <https://link.aps.org/doi/10.1103/PhysRevLett.70.379>.
- [100] K. Sumiyoshi, H. Suzuki, and H. Toki. “Influence of the symmetry energy on the birth of neutron stars and supernova neutrinos”. In: *Astron. Astrophys.* 303 (1995), p. 475. arXiv: astro-ph/9506024.

- [101] F. Douchin and P. Haensel. “Inner edge of neutron star crust with SLY effective nucleon-nucleon interactions”. In: *Phys. Lett. B* 485 (2000), pp. 107–114. DOI: 10.1016/S0370-2693(00)00672-9. arXiv: astro-ph/0006135.
- [102] P. Danielewicz, R. Lacey, and W. G. Lynch. “Determination of the equation of state of dense matter”. In: *Science* 298 (2002), pp. 1592–1596. DOI: 10.1126/science.1078070. arXiv: nucl-th/0208016.
- [103] S. Huth et al. “Constraining Neutron-Star Matter with Microscopic and Macroscopic Collisions”. In: *Nature* 606 (2022), pp. 276–280. DOI: 10.1038/s41586-022-04750-w. arXiv: 2107.06229 [nucl-th].
- [104] H. A. Buchdahl. “General Relativistic Fluid Spheres”. In: *Phys. Rev.* 116 (4 1959), pp. 1027–1034. DOI: 10.1103/PhysRev.116.1027. URL: <https://link.aps.org/doi/10.1103/PhysRev.116.1027>.
- [105] B. Brügmann. “Adaptive mesh and geodesically sliced Schwarzschild spacetime in 3+1 dimensions”. In: *Phys. Rev. D* 54 (1996), pp. 7361–7372. DOI: 10.1103/PhysRevD.54.7361. arXiv: gr-qc/9608050.
- [106] M. Campanelli and C. O. Lousto. “Second order gauge invariant gravitational perturbations of a Kerr black hole”. In: *Phys. Rev. D* 59 (1999), p. 124022. DOI: 10.1103/PhysRevD.59.124022. arXiv: gr-qc/9811019.
- [107] M. Shibata. “Fully general relativistic simulation of coalescing binary neutron stars: Preparatory tests”. In: *Phys. Rev. D* 60 (1999), p. 104052. DOI: 10.1103/PhysRevD.60.104052. arXiv: gr-qc/9908027.
- [108] S. Husa. “Numerical relativity with the conformal field equations”. In: *Lect. Notes Phys.* 617 (2003), pp. 159–192. arXiv: gr-qc/0204057 [gr-qc].
- [109] S. Bernuzzi. “Numerical simulations of relativistic star oscillations: Gravitational waveforms from perturbative and 3-dimensional codes”. PhD thesis. Parma U., 2009. URL: <http://inspirehep.net/record/1635979/files/fulltext.pdf>.
- [110] D. Radice and L. Rezzolla. “THC: a new high-order finite-difference high-resolution shock-capturing code for special-relativistic hydrodynamics”. In: *Astron. Astrophys.* 547 (2012), A26. DOI: 10.1051/0004-6361/201219735. arXiv: 1206.6502 [astro-ph.IM].

- [111] B. Daszuta et al. “GR-Athena++: Puncture Evolutions on Vertex-centered Oct-tree Adaptive Mesh Refinement”. In: *Astrophys. J. Supp.* 257.2 (2021), p. 25. DOI: 10.3847/1538-4365/ac157b. arXiv: 2101.08289 [gr-qc].
- [112] T. Damour, P. Jaranowski, and G. Schafer. “On the determination of the last stable orbit for circular general relativistic binaries at the third postNewtonian approximation”. In: *Phys. Rev. D* 62 (2000), p. 084011. DOI: 10.1103/PhysRevD.62.084011. arXiv: gr-qc/0005034 [gr-qc].
- [113] T. Damour, A. Gopakumar, and B. R. Iyer. “Phasing of gravitational waves from inspiralling eccentric binaries”. In: *Phys. Rev. D* 70 (2004), p. 064028. DOI: 10.1103/PhysRevD.70.064028. arXiv: gr-qc/0404128 [gr-qc].
- [114] T. Damour and A. Nagar. “New effective-one-body description of coalescing nonprecessing spinning black-hole binaries”. In: *Phys. Rev. D* 90.4 (2014), p. 044018. DOI: 10.1103/PhysRevD.90.044018. arXiv: 1406.6913 [gr-qc].
- [115] T. Hinderer. “Tidal Love numbers of neutron stars”. In: *Astrophys. J.* 677 (2008), pp. 1216–1220. DOI: 10.1086/533487. arXiv: 0711.2420 [astro-ph].
- [116] T. Damour and A. Nagar. “Effective One Body description of tidal effects in inspiralling compact binaries”. In: *Phys. Rev. D* 81 (2010), p. 084016. DOI: 10.1103/PhysRevD.81.084016. arXiv: 0911.5041 [gr-qc].
- [117] T. Damour, A. Nagar, and L. Villain. “Measurability of the tidal polarizability of neutron stars in late-inspiral gravitational-wave signals”. In: *Phys. Rev. D* 85 (2012), p. 123007. DOI: 10.1103/PhysRevD.85.123007. arXiv: 1203.4352 [gr-qc].
- [118] T. Dietrich et al. “Gravitational waves and mass ejecta from binary neutron star mergers: Effect of the mass-ratio”. In: *Phys. Rev. D* 95.2 (2017), p. 024029. DOI: 10.1103/PhysRevD.95.024029. arXiv: 1607.06636 [gr-qc].
- [119] D. Radice et al. “Dynamical Mass Ejection from Binary Neutron Star Mergers”. In: *Mon. Not. Roy. Astron. Soc.* 460.3 (2016), pp. 3255–3271. DOI: 10.1093/mnras/stw1227. arXiv: 1601.02426 [astro-ph.HE].
- [120] D. Radice, S. Bernuzzi, and A. Perego. “The Dynamics of Binary Neutron Star Mergers and of GW170817”. In: *Ann. Rev. Nucl. Part. Sci.* 70 (2020). DOI: 10.1146/annurev-nucl-013120-114541. arXiv: 2002.03863 [astro-ph.HE].
- [121] S. Bernuzzi. “Neutron Star Merger Remnants”. In: *Gen. Rel. Grav.* 52.11 (2020), p. 108. DOI: 10.1007/s10714-020-02752-5. arXiv: 2004.06419 [astro-ph.HE].

- [122] M. Agathos et al. “Inferring Prompt Black-Hole Formation in Neutron Star Mergers from Gravitational-Wave Data”. In: *Phys. Rev. D* 101.4 (2020), p. 044006. DOI: 10.1103/PhysRevD.101.044006. arXiv: 1908.05442 [gr-qc].
- [123] A. Bauswein et al. “Equation of state constraints from the threshold binary mass for prompt collapse of neutron star mergers”. In: *Phys. Rev. Lett.* 125.14 (2020), p. 141103. DOI: 10.1103/PhysRevLett.125.141103. arXiv: 2004.00846 [astro-ph.HE].
- [124] A. Perego et al. “Probing the incompressibility of nuclear matter at ultra-high density through the prompt collapse of asymmetric neutron star binaries”. In: (Dec. 2021). arXiv: 2112.05864 [astro-ph.HE].
- [125] D. Radice et al. “Binary Neutron Star Mergers: Mass Ejection, Electromagnetic Counterparts and Nucleosynthesis”. In: *Astrophys. J.* 869.2 (2018), p. 130. DOI: 10.3847/1538-4357/aaf054. arXiv: 1809.11161 [astro-ph.HE].
- [126] E. Berti, V. Cardoso, and A. O. Starinets. “Quasinormal modes of black holes and black branes”. In: *Class. Quant. Grav.* 26 (2009), p. 163001. DOI: 10.1088/0264-9381/26/16/163001. arXiv: 0905.2975 [gr-qc].
- [127] A. Bauswein and N. Stergioulas. “Spectral classification of gravitational-wave emission and equation of state constraints in binary neutron star mergers”. In: *J. Phys. G* 46.11 (2019), p. 113002. DOI: 10.1088/1361-6471/ab2b90. arXiv: 1901.06969 [gr-qc].
- [128] A. Perego, D. Radice, and S. Bernuzzi. “AT2017gfo: An Anisotropic and Three-component Kilonova Counterpart of GW170817”. In: *Astrophys. J.* 850.2 (2017), p. L37. DOI: 10.3847/2041-8213/aa9ab9. arXiv: 1711.03982 [astro-ph.HE].
- [129] S. Bernuzzi, T. Dietrich, and A. Nagar. “Modeling the complete gravitational wave spectrum of neutron star mergers”. In: *Phys. Rev. Lett.* 115 (2015), p. 091101. DOI: 10.1103/PhysRevLett.115.091101. arXiv: 1504.01764 [gr-qc].
- [130] A. Bauswein and N. Stergioulas. “Unified picture of the post-merger dynamics and gravitational wave emission in neutron star mergers”. In: *Phys. Rev. D* 91.12 (2015), p. 124056. DOI: 10.1103/PhysRevD.91.124056. arXiv: 1502.03176 [astro-ph.SR].
- [131] F. Foucart et al. “Monte-Carlo neutrino transport in neutron star merger simulations”. In: *Astrophys. J. Lett.* 902 (2020), p. L27. DOI: 10.3847/2041-8213/abbb87. arXiv: 2008.08089 [astro-ph.HE].

- [132] M. Cusinato et al. “Neutrino emission from binary neutron star mergers: characterizing light curves and mean energies”. In: (Nov. 2021). arXiv: 2111.13005 [astro-ph.HE].
- [133] S. Bernuzzi et al. “How loud are neutron star mergers?” In: *Phys. Rev. D* 94.2 (2016), p. 024023. DOI: 10.1103/PhysRevD.94.024023. arXiv: 1512.06397 [gr-qc].
- [134] W. Kastaun and F. Galeazzi. “Properties of hypermassive neutron stars formed in mergers of spinning binaries”. In: *Phys. Rev. D* 91.6 (2015), p. 064027. DOI: 10.1103/PhysRevD.91.064027. arXiv: 1411.7975 [gr-qc].
- [135] W. Kastaun et al. “Structure of Stable Binary Neutron Star Merger Remnants: Role of Initial Spin”. In: *Phys. Rev. D* 96.4 (2017), p. 043019. DOI: 10.1103/PhysRevD.96.043019. arXiv: 1612.03671 [astro-ph.HE].
- [136] W. Kastaun, R. Ciolfi, and B. Giacomazzo. “Structure of Stable Binary Neutron Star Merger Remnants: a Case Study”. In: *Phys. Rev. D* 94.4 (2016), p. 044060. DOI: 10.1103/PhysRevD.94.044060. arXiv: 1607.02186 [astro-ph.HE].
- [137] A. Perego et al. “Neutrino-driven winds from neutron star merger remnants”. In: *Mon. Not. Roy. Astron. Soc.* 443 (2014), p. 3134. DOI: 10.1093/mnras/stu1352. arXiv: 1405.6730 [astro-ph.HE].
- [138] D. Radice et al. “Viscous-Dynamical Ejecta from Binary Neutron Star Merger”. In: *Astrophys. J. Lett.* 869 (2018), p. L35. DOI: 10.3847/2041-8213/aaf053. arXiv: 1809.11163 [astro-ph.HE].
- [139] V. Nedora et al. “Spiral-wave wind for the blue kilonova”. In: *Astrophys. J.* 886.2 (2019), p. L30. DOI: 10.3847/2041-8213/ab5794. arXiv: 1907.04872 [astro-ph.HE].
- [140] R. Ciolfi. “Collimated outflows from long-lived binary neutron star merger remnants”. In: *Mon. Not. Roy. Astron. Soc.* 495.1 (2020), pp. L66–L70. DOI: 10.1093/mnrasl/slaa062. arXiv: 2001.10241 [astro-ph.HE].
- [141] T. Piran, E. Nakar, and S. Rosswog. “The Electromagnetic Signals of Compact Binary Mergers”. In: *Mon. Not. Roy. Astron. Soc.* 430.3 (2013), pp. 2121–2136. DOI: 10.1093/mnras/stt037. arXiv: 1204.6242 [astro-ph.HE].
- [142] A. Perego et al. “Neutrinos in the Aftermath of Neutron Star Mergers”. In: *JPS Conf. Proc.* 14 (2017), p. 020810. DOI: 10.7566/JPSCP.14.020810.

- [143] J. M. Lattimer and D. N. Schramm. “Black-hole-neutron-star collisions”. In: *Astrophys. J. Letters* 192 (Sept. 1974), pp. L145–L147. DOI: 10.1086/181612.
- [144] D. Kasen et al. “Origin of the heavy elements in binary neutron-star mergers from a gravitational wave event”. In: *Nature* (2017). [Nature551,80(2017)]. DOI: 10.1038/nature24453. arXiv: 1710.05463 [astro-ph.HE].
- [145] S. Rosswog et al. “The first direct double neutron star merger detection: implications for cosmic nucleosynthesis”. In: *Astron. Astrophys.* 615 (2018), A132. DOI: 10.1051/0004-6361/201732117. arXiv: 1710.05445 [astro-ph.HE].
- [146] B. D. Metzger. “Kilonovae”. In: *Living Rev. Rel.* 23.1 (2020), p. 1. DOI: 10.1007/s41114-019-0024-0. arXiv: 1910.01617 [astro-ph.HE].
- [147] K. Kawaguchi, M. Shibata, and M. Tanaka. “Diversity of Kilonova Light Curves”. In: *Astrophys. J.* 889.2, 171 (Feb. 2020), p. 171. DOI: 10.3847/1538-4357/ab61f6. arXiv: 1908.05815 [astro-ph.HE].
- [148] G. P. Lamb, A. J. Levan, and N. R. Tanvir. “GRB170817A as a Refreshed Shock Afterglow Viewed Off-axis”. In: *Astrophys. J.* 899.2 (2020). [Erratum: *Astrophys.J.* 910, 166 (2021)], p. 105. DOI: 10.3847/1538-4357/aba75a. arXiv: 2005.12426 [astro-ph.HE].
- [149] V. Nedora et al. “Dynamical ejecta synchrotron emission as possible contributor to the rebrightening of GRB170817A”. In: *preprint (ArXiv:2104.04537)* (Apr. 2021). arXiv: 2104.04537 [astro-ph.HE].
- [150] A. Hajela et al. “Evidence for X-Ray Emission in Excess to the Jet-afterglow Decay 3.5 yr after the Binary Neutron Star Merger GW 170817: A New Emission Component”. In: *Astrophys. J. Lett.* 927.1 (2022), p. L17. DOI: 10.3847/2041-8213/ac504a. arXiv: 2104.02070 [astro-ph.HE].
- [151] S. Bernuzzi et al. “Quasi-universal properties of neutron star mergers”. In: *Phys.Rev.Lett.* 112 (2014), p. 201101. DOI: 10.1103/PhysRevLett.112.201101. arXiv: 1402.6244 [gr-qc].
- [152] A. Bauswein, N. Stergioulas, and H.-T. Janka. “Revealing the high-density equation of state through binary neutron star mergers”. In: *Phys.Rev.* D90.2 (2014), p. 023002. DOI: 10.1103/PhysRevD.90.023002. arXiv: 1403.5301 [astro-ph.SR].

- [153] F. Zappa et al. “Black-hole remnants from black-hole–neutron-star mergers”. In: *Phys. Rev. Lett.* 123.4 (2019), p. 041102. DOI: 10.1103/PhysRevLett.123.041102. arXiv: 1903.11622 [gr-qc].
- [154] M. Breschi et al. “Kilohertz gravitational waves from binary neutron star remnants: time-domain model and constraints on extreme matter”. In: *Phys. Rev. D* 100.10 (2019), p. 104029. DOI: 10.1103/PhysRevD.100.104029. arXiv: 1908.11418 [gr-qc].
- [155] K. Hotokezaka et al. “The mass ejection from the merger of binary neutron stars”. In: *Phys. Rev. D* 87 (2013), p. 024001. DOI: 10.1103/PhysRevD.87.024001. arXiv: 1212.0905 [astro-ph.HE].
- [156] A. Bauswein, S. Goriely, and H.-T. Janka. “Systematics of dynamical mass ejection, nucleosynthesis, and radioactively powered electromagnetic signals from neutron-star mergers”. In: *Astrophys. J.* 773 (2013), p. 78. DOI: 10.1088/0004-637X/773/1/78. arXiv: 1302.6530 [astro-ph.SR].
- [157] D. Radice et al. “Long-lived Remnants from Binary Neutron Star Mergers”. In: *Mon. Not. Roy. Astron. Soc.* 481.3 (2018), pp. 3670–3682. DOI: 10.1093/mnras/sty2531. arXiv: 1803.10865 [astro-ph.HE].
- [158] M. Breschi, R. Gamba, and S. Bernuzzi. “Bayesian inference of multimessenger astrophysical data: Methods and applications to gravitational waves”. In: *Phys. Rev. D* 104.4 (2021), p. 042001. DOI: 10.1103/PhysRevD.104.042001. arXiv: 2102.00017 [gr-qc].
- [159] M. Breschi et al. <https://github.com/matteobreschi/bajes>. Bayesian Jenaer software.
- [160] T. Dietrich et al. “CoRe database of binary neutron star merger waveforms”. In: *Class. Quant. Grav.* 35.24 (2018), 24LT01. DOI: 10.1088/1361-6382/aaebc0. arXiv: 1806.01625 [gr-qc].
- [161] V. Nedora et al. “Numerical Relativity Simulations of the Neutron Star Merger GW170817: Long-Term Remnant Evolutions, Winds, Remnant Disks, and Nucleosynthesis”. In: *Astrophys. J.* 906.2 (2021), p. 98. DOI: 10.3847/1538-4357/abc9be. arXiv: 2008.04333 [astro-ph.HE].
- [162] T. Bayes. “An essay towards solving a problem in the doctrine of chances”. In: *Phil. Trans. of the Royal Soc. of London* 53 (1763), pp. 370–418.

-
- [163] P. Laplace. *Théorie analytique des probabilités*. Paris: Courcier, 1812. URL: <http://gallica.bnf.fr/ark:/12148/bpt6k88764q>.
- [164] H. Jeffreys. *Theory of Probability*. Third. Oxford, England: Oxford, 1961.
- [165] L. J. Savage. *The Foundations of Statistics*. Wiley Publications in Statistics, 1954.
- [166] M. H. DeGroot. *Optimal statistical decisions*. English. McGraw-Hill New York, 1970, xvi, 489 p. :
- [167] J. O. Berger. *Statistical decision theory and Bayesian analysis; 2nd ed.* Springer series in statistics. New York: Springer, 1985. DOI: 10.1007/978-1-4757-4286-2. URL: <https://cds.cern.ch/record/1327974>.
- [168] C. P. Robert, N. Chopin, and J. Rousseau. “Harold Jeffreys’s Theory of Probability Revisited”. In: *arXiv e-prints*, arXiv:0804.3173 (Apr. 2008), arXiv:0804.3173. arXiv: 0804.3173 [math.ST].
- [169] A. Gelman. “Objections to Bayesian statistics”. In: *Bayesian Anal.* 3.3 (Sept. 2008), pp. 445–449. DOI: 10.1214/08-BA318. URL: <https://doi.org/10.1214/08-BA318>.
- [170] D. Foreman-Mackey et al. “emcee: The MCMC Hammer”. In: *Publications of the Astronomical Society of the Pacific* 125.925 (2013), 306–312. ISSN: 1538-3873. DOI: 10.1086/670067. URL: <http://dx.doi.org/10.1086/670067>.
- [171] A. Gelman et al. *Bayesian Workflow*. 2020. arXiv: 2011.01808 [stat.ME].
- [172] B. P. Abbott et al. “GWTC-1: A Gravitational-Wave Transient Catalog of Compact Binary Mergers Observed by LIGO and Virgo during the First and Second Observing Runs”. In: *Phys. Rev. X* 9.3 (2019), p. 031040. DOI: 10.1103/PhysRevX.9.031040. arXiv: 1811.12907 [astro-ph.HE].
- [173] W. Del Pozzo et al. “Dirichlet Process Gaussian-mixture model: An application to localizing coalescing binary neutron stars with gravitational-wave observations”. In: *Mon. Not. Roy. Astron. Soc.* 479.1 (2018), pp. 601–614. DOI: 10.1093/mnras/sty1485. arXiv: 1801.08009 [astro-ph.IM].
- [174] D. Wang. “Cosmology with Type II Supernovae”. In: *Int. J. Mod. Phys. D* 28.08 (2019), p. 1950106. DOI: 10.1142/S0218271819501062. arXiv: 1804.04845 [astro-ph.CO].

- [175] R. Abbott et al. “GWTC-2: Compact Binary Coalescences Observed by LIGO and Virgo During the First Half of the Third Observing Run”. In: (Oct. 2020). arXiv: 2010.14527 [gr-qc].
- [176] H. J. Hortúa et al. “Parameter estimation for the cosmic microwave background with Bayesian neural networks”. In: *Physical Review D* 102.10 (2020). ISSN: 2470-0029. DOI: 10.1103/physrevd.102.103509. URL: <http://dx.doi.org/10.1103/PhysRevD.102.103509>.
- [177] J. Veitch and A. Vecchio. “Bayesian coherent analysis of in-spiral gravitational wave signals with a detector network”. In: *Phys.Rev.* D81 (2010), p. 062003. DOI: 10.1103/PhysRevD.81.062003. arXiv: 0911.3820 [astro-ph.CO].
- [178] J. Veitch et al. “Parameter estimation for compact binaries with ground-based gravitational-wave observations using the LALInference software library”. In: *Phys. Rev.* D91.4 (2015), p. 042003. DOI: 10.1103/PhysRevD.91.042003. arXiv: 1409.7215 [gr-qc].
- [179] B. P. Abbott et al. “A guide to LIGO–Virgo detector noise and extraction of transient gravitational-wave signals”. In: *Class. Quant. Grav.* 37.5 (2020), p. 055002. DOI: 10.1088/1361-6382/ab685e. arXiv: 1908.11170 [gr-qc].
- [180] T. Dietrich et al. “Multimessenger constraints on the neutron-star equation of state and the Hubble constant”. In: *Science* 370.6523 (2020), pp. 1450–1453. DOI: 10.1126/science.abb4317. arXiv: 2002.11355 [astro-ph.HE].
- [181] R. T. Cox. “Probability, Frequency and Reasonable Expectation”. In: *American Journal of Physics* 14.1 (1946), pp. 1–13. DOI: 10.1119/1.1990764. eprint: <https://doi.org/10.1119/1.1990764>. URL: <https://doi.org/10.1119/1.1990764>.
- [182] E. T. Jaynes. *Probability Theory: The Logic of Science*. Ed. by G. L. Bretthorst. Cambridge University Press, 2003. DOI: 10.1017/CB09780511790423.
- [183] D. J. C. MacKay. *Information Theory, Inference and Learning Algorithms*. USA: Cambridge University Press, 2002. ISBN: 0521642981.
- [184] A. Gelman et al. *Bayesian Data Analysis*. 2nd ed. Chapman and Hall/CRC, 2004.
- [185] D. S. Sivia and J. Skilling. *Data Analysis - A Bayesian Tutorial*. 2nd. Oxford Science Publications. Oxford University Press, 2006.

- [186] P.-A. Mattei. *A Parsimonious Tour of Bayesian Model Uncertainty*. 2020. arXiv: 1902.05539 [stat.ME].
- [187] J. Yao et al. “Quality of Uncertainty Quantification for Bayesian Neural Network Inference”. In: *CoRR* abs/1906.09686 (2019). arXiv: 1906.09686. URL: <http://arxiv.org/abs/1906.09686>.
- [188] R. E. Kass and A. E. Raftery. “Bayes Factors”. In: *Journal of the American Statistical Association* 90.430 (1995), pp. 773–795. DOI: 10.1080/01621459.1995.10476572. eprint: <https://amstat.tandfonline.com/doi/pdf/10.1080/01621459.1995.10476572>. URL: <https://amstat.tandfonline.com/doi/abs/10.1080/01621459.1995.10476572>.
- [189] R. Allison and J. Dunkley. “Comparison of sampling techniques for Bayesian parameter estimation”. In: *Monthly Notices of the Royal Astronomical Society* 437.4 (2013), 3918–3928. ISSN: 1365-2966. DOI: 10.1093/mnras/stt2190. URL: <http://dx.doi.org/10.1093/mnras/stt2190>.
- [190] M. C. Tichy. “Sampling of partially distinguishable bosons and the relation to the multidimensional permanent”. In: *Physical Review A* 91.2 (2015). ISSN: 1094-1622. DOI: 10.1103/physreva.91.022316. URL: <http://dx.doi.org/10.1103/PhysRevA.91.022316>.
- [191] W. J. Handley, M. P. Hobson, and A. N. Lasenby. “polychord: next-generation nested sampling”. In: *Monthly Notices of the Royal Astronomical Society* 453.4 (2015), 4385–4399. ISSN: 1365-2966. DOI: 10.1093/mnras/stv1911. URL: <http://dx.doi.org/10.1093/mnras/stv1911>.
- [192] A. Gelman and D. B. Rubin. “Inference from Iterative Simulation Using Multiple Sequences”. In: *Statist. Sci.* 7.4 (Nov. 1992), pp. 457–472. DOI: 10.1214/ss/1177011136. URL: <https://doi.org/10.1214/ss/1177011136>.
- [193] D. J. Earl and M. W. Deem. “Parallel tempering: Theory, applications, and new perspectives”. In: *Phys. Chem. Chem. Phys.* 7 (23 2005), pp. 3910–3916. DOI: 10.1039/B509983H. URL: <http://dx.doi.org/10.1039/B509983H>.
- [194] R. H. Swendsen and J.-S. Wang. “Replica Monte Carlo Simulation of Spin-Glasses”. In: *Phys. Rev. Lett.* 57 (21 1986), pp. 2607–2609. DOI: 10.1103/PhysRevLett.57.2607. URL: <https://link.aps.org/doi/10.1103/PhysRevLett.57.2607>.

- [195] R. M. Neal. “Sampling from multimodal distributions using tempered transitions”. In: *Statistics and Computing* 6.4 (1996), pp. 353–366. DOI: 10.1007/BF00143556. URL: <https://doi.org/10.1007/BF00143556>.
- [196] J. Skilling. “Nested sampling for general Bayesian computation”. In: *Bayesian Anal.* 1.4 (Dec. 2006), pp. 833–859. DOI: 10.1214/06-BA127. URL: <https://doi.org/10.1214/06-BA127>.
- [197] W. D. Pozzo and J. Veitch. <https://github.com/johnveitch/cpnest>. Parallel nested sampling algorithm in python. DOI: 10.5281/zenodo.835874.
- [198] J. S. Speagle. “dynesty: a dynamic nested sampling package for estimating Bayesian posteriors and evidences”. In: *Monthly Notices of the Royal Astronomical Society* 493.3 (2020), 3132–3158. ISSN: 1365-2966. DOI: 10.1093/mnras/staa278. URL: <http://dx.doi.org/10.1093/mnras/staa278>.
- [199] J. Buchner. “UltraNest - a robust, general purpose Bayesian inference engine”. In: *Journal of Open Source Software* 6.60 (2021), p. 3001. DOI: 10.21105/joss.03001. URL: <https://doi.org/10.21105/joss.03001>.
- [200] W. D. Vousden, W. M. Farr, and I. Mandel. “Dynamic temperature selection for parallel tempering in Markov chain Monte Carlo simulations”. In: *Monthly Notices of the Royal Astronomical Society* 455.2 (2015), 1919–1937. ISSN: 1365-2966. DOI: 10.1093/mnras/stv2422. URL: <http://dx.doi.org/10.1093/mnras/stv2422>.
- [201] V. A. Villar et al. “The Combined Ultraviolet, Optical, and Near-Infrared Light Curves of the Kilonova Associated with the Binary Neutron Star Merger GW170817: Unified Data Set, Analytic Models, and Physical Implications”. In: *Astrophys. J.* 851.1 (2017), p. L21. DOI: 10.3847/2041-8213/aa9c84. arXiv: 1710.11576 [astro-ph.HE].
- [202] S. Vitale et al. “Effect of calibration errors on Bayesian parameter estimation for gravitational wave signals from inspiral binary systems in the Advanced Detectors era”. In: *Phys. Rev. D* 85 (2012), p. 064034. DOI: 10.1103/PhysRevD.85.064034. arXiv: 1111.3044 [gr-qc].
- [203] R. Smith et al. “Fast and accurate inference on gravitational waves from precessing compact binaries”. In: *Phys. Rev. D* 94.4 (2016), p. 044031. DOI: 10.1103/PhysRevD.94.044031. arXiv: 1604.08253 [gr-qc].

- [204] I. Romero-Shaw et al. “Bayesian inference for compact binary coalescences with BILBY: Validation and application to the first LIGO–Virgo gravitational-wave transient catalogue”. In: *Mon. Not. Roy. Astron. Soc.* 499.3 (2020), pp. 3295–3319. DOI: 10.1093/mnras/staa2850. arXiv: 2006.00714 [astro-ph.IM].
- [205] G. Ashton et al. “BILBY: A user-friendly Bayesian inference library for gravitational-wave astronomy”. In: *Astrophys. J. Suppl.* 241.2 (2019), p. 27. DOI: 10.3847/1538-4365/ab06fc. arXiv: 1811.02042 [astro-ph.IM].
- [206] R. J. E. Smith et al. “Massively parallel Bayesian inference for transient gravitational-wave astronomy”. In: *Mon. Not. Roy. Astron. Soc.* 498.3 (2020), pp. 4492–4502. DOI: 10.1093/mnras/staa2483. arXiv: 1909.11873 [gr-qc].
- [207] D. Endres and J. Schindelin. “A new metric for probability distributions”. In: *IEEE Transactions on Information Theory* 49.7 (2003), pp. 1858–1860. DOI: 10.1109/TIT.2003.813506.
- [208] L. Dalcín, R. Paz, and M. Storti. “MPI for Python”. In: *Journal of Parallel and Distributed Computing* 65.9 (2005), pp. 1108–1115. ISSN: 0743-7315. DOI: <https://doi.org/10.1016/j.jpdc.2005.03.010>. URL: <http://www.sciencedirect.com/science/article/pii/S0743731505000560>.
- [209] L. Dalcin et al. “MPI for Python: Performance improvements and MPI-2 extensions”. In: *Journal of Parallel and Distributed Computing* 68.5 (2008), pp. 655–662. ISSN: 0743-7315. DOI: <https://doi.org/10.1016/j.jpdc.2007.09.005>. URL: <http://www.sciencedirect.com/science/article/pii/S0743731507001712>.
- [210] L. D. Dalcin et al. “Parallel distributed computing using Python”. In: *Advances in Water Resources* 34.9 (2011). New Computational Methods and Software Tools, pp. 1124–1139. ISSN: 0309-1708. DOI: <https://doi.org/10.1016/j.advwatres.2011.04.013>. URL: <http://www.sciencedirect.com/science/article/pii/S0309170811000777>.
- [211] A. Patil, D. Huard, and C. J. Fonnesbeck. “PyMC: Bayesian Stochastic Modelling in Python”. In: *Journal of Statistical Software, Articles* 35.4 (2010), pp. 1–81. ISSN: 1548-7660. DOI: 10.18637/jss.v035.i04. URL: <https://www.jstatsoft.org/v035/i04>.

- [212] A. Solonen et al. “Efficient MCMC for Climate Model Parameter Estimation: Parallel Adaptive Chains and Early Rejection”. In: *Bayesian Anal.* 7.3 (Sept. 2012), pp. 715–736. DOI: 10.1214/12-BA724. URL: <https://doi.org/10.1214/12-BA724>.
- [213] J. Li and Y. M. Marzouk. “Adaptive Construction of Surrogates for the Bayesian Solution of Inverse Problems”. In: *SIAM Journal on Scientific Computing* 36.3 (2014), A1163–A1186. ISSN: 1095-7197. DOI: 10.1137/130938189. URL: <http://dx.doi.org/10.1137/130938189>.
- [214] J. Šukys and M. Kattwinkel. *SPUX: Scalable Particle Markov Chain Monte Carlo for uncertainty quantification in stochastic ecological models*. 2017. arXiv: 1711.01410 [stat.CO].
- [215] C. P. Robert et al. *Accelerating MCMC Algorithms*. 2018. arXiv: 1804.02719 [stat.CO].
- [216] M. Morzfeld, X. T. Tong, and Y. M. Marzouk. *Localization for MCMC: sampling high-dimensional posterior distributions with local structure*. 2019. arXiv: 1710.07747 [stat.ME].
- [217] F. Feroz and M. P. Hobson. “Multimodal nested sampling: an efficient and robust alternative to Markov Chain Monte Carlo methods for astronomical data analyses”. In: *Monthly Notices of the Royal Astronomical Society* 384.2 (Jan. 2008), pp. 449–463. ISSN: 0035-8711. DOI: 10.1111/j.1365-2966.2007.12353.x. eprint: <https://academic.oup.com/mnras/article-pdf/384/2/449/3378518/mnras0384-0449.pdf>. URL: <https://doi.org/10.1111/j.1365-2966.2007.12353.x>.
- [218] B. J. Brewer and D. Foreman-Mackey. “DNest4: Diffusive Nested Sampling in C++ and Python”. In: (June 2016). arXiv: 1606.03757 [stat.CO].
- [219] E. Higson et al. “Sampling Errors in Nested Sampling Parameter Estimation”. In: *Bayesian Analysis* 13.3 (2018), 873–896. ISSN: 1936-0975. DOI: 10.1214/17-ba1075. URL: <http://dx.doi.org/10.1214/17-BA1075>.
- [220] B. P. Abbott et al. “Search for Post-merger Gravitational Waves from the Remnant of the Binary Neutron Star Merger GW170817”. In: *Astrophys. J.* 851.1 (2017), p. L16. DOI: 10.3847/2041-8213/aa9a35. arXiv: 1710.09320 [astro-ph.HE].

- [221] B. P. Abbott et al. “Search for gravitational waves from a long-lived remnant of the binary neutron star merger GW170817”. In: (2018). DOI: 10.3847/1538-4357/ab0f3d. arXiv: 1810.02581 [gr-qc].
- [222] M. Maggiore. *Gravitational Waves. Vol. 1: Theory and Experiments*. Oxford Master Series in Physics. Oxford University Press, 2007. ISBN: 9780198570745, 9780198520740. URL: <http://www.oup.com/uk/catalogue/?ci=9780198570745>.
- [223] K. S. Thorne. “Multipole Expansions of Gravitational Radiation”. In: *Rev. Mod. Phys.* 52 (1980), pp. 299–339.
- [224] T. Damour. “Gravitational radiation and the motion of compact bodies”. In: *Gravitational Radiation*. Ed. by N. Deruelle and T. Piran. North-Holland, Amsterdam, 1983, pp. 59–144.
- [225] T. Damour and N. Deruelle. “General relativistic celestial mechanics of binary systems. II. The post-Newtonian timing formula.” In: *Ann. Inst. Henri Poincaré Phys. Théor* 44.3 (Jan. 1986), pp. 263–292.
- [226] E. E. Flanagan and T. Hinderer. “Constraining neutron star tidal Love numbers with gravitational wave detectors”. In: *Phys.Rev.* D77 (2008), p. 021502. DOI: 10.1103/PhysRevD.77.021502. arXiv: 0709.1915 [astro-ph].
- [227] T. Damour and A. Nagar. “The Effective One Body description of the Two-Body problem”. In: *Fundam. Theor. Phys.* 162 (2011), pp. 211–252. DOI: 10.1007/978-90-481-3015-3_7. arXiv: 0906.1769 [gr-qc].
- [228] T. Damour, P. Jaranowski, and G. Schäfer. “Fourth post-Newtonian effective one-body dynamics”. In: *Phys. Rev.* D91.8 (2015), p. 084024. DOI: 10.1103/PhysRevD.91.084024. arXiv: 1502.07245 [gr-qc].
- [229] S. Bernuzzi, M. Thierfelder, and B. Brügmann. “Accuracy of numerical relativity waveforms from binary neutron star mergers and their comparison with post-Newtonian waveforms”. In: *Phys.Rev.* D85 (2012), p. 104030. DOI: 10.1103/PhysRevD.85.104030. arXiv: 1109.3611 [gr-qc].
- [230] Y. Zlochower, M. Ponce, and C. O. Lousto. “Accuracy Issues for Numerical Waveforms”. In: *Phys. Rev. D* 86 (2012), p. 104056. DOI: 10.1103/PhysRevD.86.104056. arXiv: 1208.5494 [gr-qc].

- [231] I. Hinder et al. “Error-analysis and comparison to analytical models of numerical waveforms produced by the NRAR Collaboration”. In: *Class. Quant. Grav.* 31 (2013), p. 025012. DOI: 10.1088/0264-9381/31/2/025012. arXiv: 1307.5307 [gr-qc].
- [232] S. Husa et al. “Frequency-domain gravitational waves from nonprecessing black-hole binaries. I. New numerical waveforms and anatomy of the signal”. In: *Phys. Rev. D* 93.4 (2016), p. 044006. DOI: 10.1103/PhysRevD.93.044006. arXiv: 1508.07250 [gr-qc].
- [233] J. Blackman et al. “Fast and Accurate Prediction of Numerical Relativity Waveforms from Binary Black Hole Coalescences Using Surrogate Models”. In: *Phys. Rev. Lett.* 115.12 (2015), p. 121102. DOI: 10.1103/PhysRevLett.115.121102. arXiv: 1502.07758 [gr-qc].
- [234] A. Nagar et al. “Time-domain effective-one-body gravitational waveforms for coalescing compact binaries with nonprecessing spins, tides and self-spin effects”. In: *Phys. Rev. D* 98.10 (2018), p. 104052. DOI: 10.1103/PhysRevD.98.104052. arXiv: 1806.01772 [gr-qc].
- [235] S. Schmidt et al. “Machine Learning Gravitational Waves from Binary Black Hole Mergers”. In: (Nov. 2020). arXiv: 2011.01958 [gr-qc].
- [236] L. Blanchet, T. Damour, and G. Schafer. “Postnewtonian hydrodynamics and postnewtonian gravitational wave generation for numerical relativity”. In: *Mon. Not. Roy. Astron. Soc.* 242 (1990), pp. 289–305.
- [237] G. Faye et al. “The third and a half post-Newtonian gravitational wave quadrupole mode for quasi-circular inspiralling compact binaries”. In: *Class. Quant. Grav.* 29 (2012), p. 175004. DOI: 10.1088/0264-9381/29/17/175004. arXiv: 1204.1043 [gr-qc].
- [238] M. Levi and J. Steinhoff. “Next-to-next-to-leading order gravitational spin-squared potential via the effective field theory for spinning objects in the post-Newtonian scheme”. In: *JCAP* 1601 (2016), p. 008. DOI: 10.1088/1475-7516/2016/01/008. arXiv: 1506.05794 [gr-qc].
- [239] M. Levi and J. Steinhoff. “Next-to-next-to-leading order gravitational spin-orbit coupling via the effective field theory for spinning objects in the post-Newtonian scheme”. In: *JCAP* 1601 (2016), p. 011. DOI: 10.1088/1475-7516/2016/01/011. arXiv: 1506.05056 [gr-qc].

- [240] C. K. Mishra, K. G. Arun, and B. R. Iyer. “Third post-Newtonian gravitational waveforms for compact binary systems in general orbits: Instantaneous terms”. In: *Phys. Rev. D* 91.8 (2015), p. 084040. DOI: 10.1103/PhysRevD.91.084040. arXiv: 1501.07096 [gr-qc].
- [241] M. Levi and J. Steinhoff. “Complete conservative dynamics for inspiralling compact binaries with spins at fourth post-Newtonian order”. In: (2016). arXiv: 1607.04252 [gr-qc].
- [242] N. Bleistein and R. Handelsman. *Asymptotic Expansions of Integrals*. Dover Books on Mathematics Series. Dover Publications, 1986. ISBN: 9780486650821. URL: <https://books.google.de/books?id=3GZf-bCLFxcC>.
- [243] F. Messina et al. “Quasi-5.5PN TaylorF2 approximant for compact binaries: point-mass phasing and impact on the tidal polarizability inference”. In: *Phys. Rev. D* 99 (2019), p. 124051. DOI: 10.1103/PhysRevD.99.124051. arXiv: 1904.09558 [gr-qc].
- [244] Q. Henry, G. Faye, and L. Blanchet. “Tidal effects in the gravitational-wave phase evolution of compact binary systems to next-to-next-to-leading post-Newtonian order”. In: *Phys. Rev. D* 102.4 (2020), p. 044033. DOI: 10.1103/PhysRevD.102.044033. arXiv: 2005.13367 [gr-qc].
- [245] A. Buonanno and T. Damour. “Effective one-body approach to general relativistic two-body dynamics”. In: *Phys. Rev. D* 59 (1999), p. 084006. DOI: 10.1103/PhysRevD.59.084006. arXiv: gr-qc/9811091.
- [246] T. Damour. “Coalescence of two spinning black holes: An effective one-body approach”. In: *Phys. Rev. D* 64 (2001), p. 124013. DOI: 10.1103/PhysRevD.64.124013. arXiv: gr-qc/0103018.
- [247] T. Damour, P. Jaranowski, and G. Schäfer. “Effective one body approach to the dynamics of two spinning black holes with next-to-leading order spin-orbit coupling”. In: *Phys. Rev. D* 78 (2008), p. 024009. DOI: 10.1103/PhysRevD.78.024009. arXiv: 0803.0915 [gr-qc].
- [248] D. Bini, T. Damour, and A. Geralico. “Novel approach to binary dynamics: application to the fifth post-Newtonian level”. In: *Phys. Rev. Lett.* 123.23 (2019), p. 231104. DOI: 10.1103/PhysRevLett.123.231104. arXiv: 1909.02375 [gr-qc].

- [249] D. Bini, T. Damour, and A. Geralico. “Binary dynamics at the fifth and fifth-and-a-half post-Newtonian orders”. In: *Phys. Rev. D* 102.2 (2020), p. 024062. DOI: 10.1103/PhysRevD.102.024062. arXiv: 2003.11891 [gr-qc].
- [250] D. Bini, T. Damour, and A. Geralico. “Sixth post-Newtonian local-in-time dynamics of binary systems”. In: *Phys. Rev. D* 102.2 (2020), p. 024061. DOI: 10.1103/PhysRevD.102.024061. arXiv: 2004.05407 [gr-qc].
- [251] A. Nagar, A. Bonino, and P. Rettengo. “Effective one-body multipolar waveform model for spin-aligned, quasicircular, eccentric, hyperbolic black hole binaries”. In: *Phys. Rev. D* 103.10 (2021), p. 104021. DOI: 10.1103/PhysRevD.103.104021. arXiv: 2101.08624 [gr-qc].
- [252] S. Balmelli and P. Jetzer. “Effective-one-body Hamiltonian with next-to-leading order spin-spin coupling”. In: *Phys. Rev. D* 91 (2015), p. 064011. DOI: 10.1103/PhysRevD.91.064011. arXiv: 1502.01343 [gr-qc].
- [253] A. Nagar et al. “Multipolar effective one body waveform model for spin-aligned black hole binaries”. In: *Phys. Rev. D* 102.2 (2020), p. 024077. DOI: 10.1103/PhysRevD.102.024077. arXiv: 2001.09082 [gr-qc].
- [254] R. Gamba, S. Bernuzzi, and A. Nagar. “Fast, faithful, frequency-domain effective-one-body waveforms for compact binary coalescences”. In: (Nov. 2020). arXiv: 2012.00027 [gr-qc].
- [255] S. Khan et al. “Frequency-domain gravitational waves from nonprecessing black-hole binaries. II. A phenomenological model for the advanced detector era”. In: *Phys. Rev. D* 93.4 (2016), p. 044007. DOI: 10.1103/PhysRevD.93.044007. arXiv: 1508.07253 [gr-qc].
- [256] S. Khan et al. “Phenomenological model for the gravitational-wave signal from precessing binary black holes with two-spin effects”. In: *Phys. Rev. D* 100.2 (2019), p. 024059. DOI: 10.1103/PhysRevD.100.024059. arXiv: 1809.10113 [gr-qc].
- [257] S. Khan et al. “Including higher order multipoles in gravitational-wave models for precessing binary black holes”. In: (2019). arXiv: 1911.06050 [gr-qc].
- [258] T. Dietrich, S. Bernuzzi, and W. Tichy. “Closed-form tidal approximants for binary neutron star gravitational waveforms constructed from high-resolution numerical relativity simulations”. In: *Phys. Rev. D* 96.12 (2017), p. 121501. DOI: 10.1103/PhysRevD.96.121501. arXiv: 1706.02969 [gr-qc].

- [259] C. M. Will. “The Confrontation between General Relativity and Experiment”. In: *Living Rev. Rel.* 17 (2014), p. 4. DOI: 10.12942/lrr-2014-4. arXiv: 1403.7377 [gr-qc].
- [260] K. S. Thorne. “Tidal stabilization of rigidly rotating, fully relativistic neutron stars”. In: *Phys. Rev. D* 58 (12 1998), p. 124031. DOI: 10.1103/PhysRevD.58.124031. URL: <https://link.aps.org/doi/10.1103/PhysRevD.58.124031>.
- [261] E. E. Flanagan and E. Racine. “Gravitomagnetic resonant excitation of Rossby modes in coalescing neutron star binaries”. In: *Phys. Rev. D* 75 (2007), p. 044001. DOI: 10.1103/PhysRevD.75.044001. arXiv: gr-qc/0601029 [gr-qc].
- [262] T. Damour and A. Nagar. “Relativistic tidal properties of neutron stars”. In: *Phys. Rev. D* 80 (2009), p. 084035. DOI: 10.1103/PhysRevD.80.084035. arXiv: 0906.0096 [gr-qc].
- [263] K. Yagi and N. Yunes. “Binary Love Relations”. In: *Class. Quant. Grav.* 33.13 (2016), 13LT01. DOI: 10.1088/0264-9381/33/13/13LT01. arXiv: 1512.02639 [gr-qc].
- [264] K. Yagi and N. Yunes. “Approximate Universal Relations for Neutron Stars and Quark Stars”. In: *Phys. Rept.* 681 (2017), pp. 1–72. DOI: 10.1016/j.physrep.2017.03.002. arXiv: 1608.02582 [gr-qc].
- [265] D. A. Godzieba et al. “Updated universal relations for tidal deformabilities of neutron stars from phenomenological equations of state”. In: *Phys. Rev. D* 103.6 (2021), p. 063036. DOI: 10.1103/PhysRevD.103.063036. arXiv: 2012.12151 [astro-ph.HE].
- [266] T. Regge and J. A. Wheeler. “Stability of a Schwarzschild singularity”. In: *Phys. Rev.* 108 (1957), pp. 1063–1069.
- [267] E. Poisson and C. M. Will. *Gravity: Newtonian, Post-Newtonian, Relativistic*. Cambridge University Press, 2014. DOI: 10.1017/CB09781139507486.
- [268] T. Binnington and E. Poisson. “Relativistic theory of tidal Love numbers”. In: *Phys. Rev. D* 80 (2009), p. 084018. DOI: 10.1103/PhysRevD.80.084018. arXiv: 0906.1366 [gr-qc].
- [269] T. Hinderer et al. “Tidal deformability of neutron stars with realistic equations of state and their gravitational wave signatures in binary inspiral”. In: *Phys. Rev. D* 81 (2010), p. 123016. DOI: 10.1103/PhysRevD.81.123016. arXiv: 0911.3535 [astro-ph.HE].

-
- [270] J. E. Vines and E. E. Flanagan. “Post-1-Newtonian quadrupole tidal interactions in binary systems”. In: *Phys. Rev. D* 88 (2010), p. 024046. DOI: 10.1103/PhysRevD.88.024046. arXiv: 1009.4919 [gr-qc].
- [271] J. Vines, E. E. Flanagan, and T. Hinderer. “Post-1-Newtonian tidal effects in the gravitational waveform from binary inspirals”. In: *Phys. Rev. D* 83 (2011), p. 084051. DOI: 10.1103/PhysRevD.83.084051. arXiv: 1101.1673 [gr-qc].
- [272] A. Nagar et al. “Nonlinear-in-spin effects in effective-one-body waveform models of spin-aligned, inspiralling, neutron star binaries”. In: *Phys. Rev. D* 99 (2019), p. 044007. DOI: 10.1103/PhysRevD.99.044007. arXiv: 1812.07923 [gr-qc].
- [273] D. Bini and T. Damour. “Gravitational self-force corrections to two-body tidal interactions and the effective one-body formalism”. In: *Phys. Rev. D* 90.12 (2014), p. 124037. DOI: 10.1103/PhysRevD.90.124037. arXiv: 1409.6933 [gr-qc].
- [274] S. Bernuzzi et al. “Modeling the Dynamics of Tidally Interacting Binary Neutron Stars up to the Merger”. In: *Phys. Rev. Lett.* 114.16 (2015), p. 161103. DOI: 10.1103/PhysRevLett.114.161103. arXiv: 1412.4553 [gr-qc].
- [275] S. Akcay et al. “Effective-one-body multipolar waveform for tidally interacting binary neutron stars up to merger”. In: *Phys. Rev. D* 99.4 (2019), p. 044051. DOI: 10.1103/PhysRevD.99.044051. arXiv: 1812.02744 [gr-qc].
- [276] A. H. Nitz et al. “Rapid detection of gravitational waves from compact binary mergers with PyCBC Live”. In: *Phys. Rev. D* 98.2 (2018), p. 024050. DOI: 10.1103/PhysRevD.98.024050. arXiv: 1805.11174 [gr-qc].
- [277] C. Pankow et al. “Improvements in Gravitational-Wave Sky Localization with Expanded Networks of Interferometers”. In: *Astrophys. J. Lett.* 854.2 (2018), p. L25. DOI: 10.3847/2041-8213/aaacd4. arXiv: 1801.02674 [astro-ph.HE].
- [278] P. Welch. “The use of fast Fourier transform for the estimation of power spectra: A method based on time averaging over short, modified periodograms”. In: *IEEE Transactions on Audio and Electroacoustics* 15.2 (1967), pp. 70–73.
- [279] N. J. Cornish and T. B. Littenberg. “BayesWave: Bayesian Inference for Gravitational Wave Bursts and Instrument Glitches”. In: *Class. Quant. Grav.* 32.13 (2015), p. 135012. DOI: 10.1088/0264-9381/32/13/135012. arXiv: 1410.3835 [gr-qc].

- [280] J. Lange, R. O’Shaughnessy, and M. Rizzo. “Rapid and accurate parameter inference for coalescing, precessing compact binaries”. In: (2018). arXiv: 1805.10457 [gr-qc].
- [281] N. Aghanim et al. “Planck 2018 results. VI. Cosmological parameters”. In: *Astron. Astrophys.* 641 (2020). [Erratum: *Astron. Astrophys.* 652, C4 (2021)], A6. DOI: 10.1051/0004-6361/201833910. arXiv: 1807.06209 [astro-ph.CO].
- [282] L. Dai, T. Venumadhav, and B. Zackay. “Parameter Estimation for GW170817 using Relative Binning”. In: (2018). arXiv: 1806.08793 [gr-qc].
- [283] T. Narikawa et al. “Discrepancy in tidal deformability of GW170817 between the Advanced LIGO twin detectors”. In: *Phys. Rev. Research.* 1 (2019), p. 033055. DOI: 10.1103/PhysRevResearch.1.033055. arXiv: 1812.06100 [astro-ph.HE].
- [284] R. Gamba et al. “Waveform systematics in the gravitational-wave inference of tidal parameters and equation of state from binary neutron star signals”. In: (Sept. 2020). arXiv: 2009.08467 [gr-qc].
- [285] R. Dudi et al. “Relevance of tidal effects and post-merger dynamics for binary neutron star parameter estimation”. In: (2018). arXiv: 1808.09749 [gr-qc].
- [286] A. Samajdar and T. Dietrich. “Waveform systematics for binary neutron star gravitational wave signals: effects of the point-particle baseline and tidal descriptions”. In: *Phys. Rev. D* 98.12 (2018), p. 124030. DOI: 10.1103/PhysRevD.98.124030. arXiv: 1810.03936 [gr-qc].
- [287] A. Samajdar and T. Dietrich. “Waveform systematics for binary neutron star gravitational wave signals: Effects of spin, precession, and the observation of electromagnetic counterparts”. In: *Phys. Rev. D* 100.2 (2019), p. 024046. DOI: 10.1103/PhysRevD.100.024046. arXiv: 1905.03118 [gr-qc].
- [288] T. Narikawa et al. “Reanalysis of the binary neutron star mergers GW170817 and GW190425 using numerical-relativity calibrated waveform models”. In: *Phys. Rev. Res.* 2.4 (2020), p. 043039. DOI: 10.1103/PhysRevResearch.2.043039. arXiv: 1910.08971 [gr-qc].
- [289] A. Chen et al. “Distinguishing high-mass binary neutron stars from binary black holes with second- and third-generation gravitational wave observatories”. In: *Phys. Rev. D* 101.10 (2020), p. 103008. DOI: 10.1103/PhysRevD.101.103008. arXiv: 2001.11470 [astro-ph.HE].

- [290] N. Kunert et al. “Quantifying modelling uncertainties when combining multiple gravitational-wave detections from binary neutron star sources”. In: (Oct. 2021). arXiv: 2110.11835 [astro-ph.HE].
- [291] C. Cutler and E. E. Flanagan. “Gravitational waves from merging compact binaries: How accurately can one extract the binary’s parameters from the inspiral wave form?” In: *Phys.Rev.* D49 (1994), pp. 2658–2697. DOI: 10.1103/PhysRevD.49.2658. arXiv: gr-qc/9402014 [gr-qc].
- [292] E. Poisson and C. M. Will. “Gravitational waves from inspiraling compact binaries: Parameter estimation using second postNewtonian wave forms”. In: *Phys.Rev.* D52 (1995), pp. 848–855. DOI: 10.1103/PhysRevD.52.848. arXiv: gr-qc/9502040 [gr-qc].
- [293] F. Acernese et al. “Advanced Virgo: a second-generation interferometric gravitational wave detector”. In: *Class. Quant. Grav.* 32.2 (2015), p. 024001. DOI: 10.1088/0264-9381/32/2/024001. arXiv: 1408.3978 [gr-qc].
- [294] B. P. Abbott et al. “Estimating the Contribution of Dynamical Ejecta in the Kilonova Associated with GW170817”. In: *Astrophys. J.* 850.2 (2017), p. L39. DOI: 10.3847/2041-8213/aa9478. arXiv: 1710.05836 [astro-ph.HE].
- [295] K. Hotokezaka et al. “Binary Neutron Star Mergers: Dependence on the Nuclear Equation of State”. In: *Phys.Rev.* D83 (2011), p. 124008. DOI: 10.1103/PhysRevD.83.124008. arXiv: 1105.4370 [astro-ph.HE].
- [296] A. Bauswein, T. Baumgarte, and H. T. Janka. “Prompt merger collapse and the maximum mass of neutron stars”. In: *Phys.Rev.Lett.* 111.13 (2013), p. 131101. DOI: 10.1103/PhysRevLett.111.131101. arXiv: 1307.5191 [astro-ph.SR].
- [297] S. Köppel, L. Bovard, and L. Rezzolla. “A General-relativistic Determination of the Threshold Mass to Prompt Collapse in Binary Neutron Star Mergers”. In: *Astrophys. J.* 872.1 (2019), p. L16. DOI: 10.3847/2041-8213/ab0210. arXiv: 1901.09977 [gr-qc].
- [298] M. Shibata et al. “Modeling GW170817 based on numerical relativity and its implications”. In: *Phys. Rev.* D96.12 (2017), p. 123012. DOI: 10.1103/PhysRevD.96.123012. arXiv: 1710.07579 [astro-ph.HE].

- [299] M. Ruiz, S. L. Shapiro, and A. Tsokaros. “GW170817, General Relativistic Magnetohydrodynamic Simulations, and the Neutron Star Maximum Mass”. In: *Phys. Rev. D* 97.2 (2018), p. 021501. DOI: 10.1103/PhysRevD.97.021501. arXiv: 1711.00473 [astro-ph.HE].
- [300] F. Zappa et al. “Gravitational-wave luminosity of binary neutron stars mergers”. In: *Phys. Rev. Lett.* 120.11 (2018), p. 111101. DOI: 10.1103/PhysRevLett.120.111101. arXiv: 1712.04267 [gr-qc].
- [301] L. Lindblom. “Spectral Representations of Neutron-Star Equations of State”. In: *Phys. Rev. D* 82 (2010), p. 103011. DOI: 10.1103/PhysRevD.82.103011. arXiv: 1009.0738 [astro-ph.HE].
- [302] L. Lindblom and N. M. Indik. “Spectral Approach to the Relativistic Inverse Stellar Structure Problem II”. In: *Phys. Rev. D* 89.6 (2014). [Erratum: *Phys. Rev. D* 93, 129903 (2016)], p. 064003. DOI: 10.1103/PhysRevD.89.064003. arXiv: 1310.0803 [astro-ph.HE].
- [303] M. F. Carney, L. E. Wade, and B. S. Irwin. “Comparing two models for measuring the neutron star equation of state from gravitational-wave signals”. In: *Phys. Rev. D* 98.6 (2018), p. 063004. DOI: 10.1103/PhysRevD.98.063004. arXiv: 1805.11217 [gr-qc].
- [304] E. Nakar et al. “From γ to Radio - The Electromagnetic Counterpart of GW 170817”. In: *Astrophys. J.* 867.1 (2018), p. 18. DOI: 10.3847/1538-4357/aae205. arXiv: 1803.07595 [astro-ph.HE].
- [305] M. W. Coughlin et al. “Constraints on the neutron star equation of state from AT2017gfo using radiative transfer simulations”. In: *Mon. Not. Roy. Astron. Soc.* 480.3 (2018), pp. 3871–3878. DOI: 10.1093/mnras/sty2174. arXiv: 1805.09371 [astro-ph.HE].
- [306] S. Rosswog et al. “The long-term evolution of neutron star merger remnants – I. The impact of r-process nucleosynthesis”. In: *Mon. Not. Roy. Astron. Soc.* 439.1 (2014), pp. 744–756. DOI: 10.1093/mnras/stt2502. arXiv: 1307.2939 [astro-ph.HE].
- [307] R. Fernández et al. “The interplay of disc wind and dynamical ejecta in the aftermath of neutron star–black hole mergers”. In: *Mon. Not. Roy. Astron. Soc.* 449.1 (2015), pp. 390–402. DOI: 10.1093/mnras/stv238. arXiv: 1412.5588 [astro-ph.HE].

-
- [308] B. D. Metzger and R. Fernández. “Red or blue? A potential kilonova imprint of the delay until black hole formation following a neutron star merger”. In: *Mon. Not. Roy. Astron. Soc.* 441 (2014), p. 3444. DOI: 10.1093/mnras/stu802. arXiv: 1402.4803 [astro-ph.HE].
- [309] M. Tanaka et al. “Systematic opacity calculations for kilonovae”. In: *Mon. Not. Roy. Astron. Soc.* 496.2 (Aug. 2020), pp. 1369–1392. DOI: 10.1093/mnras/staa1576. arXiv: 1906.08914 [astro-ph.HE].
- [310] V. Nedora et al. “Mapping dynamical ejecta and disk masses from numerical relativity simulations of neutron star mergers”. In: *Class. Quant. Grav.* 39.1 (2022), p. 015008. DOI: 10.1088/1361-6382/ac35a8. arXiv: 2011.11110 [astro-ph.HE].
- [311] O. Korobkin et al. “On the astrophysical robustness of neutron star merger r-process”. In: *Mon. Not. Roy. Astron. Soc.* 426 (2012), p. 1940. DOI: 10.1111/j.1365-2966.2012.21859.x. arXiv: 1206.2379 [astro-ph.SR].
- [312] J. Barnes et al. “Radioactivity and thermalization in the ejecta of compact object mergers and their impact on kilonova light curves”. In: *Astrophys. J.* 829.2 (2016), p. 110. DOI: 10.3847/0004-637X/829/2/110. arXiv: 1605.07218 [astro-ph.HE].
- [313] W. Even et al. “Composition Effects on Kilonova Spectra and Light Curves: I”. In: *Astrophys. J.* 899.1 (2020), p. 24. DOI: 10.3847/1538-4357/ab70b9. arXiv: 1904.13298 [astro-ph.HE].
- [314] K. Kawaguchi, M. Shibata, and M. Tanaka. “Radiative transfer simulation for the optical and near-infrared electromagnetic counterparts to GW170817”. In: *Astrophys. J.* 865.2 (2018), p. L21. DOI: 10.3847/2041-8213/aade02. arXiv: 1806.04088 [astro-ph.HE].
- [315] O. Korobkin et al. “Axisymmetric Radiative Transfer Models of Kilonovae”. In: (Mar. 2020). arXiv: 2004.00102 [astro-ph.HE].
- [316] D. Grossman et al. “The long-term evolution of neutron star merger remnants – II. Radioactively powered transients”. In: *Mon. Not. Roy. Astron. Soc.* 439.1 (2014), pp. 757–770. DOI: 10.1093/mnras/stt2503. arXiv: 1307.2943 [astro-ph.HE].

- [317] M. Coughlin et al. “Toward Rapid Transient Identification and Characterization of Kilonovae”. In: *Astrophys. J.* 849.1, 12 (Nov. 2017), p. 12. DOI: 10.3847/1538-4357/aa9114. arXiv: 1708.07714 [astro-ph.HE].
- [318] D. Martin et al. “Neutrino-driven winds in the aftermath of a neutron star merger: nucleosynthesis and electromagnetic transients”. In: *Astrophys. J.* 813.1 (2015), p. 2. DOI: 10.1088/0004-637X/813/1/2. arXiv: 1506.05048 [astro-ph.SR].
- [319] J. de Jesús Mendoza-Temis et al. “Nuclear robustness of the r process in neutron-star mergers”. In: *Phys. Rev. C* 92.5 (2015), p. 055805. DOI: 10.1103/PhysRevC.92.055805. arXiv: 1409.6135 [astro-ph.HE].
- [320] M.-R. Wu et al. “Production of the entire range of r-process nuclides by black hole accretion disc outflows from neutron star mergers”. In: *Mon. Not. Roy. Astron. Soc.* 463.3 (2016), pp. 2323–2334. DOI: 10.1093/mnras/stw2156. arXiv: 1607.05290 [astro-ph.HE].
- [321] W. D. Arnett. “Type I supernovae. I - Analytic solutions for the early part of the light curve”. In: *Astrophys. J.* (1982).
- [322] L. F. Roberts et al. “Electromagnetic Transients Powered by Nuclear Decay in the Tidal Tails of Coalescing Compact Binaries”. In: *Astrophys. J.* 736 (2011), p. L21. DOI: 10.1088/2041-8205/736/1/L21. arXiv: 1104.5504 [astro-ph.HE].
- [323] D. Kasen, N. R. Badnell, and J. Barnes. “Opacities and Spectra of the r-process Ejecta from Neutron Star Mergers”. In: *Astrophys. J.* 774 (2013), p. 25. DOI: 10.1088/0004-637X/774/1/25. arXiv: 1303.5788 [astro-ph.HE].
- [324] B. Metzger and E. Berger. “What is the Most Promising Electromagnetic Counterpart of a Neutron Star Binary Merger?” In: *Astrophys. J.* 746 (2012), p. 48. DOI: 10.1088/0004-637X/746/1/48. arXiv: 1108.6056 [astro-ph.HE].
- [325] K. Hotokezaka, P. Beniamini, and T. Piran. “Neutron Star Mergers as sites of r-process Nucleosynthesis and Short Gamma-Ray Bursts”. In: *Int. J. Mod. Phys. D* 27.13 (2018), p. 1842005. DOI: 10.1142/S0218271818420051. arXiv: 1801.01141 [astro-ph.HE].
- [326] V. A. Villar et al. “Theoretical Models of Optical Transients. I. A Broad Exploration of the Duration-Luminosity Phase Space”. In: *Astrophys. J.* 849 (2017), p. 70. DOI: 10.3847/1538-4357/aa8fcb. arXiv: 1707.08132 [astro-ph.HE].

- [327] D. Kasen and J. Barnes. “Radioactive Heating and Late Time Kilonova Light Curves”. In: *Astrophys. J.* 876.2, 128 (May 2019), p. 128. DOI: 10.3847/1538-4357/ab06c2. arXiv: 1807.03319 [astro-ph.HE].
- [328] R. Fernández et al. “Long-term GRMHD simulations of neutron star merger accretion discs: implications for electromagnetic counterparts”. In: *Mon. Not. Roy. Astron. Soc.* 482.3 (2019), pp. 3373–3393. DOI: 10.1093/mnras/sty2932. arXiv: 1808.00461 [astro-ph.HE].
- [329] C. Barbieri et al. “Light-curve models of black hole – neutron star mergers: steps towards a multi-messenger parameter estimation”. In: *Astron. Astrophys.* 625 (2019), A152. DOI: 10.1051/0004-6361/201935443. arXiv: 1903.04543 [astro-ph.HE].
- [330] R. Oechslin, H.-T. Janka, and A. Marek. “Relativistic neutron star merger simulations with non-zero temperature equations of state. 1. Variation of binary parameters and equation of state”. In: *Astron. Astrophys.* (2006). arXiv: astro-ph/0611047 [astro-ph].
- [331] S. Rosswog, T. Piran, and E. Nakar. “The multi-messenger picture of compact object encounters: binary mergers versus dynamical collisions”. In: *Mon. Not. Roy. Astron. Soc.* 430 (2013), p. 2585. DOI: 10.1093/mnras/sts708. arXiv: 1204.6240 [astro-ph.HE].
- [332] L. Bovard et al. “*r*-process nucleosynthesis from matter ejected in binary neutron star mergers”. In: *Phys. Rev.* D96.12 (2017), p. 124005. DOI: 10.1103/PhysRevD.96.124005. arXiv: 1709.09630 [gr-qc].
- [333] B. D. Metzger et al. “The effects of *r*-process heating on fall-back accretion in compact object mergers”. In: *Mon. Not. Roy. Astron. Soc.* 402 (2010), p. 2771. DOI: 10.1111/j.1365-2966.2009.16107.x. arXiv: 0908.0530 [astro-ph.HE].
- [334] O. Just, M. Obergaulinger, and H. T. Janka. “A new multidimensional, energy-dependent two-moment transport code for neutrino-hydrodynamics”. In: *Mon. Not. Roy. Astron. Soc.* 453.4 (2015), pp. 3386–3413. DOI: 10.1093/mnras/stv1892. arXiv: 1501.02999 [astro-ph.HE].
- [335] D. M. Siegel and B. D. Metzger. “Three-dimensional GRMHD simulations of neutrino-cooled accretion disks from neutron star mergers”. In: *Astrophys. J.* 858.1 (2018), p. 52. DOI: 10.3847/1538-4357/aabaec. arXiv: 1711.00868 [astro-ph.HE].

- [336] B. Metzger, A. Piro, and E. Quataert. “Time-Dependent Models of Accretion Disks Formed from Compact Object Mergers”. In: *Mon. Not. Roy. Astron. Soc.* 390 (2008), p. 781. DOI: 10.1111/j.1365-2966.2008.13789.x. arXiv: 0805.4415 [astro-ph].
- [337] R. Fernández and B. D. Metzger. “Delayed outflows from black hole accretion tori following neutron star binary coalescence”. In: *Mon. Not. Roy. Astron. Soc.* 435 (2013), p. 502. DOI: 10.1093/mnras/stt1312. arXiv: 1304.6720 [astro-ph.HE].
- [338] A. Perego, H. Yasin, and A. Arcones. “Neutrino pair annihilation above merger remnants: implications of a long-lived massive neutron star”. In: *J. Phys.* G44.8 (2017), p. 084007. DOI: 10.1088/1361-6471/aa7bdc. arXiv: 1701.02017 [astro-ph.HE].
- [339] V. Decoene et al. “High-energy neutrinos from fallback accretion of binary neutron star merger remnants”. In: *JCAP* 04 (2020), p. 045. DOI: 10.1088/1475-7516/2020/04/045. arXiv: 1910.06578 [astro-ph.HE].
- [340] S. Fujibayashi et al. “Mass Ejection from the Remnant of a Binary Neutron Star Merger: Viscous-Radiation Hydrodynamics Study”. In: *Astrophys. J.* 860.1 (2018), p. 64. DOI: 10.3847/1538-4357/aabafd. arXiv: 1711.02093 [astro-ph.HE].
- [341] S. Fujibayashi et al. “Postmerger Mass Ejection of Low-mass Binary Neutron Stars”. In: *Astrophys. J.* 901.2, 122 (Oct. 2020), p. 122. DOI: 10.3847/1538-4357/abafc2. arXiv: 2007.00474 [astro-ph.HE].
- [342] J. A. Cardelli, G. C. Clayton, and J. S. Mathis. “The Relationship between Infrared, Optical, and Ultraviolet Extinction”. In: *Astrophys. J.* 345 (Oct. 1989), p. 245. DOI: 10.1086/167900.
- [343] J. D. Lawrence et al. *The Importance of Prior Choice in Model Selection: a Density Dependence Example*. 2011. DOI: 10.48550/ARXIV.1108.4912. URL: <https://arxiv.org/abs/1108.4912>.
- [344] S. Vitale et al. “Impact of Bayesian Priors on the Characterization of Binary Black Hole Coalescences”. In: *Phys. Rev. Lett.* 119.25 (2017), p. 251103. DOI: 10.1103/PhysRevLett.119.251103. arXiv: 1707.04637 [gr-qc].
- [345] S. Bhagwat et al. “The importance of priors on LIGO-Virgo parameter estimation: the case of primordial black holes”. In: *JCAP* 01 (2021), p. 037. DOI: 10.1088/1475-7516/2021/01/037. arXiv: 2008.12320 [astro-ph.CO].

- [346] J. Barnes et al. “Kilonovae across the nuclear physics landscape: The impact of nuclear physics uncertainties on r-process-powered emission”. In: *Preprint (ArXiv:2010.11182)* (Oct. 2020). arXiv: 2010.11182 [astro-ph.HE].
- [347] Y. Zhu et al. “Modeling Kilonova Light Curves: Dependence on Nuclear Inputs”. In: *preprint (ArXiv:2010.03668)* (Oct. 2020). arXiv: 2010.03668 [astro-ph.HE].
- [348] A. Endrizzi et al. “Thermodynamics conditions of matter in the neutrino decoupling region during neutron star mergers”. In: *Eur. Phys. J. A* 56.1 (2020), p. 15. DOI: 10.1140/epja/s10050-019-00018-6. arXiv: 1908.04952 [astro-ph.HE].
- [349] D. Radice and L. Dai. “Multimessenger Parameter Estimation of GW170817”. In: *Eur. Phys. J. A* 55.4 (2019), p. 50. DOI: 10.1140/epja/i2019-12716-4. arXiv: 1810.12917 [astro-ph.HE].
- [350] M. W. Coughlin et al. “Multimessenger Bayesian parameter inference of a binary neutron star merger”. In: *Mon. Not. Roy. Astron. Soc.* 489.1 (2019), pp. L91–L96. DOI: 10.1093/mnrasl/slz133. arXiv: 1812.04803 [astro-ph.HE].
- [351] J. Lippuner and L. F. Roberts. “r-Process Lanthanide Production and Heating Rates in Kilonovae”. In: *Astrophys. J.* 815.2 (2015), p. 82. DOI: 10.1088/0004-637X/815/2/82. arXiv: 1508.03133 [astro-ph.HE].
- [352] J. M. Miller et al. “Full Transport Model of GW170817-Like Disk Produces a Blue Kilonova”. In: *Phys. Rev. D* 100.2 (2019), p. 023008. DOI: 10.1103/PhysRevD.100.023008. arXiv: 1905.07477 [astro-ph.HE].
- [353] D. Kasen, R. Fernández, and B. Metzger. “Kilonova light curves from the disc wind outflows of compact object mergers”. In: *Mon. Not. Roy. Astron. Soc.* 450 (2015), pp. 1777–1786. DOI: 10.1093/mnras/stv721. arXiv: 1411.3726 [astro-ph.HE].
- [354] S. De et al. “Tidal Deformabilities and Radii of Neutron Stars from the Observation of GW170817”. In: *Phys. Rev. Lett.* 121.9 (2018). [Erratum: *Phys. Rev. Lett.* 121, no. 25, 259902 (2018)], p. 091102. DOI: 10.1103/PhysRevLett.121.259902, 10.1103/PhysRevLett.121.091102. arXiv: 1804.08583 [astro-ph.HE].
- [355] E. Annala et al. “Gravitational-wave constraints on the neutron-star-matter Equation of State”. In: *Phys. Rev. Lett.* 120.17 (2018), p. 172703. DOI: 10.1103/PhysRevLett.120.172703. arXiv: 1711.02644 [astro-ph.HE].

- [356] G. Raaijmakers et al. “Constraining the dense matter equation of state with joint analysis of NICER and LIGO/Virgo measurements”. In: *Astrophys. J. Lett.* 893.1 (2020), p. L21. DOI: 10.3847/2041-8213/ab822f. arXiv: 1912.11031 [astro-ph.HE].
- [357] C. D. Capano et al. “Stringent constraints on neutron-star radii from multimessenger observations and nuclear theory”. In: *Nature Astron.* 4.6 (2020), pp. 625–632. DOI: 10.1038/s41550-020-1014-6. arXiv: 1908.10352 [astro-ph.HE].
- [358] R. Essick et al. “Direct Astrophysical Tests of Chiral Effective Field Theory at Supranuclear Densities”. In: *Phys. Rev. C* 102.5 (2020), p. 055803. DOI: 10.1103/PhysRevC.102.055803. arXiv: 2004.07744 [astro-ph.HE].
- [359] G. P. Lamb et al. “The optical afterglow of GW170817 at one year post-merger”. In: *Astrophys. J. Lett.* 870.2 (2019), p. L15. DOI: 10.3847/2041-8213/aaf96b. arXiv: 1811.11491 [astro-ph.HE].
- [360] W.-f. Fong et al. “The Optical Afterglow of GW170817: An Off-axis Structured Jet and Deep Constraints on a Globular Cluster Origin”. In: *Astrophys. J. Lett.* 883.1 (2019), p. L1. DOI: 10.3847/2041-8213/ab3d9e. arXiv: 1908.08046 [astro-ph.HE].
- [361] R. Abbott et al. “Observation of Gravitational Waves from Two Neutron Star–Black Hole Coalescences”. In: *Astrophys. J. Lett.* 915.1 (2021), p. L5. DOI: 10.3847/2041-8213/ac082e. arXiv: 2106.15163 [astro-ph.HE].
- [362] S. Kim et al. “ALMA and GMRT constraints on the off-axis gamma-ray burst 170817A from the binary neutron star merger GW170817”. In: *Astrophys. J. Lett.* 850.2 (2017), p. L21. DOI: 10.3847/2041-8213/aa970b. arXiv: 1710.05847 [astro-ph.HE].
- [363] P. T. H. Pang et al. “NMMA: A nuclear-physics and multi-messenger astrophysics framework to analyze binary neutron star mergers”. In: (May 2022). arXiv: 2205.08513 [astro-ph.HE].
- [364] D. A. Godzieba, D. Radice, and S. Bernuzzi. “On the maximum mass of neutron stars and GW190814”. In: *Astrophys. J.* 908 (2021), p. 122. DOI: 10.3847/1538-4357/abd4dd. arXiv: 2007.10999 [astro-ph.HE].

- [365] J.-L. Jiang et al. “PSR J0030+0451, GW170817 and the nuclear data: joint constraints on equation of state and bulk properties of neutron stars”. In: *Astrophys. J.* 892 (2020), p. 1. DOI: 10.3847/1538-4357/ab77cf. arXiv: 1912.07467 [astro-ph.HE].
- [366] M. Al-Mamun et al. “Combining Electromagnetic and Gravitational-Wave Constraints on Neutron-Star Masses and Radii”. In: *Phys. Rev. Lett.* 126.6 (2021), p. 061101. DOI: 10.1103/PhysRevLett.126.061101. arXiv: 2008.12817 [astro-ph.HE].
- [367] M. Nicholl et al. “Tight multimessenger constraints on the neutron star equation of state from GW170817 and a forward model for kilonova light-curve synthesis”. In: *Mon. Not. Roy. Astron. Soc.* 505.2 (2021), pp. 3016–3032. DOI: 10.1093/mnras/stab1523. arXiv: 2102.02229 [astro-ph.HE].
- [368] A. Ayriyan et al. “Bayesian analysis of multimessenger M-R data with interpolated hybrid EoS”. In: *Eur. Phys. J. A* 57.11 (2021), p. 318. DOI: 10.1140/epja/s10050-021-00619-0. arXiv: 2102.13485 [astro-ph.HE].
- [369] L. Brandes, W. Weise, and N. Kaiser. “Inference of the sound speed and related properties of neutron stars”. In: (Aug. 2022). arXiv: 2208.03026 [nucl-th].
- [370] A. Le Fèvre et al. “Constraining the nuclear matter equation of state around twice saturation density”. In: *Nucl. Phys. A* 945 (2016), pp. 112–133. DOI: 10.1016/j.nuclphysa.2015.09.015. arXiv: 1501.05246 [nucl-ex].
- [371] P. Russotto et al. “Results of the ASY-EOS experiment at GSI: The symmetry energy at suprasaturation density”. In: *Phys. Rev. C* 94.3 (2016), p. 034608. DOI: 10.1103/PhysRevC.94.034608. arXiv: 1608.04332 [nucl-ex].
- [372] K. Hotokezaka et al. “Remnant massive neutron stars of binary neutron star mergers: Evolution process and gravitational waveform”. In: *Phys. Rev.* D88.4 (2013), p. 044026. DOI: 10.1103/PhysRevD.88.044026. arXiv: 1307.5888 [astro-ph.HE].
- [373] K. Takami, L. Rezzolla, and L. Baiotti. “Spectral properties of the post-merger gravitational-wave signal from binary neutron stars”. In: *Phys. Rev.* D91.6 (2015), p. 064001. DOI: 10.1103/PhysRevD.91.064001. arXiv: 1412.3240 [gr-qc].

- [374] J. A. Clark et al. “Observing Gravitational Waves From The Post-Merger Phase Of Binary Neutron Star Coalescence”. In: *Class. Quant. Grav.* 33.8 (2016), p. 085003. DOI: 10.1088/0264-9381/33/8/085003. arXiv: 1509.08522 [astro-ph.HE].
- [375] K. Chatziioannou et al. “Inferring the post-merger gravitational wave emission from binary neutron star coalescences”. In: *Phys. Rev. D* 96.12 (2017), p. 124035. DOI: 10.1103/PhysRevD.96.124035. arXiv: 1711.00040 [gr-qc].
- [376] P. J. Easter et al. “Computing Fast and Reliable Gravitational Waveforms of Binary Neutron Star Merger Remnants”. In: *Phys. Rev. D* 100.4 (2019), p. 043005. DOI: 10.1103/PhysRevD.100.043005. arXiv: 1811.11183 [gr-qc].
- [377] S. Bose et al. “Neutron-star Radius from a Population of Binary Neutron Star Mergers”. In: *Phys. Rev. Lett.* 120.3 (2018), p. 031102. DOI: 10.1103/PhysRevLett.120.031102. arXiv: 1705.10850 [gr-qc].
- [378] K. W. Tsang, T. Dietrich, and C. Van Den Broeck. “Modeling the postmerger gravitational wave signal and extracting binary properties from future binary neutron star detections”. In: *Phys. Rev. D* 100.4 (2019), p. 044047. DOI: 10.1103/PhysRevD.100.044047. arXiv: 1907.02424 [gr-qc].
- [379] P. J. Easter et al. “Detection and parameter estimation of binary neutron star merger remnants”. In: *Phys. Rev. D* 102.4 (2020), p. 043011. DOI: 10.1103/PhysRevD.102.043011. arXiv: 2006.04396 [astro-ph.HE].
- [380] T. Sultani, A. Bauswein, and N. Stergioulas. “Analytic model of the spectral properties of gravitational waves from neutron star merger remnants”. In: (Nov. 2021). arXiv: 2111.08353 [astro-ph.HE].
- [381] M. Wijngaarden et al. “Probing neutron stars with the full pre-merger and post-merger gravitational wave signal from binary coalescences”. In: (Feb. 2022). arXiv: 2202.09382 [gr-qc].
- [382] T. Whittaker et al. “Using machine learning to parametrize postmerger signals from binary neutron stars”. In: (Jan. 2022). arXiv: 2201.06461 [gr-qc].
- [383] M. Breschi et al. “Kilohertz Gravitational Waves From Binary Neutron Star Mergers: Numerical-relativity Informed Postmerger Model”. In: (May 2022). arXiv: 2205.09112 [gr-qc].

-
- [384] M. Shibata and K. Uryu. “Gravitational waves from the merger of binary neutron stars in a fully general relativistic simulation”. In: *Prog. Theor. Phys.* 107 (2002), p. 265. DOI: 10.1143/PTP.107.265. arXiv: gr-qc/0203037.
- [385] N. Stergioulas et al. “Gravitational waves and nonaxisymmetric oscillation modes in mergers of compact object binaries”. In: *Mon.Not.Roy.Astron.Soc.* 418 (2011), p. 427. DOI: 10.1111/j.1365-2966.2011.19493.x. arXiv: 1105.0368 [gr-qc].
- [386] A. Bauswein and H.-T. Janka. “Measuring neutron-star properties via gravitational waves from binary mergers”. In: *Phys.Rev.Lett.* 108 (2012), p. 011101. DOI: 10.1103/PhysRevLett.108.011101. arXiv: 1106.1616 [astro-ph.SR].
- [387] A. Bauswein et al. “Equation-of-state dependence of the gravitational-wave signal from the ring-down phase of neutron-star mergers”. In: *Phys. Rev. D* 86 (2012), p. 063001. DOI: 10.1103/PhysRevD.86.063001. arXiv: 1204.1888 [astro-ph.SR].
- [388] K. Takami, L. Rezzolla, and L. Baiotti. “Constraining the Equation of State of Neutron Stars from Binary Mergers”. In: *Phys.Rev.Lett.* 113 (2014), p. 091104. DOI: 10.1103/PhysRevLett.113.091104. arXiv: 1403.5672 [gr-qc].
- [389] D. Radice, S. Bernuzzi, and C. D. Ott. “One-armed spiral instability in neutron star mergers and its detectability in gravitational waves”. In: *Phys. Rev.* D94.6 (2016), p. 064011. DOI: 10.1103/PhysRevD.94.064011. arXiv: 1603.05726 [gr-qc].
- [390] L. Lehner et al. “Unequal mass binary neutron star mergers and multimessenger signals”. In: *Class. Quant. Grav.* 33.18 (2016), p. 184002. DOI: 10.1088/0264-9381/33/18/184002. arXiv: 1603.00501 [gr-qc].
- [391] T. Dietrich et al. “Gravitational waves and mass ejecta from binary neutron star mergers: Effect of the stars’ rotation”. In: *Phys. Rev.* D95.4 (2017), p. 044045. DOI: 10.1103/PhysRevD.95.044045. arXiv: 1611.07367 [gr-qc].
- [392] M. Shibata and K. Uryu. “Simulation of merging binary neutron stars in full general relativity: $\Gamma = 2$ case”. In: *Phys. Rev.* D61 (2000), p. 064001. DOI: 10.1103/PhysRevD.61.064001. arXiv: gr-qc/9911058.
- [393] S. Bernuzzi et al. “Mergers of binary neutron stars with realistic spin”. In: *Phys.Rev.* D89 (2014), p. 104021. DOI: 10.1103/PhysRevD.89.104021. arXiv: 1311.4443 [gr-qc].

- [394] H. Dimmelmeier, N. Stergioulas, and J. A. Font. “Non-linear axisymmetric pulsations of rotating relativistic stars in the conformal flatness approximation”. In: *Mon. Not. Roy. Astron. Soc.* 368 (2006), pp. 1609–1630. DOI: 10.1111/j.1365-2966.2006.10274.x. arXiv: astro-ph/0511394.
- [395] A. Passamonti, N. Stergioulas, and A. Nagar. “Gravitational waves from non-linear couplings of radial and polar nonradial modes in relativistic stars”. In: *Phys. Rev. D* 75 (2007), p. 084038. eprint: gr-qc/0702099.
- [396] L. Baiotti et al. “Gravitational-Wave Extraction from Neutron Stars Oscillations: comparing linear and nonlinear techniques”. In: *Phys. Rev. D* 79 (2009), p. 024002. DOI: 10.1103/PhysRevD.79.024002. arXiv: 0808.4002 [gr-qc].
- [397] S. Chandrasekhar. “The Effect of Gravitational Radiation on the Secular Stability of the Maclaurin Spheroid”. In: *Astrophys. J.* 161 (Aug. 1970), p. 561.
- [398] J. L. Friedman and B. F. Schutz. “Lagrangian perturbation theory of nonrelativistic fluids”. In: *Astrophys. J.* 221 (May 1978), pp. 937–957. DOI: 10.1086/156098.
- [399] W. E. East et al. “Relativistic Simulations of Eccentric Binary Neutron Star Mergers: One-arm Spiral Instability and Effects of Neutron Star Spin”. In: *Phys. Rev. D* 93.2 (2016), p. 024011. DOI: 10.1103/PhysRevD.93.024011. arXiv: 1511.01093 [astro-ph.HE].
- [400] F. Foucart, T. Hinderer, and S. Nissanke. “Remnant baryon mass in neutron star-black hole mergers: Predictions for binary neutron star mimickers and rapidly spinning black holes”. In: *Phys. Rev. D* 98.8 (2018), p. 081501. DOI: 10.1103/PhysRevD.98.081501. arXiv: 1807.00011 [astro-ph.HE].
- [401] A. Bauswein et al. “Identifying a first-order phase transition in neutron star mergers through gravitational waves”. In: *Phys. Rev. Lett.* 122.6 (2019), p. 061102. DOI: 10.1103/PhysRevLett.122.061102. arXiv: 1809.01116 [astro-ph.HE].
- [402] M. Breschi et al. “Kilohertz Gravitational Waves from Binary Neutron Star Mergers: Inference of Postmerger Signals with the Einstein Telescope”. In: (May 2022). arXiv: 2205.09979 [gr-qc].
- [403] K. D. Kokkotas and B. G. Schmidt. “Quasi-normal modes of stars and black holes”. In: *Living Rev. Rel.* 2 (1999), p. 2. arXiv: gr-qc/9909058.

- [404] P. Iosif and N. Stergioulas. “Models of binary neutron star remnants with tabulated equations of state”. In: *Mon. Not. Roy. Astron. Soc.* 510.2 (2022), pp. 2948–2967. DOI: 10.1093/mnras/stab3565. arXiv: 2104.13672 [astro-ph.HE].
- [405] K. Kawaguchi et al. “Frequency-domain gravitational waveform models for inspiraling binary neutron stars”. In: *Phys. Rev.* D97.4 (2018), p. 044044. DOI: 10.1103/PhysRevD.97.044044. arXiv: 1802.06518 [gr-qc].
- [406] K. Kiuchi et al. “Sub-radian-accuracy gravitational waveforms of coalescing binary neutron stars in numerical relativity”. In: *Phys. Rev.* D96.8 (2017), p. 084060. DOI: 10.1103/PhysRevD.96.084060. arXiv: 1708.08926 [astro-ph.HE].
- [407] K. Kiuchi et al. “Sub-radian-accuracy gravitational waves from coalescing binary neutron stars II: Systematic study on the equation of state, binary mass, and mass ratio”. In: (2019). arXiv: 1907.03790 [astro-ph.HE].
- [408] R. Ciolfi et al. “First 100 ms of a long-lived magnetized neutron star formed in a binary neutron star merger”. In: *Phys. Rev.* D100.2 (2019), p. 023005. DOI: 10.1103/PhysRevD.100.023005. arXiv: 1904.10222 [astro-ph.HE].
- [409] E. Berti et al. “Spectroscopy of Kerr black holes with Earth- and space-based interferometers”. In: *Phys. Rev. Lett.* 117.10 (2016), p. 101102. DOI: 10.1103/PhysRevLett.117.101102. arXiv: 1605.09286 [gr-qc].
- [410] W. Del Pozzo and A. Nagar. “Analytic family of post-merger template waveforms”. In: *Phys. Rev. D* 95.12 (2017), p. 124034. DOI: 10.1103/PhysRevD.95.124034. arXiv: 1606.03952 [gr-qc].
- [411] S. Bernuzzi and T. Dietrich. “Gravitational waveforms from binary neutron star mergers with high-order weighted-essentially-nonscillatory schemes in numerical relativity”. In: *Phys. Rev.* D94.6 (2016), p. 064062. DOI: 10.1103/PhysRevD.94.064062. arXiv: 1604.07999 [gr-qc].
- [412] Y. Fujimoto et al. “Gravitational Wave Signal for Quark Matter with Realistic Phase Transition”. In: (May 2022). arXiv: 2205.03882 [astro-ph.HE].
- [413] D. Radice. “General-Relativistic Large-Eddy Simulations of Binary Neutron Star Mergers”. In: *Astrophys. J.* 838.1 (2017), p. L2. DOI: 10.3847/2041-8213/aa6483. arXiv: 1703.02046 [astro-ph.HE].

- [414] R. Storn and K. Price. “Differential Evolution – A Simple and Efficient Heuristic for Global Optimization over Continuous Spaces”. In: *J. of Global Optimization* 11.4 (Dec. 1997), 341–359. ISSN: 0925-5001. DOI: 10.1023/A:1008202821328. URL: <https://doi.org/10.1023/A:1008202821328>.
- [415] T. Damour, A. Nagar, and M. Trias. “Accuracy and effectualness of closed-form, frequency- domain waveforms for non-spinning black hole binaries”. In: *Phys. Rev. D* 83 (2011), p. 024006. DOI: 10.1103/PhysRevD.83.024006. arXiv: 1009.5998 [gr-qc].
- [416] K. Chatziioannou et al. “Constructing Gravitational Waves from Generic Spin-Precessing Compact Binary Inspirals”. In: *Phys. Rev. D* 95.10 (2017), p. 104004. DOI: 10.1103/PhysRevD.95.104004. arXiv: 1703.03967 [gr-qc].
- [417] M. Maggiore et al. “Science Case for the Einstein Telescope”. In: *JCAP* 03 (2020), p. 050. DOI: 10.1088/1475-7516/2020/03/050. arXiv: 1912.02622 [astro-ph.CO].
- [418] A. Torres-Rivas et al. “Observing the post-merger signal of GW170817-like events with improved gravitational-wave detectors”. In: *Phys. Rev. D* 99.4 (2019), p. 044014. DOI: 10.1103/PhysRevD.99.044014. arXiv: 1811.08931 [gr-qc].
- [419] D. Martynov et al. “Exploring the sensitivity of gravitational wave detectors to neutron star physics”. In: *Phys. Rev. D* 99.10 (2019), p. 102004. DOI: 10.1103/PhysRevD.99.102004. arXiv: 1901.03885 [astro-ph.IM].
- [420] M. Punturo et al. “The third generation of gravitational wave observatories and their science reach”. In: *Class. Quant. Grav.* 27 (2010), p. 084007. DOI: 10.1088/0264-9381/27/8/084007.
- [421] D. Reitze et al. “Cosmic Explorer: The U.S. Contribution to Gravitational-Wave Astronomy beyond LIGO”. In: *Bull. Am. Astron. Soc.* 51 (July 2019), p. 035. arXiv: 1907.04833 [astro-ph.IM].
- [422] K. Ackley et al. “Neutron Star Extreme Matter Observatory: A kilohertz-band gravitational-wave detector in the global network”. In: *Publ. Astron. Soc. Austral.* 37 (2020), e047. DOI: 10.1017/pasa.2020.39. arXiv: 2007.03128 [astro-ph.HE].
- [423] M. Evans et al. “A Horizon Study for Cosmic Explorer: Science, Observatories, and Community”. In: (Sept. 2021). arXiv: 2109.09882 [astro-ph.IM].

- [424] S. Hild, S. Chelkowski, and A. Freise. “Pushing towards the ET sensitivity using ‘conventional’ technology”. In: (2008). arXiv: 0810.0604 [gr-qc].
- [425] B. Sathyaprakash et al. “Scientific Potential of Einstein Telescope”. In: *46th Rencontres de Moriond on Gravitational Waves and Experimental Gravity*. Aug. 2011, pp. 127–136. arXiv: 1108.1423 [gr-qc].
- [426] B. Sathyaprakash et al. “Scientific Objectives of Einstein Telescope”. In: *Class. Quant. Grav.* 29 (2012). Ed. by M. Hannam et al. [Erratum: *Class.Quant.Grav.* 30, 079501 (2013)], p. 124013. DOI: 10.1088/0264-9381/29/12/124013. arXiv: 1206.0331 [gr-qc].
- [427] F. Amann et al. “Site-selection criteria for the Einstein Telescope”. In: *Rev. Sci. Instrum.* 91.9 (2020), p. 9. DOI: 10.1063/5.0018414. arXiv: 2003.03434 [physics.ins-det].
- [428] M.-A. Bizouard and M. A. Papa. “Searching for gravitational waves with the LIGO and Virgo interferometers”. In: *Comptes Rendus Physique* 14 (2013), pp. 352–365. DOI: 10.1016/j.crhy.2013.03.001. arXiv: 1304.4984 [gr-qc].
- [429] J. Aasi et al. “Enhancing the sensitivity of the LIGO gravitational wave detector by using squeezed states of light”. In: *Nature Photon.* 7 (2013), pp. 613–619. DOI: 10.1038/nphoton.2013.177. arXiv: 1310.0383 [quant-ph].
- [430] B. P. Abbott et al. “Sensitivity of the Advanced LIGO detectors at the beginning of gravitational wave astronomy”. In: *Phys. Rev. D* 93.11 (2016). [Addendum: *Phys.Rev.D* 97, 059901 (2018)], p. 112004. DOI: 10.1103/PhysRevD.93.112004. arXiv: 1604.00439 [astro-ph.IM].
- [431] T. Callister. “A Thesaurus for Common Priors in Gravitational-Wave Astronomy”. In: (Apr. 2021). arXiv: 2104.09508 [gr-qc].
- [432] S. Nissanke et al. “Exploring short gamma-ray bursts as gravitational-wave standard sirens”. In: *Astrophys. J.* 725 (2010), pp. 496–514. DOI: 10.1088/0004-637X/725/1/496. arXiv: 0904.1017 [astro-ph.CO].
- [433] R. Abbott et al. “The population of merging compact binaries inferred using gravitational waves through GWTC-3”. In: (Nov. 2021). arXiv: 2111.03634 [astro-ph.HE].

- [434] N. Stergioulas, T. A. Apostolatos, and J. A. Font. “Nonlinear Pulsations in Differentially Rotating Neutron Stars: Mass-Shedding-Induced Damping and Splitting of the Fundamental Mode”. In: *Mon. Not. Roy. Astron. Soc.* 352 (2004), p. 1089. eprint: astro-ph/0312648.
- [435] S. Bernuzzi and A. Nagar. “Gravitational waves from pulsations of neutron stars described by realistic Equations of State”. In: *Phys. Rev.* D78 (2008), p. 024024. DOI: 10.1103/PhysRevD.78.024024. arXiv: 0803.3804 [gr-qc].
- [436] D. Radice, L. Rezzolla, and T. Kellermann. “Critical Phenomena in Neutron Stars I: Linearly Unstable Nonrotating Models”. In: *Class. Quant. Grav.* 27 (2010), p. 235015. DOI: 10.1088/0264-9381/27/23/235015. arXiv: 1007.2809 [gr-qc].
- [437] Y. Sekiguchi et al. “Effects of hyperons in binary neutron star mergers”. In: *Phys.Rev.Lett.* 107 (2011), p. 211101. DOI: 10.1103/PhysRevLett.107.211101. arXiv: 1110.4442 [astro-ph.HE].
- [438] E. R. Most et al. “Signatures of quark-hadron phase transitions in general-relativistic neutron-star mergers”. In: *Phys. Rev. Lett.* 122.6 (2019), p. 061101. DOI: 10.1103/PhysRevLett.122.061101. arXiv: 1807.03684 [astro-ph.HE].
- [439] A. Ghosh et al. “Testing general relativity using golden black-hole binaries”. In: *Phys. Rev.* D94.2 (2016), p. 021101. DOI: 10.1103/PhysRevD.94.021101. arXiv: 1602.02453 [gr-qc].
- [440] A. Bauswein, N. Stergioulas, and H.-T. Janka. “Exploring properties of high-density matter through remnants of neutron-star mergers”. In: *Eur. Phys. J.* A52.3 (2016), p. 56. DOI: 10.1140/epja/i2016-16056-7. arXiv: 1508.05493 [astro-ph.HE].
- [441] C. A. Raithel and E. R. Most. “Characterizing the breakdown of quasi-universality in the post-merger gravitational waves from binary neutron star mergers”. In: (Jan. 2022). arXiv: 2201.03594 [astro-ph.HE].
- [442] B. D. Lackey et al. “Extracting equation of state parameters from black hole-neutron star mergers. I. Nonspinning black holes”. In: *Phys.Rev.* D85 (2012), p. 044061. DOI: 10.1103/PhysRevD.85.044061. arXiv: 1109.3402 [astro-ph.HE].
- [443] J. S. Read et al. “Matter effects on binary neutron star waveforms”. In: *Phys. Rev.* D88 (2013), p. 044042. DOI: 10.1103/PhysRevD.88.044042. arXiv: 1306.4065 [gr-qc].

- [444] P. Landry and R. Essick. “Nonparametric inference of the neutron star equation of state from gravitational wave observations”. In: *Phys. Rev. D* 99.8 (2019), p. 084049. DOI: 10.1103/PhysRevD.99.084049. arXiv: 1811.12529 [gr-qc].
- [445] R. Essick, P. Landry, and D. E. Holz. “Nonparametric Inference of Neutron Star Composition, Equation of State, and Maximum Mass with GW170817”. In: *Phys. Rev. D* 101.6 (2020), p. 063007. DOI: 10.1103/PhysRevD.101.063007. arXiv: 1910.09740 [astro-ph.HE].
- [446] G. Lioutas, A. Bauswein, and N. Stergioulas. “Frequency deviations in universal relations of isolated neutron stars and postmerger remnants”. In: *Phys. Rev. D* 104.4 (2021), p. 043011. DOI: 10.1103/PhysRevD.104.043011. arXiv: 2102.12455 [astro-ph.HE].
- [447] S. Borhanian. “GWBENCH: a novel Fisher information package for gravitational-wave benchmarking”. In: *Class. Quant. Grav.* 38.17 (2021), p. 175014. DOI: 10.1088/1361-6382/ac1618. arXiv: 2010.15202 [gr-qc].
- [448] M. Agathos et al. “Constraining the neutron star equation of state with gravitational wave signals from coalescing binary neutron stars”. In: *Phys. Rev. D* 92.2 (2015), p. 023012. DOI: 10.1103/PhysRevD.92.023012. arXiv: 1503.05405 [gr-qc].
- [449] K. Barkett et al. “Gravitational waveforms of binary neutron star inspirals using post-Newtonian tidal splicing”. In: *Phys. Rev. D* 102.2 (2020), p. 024031. DOI: 10.1103/PhysRevD.102.024031. arXiv: 1911.10440 [gr-qc].
- [450] Z. Wu et al. “Radiation hydrodynamics modelling of kilonovae with SNEC”. In: *Mon. Not. Roy. Astron. Soc.* 512.1 (2022), pp. 328–347. DOI: 10.1093/mnras/stac399. arXiv: 2111.06870 [astro-ph.HE].
- [451] H. T. Janka et al. “Black hole: Neutron star mergers as central engines of gamma-ray bursts”. In: *Astrophys. J. Lett.* 527 (1999), p. L39. DOI: 10.1086/312397. arXiv: astro-ph/9908290.
- [452] E. Berger. “Short-Duration Gamma-Ray Bursts”. In: *Ann. Rev. Astron. Astrophys.* 52 (2014), pp. 43–105. DOI: 10.1146/annurev-astro-081913-035926. arXiv: 1311.2603 [astro-ph.HE].
- [453] K. P. Mooley et al. “A mildly relativistic wide-angle outflow in the neutron star merger GW170817”. In: *Nature* 554 (2018), p. 207. DOI: 10.1038/nature25452. arXiv: 1711.11573 [astro-ph.HE].

- [454] S. Rosswog and E. Ramirez-Ruiz. “Jets, winds and bursts from coalescing neutron stars”. In: *Mon. Not. Roy. Astron. Soc.* 336 (2002), p. L7. DOI: 10.1046/j.1365-8711.2002.05898.x. arXiv: astro-ph/0207576 [astro-ph].
- [455] K. Kiuchi et al. “Exploring binary-neutron-star-merger scenario of short- gamma-ray bursts by gravitational-wave observation”. In: *Phys. Rev. Lett.* 104 (2010), p. 141101. DOI: 10.1103/PhysRevLett.104.141101. arXiv: 1002.2689 [astro-ph.HE].
- [456] M. Ruiz et al. “Binary Neutron Star Mergers: a jet Engine for Short Gamma-ray Bursts”. In: *Astrophys. J.* 824.1 (2016), p. L6. DOI: 10.3847/2041-8205/824/1/L6. arXiv: 1604.02455 [astro-ph.HE].
- [457] T. Kawamura et al. “Binary Neutron Star Mergers and Short Gamma-Ray Bursts: Effects of Magnetic Field Orientation, Equation of State, and Mass Ratio”. In: *Phys. Rev. D* 94.6 (2016), p. 064012. DOI: 10.1103/PhysRevD.94.064012. arXiv: 1607.01791 [astro-ph.HE].
- [458] A. Murguia-Berthier et al. “The Properties of Short gamma-ray burst Jets Triggered by neutron star mergers”. In: *Astrophys. J. Lett.* 835.2 (2017), p. L34. DOI: 10.3847/2041-8213/aa5b9e. arXiv: 1609.04828 [astro-ph.HE].
- [459] V. Paschalidis. “General relativistic simulations of compact binary mergers as engines for short gamma-ray bursts”. In: *Class. Quant. Grav.* 34.8 (2017), p. 084002. DOI: 10.1088/1361-6382/aa61ce. arXiv: 1611.01519 [astro-ph.HE].
- [460] A. Pavan et al. “Short gamma-ray burst jet propagation in binary neutron star merger environments”. In: *Mon. Not. Roy. Astron. Soc.* 506.3 (2021), pp. 3483–3498. DOI: 10.1093/mnras/stab1810. arXiv: 2104.12410 [astro-ph.HE].
- [461] L. Sun et al. “Jet launching from binary neutron star mergers: Incorporating neutrino transport and magnetic fields”. In: *Phys. Rev. D* 105.10 (2022), p. 104028. DOI: 10.1103/PhysRevD.105.104028. arXiv: 2202.12901 [astro-ph.HE].
- [462] C. Palenzuela, S. Liebling, and B. Miñano. “Large eddy simulations of magnetized mergers of neutron stars with neutrinos”. In: *Phys. Rev. D* 105.10 (2022), p. 103020. DOI: 10.1103/PhysRevD.105.103020. arXiv: 2204.02721 [gr-qc].
- [463] J. Goodman. “Are gamma-ray bursts optically thick?” In: *Astrophys. J. Letters* 308 (Sept. 1986), p. L47. DOI: 10.1086/184741.
- [464] B. Paczynski. “Gamma-ray bursters at cosmological distances”. In: *Astrophys. J.* 308 (1986), pp. L43–L46.

- [465] D. Radice. “Binary Neutron Star Merger Simulations with a Calibrated Turbulence Model”. In: *Symmetry* 12.8 (2020), p. 1249. DOI: 10.3390/sym12081249. arXiv: 2005.09002 [astro-ph.HE].
- [466] D. Radice et al. “A new moment-based general-relativistic neutrino-radiation transport code: Methods and first applications to neutron star mergers”. In: *Mon. Not. Roy. Astron. Soc.* 512.1 (2022), pp. 1499–1521. DOI: 10.1093/mnras/stac589. arXiv: 2111.14858 [astro-ph.HE].
- [467] S. Akcay, R. Gamba, and S. Bernuzzi. “A hybrid post-Newtonian – effective-one-body scheme for spin-precessing compact-binary waveforms”. In: (May 2020). arXiv: 2005.05338 [gr-qc].
- [468] R. Gamba et al. “Effective-one-body waveforms for precessing coalescing compact binaries with post-Newtonian Twist”. In: (Nov. 2021). arXiv: 2111.03675 [gr-qc].
- [469] S. V. Chaurasia et al. “Gravitational waves and mass ejecta from binary neutron star mergers: Effect of large eccentricities”. In: *Phys. Rev. D* 98.10 (2018), p. 104005. DOI: 10.1103/PhysRevD.98.104005. arXiv: 1807.06857 [gr-qc].
- [470] H. Yang. “Inspiralling eccentric binary neutron stars: Orbital motion and tidal resonance”. In: *Phys. Rev. D* 100.6 (2019), p. 064023. DOI: 10.1103/PhysRevD.100.064023. arXiv: 1904.11089 [gr-qc].
- [471] J. Calderón Bustillo et al. “Mapping the Universe Expansion: Enabling Percent-level Measurements of the Hubble Constant with a Single Binary Neutron-star Merger Detection”. In: *Astrophys. J. Lett.* 912.1 (2021), p. L10. DOI: 10.3847/2041-8213/abf502. arXiv: 2006.11525 [gr-qc].
- [472] K. Kiuchi et al. “Global simulations of strongly magnetized remnant massive neutron stars formed in binary neutron star mergers”. In: *Phys. Rev. D* 97.12 (2018), p. 124039. DOI: 10.1103/PhysRevD.97.124039. arXiv: 1710.01311 [astro-ph.HE].
- [473] M. L. Chan et al. “Binary Neutron Star Mergers and Third Generation Detectors: Localization and Early Warning”. In: *Phys. Rev. D* 97.12 (2018), p. 123014. DOI: 10.1103/PhysRevD.97.123014. arXiv: 1803.09680 [astro-ph.HE].
- [474] S. Grimm and J. Harms. “Multiband gravitational-wave parameter estimation: A study of future detectors”. In: *Phys. Rev. D* 102.2 (2020), p. 022007. DOI: 10.1103/PhysRevD.102.022007. arXiv: 2004.01434 [gr-qc].

- [475] J. Harms et al. “GWFish: A simulation software to evaluate parameter-estimation capabilities of gravitational-wave detector networks”. In: (May 2022). arXiv: 2205.02499 [gr-qc].
- [476] M. J. Williams, J. Veitch, and C. Messenger. “Nested sampling with normalizing flows for gravitational-wave inference”. In: *Phys. Rev. D* 103.10 (2021), p. 103006. DOI: 10.1103/PhysRevD.103.103006. arXiv: 2102.11056 [gr-qc].
- [477] B. Zackay, L. Dai, and T. Venumadhav. “Relative Binning and Fast Likelihood Evaluation for Gravitational Wave Parameter Estimation”. In: (June 2018). arXiv: 1806.08792 [astro-ph.IM].
- [478] N. J. Cornish. “Heterodyned likelihood for rapid gravitational wave parameter inference”. In: *Phys. Rev. D* 104.10 (2021), p. 104054. DOI: 10.1103/PhysRevD.104.104054. arXiv: 2109.02728 [gr-qc].
- [479] C. Barbieri et al. “Electromagnetic counterparts of black hole-neutron star mergers: dependence on the neutron star properties”. In: *Eur. Phys. J. A* 56.1 (2020), p. 8. DOI: 10.1140/epja/s10050-019-00013-x. arXiv: 1908.08822 [astro-ph.HE].
- [480] R. Abbott et al. “Observation of Gravitational Waves from Two Neutron Star–Black Hole Coalescences”. In: *The Astrophysical Journal Letters* 915.1 (2021), p. L5. ISSN: 2041-8213. DOI: 10.3847/2041-8213/ac082e. URL: <http://dx.doi.org/10.3847/2041-8213/ac082e>.
- [481] L. Rezzolla, E. R. Most, and L. R. Weih. “Using gravitational-wave observations and quasi-universal relations to constrain the maximum mass of neutron stars”. In: *Astrophys. J.* 852.2 (2018). [*Astrophys. J. Lett.* 852, L25 (2018)], p. L25. DOI: 10.3847/2041-8213/aaa401. arXiv: 1711.00314 [astro-ph.HE].
- [482] I. Sagert et al. “Signals of the QCD Phase Transition in Core-Collapse Supernovae”. In: *Phys. Rev. Lett.* 102 (8 2009), p. 081101. DOI: 10.1103/PhysRevLett.102.081101. URL: <https://link.aps.org/doi/10.1103/PhysRevLett.102.081101>.
- [483] H.-T. Janka. “Explosion Mechanisms of Core-Collapse Supernovae”. In: *Ann. Rev. Nucl. Part. Sci.* 62 (2012), pp. 407–451. DOI: 10.1146/annurev-nucl-102711-094901. arXiv: 1206.2503 [astro-ph.SR].

- [484] A. W. Steiner, M. Hempel, and T. Fischer. “Core-collapse supernova equations of state based on neutron star observations”. In: *Astrophys. J.* 774 (2013), p. 17. DOI: 10.1088/0004-637X/774/1/17. arXiv: 1207.2184 [astro-ph.SR].
- [485] R. Abbott et al. “All-sky search for continuous gravitational waves from isolated neutron stars using Advanced LIGO and Advanced Virgo O3 data”. In: (Jan. 2022). arXiv: 2201.00697 [gr-qc].
- [486] P. O. Juliana. “Status and perspectives of Continuous Gravitational Wave searches”. In: *Galaxies* 10 (2022), p. 72. DOI: 10.3390/galaxies10030072. arXiv: 2202.01088 [gr-qc].
- [487] P. B. Covas et al. “Constraints on r-modes and Mountains on Millisecond Neutron Stars in Binary Systems”. In: *Astrophys. J. Lett.* 929.2 (2022), p. L19. DOI: 10.3847/2041-8213/ac62d7. arXiv: 2203.01773 [gr-qc].
- [488] R. Essick, S. Vitale, and M. Evans. “Frequency-dependent responses in third generation gravitational-wave detectors”. In: *Phys. Rev. D* 96.8 (2017), p. 084004. DOI: 10.1103/PhysRevD.96.084004. arXiv: 1708.06843 [gr-qc].
- [489] A. Gelman, W. R. Gilks, and G. O. Roberts. “Weak convergence and optimal scaling of random walk Metropolis algorithms”. In: *The Annals of Applied Probability* 7.1 (1997), pp. 110–120. DOI: 10.1214/aoap/1034625254. URL: <https://doi.org/10.1214/aoap/1034625254>.
- [490] J. Goodman and J. Weare. “Ensemble samplers with affine invariance”. In: *Comm. App. Math. and Comp. Sci.* 5.1 (2010). DOI: 10.2140/camcos.2010.5.65.
- [491] J. A. Christen and C. Fox. “A General Purpose Sampling Algorithm for Continuous Distributions (the t-walk)”. In: *Bayesian Analysis* 5.2 (2010), 263–282. DOI: DOI:10.1214/10-BA603.
- [492] R. M. Neal. “Slice sampling”. In: *Ann. Statist.* 31.3 (June 2003), pp. 705–767. DOI: 10.1214/aos/1056562461. URL: <https://doi.org/10.1214/aos/1056562461>.
- [493] B. Nelson, E. B. Ford, and M. J. Payne. “RUN DMC: An efficient parallel code for analyzing radial velocity observations using N -body integrations and differential evolution Markov chain Monte Carlo”. In: *The Astrophysical Journal Supplement Series* 210.1 (2013), p. 11. DOI: 10.1088/0067-0049/210/1/11. URL: <https://doi.org/10.1088%2F0067-0049%2F210%2F1%2F11>.

- [494] C. J. F. ter Braak and J. A. Vrugt. “Differential Evolution Markov Chain with snooker updater and fewer chains”. In: *Statistics and Computing* 18.4 (2008), pp. 435–446. DOI: 10.1007/s11222-008-9104-9.
- [495] G. O. Roberts and J. S. Rosenthal. “Optimal Scaling for Various Metropolis-Hastings Algorithms”. In: *Statistical Science* 16.4 (2001), pp. 351–367. ISSN: 08834237. URL: <http://www.jstor.org/stable/3182776>.
- [496] M. Karamanis and F. Beutler. “Ensemble Slice Sampling”. In: (Feb. 2020). arXiv: 2002.06212 [stat.ML].
- [497] P. M. Goggans and Y. Chi. “Using Thermodynamic Integration to Calculate the Posterior Probability in Bayesian Model Selection Problems”. In: *AIP Conference Proceedings* 707.1 (2004), pp. 59–66. DOI: 10.1063/1.1751356. URL: <https://aip.scitation.org/doi/abs/10.1063/1.1751356>.
- [498] S. Gupta et al. “Evaluation of Parallel Tempering to Accelerate Bayesian Parameter Estimation in Systems Biology”. In: (2018). arXiv: 1801.09831 [q-bio.QM].
- [499] N. Chopin and C. P. Robert. “Properties of nested sampling”. In: *Biometrika* 97.3 (2010), 741–755. ISSN: 1464-3510. DOI: 10.1093/biomet/asq021. URL: <http://dx.doi.org/10.1093/biomet/asq021>.
- [500] M. Betancourt et al. “Nested Sampling with Constrained Hamiltonian Monte Carlo”. In: (2011). DOI: 10.1063/1.3573613. URL: <http://dx.doi.org/10.1063/1.3573613>.
- [501] J. D. Hol, T. B. Schon, and F. Gustafsson. “On Resampling Algorithms for Particle Filters”. In: *2006 IEEE Nonlinear Statistical Signal Processing Workshop*. 2006, pp. 79–82. DOI: 10.1109/NSSPW.2006.4378824.
- [502] T. Dietrich et al. “Matter imprints in waveform models for neutron star binaries: Tidal and self-spin effects”. In: *Phys. Rev. D* 99.2 (2019), p. 024029. DOI: 10.1103/PhysRevD.99.024029. arXiv: 1804.02235 [gr-qc].
- [503] B. Brügmann et al. “Calibration of Moving Puncture Simulations”. In: *Phys. Rev. D* 77 (2008), p. 024027. DOI: 10.1103/PhysRevD.77.024027. arXiv: gr-qc/0610128 [gr-qc].
- [504] M. Thierfelder, S. Bernuzzi, and B. Brügmann. “Numerical relativity simulations of binary neutron stars”. In: *Phys. Rev. D* 84 (2011), p. 044012. DOI: 10.1103/PhysRevD.84.044012. arXiv: 1104.4751 [gr-qc].

Bibliography

- [505] S. Bernuzzi, A. Nagar, and R. De Pietri. “Dynamical excitation of space-time modes of compact objects”. In: *Phys. Rev. D* 77 (2008), p. 044042. DOI: 10.1103/PhysRevD.77.044042. arXiv: 0801.2090 [gr-qc].
- [506] E. Berti and A. Klein. “Mixing of spherical and spheroidal modes in perturbed Kerr black holes”. In: *Phys. Rev. D* 90.6 (2014), p. 064012. DOI: 10.1103/PhysRevD.90.064012. arXiv: 1408.1860 [gr-qc].
- [507] A. Nagar et al. “Multipolar effective one body model for nonspinning black hole binaries”. In: *Phys. Rev. D* 101.2 (2020), p. 024041. DOI: 10.1103/PhysRevD.101.024041. arXiv: 1904.09550 [gr-qc].

Curriculum Vitae

Personal details

Name Matteo
Surname Breschi
Address Kahlaische strasse 18, 07745 Jena, Germany
Email matteo.breschi@yahoo.it
Birth date 06.05.1992
Nationality Italian

Education

2018–2022 *Ph.D. in Theoretical Physics*

Friedrich-Schiller-Universität Jena, Theoretisch-Physikalisches Institute, Jena, Germany

SUPERVISOR Prof. Sebastiano Bernuzzi, sebastiano.bernuzzi@uni-jena.de
PROJECT TITLE Bayesian analysis of multi-messenger signals from compact binary system

2016–2018 *Master's degree in Theoretical Physics*

University of Pisa, Physics Department "E. Fermi", Pisa, Italy

SUPERVISOR Prof. Walter Del Pozzo, walter.delpozzo@unipi.it
PROJECT TITLE Hierarchical Bayesian analysis of post-Newtonian gravitational waveforms
GRADUATION October 2018

2011–2016 *Bachelor's degree in Physics*

University of Pisa, Physics Department "E. Fermi", Pisa, Italy

SUPERVISOR Prof. Giancarlo Cella, giancarlo.cella@unipi.it
PROJECT TITLE The Hulse-Taylor binary pulsar
GRADUATION March 2016

Achievements

2018 Scholarship for INFN–NSF/LIGO Exchange Summer School
at Rochester Institute of Technology (Rochester, NY, USA)
MENTOR: Prof. Richard O’Shaughnessy, richard.oshaughnessy@ligo.org

Ort, Datum

Unterschrift